UNIVERSIDADE DE LISBOA
FACULDADE DE CIÊNCIAS
DEPARTAMENTO DE ENGENHARIA GEOGRÁFICA, GEOFÍSICA
E ENERGIA

Joint inversion of geophysical and hydrologic data during water infiltration

Mohammad Farzamian

DOUTORAMENTO EM CIÊNCIAS GEOFÍSICAS E DA
GEOINFORMAÇÃO
(Especialidade em Geofísica)

2014

UNIVERSIDADE DE LISBOA
FACULDADE DE CIÊNCIAS
DEPARTAMENTO DE ENGENHARIA GEOGRÁFICA, GEOFÍSICA
E ENERGIA

Joint inversion of geophysical and hydrologic data during water infiltration

Mohammad Farzamian

Tese orientada pelo Prof. Doutor Fernando Monteiro Santos,
especialmente elaborada para a obtenção do grau de
doutor em Ciências Geofísicas e da Geoinformação
(Especialidade em Geofísica)

2014

Abstract

Soil apparent electrical conductivity is being considerably used as a surrogate measure for soil properties and hydraulic parameters. In this study, measurements of electrical conductivity were accomplished with Electrical Resistivity Tomography (ERT) and EM38 to develop the multiple datasets for defining spatiotemporal moisture content changes and also estimating the hydraulic properties of unsaturated soil under natural conditions and water injection test in two different sites.

The First study was conducted at the campus of University of Lisbon in a location where had a loam soil, low permeability and high water retention capacity and the second site was a sandy soil with high permeability and low water retention capacity located in the east of Lisbon. Appropriate relationships were derived based on the determination of the experimental curve ρ vs. S by in-situ investigation to convert the electrical conductivity maps inferred from ERT and Em38 data to moisture content distribution images. In addition, the subsurface temperature variations during the experiment was measured and the effect of temperature variations over ERT images were removed by assuming 2% change in electrical resistivity per°C change in temperature.

To estimate the hydraulic properties of unsaturated soil, flow simulations were firstly developed based on Richards' equation and the retention and hydraulic conductivity functions of van Genuchten parametric models. Afterward, Uncoupled and coupled hydrogeophysical approaches were used in order to constrain the van Genuchten parameters.

Resumo

A condutividade eléctrica tem sido frequentemente usada na investigação das propriedades e de parâmetros hidráulicos do solo. Neste estudo, foram realizadas medições de condutividade eléctrica usando a tomografia eléctrica (ERT) e o instrumento EM38, para a construção de uma base de dados a utilizar na avaliação das variações espacial e temporal das propriedades hidráulicas da camada não saturada do solo, em condições naturais e sujeito a um teste de injecção. Os estudos foram realizados em dois locais distintos.

O primeiro estudo foi realizado no Campus da Universidade de Lisboa, num terreno argiloso, com baixa permeabilidade e com uma elevada capacidade de retenção de água. O segundo estudo foi realizado num local com um solo arenoso, com permeabilidade elevada e fraca capacidade de retenção de água, localizado a leste de Lisboa. A partir dos modelos calculados dos dados de ERT e EM38, e de resultados laboratoriais de amostras colhidas nos locais, foram obtidas relações experimentais entre a resistividade e o conteúdo de água no solo. Estas relações foram posteriormente usadas para a conversão dos modelos ERT e EM38 em mapas de conteúdo de água. A temperatura em profundidade foi também medida durante a realização dos perfis. Estes valores foram usados para corrigir os dados de ERT, assumindo uma variação de 2% no valor da resistividade pela variação da temperatura, de 1º Celsius.

Foram realizadas simulações de fluxo de água, baseadas na equação de Richard, considerando os parâmetros de van Genuchten para a representação da retenção de condutividade hidráulica do solo, com o objectivo de obter estimativas das propriedades hidráulicas da camada não saturada do solo.

Keywords

ERT

EM38

Unsaturated zone

1D Coupled Hydrogeoelectrical Model

Moisture Content Estimation

Hydraulic Conductivity Estimation

Van Genuchten Parameters Estimation

Water Injection Test

Spatial Moment Analysis

Abbreviations

ERT- Electrical Resistivity Tomography

ECa- Apparent Electrical Conductivity

GPR- Ground-Penetrating Radar

EM- Electromagnetic Methods

LHS - Latin Hypercube Sampling

RMS - Root Mean Square

ACKNOWLEDGEMENTS

Undertaking the PhD program at University of Lisbon in the past four years was a truly exceptional experience in my life.
First of all I would like to acknowledge the expert guidance I received from my supervisor, Prof. Fernando Santos. I am very grateful to Fernando for the time and effort he has invested in helping me to achieve this goal. His profound understanding and insight about geophysics encouraged me to progress this research.

Throughout the achievement of this project I had support from a number of people, to whom I am deeply grateful. I wish to acknowledge Ivo Manuel Bernardo, Antonio Soares, Maria Caldeira and Joana Ribeiro for their continued technical support. I also thank Mohamed Ahmed Khalil, Miguel Esteves, Jamil Al-Halbouni and Milenko Markovic who have contributed to data collection and equipments preparation and installation.

I specially thank to Prof. Isabel Moitinho de Almeida and Vera Lopes from Geology Department of University of Lisbon for their continued technical support in the laboratory facilities and samples analysis during the Phd project.

The work would not have been possible without agreement of site access by “Companhia das Lezírias”. I am grateful to Jorge Simoes from “Companhia das Lezírias” for continued support for our work in Semora Correira. His support was always available at just the right moments.

I acknowledge the financial support from the grant of FCT (Referencia da bolsa: SFRH / BD / 66665/2009) that made this study possible

I would like to thank my all family members, my parents and brother for their support during my stay in Portugal. Finally, I would specially like to thank my fiancé Sana, for her support and encouragement while I was focused on finishing my thesis.

Table of contents

List of Tables

List of Figures

CHAPTER-ONE

Introduction

1.1. Introduction

The importance of soil characterization in the top 1-2 meters is widely recognized as a key parameter in agriculture and is critical in determining crop productivity through its impact on germination and growth of the plants. Development of the means to monitor soil moisture spatiotemporally in agricultural fields is very important for effective soil moisture management. Moreover, hydraulic conductivity is an important soil property when determining the potential for water movement in topsoil and in spite of its importance; soil hydraulic conductivity remains one of the most difficult of soil properties to assess and laboratory methods have limitations due to the size of the samples and usually in-situ methods are required to estimate hydraulic conductivity. Recent researches have shown that geophysical surveys using non-invasive and cost-effective methods are a viable alternative to direct and invasive measurements techniques for hydrologic characterization. Direct methods are based on drilling and cause major disturbance to the natural conditions. In addition, direct measurements by sample collection cannot be repeated over time on the same place, while hydrologic characterization of topsoil requires a repetition of data collection from a specified field site. Moreover, direct measurements do not usually cover a large area allowing only localized investigation which might cause uncertainty in hydrologic characterization of unsaturated zone. Geophysical methods, particularly ground-penetrating radar (GPR) and electrical resistivity tomography (ERT) (e.g. Binley et al., 2001, 2002a, 2002b; Cassiani et al., 2004; Binley and Kemna, 2005; Looms et al. 2008a, 2008b) and also Electromagnetic methods (EM) (e.g. McNeill 1986; Williams and Hoey, 1987; Kachanoski et al. 1988; Brevik and Fenton, 2002; Hezarjaribi and Sourell, 2007; Triantafilis and Santos, 2009, 2010) have been widely used to investigate the unsaturated zone.

Soil apparent electrical conductivity (ECa) measured by ERT and EM methods is a surrogate measure for soil properties and can be correlated with soil properties such as cation exchange capacity (e.g. Triantafilis et al. 2009), depth to bedrock and soil texture (e.g. Zhu et al., 2010), clay content and salinity (e.g. Corwin and Lesch, 2005) or moisture content (e.g. Binley et al., 2001) by empirical or semiempirical relationships (e.g. Archie, 1942) or established in-situ relationships (e.g. Binley et al., 2002a). Consequently, resistivity changes interpretation might be complicated unless variation in resistivity is dominated by one of these parameters.

Time-lapse geophysical monitoring is also a powerful tool to estimate those hydrologic variables that are time dependent such as water movement or hydraulic conductivity (e.g. Deiana et al., 2007). The major aim of time-lapse monitoring is to identify changes in resistivity at selected locations at different times accurately. This method is widely used to track tracer migration (e.g. Daily et al., 1992; Kemna et al., 2002; Slater and Sandberg, 2000, Singha and Gorelick, 2006; Vanderborght et al., 2005) monitor infiltration (e.g. Barker and Moore, 1998; Binley et al., 2002a; French and Binley, 2004; Dienna et al. 2007; Looms et al. 2008a, 2008b), underground steam injection (Ramirez et al., 1993); trichloroethylene remediation (Daily and Ramirez, 1995) and environmental studies to monitor the remediation and migration of contaminants (Hayley et al., 2009; LaBrecque et al., 1996a; Shima et al., 1996).

Selecting appropriate method and devise and designing a suitable configuration depends on several factors such as the depth of investigation, required accuracy and the site specification. Many researchers (e.g. van Overmeeren et al., 1997; Huisman et al., 2001, 2002; Cassiani et al., 2006) could successfully monitor the unsaturated zone by ground surface geophysical measurements where the depth of investigation was not deeper than a few meters below ground. As pointed out by Binley and Kemna, (2005) and discussed in Dienna et al. (2007), ground surface geophysical measurements is easier to achieve rather than borehole geophysical measurements which requires purpose-drilled boreholes and good contact between electrodes and formations and also requires less sophisticated data acquisition. Processing techniques are usually less time consuming and complex; however, ground surface geophysical measurements is rarely applied to the study of vadose-zone processes deeper than a few meters because of the limited sensitivity at depth.

In this study, measurements of ECa was accomplished by ground surface ERT and multi-height EM38 under natural condition and forced infiltration experiment to provide an insight into spatiotemporal soil moisture distribution and estimate hydrological parameters particularly hydraulic conductivity in unsaturated soil. We also investigated the EM38 quality and precision in monitoring ECa changes in comparison with ERT images.

1.2. Thesis aim and objectives

The main aim of this thesis is to explore the potential of ERT and EM38 for soil moisture determination and hydraulic conductivity estimation in unsaturated zone. To achieve the main aim, the key thesis objectives were to:

1. Two filed sites with different soil texture were selected to conduct geophysical measurements in topsoil. The first field site is a loam soil with low permeability and high water retention capacity while the second study was conducted in a deep Arenosol soil with high permeability and a low water retention capacity.

2. A capacitance sensor was used to monitor moisture content variations during the experiment in order to control the geophysical approach.

3. Studies of moisture content soil distribution in topsoil and water movement under forced-infiltration experiment were conducted using time-lapse ground surface ERT and multi height EM38.

4. In-situ relationships were derived based on the determination of the ECa and moisture content to convert the ECa changes to moisture content changes.

5. The subsurface temperature variations during the water–injection test were measured by using suitably placed sensors and the effect of the temperature variations over ERT images was removed.

6. Unsaturated flow model were simulated in order to estimate the hydraulic conductivity and constrain the hydrological model through a comparison of flow simulations with time-lapse geophysical images.

7. The mass loss, centre-of-mass vertical motion and vertical spread of geophysical images were evaluated using moment analysis.

8. A 1D coupled geoelectric-infiltration model was developed in order to estimate hydraulic conductivity.

1.3.Thesis organization

This thesis is divided into seven chapters:

Chapter One: provides a brief overview on geophysical application in unsaturated soil characterization and a description of the primary aim and objectives of the thesis.

Chapter Two: describes the study area including location, climate and soil information.

Chapter Three: describe and discuss ERT and electromagnetic (EM38) theory, equipments and forward and inversion process briefly. We also discuss soil texture test method, soil moisture sensors types, temperature influence in ERT and EM data, unsaturated flow simulation and moment analysis.

Chapter Four: investigates the ability of the EM38 sensor and ERT in monitoring moisture content changes and hydraulic conductivity estimation under natural condition and forced-infiltration experiment at the campus of university of Lisbon on a loam soil with low permeability and high water retention capacity.

Chapter Five: investigates the ability of the EM38 sensor and ERT in monitoring moisture content changes and hydraulic conductivity estimation under natural condition and forced-infiltration experiment in a deep Arenosol soil with high permeability and a low water retention capacity in Samora-Correia.

Chapter Six: Development of a 1D coupled geoelectric-infiltration model in order to estimate the hydraulic conductivity.

Chapter Seven: provides the key conclusions from the study and discusses recommendations for future study.

CHAPTER-TWO

Study Area

2.1. Location

Two study areas were selected to conduct the experiments. First study was carried out at the campus of University of Lisbon in a location where had a loam soil, low permeability and high water retention capacity. The second site was located at the state of Campanhia das Lezirias – Samorra Correia, approximately 50 km east of Lisbon. The soil was a deep Arenosol (FAO, 1988) with high permeability and a low water retention capacity. Locations of the first and second study areas are shown in Fig.2.1 and Fig.2.2 respectively.

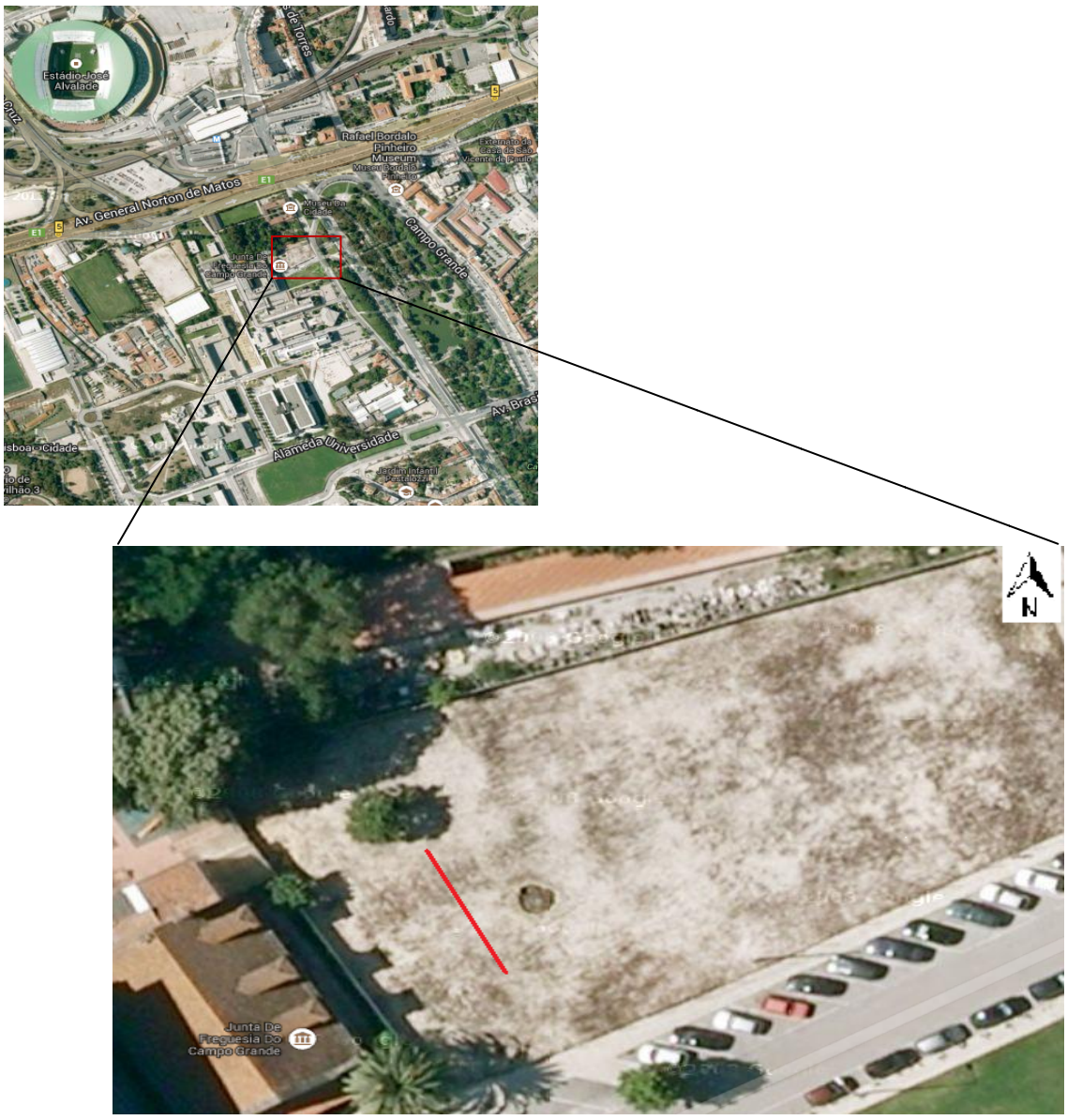

Fig.2.1. Location of the first study area at the campus of University of Lisbon.

Fig.2.2. Location of the second study area at the state of Campanhia das Lezirias – SamorraCorreia.

2.2. Site description

2.2.1. Campus of University of Lisbon

A field site with 20m length and 2m width was established to conduct the experiment on a 2m unsaturated soil. A tipping bucket rain gauge (Young Model 52202) was installed to measure the amount of precipitation over the period of experiment. The evaporation data was also collected from a nearby station to take in account for moisture content simulation. Transpiration amount was negligible in the field site.The study was carried out from September 2010 to August 2011. The mean maximum and minimum temperatures during the experiment period are shown in Fig. 2.3. In winter, the temperature occasionally dropped as low as 5 °C. The coldest month was January with monthly mean maximum and minimum temperatures of 14 °C and 9 °C. In summer, the temperature never exceeded 36 °C. The hottest month was Augusts with monthly mean maximum and minimum temperatures of 28 °C and 18°C. The monthly total rainfall and evaporation during the experiment are shown in Fig. 2.4. December had the highest monthly total rainfall with 294.5 mm (Figure 2.4) and an average of 17 rainy days. June and July were

almost without rainfall. The maximum total evaporation was observed in June with a total amounting to 101.9 mm. December had the lowest total evaporation.

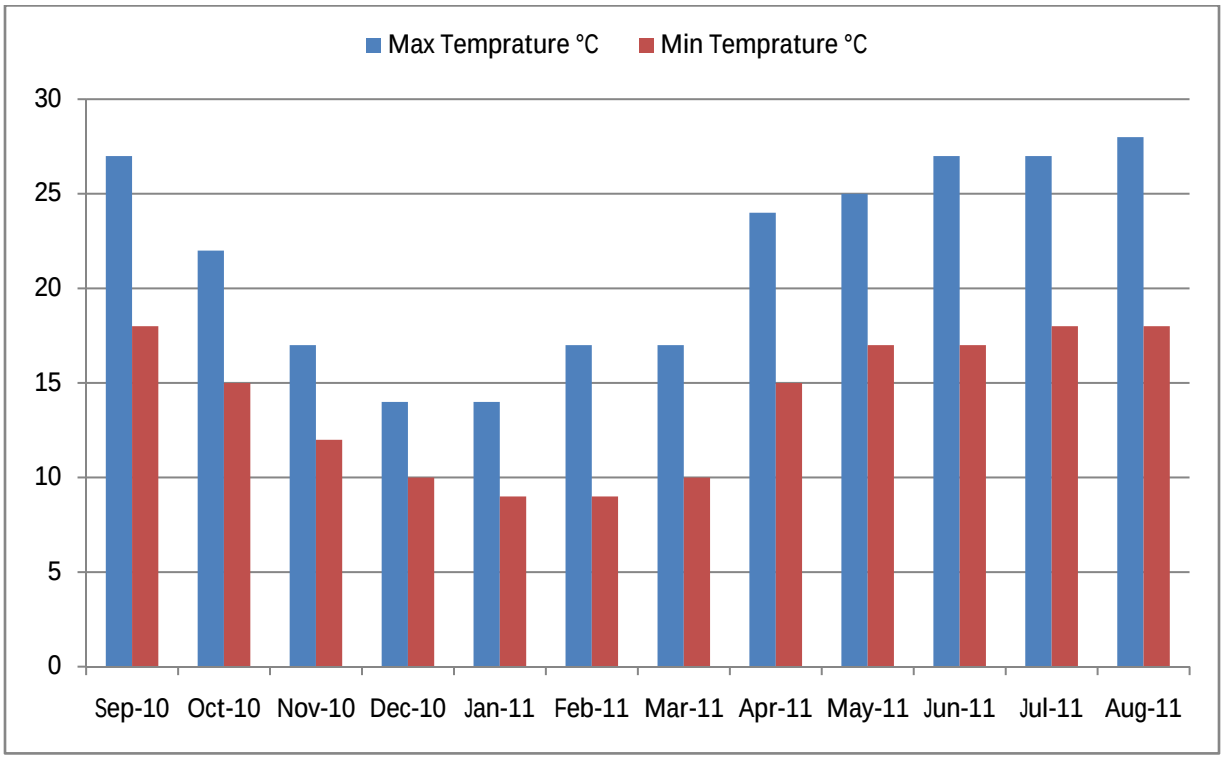

Fig. 2.3. Monthly mean maximum and minimum temperatures (°C) during the study period.

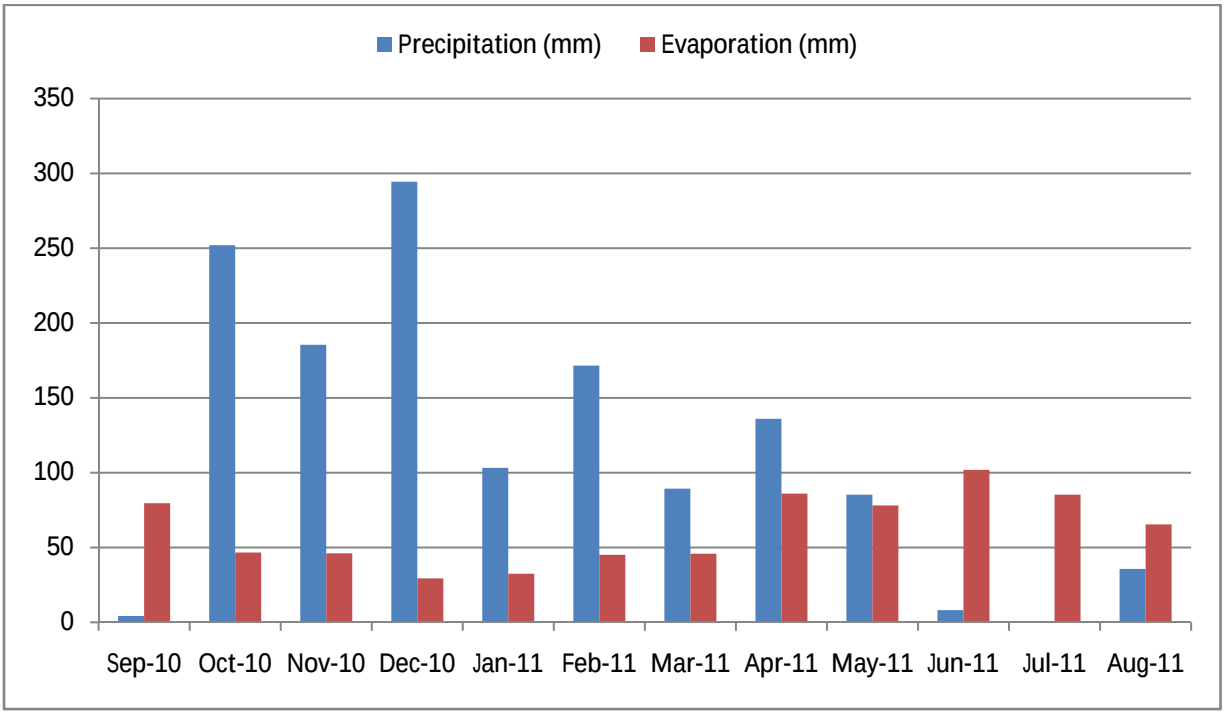

Fig.2.4. Monthly total rainfall and evaporation (mm) during the study period.

2.2.2. Campanhia das Lezirias – SamorraCorreia

A field site with 20m length and 2m width was established to conduct the experiment on a 2.5 m deep unsaturated sandy soil. Same to the previous study, a tipping bucket rain gauge (Young Model 52202) was installed to measure the amount of precipitation over period of experiment. Evaporation data was collected from a nearby station and used for moisture content simulation. Transpiration amount was negligible in the field site. The study was carried out from September 2011 to August 2012.

The mean maximum and minimum temperatures, monthly total rainfall and amount of evaporation during the experiment period are shown in Fig. 2.5 and 2.6. February had 14 rainy days and the highest monthly total rainfall amounting to 255.4 mm (Figure 2.5). June had the lowest monthly total rainfall with no precipitation. February and June had also the lowest and highest monthly total evaporation amounting to 30 mm and 102.2 mm respectively. The hottest month was August with average maximum and minimum daily temperatures of 29 °C and 19 °C. The coldest month was February with mean maximum and minimum monthly temperatures of 14 °C and 9 °C.

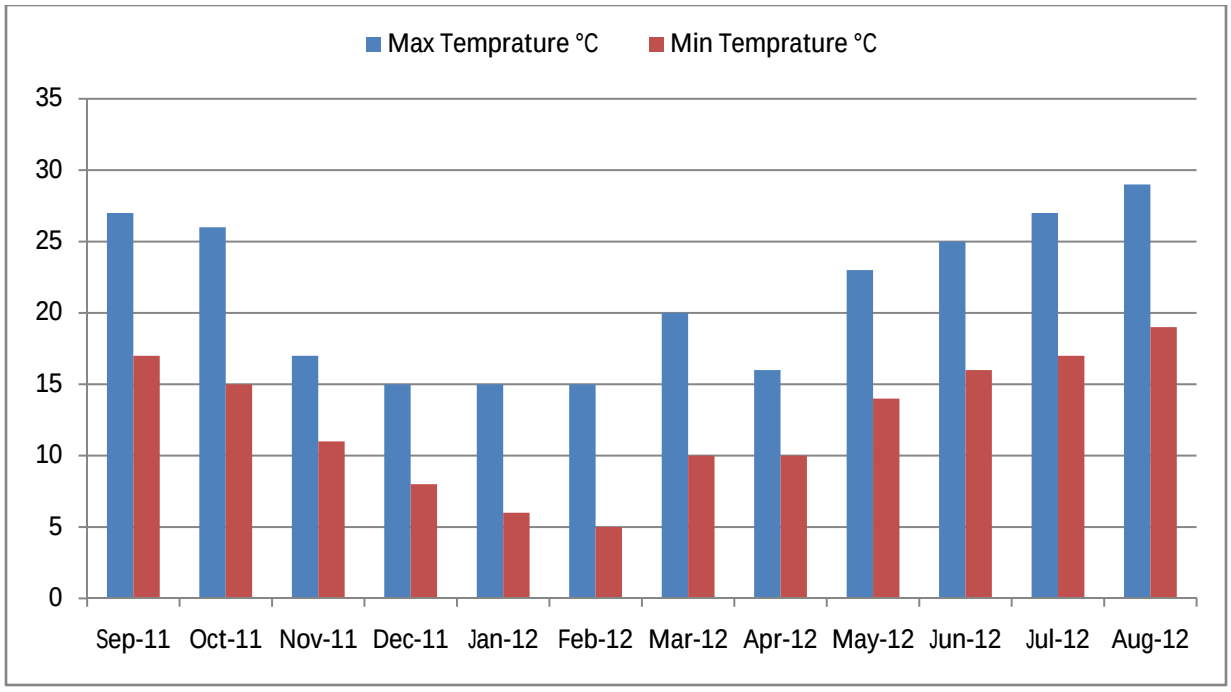

Fig. 2.5. Monthly mean maximum and minimum temperatures (°C) during the study period.

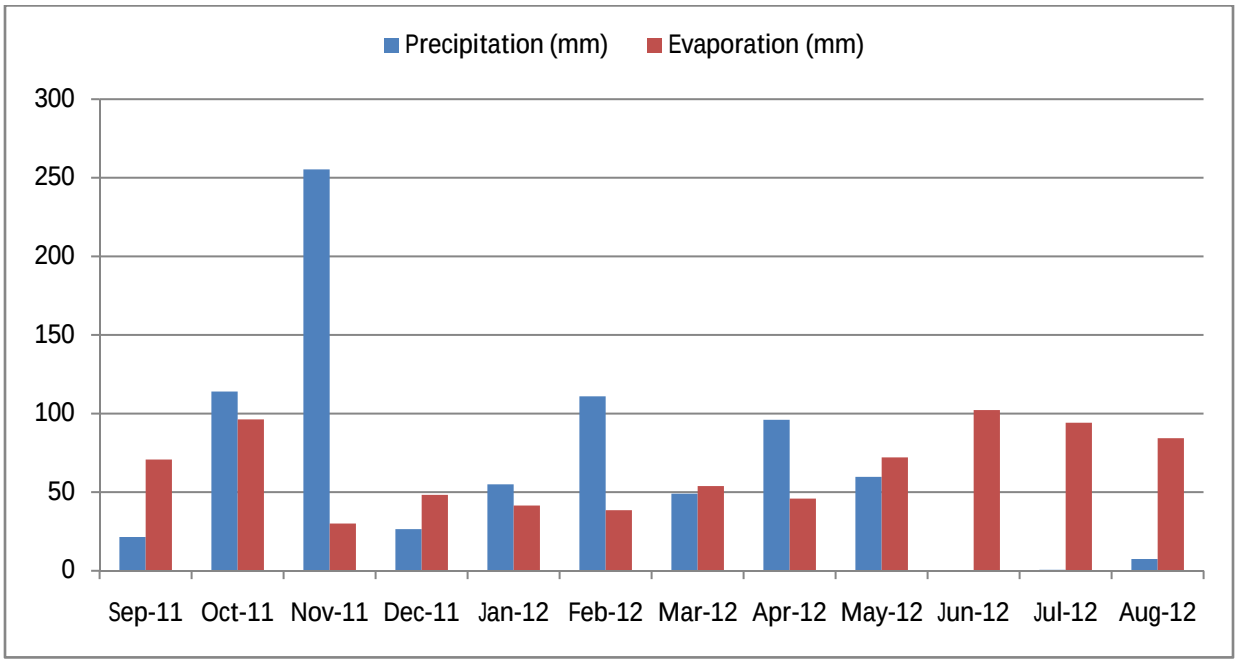

Fig.2.6. Monthly total rainfall and evaporation (mm) during the study period.

CHAPTER-THREE

Materials and Methods

3. Materials and Methods

Studies of water movement in the unsaturated sandstone were conducted using ground surface ERT and EM methods. We discuss the following aspects: 1) ERT and EM methods in monitoring of unsaturated zone, 2) inversion process, 3) unsaturated flow simulation, 4) moment analysis, 5) soil test methods, 6) field sensors for soil moisture measurement and 7) temperature influence in ERT and EM data.

3.1. EM methods

EM sensors typically integrate the below-ground response to interrogate electromagnetic fields, and if the depth response function of the probe is known, the potential exists to invert the integrated response to give a depth profile of the driving soil attribute (for example electrical conductivity). The EM technique was initially introduced for measuring and mapping soil salinity (Halvorson and Rhoades, 1974; McNeill, 1986; Wollenhaupt et al., 1986) and was extended to quantifying and mapping soil moisture content. The relationship between soil moisture content and ECa has been established by many investigators (e.g. Sheets and Hendrickx, 1995; Hanson and Kaita, 1997; Reedy and Scanlon, 2003; Brevik et al., 2006; Hezarjaribi and Sourell, 2007). Hossain, (2008) presented a comprehensive review of EM sensors in water content estimation. Different methods were used to calibrate the EM sensors against water content. For instance Kachanoski et al. (1988) developed the relationship between ECa and moisture content, in a non-saline soil with low concentrations of dissolved electrolytes and found that the ECa explained 96% of the spatial variation in the soil moisture (surface to 0.5 m depth) in a 1.8-ha study area. However, they did not find any significant relationship between ECa and moisture content at depths below 0.5 m. Hanson and Kaita, (1997) conducted an experiment to observe the response of moisture content in soils of three salinity levels. The R^2 values for the horizontal dipole orientation were 0.81, 0.89, 0.92 for low, medium and high salinity level, respectively, and for the vertical dipole orientation were 0.76, 0.94 and 0.95. The EM38 was calibrated against neutron probe-based estimates of moisture content. Sherlock and McDonnell, (2003) found a good relationship (R2 = 0.70) between ECa and gravimetrically determined moisture content from soil samples taken at a depth of 0.2 m. The same relationship was observed by Brevik et al., (2006).

3.1.1.The EM38

The EM38 is a widely-used electromagnetic instrument for soil characterization developed by Geonics Ltd. (Ontario, Canada). It comprises two electrical coils, one a transmitter (Tx) and the other a receiver (Rx), placed 1 meter apart in a wooden frame (Fig.3.1). The transmitter coil is excited with a sinusoidal current at a frequency of 14.6 kHz that creates a time-varying magnetic field in the vicinity of the coil and when activated, the time-varying magnetic field induces eddy currents in the soil. The magnitude of the eddy currents is proportional to the electrical conductivity of the soil in that layer of the soil (Fig.3.2). Each current loop generates a secondary magnetic field proportional to the value of the current flowing within the loop. A fraction of the secondary magnetic field from each loop is intercepted by the receiver coil of the instrument; the sum of these signals is amplified and formed into an output voltage. The process of electromagnetic induction results in a secondary magnetic field which is 90º out of phase with the primary field. The sensor coil is designed to measure this out-of-phase component, hence the notion of quadrature (Hossain, 2008). At low induction numbers, the apparent conductivity σ_a in the vicinity of the transmitter coil is determined by the ratio of the magnitudes of the out-of-phase secondary to primary magnetic fields using the following equation (McNeill, 1980):

$$\sigma_a = \frac{4}{i\omega\mu_0\sigma s^2}\left[\frac{H_s}{H_p}\right]_Q \qquad (3.1)$$

where $\left[\frac{H_s}{H_p}\right]_Q$ is the ratio of the out-of-phase secondary to primary magnetic fields,

(Subscript 'Q' denotes quadrature, that is, 90° out of phase)

σ_a= apparent electrical conductivity

$\omega = 2\pi f$ (f = frequency in Hz)

μ_0= permeability of free space = $4\pi * 10^{-7}$ kg m/s2.A2

s = distance between transmitter and sensing coils or inter-coil spacing and is equal to 1 m in EM38

A = area of the (transmitter) coil

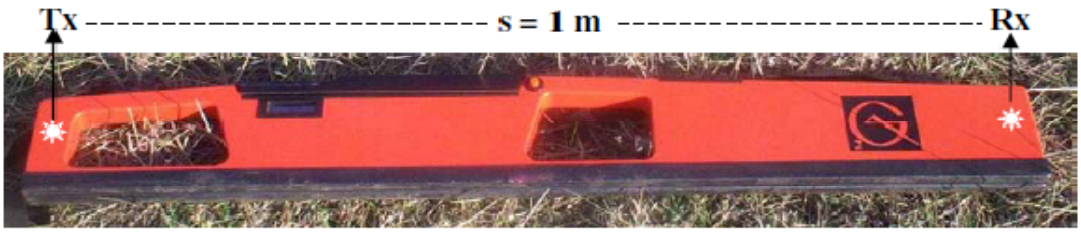

Figure.3.1. The photograph of the EM38 showing the locations of transmitter coil (Tx), receiver coil (Rx), and inter-coil spacing (s) (Hossain, 2008).

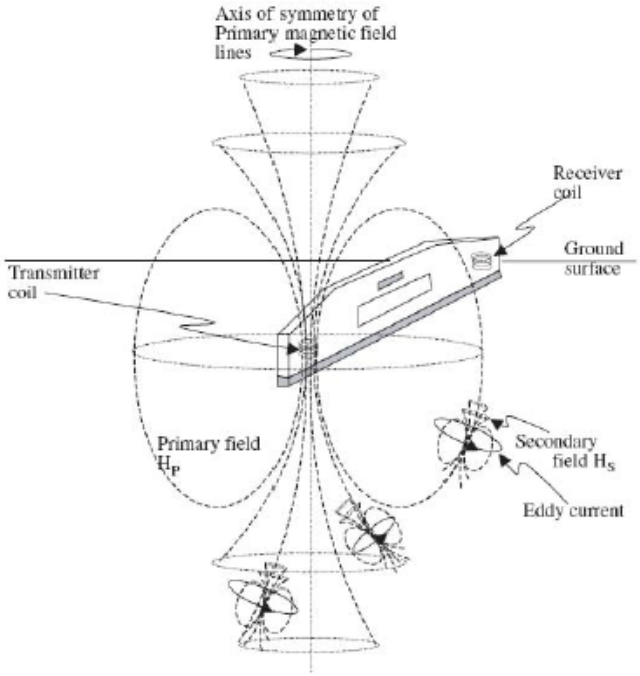

Figure 3.2. Schematic diagram of the Geonics EM38 unit showing locations of transmitter and receiver coils, the spatial structure of the primary magnetic field during the peak current phase within the transmitter coil and that of the secondary magnetic fields generated in response eddy currents generated in the conductive medium. In this vertical dipole mode of operation, the primary field lines shown (HP) have cylindrical symmetry around the vertical axis (Lamb *et al.* 2005)

In cylindrical coordinates, the axial and radial components of the primary magnetic field in the vicinity of a magnetic dipole are given respectively by (Wait, 1982):

$$H_{pz}(r,z) = \frac{IA}{4\pi}\left[\frac{3z^2}{(r^2+z^2)^{5/2}} - \frac{1}{(r^2+z^2)^{3/2}}\right] \quad (3.2)$$

$$H_{Pr}(r,z) = \frac{IA}{4\pi}\left[\frac{3rz}{(r^2+z^2)^{5/2}}\right] \quad (3.3)$$

where, H_{pz} is the axial component of the magnetic field

H_{Pr} is the radial component of the magnetic field

z is the axial distance, along the axis of the field symmetry, from the coil

r is the radial distance, perpendicular to the axis of field symmetry, from the coil

A is the area of the (transmitter) coil

The approximation in (Equation 3.1) holds for both horizontal as well as vertical dipole modes (McNeill, 1980).

A key assumption in understanding the nature of the integrated response of the surface measurement of EM instruments like the EM38 is that individual, below ground 'current loops' are not influenced by others nearby (McNeill, 1980). Consequently, the net secondary magnetic field at the receiver is the sum of the independent secondary magnetic fields from each of the individual current loops. This gives rise to the notional depth-response of the EM sensor according to the relative contributions of secondary magnetic fields arising from different depths directly below the sensor. For vertical and horizontal dipole configurations (McNeill, 1980), these contributions are given respectively as:

$$\varphi^V(z) = \left[\frac{4z}{(4z^2+1)^{3/2}}\right] \quad (3.4)$$

$$\varphi^H(z) = 2 - \left[\frac{4z}{(4z^2+1)^{1/2}}\right] \quad (3.5)$$

Here z is the ratio of axial distance below the sensor, and s is inter-coil spacing (1 m). Both of these expressions, shown graphically in Figure 3.3(a), are developed from the notion that the sensor is placed, regardless of vertical or horizontal dipole mode of operation, on the surface of a conductive half-layer, whereby there is no conductive medium above the surface ($z > 0$) and a conductive medium below the surface ($z < 0$) (Hossain, 2008). The exact amplitude and phase of the secondary field will differ from those of the primary field as a result of soil properties (e.g. clay content, moisture content and salinity), spacing of the coils and their orientation, frequency, and distance from the soil surface (Hendrickx et al., 2002). Although Equations 3.4 and 3.5

imply no limit to the penetration depth of EM38, the 'effective' measurement depth of operation is accepted as 1.5 m and 0.75 m as 70% of the integrated response generated from those depths for vertical and horizontal dipole operations respectively (McNeill, 1980). Rhoades and Corwin, (1981), on the other hand report that the EM38 is primarily responsive to a depth of 1.2 m compared to other depths. Notwithstanding this discrepancy, the effective measurement depths of EM38 is accepted as being appropriate to agriculture as the depths represent the root zone area (Corwin and Lesch, 2005).

3.1.2. Cumulative response of a multilayered earth

The secondary magnetic field measured at the receiver is the sum of the independent magnetic fields from each individual induced current loop. The relative contribution to the secondary magnetic field, measured at the receiver, due to the homogeneous material within a thin horizontal layer at a depth z was estimated in Equation 3.4 and 3.5 and shown in Fig.3.3a. Then the relative contribution to the secondary magnetic field from all material below a depth z can be expressed by the cumulative function $R_{H,V}$ (for horizontal or vertical coplanar transmitter–receiver dipole configurations) as defined by McNeill, (1980):

$$R_{H,V} = \int_z^{\infty} \varphi_{H,V}(z)dz \tag{3.6}$$

Taking into account these definitions, the response of an M-layer earth is calculated adding the contribution from each layer independently, weighted accordingly to its conductivity and depth as:

$$\sigma_a = \sigma_1[1 - R(Z_1)] + \sum \sigma_i[R(Z_{i-1} - R(Z_i)] + \sigma_M R(Z_{M-1}) \tag{3.7}$$

The sum is extended from layer 2 up to layer M-1. σ_i represents the conductivity of the ith layer and z_i is the depth of the ith layer divided by intercoil spacing. The expressions for the functions R(Z) are (McNeill, 1980):

$$R_V(Z) = \frac{1}{(4Z^2+1)^{1/2}} \tag{3.8}$$

$$R_H(Z) = (4Z^2 + 1)^{1/2} - 2Z \quad (3.9)$$

where Z is the depth z divided by intercoil spacing s. The use of the cumulative function in layered-earth models is mainly determined by the low induction number condition that, in a homogeneous half-space, happens when the ratio of the transmitter–receiver separation to the skin depth is much lesser than 1(McNeill, 1980).

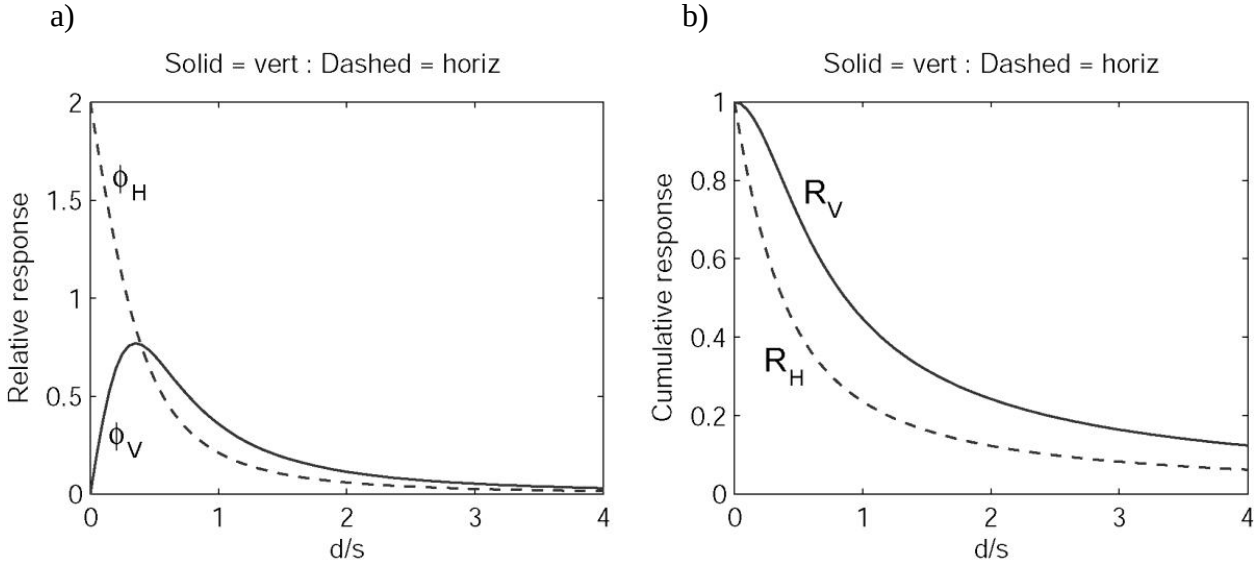

Figure 3.3 a) Relative responses of EM38 to the secondary magnetic field in a homogenous profile at different depths for the vertical (—) and horizontal (---) dipole configurations. b) Cumulative responses versus depth for vertical (—) and horizontal (---) dipole configurations from all material below depth (z). Curves calculated from McNeill (1980).

3.1.3. Inversion algorithm

The nonlinear smoothness-constrained inversion algorithm given in Sasaki (1989) has been adopted in this work. Relevant aspects of this algorithm application will be given here (See Sasaki (1989) for full description of this algorithm). The earth model used in the inversion process consists of a number of blocks whose distribution and size depend on the locations and number of intercoil spacing used in data acquisition. A forward modeling subroutine, based on the cumulative response explained in 3.1.2 is used to calculate the apparent conductivity response of the model. The optimization equations are represented as follows (Sasaki, 1989):

$$(W^T J^T W J + \lambda C^T C)\delta p = W J^T W \delta d \quad (3.10)$$

where δp is the vector containing the corrections applicable to the parameters (block conductivities, σj) of an initial model, δd is the vector of the differences between calculated and observed apparent conductivity (y). J is the Jacobian matrix whose elements are given by:

$$J_{ij} = \frac{\partial y_i}{\partial \sigma_j} \quad (3.11)$$

The diagonal matrix W describes the accuracy of the measured data and includes the reciprocals of the data variances. The superscript T denotes the transpose operation. The quantity λ is a Lagrange multiplier (damping factor, sensu stricto) that controls the amplitude of the parameter corrections and whose best value is empirically determined. The elements of the matrix C are the coefficients of the values of the roughness in each parameter, which is defined in terms of the four neighbors (north, south, east and west), as:

$$\delta r_j = \delta_{PjE} + \delta_{PjW} - 4\delta_P + \delta_{PjN} + \delta_{PjS} \quad (3.12)$$

that is, the elements of C are -4, 1 or 0. An iterative process allows obtaining the final model, with its response fitting the data set in a least square sense. The misfit between data and model response is given by:

$$Q = \left(\frac{\delta d^T \delta d}{N}\right)^{1/2} \quad (3.13)$$

where N represents the number of data points (Santos, 2004).

3.2. ERT

3.2.1. Basic resistivity theory

ERT is the method for calculation of the subsurface resistivity distribution from multiple electrical resistance measurements made using a quadrapole arrangement of electrodes (Fig.3.4). The electrodes are placed either on the ground surface or in the borehole and a 2-D or 3-D image

of the resistivity can be achieved by varying the location and spacing of the electrodes. The fundamental physical law used in resistivity surveys is Ohm's Law that governs the flow of current in the ground. Different quadrapole arrangements of electrodes are used in order to images resistivity distribution. In practically all surveys, the potential difference between two points (normally on the ground surface) is measured (Fig.3.4). The potential difference is then given by:

$$\rho_a = k \frac{\Delta \emptyset}{I} \tag{3.14}$$

$$K = \frac{2\pi}{\left[\frac{1}{r_{AM}} - \frac{1}{r_{BM}} - \frac{1}{r_{AN}} - \frac{1}{r_{BN}}\right]} \tag{3.15}$$

K is a geometric factor that depends on the arrangement of the four electrodes. The calculated resistivity value is an apparent resistivity value that is the resistivity of a homogeneous ground that will give the same resistance value for the same electrode arrangement. The relationship between the apparent resistivity and the true resistivity is a complex relationship and need to be achieved using inversion theory (will be briefly discussed 3.2.4) to determine the true subsurface resistivity from the apparent resistivity. Figure 3.5 shows the most common arrays used in resistivity surveys together with their geometric factors. In our study, we performed 2-D imaging surveys using Wenner, Schlumberger and dipole-dipole arrays. Among the characteristics of an array usually the depth of investigation, the sensitivity of the array to vertical and horizontal changes in the subsurface resistivity and the signal strength are the most important to consider. Loke (2001) presented a comprehensive study of different arrays weaknesses and strengths. The Wenner array is relatively sensitive to vertical changes in the subsurface resistivity below the center of the array. However, it is less sensitive to horizontal changes in the subsurface resistivity. In general, the Wenner array is good in resolving vertical changes (i.e. horizontal structures), but relatively poor in detecting horizontal changes (i.e. narrow vertical structures). The Wenner array has a moderate depth of investigation. The signal strength is inversely proportional to the geometric factor used to calculate the apparent resistivity value for the array. Among the common arrays, the Wenner array has the strongest signal strength. This can be an important factor if the survey is carried in areas with high background noise. In contrast, the dipole-dipole array is very sensitive to horizontal changes in resistivity, but relatively insensitive to vertical changes in the resistivity. That means that it is good in mapping vertical structures,

such as dykes and cavities, but relatively poor in mapping horizontal structures such as sills or sedimentary layers and also this array has the very small signal strength for large values of the “n” factor. The voltage is inversely proportional to the cube of the “n” factor. The Schlumberger array is moderately sensitive to both horizontal and vertical structures. In areas where both types of geological structures are expected, this array might be a good compromise between the Wenner and the dipole-dipole array.

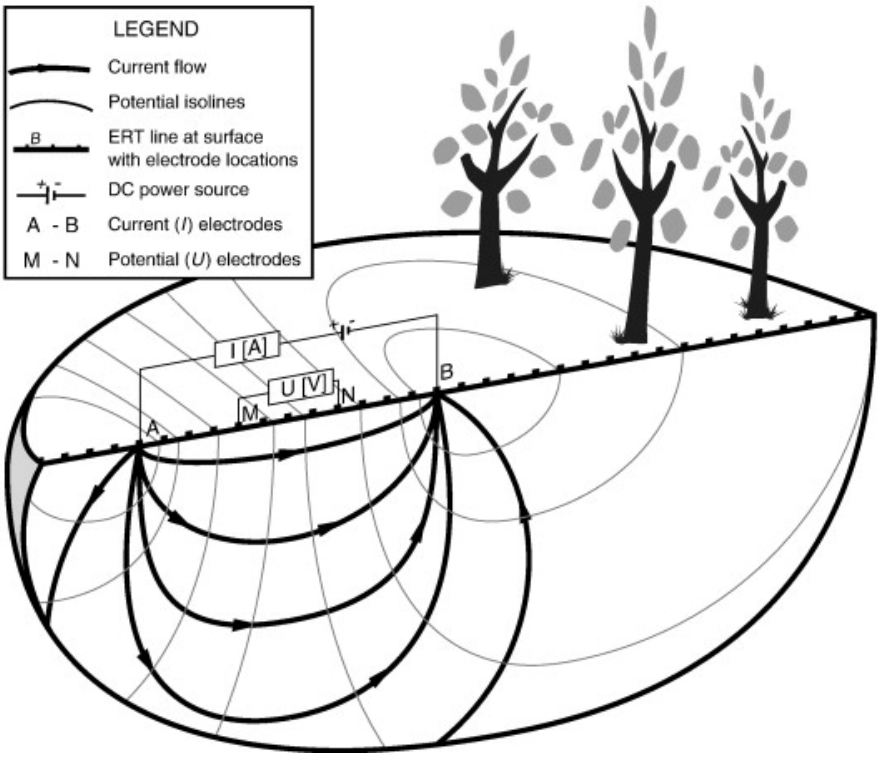

Fig.3.4. A conventional array with four electrodes to measure the subsurface resistivity

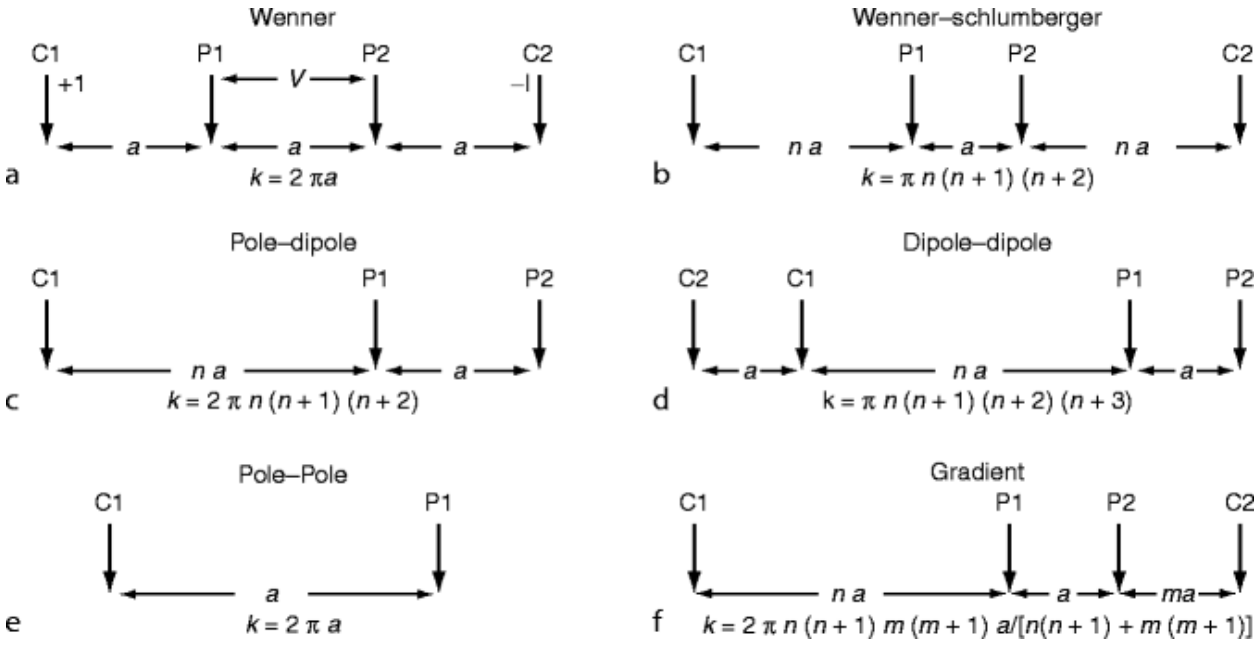

Fig.3.5. Common arrays used in resistivity surveys and their geometric factors

3.2.2. 4 point light 10W

4 point light 10W is a resistivity meters from Lippman company for geoelectric resistivity sounding and induced polarization measurement. The devise is high power, very low cost induced polarization earth resistivity meter in a small package (Fig.3.6) and covers Schlumberger soundings up to AB/2 = 1km. It is suitable for mapping, monitoring and laboratory works. Geotest software is a software package (Fig.3.7) for remote controlling of 4 point light 10W in combination with active boxes (Fig.3.8) for geoelectric tomography using multi-electrodes (Fig.3.9). Two electrodes serve as current emitting electrodes and are usually named A and B. Two other electrodes (M and N) measure the potential difference (Fig.3.7).

Fig.3.6. 4 point light 10W device for resistivity and IP measurements.

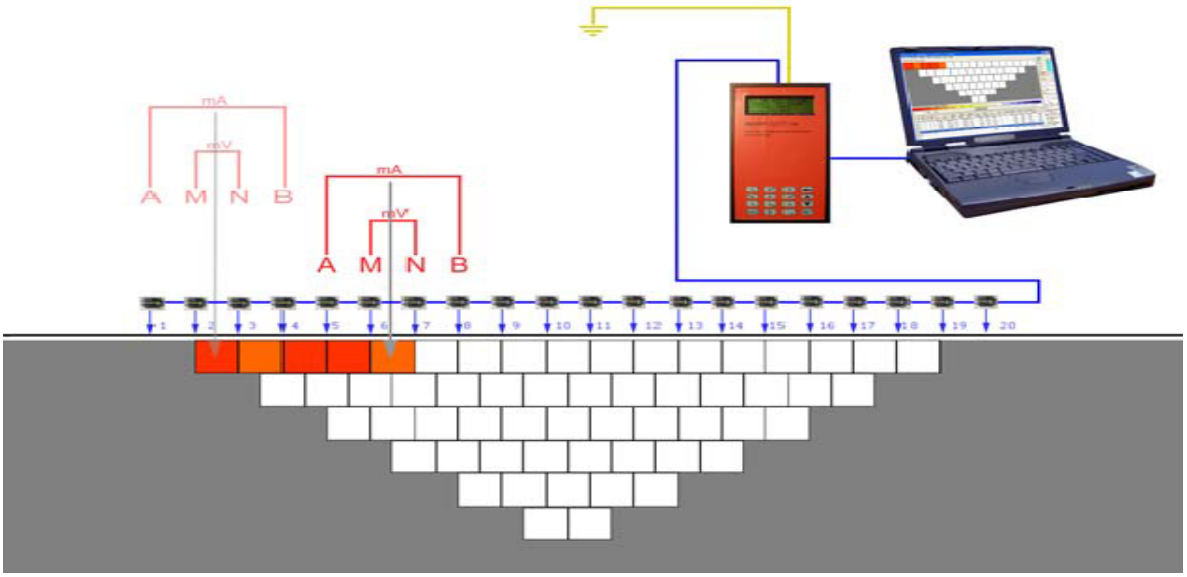

Fig. 3.7. The graphical display of the measured resistiviteis (Pseudo Section) by using multi-electrode connections in Geotest software. The displayed example explains resistivity monitoring using Wenner configuration. The electrode distances are integer multiples of the minimum electrode separation. Expanding the spread results in an increasing investigation depth.

Fig.3.8. A sample of active box for multi-electrode connection.

Fig.3.9. A view of resistivity mapping using 4 point light 10W device and chain of active boxes for multi-electrodes connections.

3.2.3. 1D resistivity forward modeling

The potential due to a point source of current I at a point (r,o) on the surface of a stratified earth expressed by:

$$V(r,o) = \frac{I}{2\pi}\int_0^\infty T(\lambda)J_0(\lambda r)d\lambda \quad (3.16)$$

where

$$T(\lambda) = \rho[1 + 2B(\lambda)] \quad (3.17)$$

where

λ = integration variable; has the dimension of inverse distance,

$B(\lambda)$ = kernel function,

$T(\lambda)$ = resistivity transform function.

The following relation also exists between kernel function and raised kernel function:

$$H(\lambda) = B(\lambda) + \frac{1}{2} = T(\lambda)/(2\rho) \quad (3.18)$$

where $H(\lambda)$ is raised kernel function.

The ERT surveys were carried out using Schlumberger electrode configuration in forced-infiltration experiment for development of 1D coupled geoelectric-infiltration and therefore, numerical solution for this array will be discussed here briefly which will be used in chapter 6. For Schlumberger electrode configuration using Equation (3.16) we have:

$$\rho_a = s^2\int_0^\infty T(\lambda)\, J_1(\lambda s)\lambda d\lambda \quad (3.19)$$

where s is half the current electrode spacing.

An explicit expression for the resistivity transform can be obtained by applying Hankel's inversion (see Watson, 1966) of the Fourier-Bessel integral to the expression of the apparent resistivity in the Schlumberger arrangement given by:

$$T(\lambda) = \int_0^{\infty} [\rho_a(s)\ \ J_1(\lambda s)/s\ ]\lambda d\lambda \quad (3.20)$$

New variables are introduced defined by:

$$x = \ln s \text{ and } y = \ln(1/\lambda) \quad (3.21)$$

Substituting (3.21) in (3.20) we have:

$$T(\lambda) = \int_{-\infty}^{\infty} \rho_a(x)\ J_1(1/e^{y-x})dx \quad (3.22)$$

This is a convolution integral relating the input $\rho_a(x)$ to the output T(y). In the frequency domain the input-output relationship given by (3.22) takes the simple algebraic form since that the ρ_a and T functions belong to a linear system (Robinson, 1967):

$$F(f) = Gs(f)\ Hs(f) \quad (3.23)$$

where $F(f) \longleftrightarrow T(y)$; $Gs(f) \longleftrightarrow \rho_a(x)$

Hs(f) = Frequency characteristic of the resistivity filter, or simply the filter characteristic.

The symbol $\longleftrightarrow$ denotes a Fourier transform pair.

To determine the filter characteristic, following partial resistivity function for the Schlumberger system was chosen whose exact resistivity transform was known (Koefoed, 1968).

$$\Delta\rho_{as}(x) = (\exp 3x)/(1 + \exp 2x)^{5/2} \quad (3.24)$$

$$T(y) = \frac{1}{3}\exp(-y)\exp(-\exp(-y)) \quad (3.25)$$

Their Fourier transforms are then found by numerical integration, and the modulus Q(f) and phase Φ(f) of the quotient F/G determine H. For a given sampling interval Δx the Nyquist frequency is $f_N = 1/(2\Delta x)$, and the corresponding sinc-response function is given by:

$$C(x) = 1/f_n \int_0^{f_n} Q(f)\cos(\Phi(f) + 2\pi fx)\, df \quad (3.26)$$

The apparent resistivity ρ_{as} in the sampling points $x_i = i\Delta x$ is then given approximately by:

$$\Delta\rho_{as}(i\Delta x) \sim \sum_{j_{Min}}^{j_{Max}} T((i-j)\,\Delta x + s)c(j\Delta x - s) \tag{3.27}$$

where j_{Min} and j_{Max} are chosen so that the filter coefficients with smaller or larger indices can be neglected. As the expression of the apparent resistivity function is complicated, the Fourier transform of the T(y) functions were first determined and the Fourier transform of the apparent resistivity functions were then obtained from it by the application of (3.23) (Ghosh, 1971). Fourier transform of the T(y) functions were estimated in Johansen, (1975). Apart from the sampling frequency there are two factors affecting the accuracy: the tails of the filter must be cut off at some point, and the coefficients can only be calculated with a limited precision. The analysis of the asymptotic behavior (demonstrated in Johansen, 1975) indicates that j= (-100) – (40) fulfills the expectations. The filter coefficients corresponding to a sampling frequency of 10 points per decade were calculated in Johansen, (1975) and the actual precision of the filter was also tested and proved in the same way as suggested by Ghosh, (1971).

3.2.4. 1D resistivity inversion

Let the m-dimensional vector p (p_l, p_2... p_n) stand for the m = 2N-1 resistivities and thicknesses (ρ_1, d_l, ... , ρ_N) i.e.

$$p_{2j-1} = \rho_j \qquad j = 1, \dots, N \tag{3.29}$$

$$p_{2j} = d_j \qquad j = 1, \dots, N-1 \tag{3.30}$$

And

$$x = (x_1, \dots, x_m) \qquad where\ x_j = lnp_j, j = 1, \dots, m \tag{3.31}$$

Let Y_i be the measured values of ρ_{app} at abscissas ξi, i= 1, ... , n. Let us assume that the logarithm of Y_i has a normal distribution for each abscissa ξi with standard deviation independent of i (Johansen, 1977). Our problem is to minimize:

$$Q = 1/\sigma^2 \sum_{i=1}^{n} \left[lny_i - ln\rho_{app}(\xi i, x) \right]^2 \tag{3.32}$$

with respect to xj = In P_j, j = 1, ... , m.

From the trial-and-error procedure we have a starting model x which is hopefully not too far from the optimum solution x^0 which minimizes Q. Expanding in ρ_{app} in a Taylor series around x and discarding all terms of order higher than the first we get :

$$Q = 1/\sigma^2 \sum_{i=1}^{n} \left[lny_i ln\rho_{app}(\xi i, x) - \sum_{j=1}^{n} \frac{\partial ln\rho_{app}}{\partial x_j} \delta x_j \right]^2 \quad (3.33)$$

ρ_{app} and its partial derivatives with respect to (P_j) are calculated by the linear filter method (Johansen, I975) discussed in 3.2.3 . The connection to the partial derivatives involved here is established by:

$$\partial ln\rho_{app}/\partial x_j = \frac{\rho_{app}}{\partial p_j} \frac{p_j}{\rho_{app}} \quad (3.34)$$

Minimization of (3.34) determines a correction vector δx. The process is repeated with x set to x + δx until there is no further decrease in Q, that is when $x = x^o$.

3.2.5. 2D Resistivity forward modeling and inversion

The inversion of resistivity data will be carried out using RES2DINV. RES2DINV is a computer program that will automatically determine a two dimensional (2-D) resistivity model for the subsurface for the data obtained from electrical imaging surveys (Griffiths and Barker, 1993). This program is designed to invert large data sets collected with a system with a large number of electrodes. The 2-D model used by the inversion program, which consists of a number of rectangular blocks, is shown in Figure 3.10. The arrangement of the blocks is loosely tied to the distribution of the data points in the pseudosection. The distribution and size of the blocks is automatically generated by the program using the distribution of the data points as a rough guide. The depth of the bottom row of blocks is set to be approximately equal to the equivalent depth of investigation (Edwards, 1977) of the data points with the largest electrode spacing. The survey is usually carried out with a system where the electrodes are arranged along a line with a constant spacing between adjacent electrodes. A forward modeling subroutine is used to calculate the apparent resistivity values, and a non-linear least-squares optimization technique is used for the

inversion routine (deGroot-Hedlin and Constable, 1990; Loke and Barker, 1996). The program supports both the finite-difference and finite-element forward modeling techniques and covers Wenner, pole-pole, dipole-dipole, pole-dipole, Wenner-Schlumberger and equatorial dipole-dipole (rectangular) arrays. In addition to these common arrays, the program even supports non-conventional arrays with an almost unlimited number of possible electrode configurations (Loke, 2001)

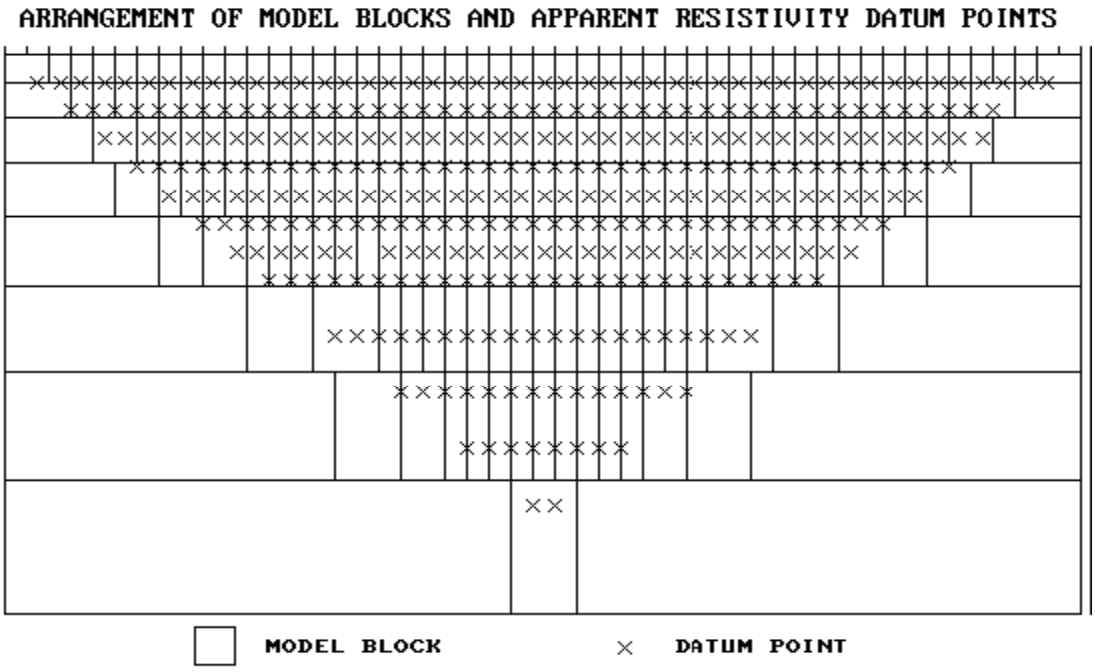

Fig.3.10. Arrangement of the blocks used in a model together with the data points in the pseudosection

3.3.Time-lapse Inversion

The major aim of time-lapse inversion is to identify changes in resistivity at selected locations at different times accurately. Independent data inversions can be carried out separately and changes in ERT images with time can be obtained by simply subtraction of pixel-by-pixel values from a background image, but in most cases, changes over time do not guarantee that the differences in resistivity values are only due to actual changes in the subsurface resistivity without taking the reference model and priori information into account Deiana et al. (2007). Different time-lapse inversion techniques are proposed to achieve accurate images of electrical conductivity

variations. The ratio method, the difference inversion and the cross-model regularization are commonly used in time-lapse inversion methods.

The ratio method was proposed by Daily et al. (1992). In this method, ratios of initial and subsequent datasets are inverted to highlight the areas of resistivity changes. This method has been widely used to monitor resistivity changes (e.g. Binley et al., 2002b). Presenting a quantitative resistivity change estimates are difficult for interpretation of petrophysical models, but this approach can give a qualitative indication where resistivity changes are occurring (Hayley et al. 2011)

LaBrecque and Yang, (2001) proposed the difference inversion method. This method minimizes the misfit between the difference in two datasets and the difference between two model responses and smoothness is imposed directly on the time-lapse model change. This approach has been used for instance by Kemna et al. (2002) for tracer test monitoring and by Diena et al. (2007) for characterization of vadose zone via water injection.

The crossmodel regularization assumes that the material changes can be ignored during data collection and therefore a time-invariant static model is used in this method. The inversion result of an initial dataset is used as a reference model for the inversion of subsequent datasets (Loke, 1999; Oldenborger et al., 2007) in this approach. This method minimizes the changes in the EC image that are not supported by data through adding a constraint that the second inversion result should be similar to the first. Both crossmodel inversion and difference inversion require an independent inversion of the first dataset. Therefore, artifacts in the initial independent inversion will introduce artifacts into the time-lapse inversion. Moreover, LaBrecque et al. (1996b) noticed that the initial dataset collected with permanently installed electrodes was the nosiest, thus, using these methods will cause serious consequence if the initial dataset includes considerable level of noise.

Hayley et al. (2011) presented a comprehensive comparison of the above mentioned methods using the results of two examples. The authors found out that the ratio method is very sensitive to noise. They also reported the difficulties they had with crossmodel regularization to not introduce anomalies into the difference image due to differences in the resolution of the background structure between the two inversions and necessity of heavy regularization to

overcome this weakness. They found that the difference inversion approach produces the best resolution of time-lapse changes among the commonly used approach and less susceptible to noise than the ratio method and crossmodel regularization. They mentioned that a careful selection of inversion parameters in the first inversion should be taken to resolve the background structure and avoid introducing artifacts into the difference inversion.

Kim et al. (2009) defined a subsurface structure and the entire monitoring data in the space–time domain to obtain a four-dimensional space–time model using just one inversion process. They developed a new least-squares inversion algorithm that allows for the subsurface properties to continuously change in time. They introduced the regularizations not only in the space domain but also in time, resulting in reduced inversion artifacts and improved stability of the inverse problem. The algorithm was designed to provide reasonable subsurface images even if changes in the subsurface properties during the data acquisition cannot be ignored.

3.4.Electrical conductivity of Soils

Electric current flows in earth materials at shallow depths through two main methods namely electronic conduction and electrolytic conduction. In electronic conduction, the current flow is via free electrons, such as in metals while, in electrolytic conduction, the current flow is via the movement of ions in groundwater. In our study for soil characterization, electrolytic conduction is the main mechanism. Sedimentary rocks usually have resistivity range from 10 to about 10000 Ω.m, with most values below 1000 Ω.m. Unconsolidated sediments generally have lower resistivity values than sedimentary rocks; with values ranging from about 10 to less than 1000 Ω.m. Clayey soil normally has a lower resistivity value than sandy soil. However, the overlaps in the resistivity values of the different classes of soils are usually expected. This is because the resistivity of a particular rock or soil sample depends on a number of factors such as the porosity, the degree of water saturation and the concentration of dissolved salts.

The widely used relationship between resistivity and soil moisture is expressed as (Archie, 1942)

$$\rho_a = a\emptyset^{-m}s^{-n}\rho_w \tag{3.35}$$

where a, m, and n are petrophysical constants that are characteristic of the porous medium, ρ_a is the resistivity of the porous medium, ρ_w is the pore-water resistivity, Φ is the porosity, and S is saturation, which is the ratio of the water content and porosity. During an infiltration event, the moisture content of a geological medium is generally the only factor that undergoes dramatic changes, and the changes in resistivity can be related to changes in moisture content.

3.5. Hydrologic Model

3.5.1. Governing Flow Equation

Richards' equation is used to describe variably saturated flow in porous media. Three-dimensional Richards' equation can be expressed as:

$$\partial/\partial x\left[K_H(h)\frac{\partial h}{\partial x}\right]+\partial/\partial y\left[K_H(h)\frac{\partial h}{\partial y}\right]+\partial/\partial z\left[K_v(h)\frac{\partial(h+z)}{\partial z}\right]=\frac{\partial\theta}{\partial t} \quad (3.36)$$

where h [L] is pressure head, z [L] is elevation, θ is volumetric moisture, $K_H(h)$ and $K_V(h)$ are the horizontal and vertical unsaturated hydraulic conductivity [L/T] respectively as a function of pressure head. The system is isotropic if $K_H(h) = K_V(h)$. Equation (3.36) must be supplemented with relevant constitutive models linking h, θ and K.

3.5.2. The Unsaturated Soil Hydraulic Properties

The unsaturated soil hydraulic properties, θ(h) and K(h), in (3.36) are in general highly nonlinear functions of the pressure head. Five different analytical models for the hydraulic properties were proposed by Brooks and Corey, (1964); van Genuchten, (1980); Vogel and Císlerová, (1988); Kosugi, (1995) and Durner, (1994) and commonly used in flow simulations. We assume here that the retention and hydraulic conductivity functions can be represented by the parametric models of van Genuchten, (1980) who used the statistical pore-size distribution model of Mualem, (1976) to obtain a predictive equation for the unsaturated hydraulic conductivity function in terms of soil water retention parameters:

$$q = \begin{cases} f & ,h \geq 0 \\ q_r + (f - q_r) \cdot \left[1 + (-a\,h)^n\right]^{-m} & ,h < 0 \end{cases} \quad m = 1 - 1/n \tag{3.37}$$

$$K = \begin{cases} Ks & ,h \geq 0 \\ Ks \cdot Kr = Ks \cdot Se^{1/2} \cdot \left[1 - \left(1 - Se^{1/m}\right)^m\right]^2 & ,h < 0 \end{cases} \quad Se = \frac{q - q_r}{f - q_r} \tag{3.38}$$

Where θs is the saturated water content, θr is the residual water content, defined as the water content for which the gradient dθ/dh becomes zero, α and n are empirical parameters and Ks is the saturated hydraulic conductivity (Simunek et al, 2006). Therefore, to achieve an infiltration model, all five van Genuchten´s parameters (θr, θs, α, n, and Ks) must be first estimated. These parameters were estimated by using the Rosetta software (Schaap et al. 2001). Rosetta implements pedotransfer functions based on artificial neural networks which predict water retention and saturated hydraulic conductivity from soil textural data and bulk density. In addition, we also used mini disk infiltrometer to evaluate these parameters in our study in the field.

3.5.3. 1D Flow Simulation

A one-dimensional of Richards' equation (3.36) is expressed by:

$$\frac{\partial q}{\partial t} = \frac{\partial}{\partial z}\left[K \frac{\partial H}{\partial z}\right] \tag{3.39}$$

The Richards' equation can be solved based on either h- or θ- form of the Richards equation to describe flow in a variably saturated soil. (e.g. Davis and Neuman, 1983; Huyakorn et al., 1983, 1989; Hills et al., 1989; Kool and Van Genuchten, 1991; Kirkland et al., 1992). A limitation of the θ -based formulation is that this form cannot be used to describe flow in the saturated zone, and flow in layered soils is also not easily simulated. The h-based formulation of (3.39) is considered to be more useful for practical problems involving flow in layered or spatially heterogeneous soils, as well as for variably saturated flow problems. Unfortunately, simulation of infiltration using the h-based formulation also often faces difficulties in conserving mass. (Haung et al. 1995)

In this study, h-based formulation was used to develop a 1d coupled geoelectric-infiltration model for unsaturated hydraulic parameters characterization and we briefly discuss how to numerically solve Equation (3.39) using h-based formulation by finite difference approach.

The water content, θ in Equation (3.39) is dependent on the pressure head, h. Therefore $\frac{\partial\theta}{\partial t}$ term can be expressed as $\frac{\partial\theta}{\partial h}\frac{\partial h}{\partial t}$. The $\frac{\partial\theta}{\partial h}$ term is equal to c(h) and is the water capacity (1/m). Let retention and hydraulic conductivity functions can be represented by (3.37) and (3.38). Therefore, c(h) can be expressed by:

$$\frac{\partial q}{\partial h} = c(h) \cong \begin{cases} 10^{-20} & , h \geq 0 \\ \dfrac{(f - q_r)\cdot n \cdot m \cdot a \cdot (-a\ h)^{n-1}}{\left[1+(-a\ h)^{n}\right]^{m+1}} + 10^{-20} & , h < 0 \end{cases} \tag{3.40}$$

we added 10^{-20} to the function to aid in the numerical solution, which can be sensitive to values of c(h) = 0.

Using the definition of total head, H = z+h, and applying $\frac{\partial\theta}{\partial h}\frac{\partial h}{\partial t}$ term to equation (3.39), we get the flowing expression of 1d Richards' equation:

$$\frac{\partial q}{\partial h}\cdot\frac{\partial h}{\partial t} = c(h)\frac{\partial h}{\partial t} = \frac{\partial}{\partial z}\left[K\cdot\left(1+\frac{\partial h}{\partial z}\right)\right] \tag{3.41}$$

The ordinary finite difference was applied to get following equation:

$$c_i\frac{h_i^{j+1}-h_i^{j}}{\Delta t} = \frac{1}{\Delta z}\cdot\left[K_{ip} - K_{im} + K_{ip}\cdot\frac{h_{i+1}^{j+1}-h_i^{j+1}}{\Delta z} - K_{im}\cdot\frac{h_i^{j+1}-h_{i-1}^{j+1}}{\Delta z}\right] \tag{3.42}$$

where K_{im} is the mean conductivity between the grid points at z_i and z_{i-1}, and K_{ip} is the mean conductivity between the grid points at z_{i+1} and z_i .We should estimate an average of the values of K_{i-1} and K_i for K_{im} and K_i and K_{i+1} for K_{ip}, to calculate flow from Darcy's law between z_{i-1} and z_i. The arithmetic means, $K_{im} = (K_{i-1}+K_i)/2$ and $K_{ip} = (K_i+K_{i+1})/2$ were used in this approach. Because of the time-stepping method we use here, all the other variables, ci and Ki, are taken

from the values of h_i^j and j and j+1 time levels are only given to the pressure head. In a truly implicit solution, j time level solution would all be taken from the j+1 time level. The only way to numerically solve (3.42) is to repeatedly calculate the time step, each time recalculating the values of c_i and K_i with the updated values of h_i^{j+1} until solution converges to a fixed limit (Barker and Scott, 1998). The tridiagonal system of equations away from the boundaries may be rearranged to:

$$-rzz \cdot K_{im} \cdot h_{i-1}^{j+1} + \left(c_i + rzz \cdot \left(K_{im} + K_{ip}\right)\right) \cdot h_i^{j+1} - rzz \cdot K_{ip} \cdot h_{i+1}^{j+1} = c_i \cdot h_i^j + rz \cdot \left(K_{ip} - K_{im}\right) \tag{3.43}$$

where $rzz = \Delta t/\Delta z^2$ and $rz = \Delta t/\Delta z$.

We will assume that the bottom boundary at z_0 is a constant pressure head, h_0, therefore for bottom boundary, the equation is expressed by:

$$For\ i = 1$$

$$\left(c_i + rzz \cdot \left(K_{im} + K_{ip}\right)\right) \cdot h_1^{j+1} - rzz \cdot K_{ip} \cdot h_2^{j+1} = c_i \cdot h_1^j + rz \cdot \left(K_{ip} - K_{im}\right) + rzz \cdot K_{im} \cdot h_0 \tag{3.44}$$

The infiltration flow at the upper boundary condition requires special treatment. We consider that the mean flow between two grid points z_i and z_{i+1}. Since, the space steps, Δz, are uniform; we center $q_{i+1/2}$ halfway between. In order to put the infiltration, q_{inf}, at the soil surface, the coordinate system was shifts up by $\Delta z/2$ (Barker and Scott, 1998). This does not change the finite difference equations, but changes our interpretation of where they solve.

$$c(h) \cdot \frac{\partial h}{\partial t} = -\frac{\partial q}{\partial z} \rightarrow \frac{-q_{i+1/2} + q_{i-1/2}}{\Delta z} = \frac{-q_{\text{inf}}}{\Delta z} - \frac{K_{im}}{\Delta z} \cdot \left[1 + \frac{h_{np-1}^{j+1} - h_{np-2}^{j+1}}{\Delta z}\right] \tag{3.45}$$

The Mass Balance equation above shows how this approach works. We replace only the flow between z_{np-1} and z_{np-2} with Darcy's law, leaving the soil surface flow, q_{inf}, intact. Therefore after proper substitutions into equation (3.43) for the top boundary, we get the following equation:

$$For\ i = np - 1$$

$$-rzz \cdot K_{im} \cdot h_{np-2}^{j+1} + \left(c_{np-1} + rzz \cdot K_{im}\right) \cdot h_{np-1}^{j+1} = \\ c_{np-1} \cdot h_{np-1}^{j} - rz \cdot \left(K_{im} + q_{\inf}\right) \tag{3.46}$$

All flows are positive upwards in our coordinate system, so the infiltration flow, q_{inf}, must be negative during rain and positive for evaporation.

As was discussed, the head-based approach used in this study, is known to produce mass balance errors. In other words, the change in water content does not match the net inflow. Celia et al. (1987) and Celia et al. (1990) proposed a mass-conservative numerical scheme to solve the mixed-form Richards equation:

$$\frac{\partial q}{\partial t} = \frac{\partial}{\partial z}\left[K \cdot \left(1 + \frac{\partial h}{\partial z}\right)\right] \Rightarrow \frac{q_i^{j+1} - q_i^{j}}{\Delta t} = \frac{1}{\Delta z} \cdot \left[K_{ip} \cdot \frac{H_{i+1}^{j+1} - H_i^{j+1}}{\Delta z} - K_{im} \cdot \frac{H_i^{j+1} - H_{i-1}^{j+1}}{\Delta z}\right] \tag{3.47}$$

The modified Picard method solves the mixed-q/h-form of Richards' equation. The mixed form of the Richards equation was thought to maintain the mass conservative property inherent in the θ-based equation, while providing solutions in terms of the pressure head, h.

3.5.4. HYDRUS Package

HYDRUS is a general software package for simulating water, heat, and solute movement in two- and three- dimensional variably saturated media (Simunek et al., 2006). The software package consists of the computation computer program, and the interactive graphics-based user interface. The HYDRUS program numerically solves the Richards equation for saturated unsaturated water flow and the convection-dispersion equation for heat and solute transport. The Galerkin finite element method (Neuman, 1975; Zienkiewicz, 1977; Pinder and Gray, 1977) with linear basis functions is used to obtain a solution of the flow in equation (3.36) subject to the imposed initial and boundary conditions. The HYDRUS code uses the mass conservative method proposed by Celia et al. (1990).

3.5.5. Mini disk infiltrometer

Mini disk infiltrometers are being considerably used for in-situ measurement of the unsaturated hydraulic properties of soil. These data are commonly used to evaluate the saturated and unsaturated hydraulic conductivity. Simunek and van Genuchten, (1996) discussed on how to estimate parameters in van Genuchten's model of the unsaturated soil-hydraulic properties from observed cumulative infiltration data during transient water flow. They showed that the infiltration data measured at only a constant tension does not yield enough information to estimate more than 2 parameters. They also showed how information could improve the uniqueness of the solution. Simunek and van Genuchten, (1997) continued their study with considering several different scenarios with using different additional information and concluded that the best practical scenario is to estimate the parameters in van Genuchten's model from the cumulative infiltration curve measured at several consecutive tensions applied to the soil surface, in conjunction with knowledge of the initial and final water content. We used the DISC computer software (developed by Simunek and Van Genuchten, 2000) for analyzing the cumulative infiltration curve. A Marquardt-Levenberg type parameter optimization algorithm is used in this software for inverse estimation of soil hydraulic properties from measured transient cumulative infiltration and related data.

3.6. Moment analysis

2D spatial moments were calculated from the resistivity images according to

$$M_{ij}(t) = \iint_{\Gamma} \Delta\theta(x,z) x^i z^j \, dxdz \qquad (3.48)$$

The zeroth, first and second spatial moments correspond to i + j + k = 0, 1, and 2, respectively. $\Delta\theta$ is the water content changes based on the resistivity changes estimation (inferred from time-lapse ERT images), where the background water content has been removed. Γ is the volume of interest (For a full description of moment analysis, see e.g. Ye et al., 2005).

In moment analysis, the mass of the system and location of the center of mass and how the mass spread at consecutive times is quantified. The zeroth moment, M00, is the mass in the system. The first moment, M01 normalized by the mass, defines the vertical center of mass and finally

the spread of the mass about its centre is related to the second spatial moment. For instance, the vertical spread of water in flow direction is defined using following equation:

$$\sigma_{xx}^2 = \frac{M_{02}}{M_0} - (\frac{M_{01}}{M_0})^2 \quad (3.49)$$

3.7. Soil test

Soil texture test is a qualitative classification tool to determine the Particle-size distribution (PSD) for soils. The texture of the soil depends on the relative sizes and shapes of the particles, and the distribution of those sizes. The classes are separated by the relative proportions of sand, silt and clay using grading sieves. The class is then used to determine the soils responses to environmental and management conditions and also crop suitability. Based on the textures the soil can be divided into two coarse (sand and gravel) and fine (silt and clay) grained soils groups. The particle-size separation was carried out in two following steps:

3.7.1. Sieve Analysis

Standard set of sieves are used to divide sand into classes, and to separate sand fractions from silt and clay fractions in the soil. The silt and clay fractions cannot be distinguished from one another by sieve analysis. For soil sieving analysis, following steps were performed:

1. The soil samples were mixed with water and then were washed trough the sieves 0.063 mm. The retained soils on the sieves were collected and oven-dried for sieving analysis.
2. All pieces of visible organic matter from the soil sample were removed.
3. Approximately 50 g of each soil sample was weighted and the exact weight (Ws) was recorded.
4. The sieves, with the largest mesh on the top by successively finer meshes beneath were placed. Samples were then poured into top sieve. The samples were shaken for 15 minutes using a shaker.
5. Residues from each sieve were carefully collected for weighing.

3.7.2. Malvern Particle Size Analyzer

To determine the 'clay to silt ratio', the fraction of the soil passing through the last (0.063 mm) sieve was analyzed using laser granulometer Malvern Particle Size Analyzer MS2000 after deflocculating with 30% sodium hexametaphosphate. The principle of operation consists in measuring the size of particles using the diffraction and diffusion of a laser beam. These particles scatter light at an angle that is inversely proportional to their size. The angular intensity of the scattered light is then measured by a series of photosensitive detectors. The map of scattering intensity versus angle is the primary source of information used to calculate the particle size.

3.8. Soil moisture measurement

Methods of soil moisture determination are classified into direct and indirect methods (Muñoz-Carpena, 2004).

3.8.1. Direct methods

In direct methods, the weight of a soil sample is measured before and after oven drying. The removal of moisture from a soil sample in this process is commonly referred as gravimetric moisture content (kg/kg). Measurement of soil bulk density then enables the gravimetric moisture content to be converted to volumetric moisture content which is expressed as a volume of water in a volume of undisturbed soil (m3/m3) (Hossain, 2008).

3.8.2. Indirect methods

Indirect measurement methods are based on the estimation of physical and chemical properties of a soil such as electrical conductivity, heat capacity, dielectric constant, hydrogen content or magnetic susceptibility that ultimately relates to soil moisture content (Hossain, 2008).

In this study, a capacitance sensor from Sentek Company was used to monitor moisture content variations during the experiment in order to control the geophysical approach. The capacitance technique for soil moisture determination involves the measurement of the soil dielectric constant by measuring the capacitance between two electrodes of a probe placed into the soil profile. The dielectric constant is a measure of the capacity of a non-conducting material to transmit electromagnetic waves or pulses. The theory of the capacitance technique was described by Dean et al. (1987) and Whalley et al. (1992). The capacitance change of the soil-water-air

matrix is mainly governed by the soil moisture content as the dielectric constant of water is 81, much higher than that of other soil components i.e. soil minerals and soil air valued of 2-5 and 1 respectively (Evett and Steiner, 1995; Muñoz-Carpena, 2004). Therefore, the measurement of the dielectric constant of a soil is primarily determined by the volumetric soil moisture content.

3.9. Temperature Changes

The goal of this experiment is to monitor electrical resistivity changes due to variations in the water content in the unsaturated zone. In order to accomplish this, all other transient factors that affect the soil must be accounted for. Temperature has a strong influence on the electrical conductivity of the subsurface (Sen and Goode, 1992; Waxman and Thomas, 1974). Rein et al. (2004) studied the effect of temperature, soil moisture, and temporal variation of the ambient ionic concentration on tracer tests, and concluded that even diurnal temperature variations can have a relatively large effect. Yet in most time-lapse studies, the influence of temperature variations has not been accounted for. Several attempts have clearly accounted for subsurface temperature variation in resistivity map (e.g. Hauck, 2002; Michot et al., 2003; Hayley et al., 2007; Hayley et al., 2009). It is common practice in electrical geophysics to assume a linear variation in resistivity with temperature over the typical range of temperatures encountered in shallow surveys (Musgrave and Binley, 2011). Schön, (2004) for instance proposed a 2.5% change in electrical resistivity per °C change in temperature. Hayley et al. (2007) using a variety of near surface materials found out that the slope of the low temperature linear model is quite consistent and a value between 1.8% and 2.2% change in electrical resistivity per ºC change in temperature can be used if no other information is available.

CHAPTER-FOUR

Using EM38 and ERT methods in soil characterization at the campus of university of Lisbon

4. Study of EM38 and ERT methods at the Campus of University of Lisbon

Study of the EM38 sensor and ERT were conducted in the campus of university on a loam soil with low permeability and high water retention capacity under natural condition and forced-infiltration experiment in order to monitor moisture content changes and hydraulic conductivity estimation. This chapter investigates the result of the EM38 and ERT data to detect and describe the soil moisture content. In addition, the ability of the EM38 and ERT methods in hydraulic conductivity estimation are evaluated using the flow simulations and EM38 and ERT images comparison.

4.1. Soil Test

Four soil cores down to a depth of approximately 1.5-2m were extracted along the profile in 3 and 6m in 2-Dec 2010, 9m in 21-Apr 2011 and 12m in 20-June 2011. These cores were sectioned into 0.2 m lengths and prepared for laboratory analysis of physical properties namely particle density, bulk density, texture and gravimetric moisture content. The texture of extracted soil samples from 6 and 9 meters are shown in Fig.4.1 and Fig.4.2. the method discussed in 3.7 were used to determine soil texture. The particle size distribution analysis of all four boreholes indicates a fairly homogeneous soil with Loam texture class composed of 30-50%, 40-50% and 15-25% concentration of sand, silt and clay respectively. The analysis of the third and fourth boreholes in 9 and 12 m shows a slightly greater sand concentration and lower amount of clay and silt contents than the first and second borehole. The average concentration of sand, silt and clay in the first and second borehole is about 35.5%, 45% and 19.5% respectively while in the third and fourth borehole is 41%, 43.5% and 15.5% respectively. Moreover, particle densities for the second, fifth and last samples of each core were measured by pycnometer in the lab. The estimated particle density was 2.65 with 0.03 tolerances. Bulk density measured using clod method was 1.72 with 0.05 tolerances. Therefore, the average porosity is about 35%.

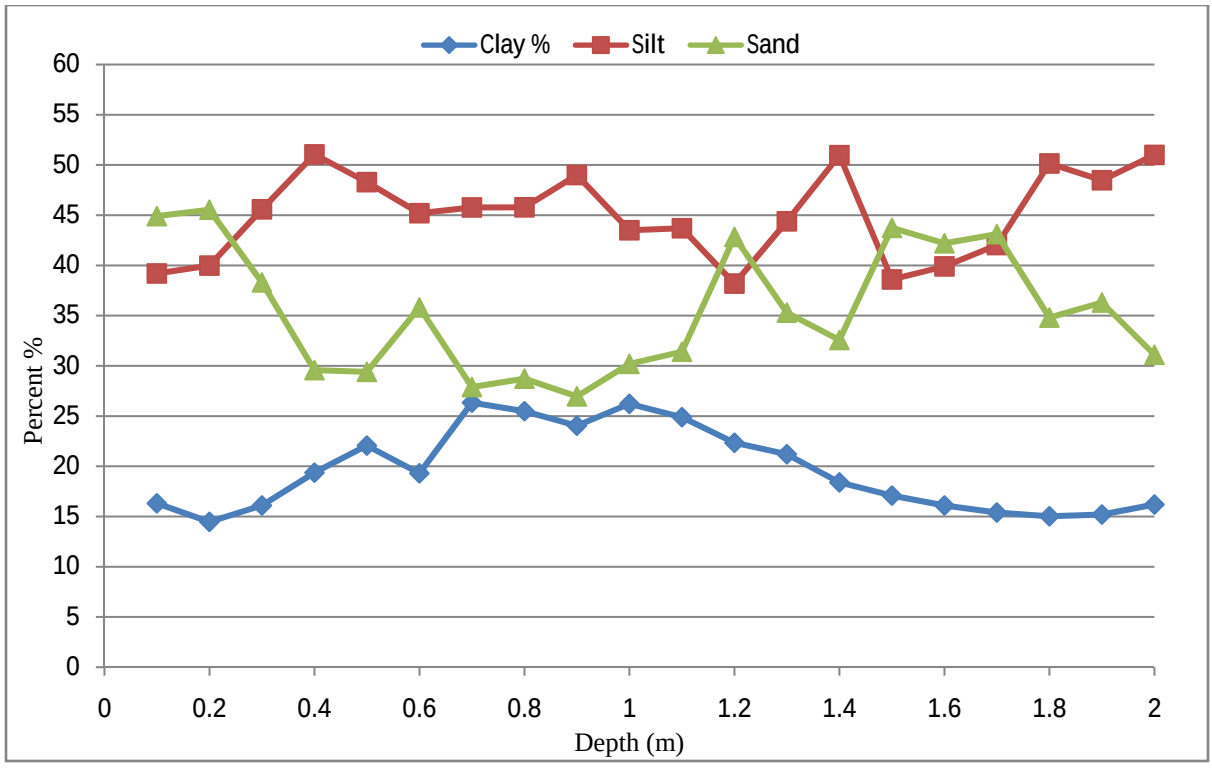

Fig.4.1. Soil texture grade of extracted soil samples from x=6m

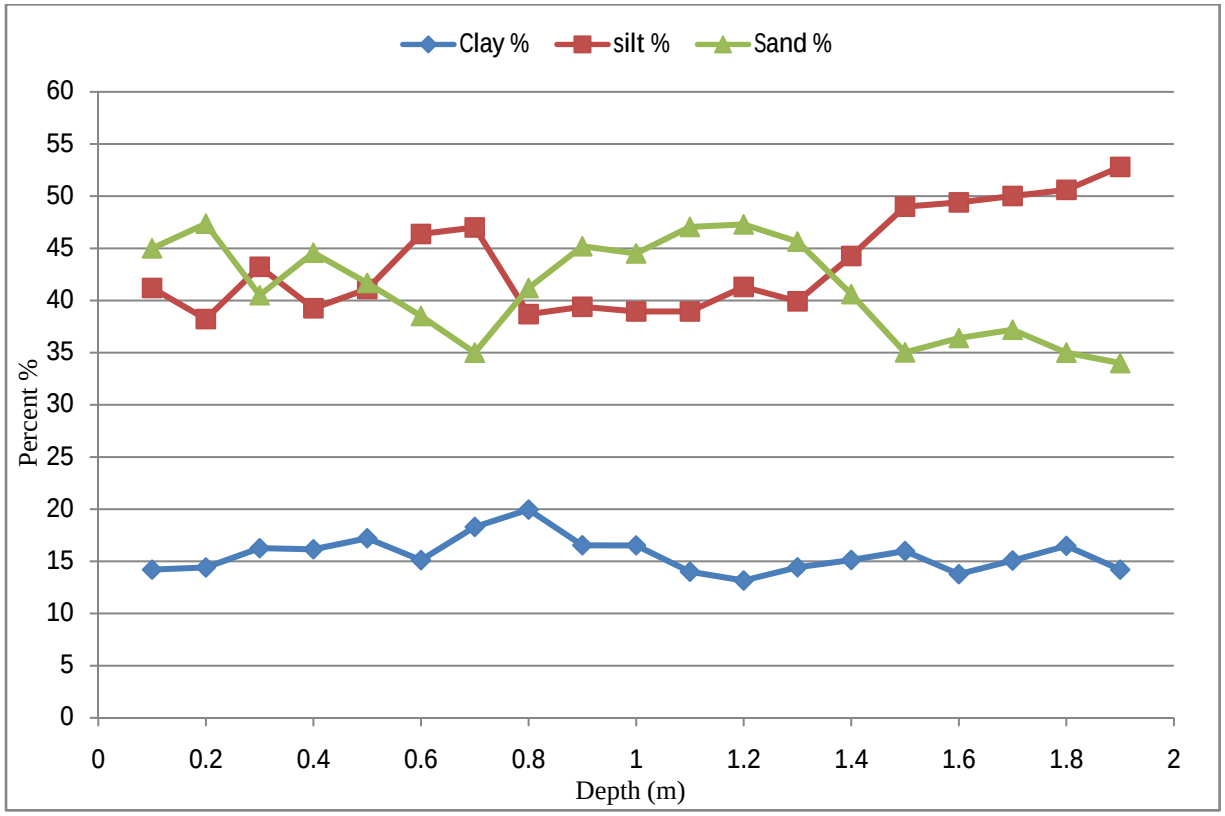

Fig.4.2. Soil texture grade of extracted soil samples from x=9m

4.2. Geophysical monitoring

The evolution of the moisture distribution were monitored by the ground surface ERT and multi-height EM38 surveys since 28-Oct 2010 until 20-Jun 2011. Geophysical surveys were repeated weekly. If the equipment were available, ERT and EM38 were collected at the same day. Fig.4.3 shows a view of geophysical acquisition at field site.

Fig.4.3. A view of geophysical acquisition at field site using ground surface ERT and multi height EM38

4.2.1. Geoeletrical monitoring

In this experiment a 2D ground surface ERT survey was performed. Wenner, Schlumberger and Dipole-Dipole electrode configurations were employed using 4 point light 10W devise. Expansion and electrode spacing were 14.25m and 0.75 respectively. A total of 57, 81 and 153 measurements were made for each dataset respectively using Wenner, Schlumberger and Dipole-Dipole electrode configurations. The first ERT dataset in 28-Oct 2010 was inverted so as to generate background images. Fig 4.4 presents the results of background image. The modeling results indicate smooth resistivity variations along the profile. Greater resistivity values are seen

on the right side of the models where the soil texture analysis indicates lower clay content concentration. While there is a high similarity between models generated using Wenner and Schlumberger electrode configurations, using a Dipole-Dipole electrode configuration resulted in a model that showed greater resistivity values along the profile and a slightly different pattern of resistivity.

In the next step, the time-lapse ERT data was inverted by RES2DINVx32 ver. 3.71. This version was developed based on Kim et al. (2009) method. Effect of change in temperature with respect to background dataset was removed from all ERT data by applying a value of 2% change per degree before inversion. Fig. 4.5, 4.6 and 4.7 show the results of resistivity inversions in terms of percentage resistivity changes with respect to background obtained using Wenner, Schlumberger and Dipole-Dipole electrode configurations respectively in 4-Nov 2010, 11-Feb, 21-Apr and 20-Jun 2011. It is worth mentioning that, the first dataset (4-Nov 2010) were collected with four days delay after three days continuous rain with amount of 75, 60 and 10 mm respectively. The second dataset (11-Feb 2011) were collected by two weeks delay after the last rain, the third shown dataset were surveyed immediately after the rain and finally the last shown dataset were collected in dry season. The decrease of resistivity during the rain period is clearly visible in the first and third shown models in Fig.4.5-7 (a, c). In contrast, there is no remarkable change in the second dataset in Fig.4.5-6 (b) and finally last model shown in Fig.4.5-7 (d) show a considerable resistivity increase in dry season. A comparison of the obtained models using different electrode configurations show an obvious similarity between Wenner and Schlumberger electrode configurations results, while Dipole-Dipole electrode configuration show a greater change with more scatter distribution. We also observed the same level of discrepancy in other dataset (not shown here) with Wenner and Schlumberger electrode configurations. The observed noise level of data collected using Dipole-Dipole electrode configuration in this study was significantly greater than others.

a)

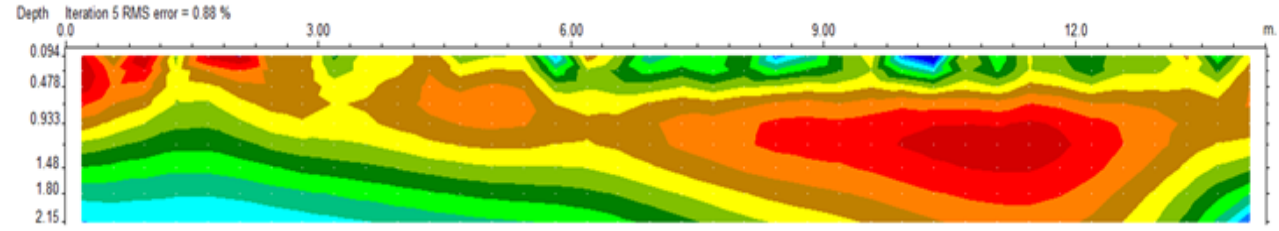

b)

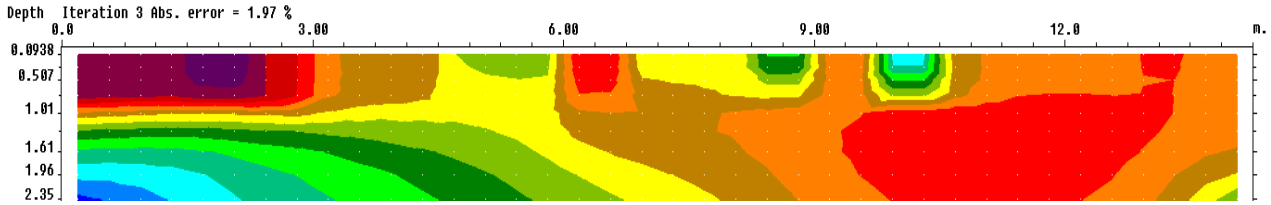

c)

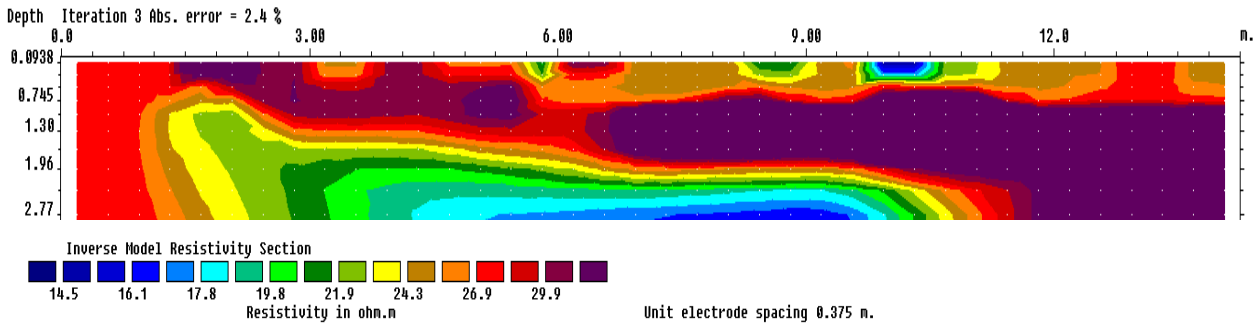

Fig.4.4. 2D vertical resistivity models of ERT background using by a) Wenner b) Schlumberger, and c) Dipole-Dipole electrode configurations.

a)

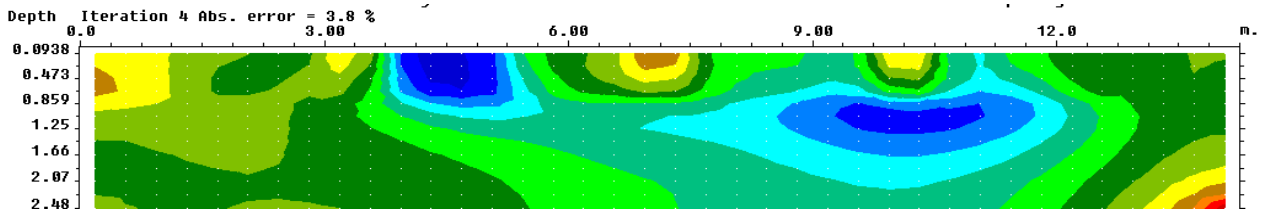

b)

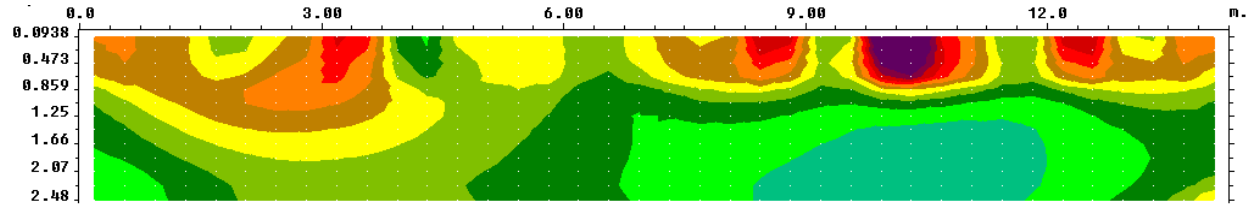

c)

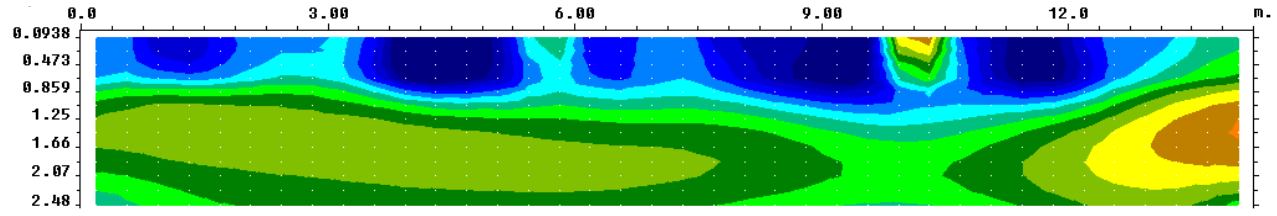

d)

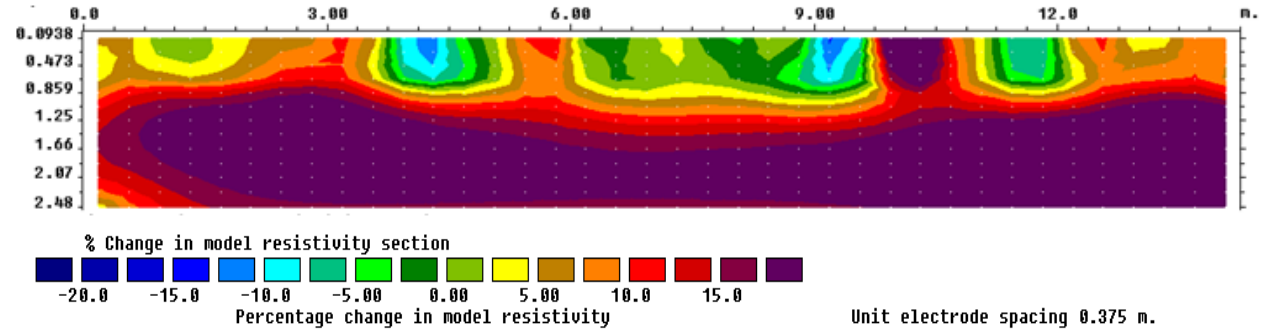

Fig.4.5. Sequence of percentage resistivity changes inferred from inversion results using Wenner electrode configuration with respect to background in a) 4-Nov 2010, b) 11-Feb, c) 21-Apr and d) 20- Jun 2011 respectively.

a)

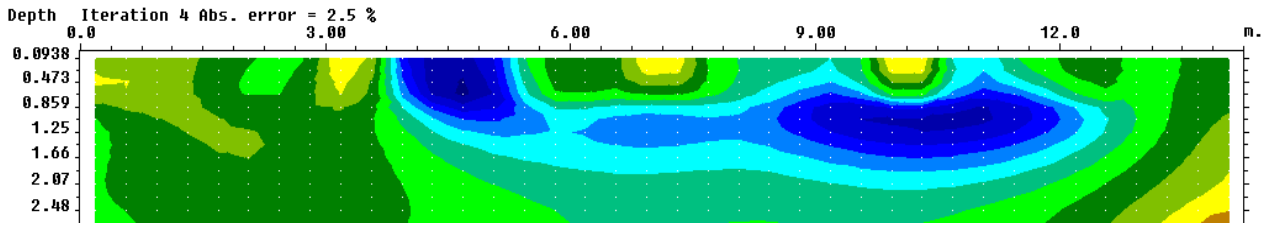

b)

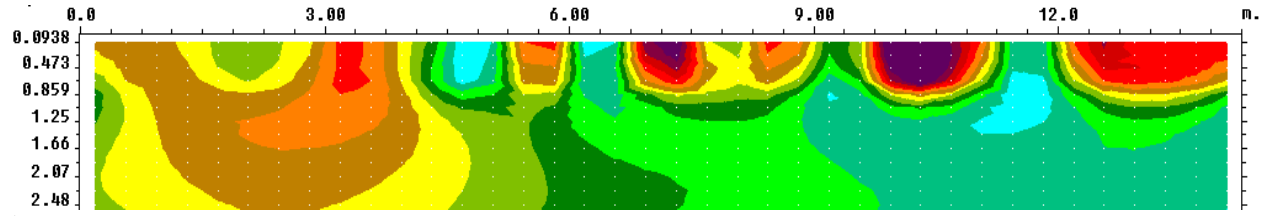

c)

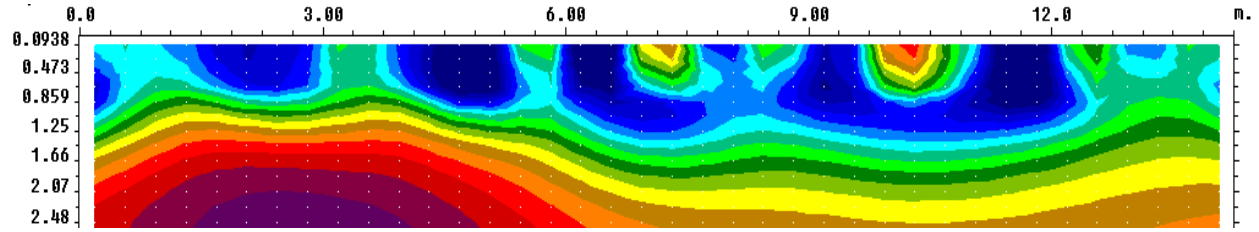

d)

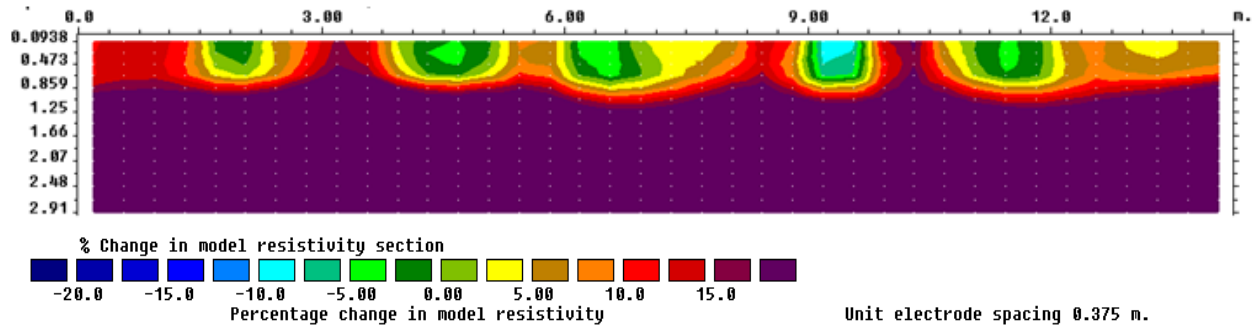

Fig.4.6. Sequence of percentage resistivity changes inferred from inversion results using Schlumberger electrode configuration with respect to background in a) 4-Nov 2010, b) 11-Feb, c) 21-Apr and d) 20- Jun 2011 respectively.

a)

b)

c)

d)

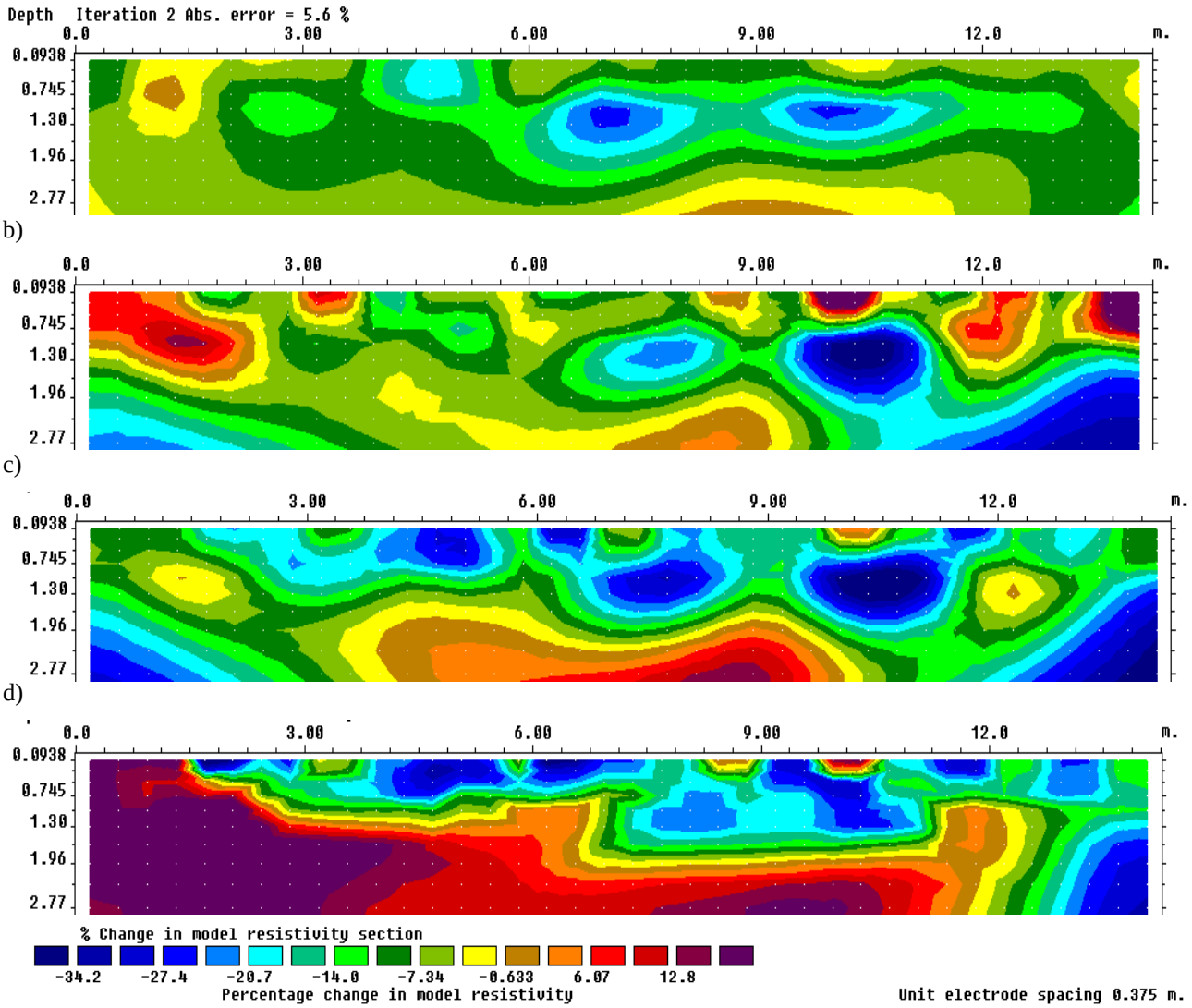

Fig4.7. Sequence of percentage resistivity changes inferred from inversion results using Dipole-Dipole electrode configuration with respect to background in a) 4-Nov 2010, b) 11-Feb, c) 21-Apr and d) 20- Jun 2011 respectively.

4.2.2. The EM38

EM38 measurements were made in the vertical (EM38v) and horizontal (EM38h) modes of operation with 0.75m separation along the profile. Consequently 20 points were measured in each survey. Given the operating frequency of the EM38 (i.e. 14.5 kHz) and coil spacing (1.0 m), the theoretical depth of exploration is 1.5 and 0.75m respectively for EM38V and EM38h when the instrument is placed on the ground. To facilitate multi-height EM38 measurement, a specially-designed polymer-plastic ladder (Fig.4.3) was constructed at heights corresponding to 0.3, 0.6 and 0.9 m. EM38 measurements were collected in both vertical and horizontal in mentioned heights. Fig.4.8 shows the apparent soil electrical conductivity (mS/m) data collected in 28-Oct 2010 using EM38 in vertical and horizontal modes of operation. Joint inversion of multi-height EM38 measurements was carried out using the algorithm proposed by Santos, (2004). The data of each survey was inverted considering a same initial five- layer earth model. The first four layers were initialized with the same depth of 0.3m and electrical conductivity of 15, 20, 25 and 35 mS/m respectively from the ground surface. The electrical conductivity of the last layer was selected to be 50 mS/m. These values were estimated based on the apparent soil electrical conductivity values collected by EM38 and the resistivity model obtained in previous section. Fig 4.9 (a-c) shows the inverted models of the first EM38 dataset measured in 28-Oct 2010. These models were generated using all 8 dataset shown in Fig.4.8 by applying the 1-D laterally constrained inversion and using different values of damping factor. Each model was obtained after 15 iterations. Fig.4.9a was obtained using a small damping factor of $\lambda = 0.3$ which corresponds to a less constrained inversion. The response of this model with total misfit of 4.85% shows a robust model with significant lateral changes along the profile. The background resistivity value of this model is about 35 ohm.m which is reasonably consistent with the geoelectrical model. Fig.4.9b was obtained using damping factor value of 3. The resistivity changes along the profile are smoother than the first model, but the lateral changes are still obvious in this model. The misfit error is slightly greater than the first model with 5.18%. Finally the last model using $\lambda = 30$ is shown in Fig.4.9c. This high damping factor (k) forces the calculation of a solution with a significant degree of smoothness for a more uniform model. The model shows very smooth changes along the profile and there is a substantial disagreement between model obtained using $\lambda = 30$ with the geoelectrical model response in section 4.2.1 and

soil texture test results. The total misfit is 7.67% which is greater than the first and second models.

All EM38 dataset collected during one year, were inverted through the same procedure using damping factor values of 0.3,3 and 30 (not shown here). The models then were analyzed and compared with resistivity model produced in section 4.2.1. We figured out that when $\lambda = 3$ the models well reflect the resistivity changes in our study. Although, small values of λ yield better fit, the lateral changes were exaggerated and artificial anomalies were produced in many cases. Furthermore, after finding the suitable value for damping factor, we inverted all EM38 datasets using vertical and horizontal modes of operation on the ground and 0.3m height level where shows the significant changes in raw data along the profile. Our analysis indicates that using only these data slightly improves the models and reduces the total misfit. Fig.4.9d shows the obtained model using the ground surface and 0.3m height data with a damping factor of 3. Therefore, for further investigation we used the models which were obtained using vertical and horizontal modes of operation of the ground surface and 0.3m height level by applying a damping factor of 3 and 15 iterations. An investigation of EM38 background model in Fig.4.9d shows smooth resistivity changes along the profile with the average resistivity of 30 ohm.m. The model shows a very good consistency with ERT images in resistivity changes along the profile. Higher resistivity values are seen in the right and left upper zone of the profile. Afterward, independent EM38 datasets inversions were carried out separately. Obtained model were changed by subtracting pixel-by-pixel values from a background image. The effect of the temperature change with respect to background in 28-Oct 2010 was removed from EM38 data before inversion. Fig.4.10 (a-e) show the results of multi-height EM38 data inversions in terms of percentage resistivity changes with regard to background in 4 and 25-Nov 2010, 20-Jan, 11-Feb and 20- Jun 2011. The EM38 data in 4-Nov 2010, 11-Feb and 20- Jun 2011 (Fig.4.10a, c, d) were collected right before ERT surveys in these days. Although there is some difference between trends of resistivity changes inferred from EM38 and ERT images, pattern of results are reasonably similar. Both EM38 and ERT results show a decrease during the rain period in 4-Nov 2010 and a significant increase in 20- Jun 2011 in dry season. The second dataset (25-Nov 2010) were collected after 12 days of continuous rain amounting to170 mm. The model obtained in 25-Nov 2010 shows the greatest resistivity changes during the experiment with an average of 20%

decrease with regard to background. The maximum increase (about 20%) in both ERT andEM38 images are seen in dry season in 20 Jun 2011 as expected.

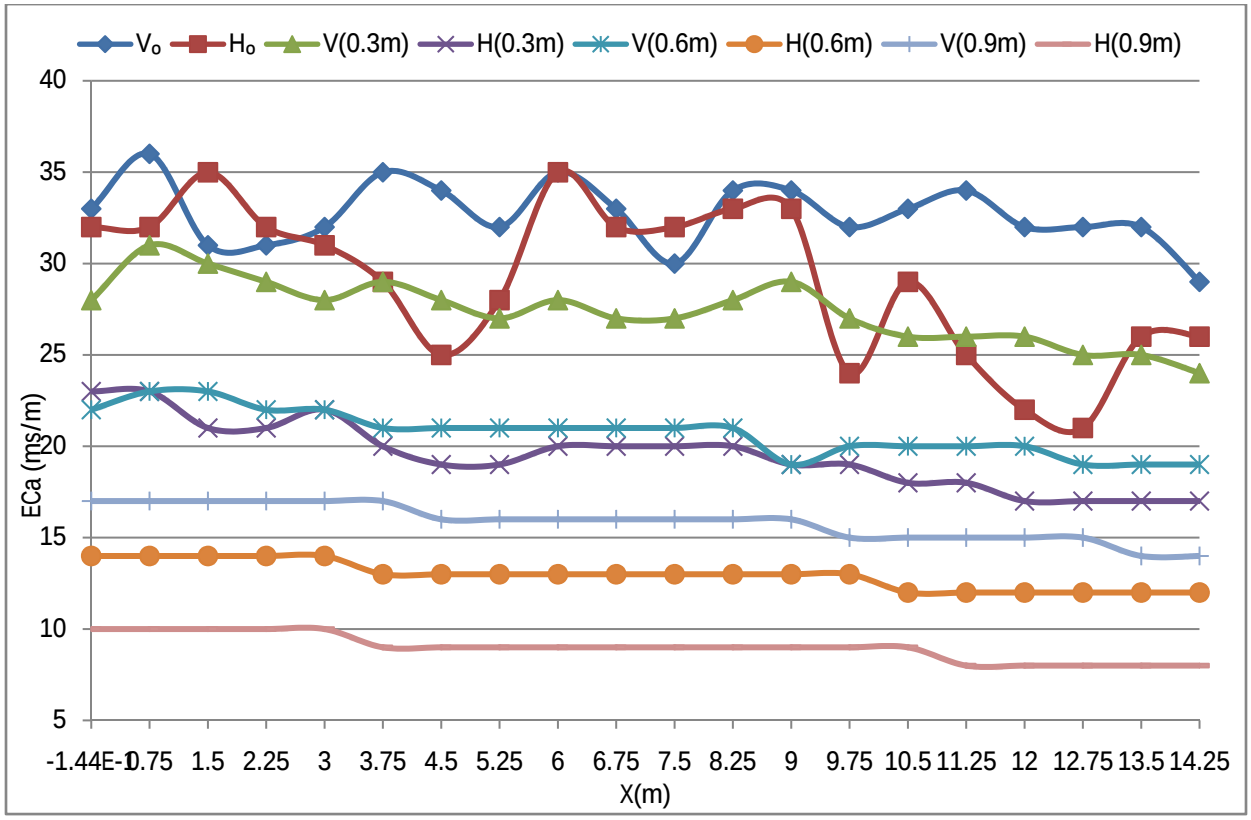

Fig.4.8. Spatial distribution of ECa (mS/m) along the profile in 28-Oct 2010 using EM38 in vertical and horizontal modes of operation on the ground and heights of0.3,0.6, and 0.9 m.

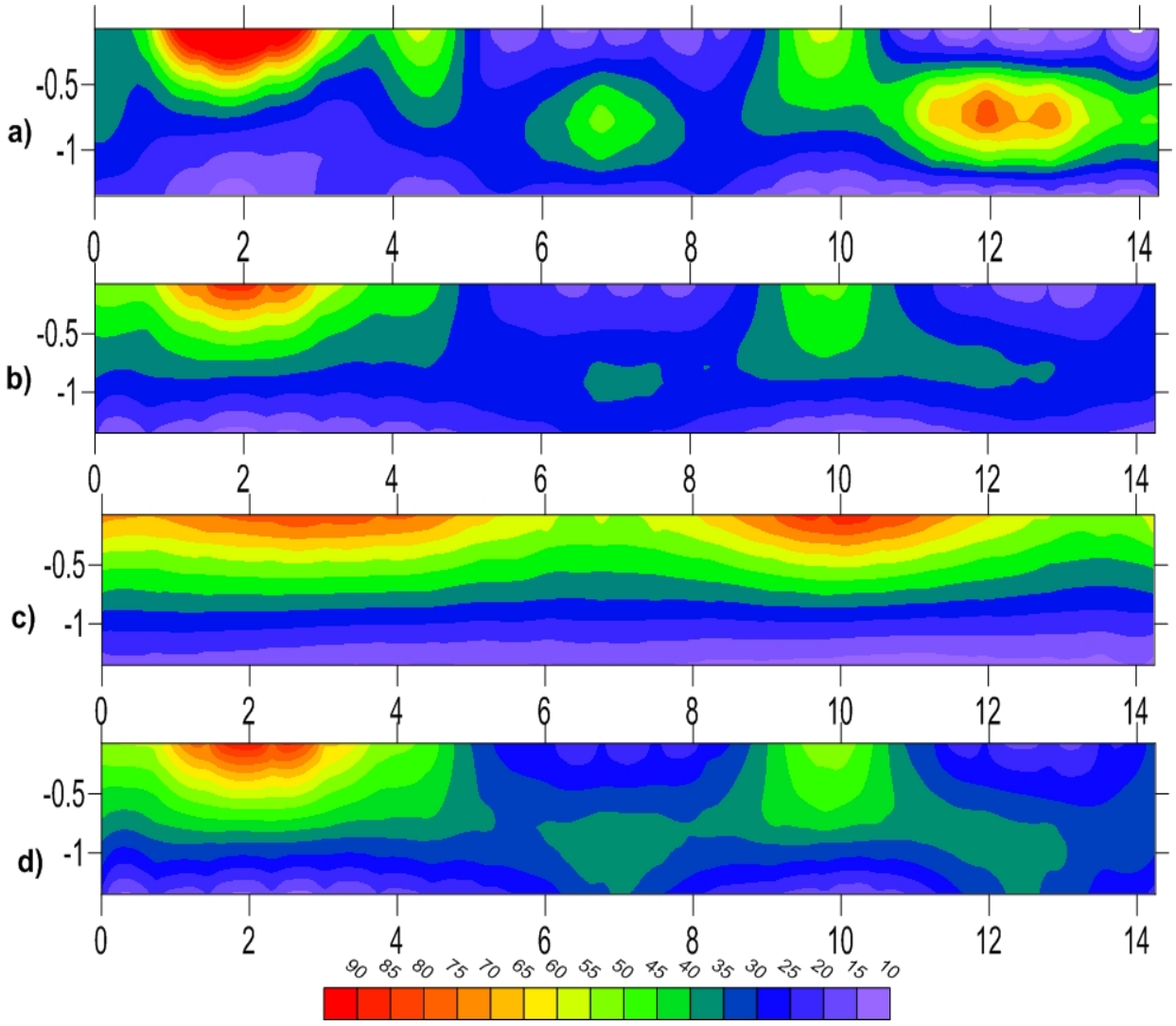

Fig.4.9. Joint inversion of multi-height EM38 using vertical and horizontal apparent soil electrical conductivity of collected data at height of 0, 0.3, 0.6 and 0.9 m , estimated using a 1-D inversion algorithm with 2-D smoothness constraints using a damping factor of a) 0.3, b) 3, and c) 30. d) Was obtained by joint inversion of EM38 data at heights of 0 and 0.3 m by using damping factor of 3. All images were obtained using 15 iterations.

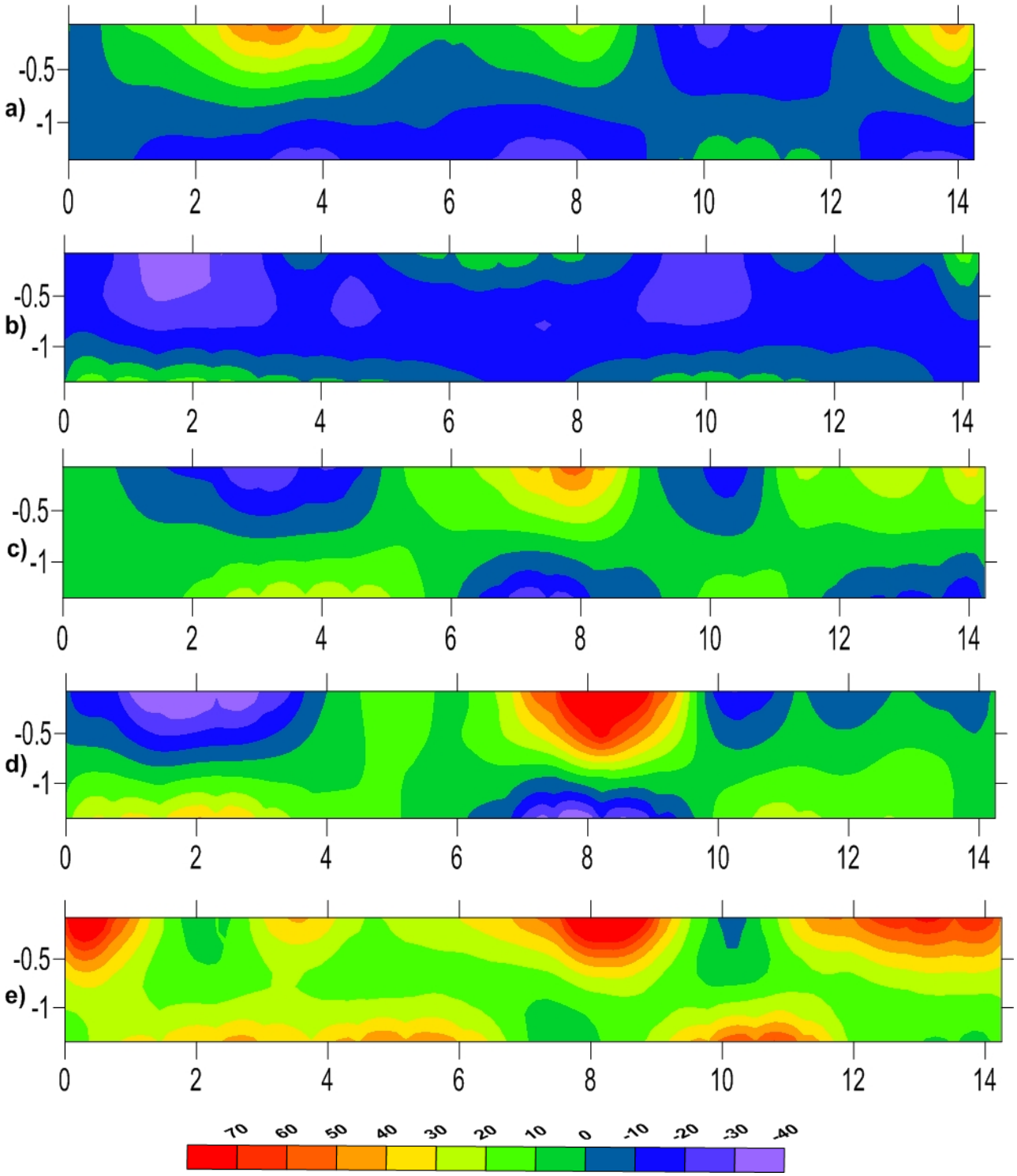

Fig.4.10.Sequence of percentage resistivity changes inferred from inversion results using multi-height EM38 with respect to background in a) 4-Nov, b) 25-Nov 2010, c) 20-Jan d) 11-Feb and e) 20- Jun 2011 respectively.

4.3. In-situ resistivity and saturation relationship

To determine changes in soil moisture from ERT images, we did not assume the validity of Archie's law. In fact, we established an in-situ approach based on ρ vs. S changes by plotting the inverted value of resistivity of the extracted sample as a function of the saturation. The plot allowed us to obtain an empirical relationship between ρ and S from the best match of the experimental data. To achieve this objective, we used the ERT images collected right before sampling and then the inverted resistivity values of related pixels were extracted and plotted as a function of saturation (Fig.4.11, a-c) to find out the best match of resistivity-moisture content changes. The obtained relationship is given by the following equation:

$$\rho_{wenner} = 18.68\ s^{-1.81} \quad (4.1a)$$

$$\rho_{Sch} = 20.243\ s^{-1.70} \quad (4.1b)$$

$$\rho_{Dip} = 19.879\ s^{-1.79} \quad (4.1c)$$

where S is the degree of saturation and ρ_{wenner}, ρ_{sch} and ρ_{Dip} are the resistivity of the porous medium in relevant degree of saturation obtained using Wenner, Schlumberger and Dipole-Dipole electrode configurations respectively. The resistivity and saturation shows a strong relationship in all electrode configurations in this study. The same procedure was applied to determine changes in soil moisture from EM38 images. The resistivity- saturation changes were plotted in Fig.4.11 (d). Resistivity and saturation shows weaker relationship in comparison with ERT images and expressed by:

$$\rho_{EM38} = 22.175\ s^{-1.203} \quad (4.1d)$$

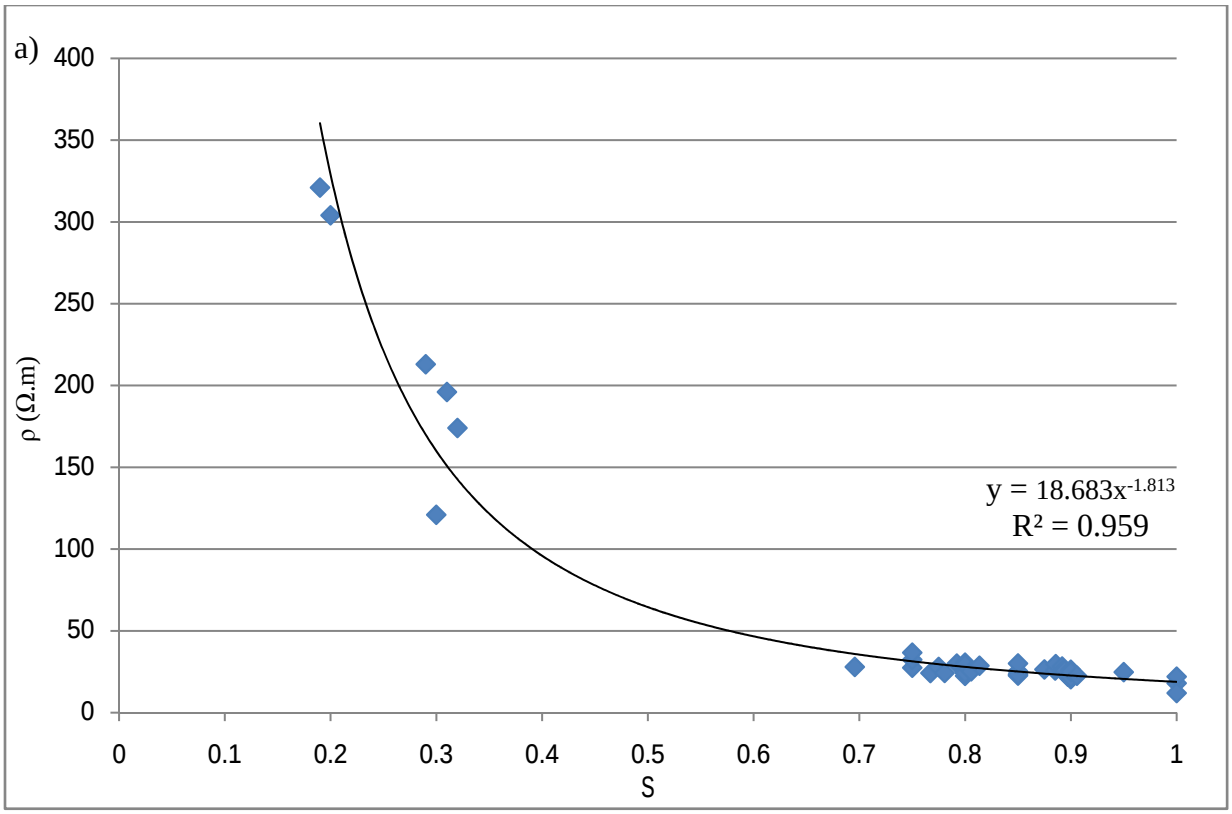
a)
400
350
300
250
200
150
100
50
0
ρ (Ω.m)
0
0.1
0.2
0.3
0.4
0.5
0.6
0.7
0.8
0.9
1
S
y = 18.683x-1.813
R² = 0.959

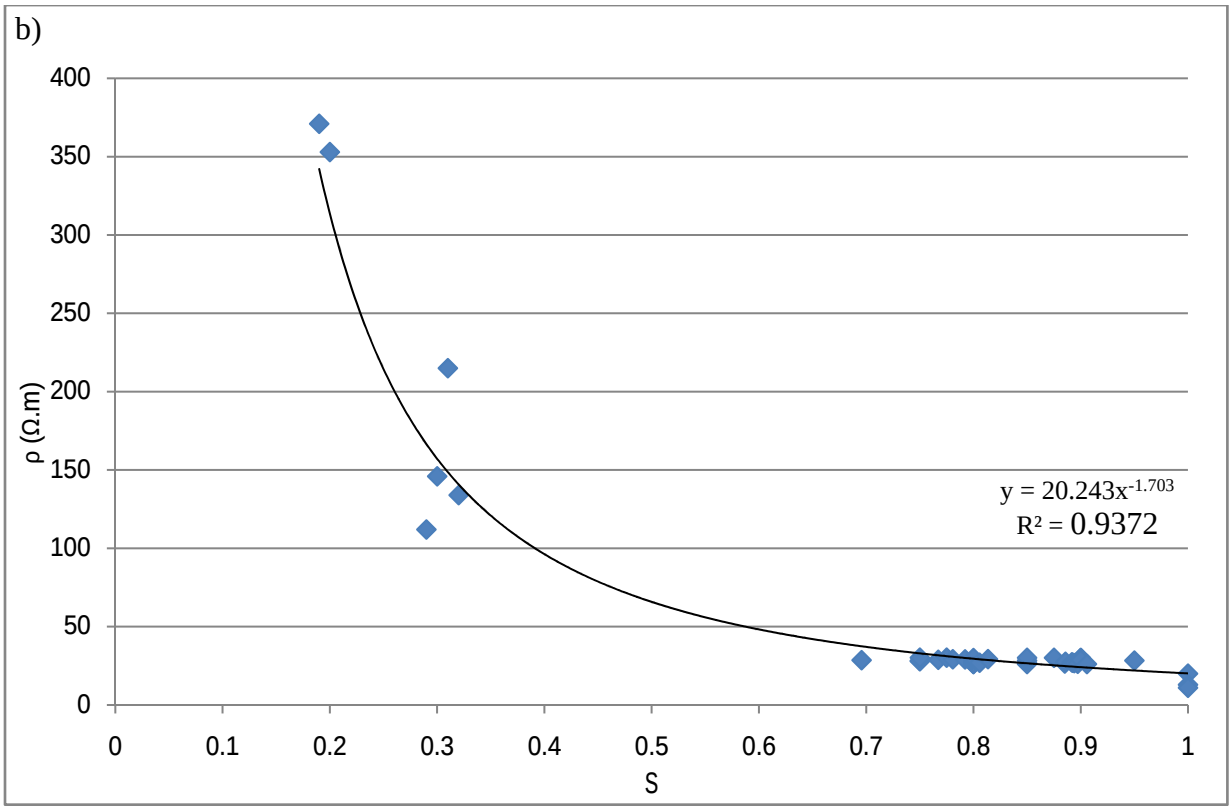
b)
400
350
300
250
200
150
100
50
0
ρ (Ω.m)
0
0.1
0.2
0.3
0.4
0.5
0.6
0.7
0.8
0.9
1
S
y = 20.243x-1.703
R² = 0.9372

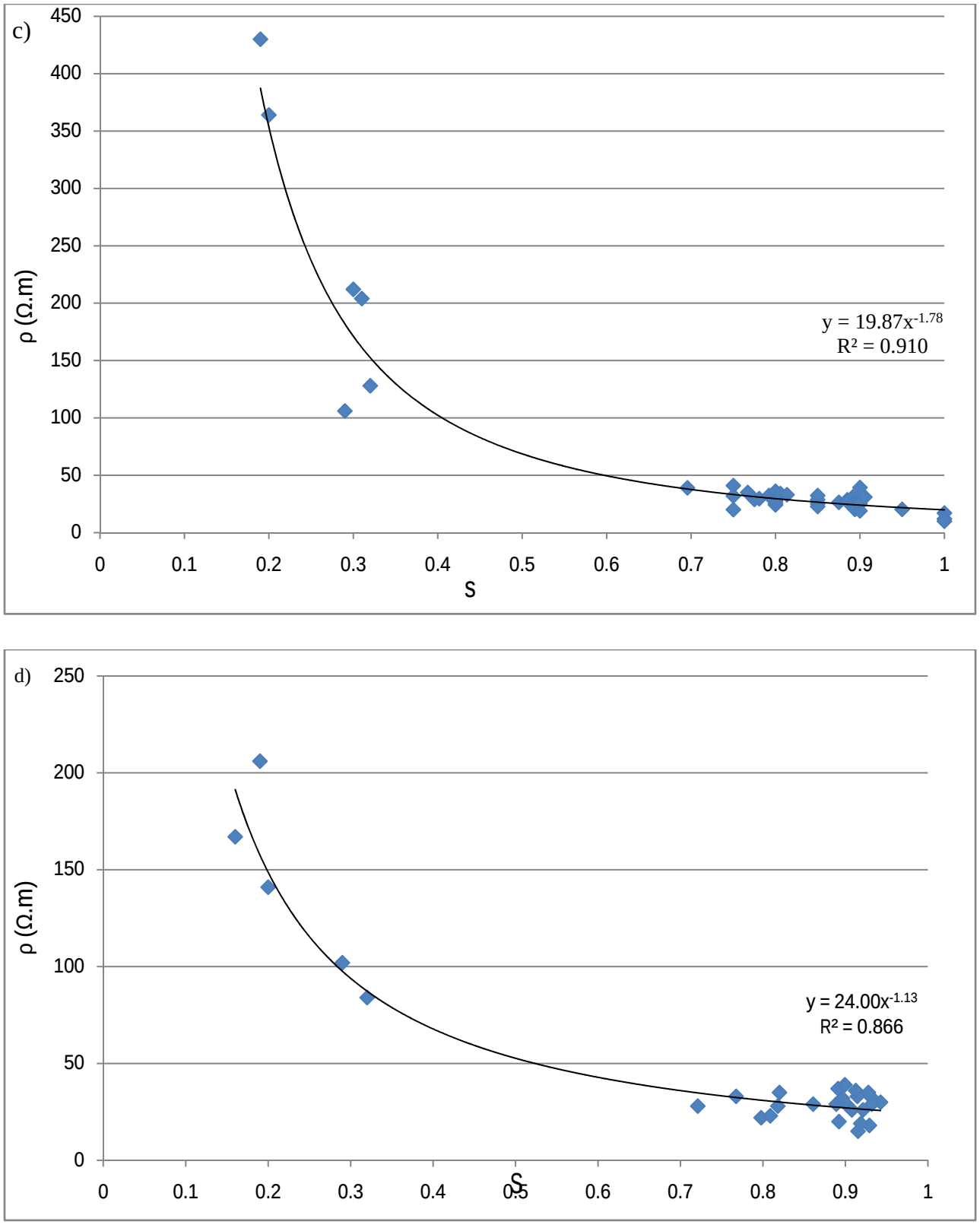

Fig.4.11. Electrical resistivity of extracted samples as a function of the saturation inferred from ERT images obtained by a) Wenner b) Schlumberger, and c) Dipole-Dipole electrode configurations and d) EM38 images.

4.4. Soil moisture measurement using capacitance sensor

Two Sentek PVC access tubes were fitted immediately after digging two holes in x=6 and x=9 meters. Access tubes were pushed down the hole to the depth of 2 m for the measuring probes. Tubes were fitted well to the soil to prevent vertical leaking of surface water around the tube and to minimize air gaps. One capacitance sensor was used and data was collected every 0.1 m in depth along the access tubes. Soil moisture measurements were started in 16- Dec, 2010 and were repeated weekly until March, 2011 for four months.

Before readings, the sensor was normalized to air and water. Afterwards, volumetric soil water content was estimated by following equation:

$$SF = A \times \theta_v^B + C \quad (4.2)$$

where θ_v is the volumetric soil moisture content measured by the capacitance sensor and SF is scaled frequency and is generated by comparing the probe response in the access tube in the soil to the probe responses in air and water (Sentek, 2001; Hossain, 2008). Coefficient A, exponent B and constant C were selected from Senetek calibration for loam soil and are equal to 0.013, 1 and 0.326 respectively.

Volumetric soil moisture content variations relative to a background measured in 16- Dec 2010 for each of the tubes is illustrated at various depth levels in Figures 4.12 and 4.13. Each figure shows the volumetric soil moisture content variations in 23- Dec 2010, 7 and 28 Jan, 22-Feb and 4- Mar 2011. In 16- Dec, 23- Dec 2010 and 7-Jan, 2011, data were measured in a period of intermittent moderate to heavy rainfall, while data obtained in 28-Jan and 22- Feb, 2011 were measured during the sporadic rainfall. Finally last dataset in 4- Mar 2011 were measured two weeks after the last rain. An investigation of the both tube access results indicates that the moisture content decreased significantly in 4-Mar, 2011 as expected. Furthermore, each of the tube access shows visible decrease in 28-Jan and 22-Feb. No significant variations are seen in 29-Dec 2010 and 7-Jan 2011. Moreover, the observed variations in the first tube access are not consistent with the second tube access. The moisture content variations hardly exceeded 10% during the experiment. The most remarkable moisture changes are seen in the first 50 cm of topsoil during the data collection. To present a closer inspection of the quality of the moisture data obtained with capacitance sensor, the weekly moisture content changes in one month from

each of the access tubes were shown in Fig.4.14 and.4.15. The results were then compared to moisture content changes inferred from resistivity models in the same place. Fig.4.16 and 4.17 were calculated from resistivity data near the first and second access tubes respectively. Fig.4.14 and 4.15 show a very scattered and noisy moisture content variation during one month, while moisture content changes inferred from the resistivity model show a smooth change with depth. Considering daily rainfall data, trends observed in moisture content variations inferred from resistivity models are more consistent with our expectation. For instance, the data obtained in 14-Jan, 2011 were collected 8 days after the last rainfall, while the data in 23-Dec, 2010 were collected immediately after continuous heavy rain started in 18-Dec, 2010. Therefore the maximum increase and decrease in moisture in shallower zone are expected in 23-Dec, 2010 and 14-Jan, 2011 respectively. We also compared moisture content inferred from resistivity models with those collected by the capacitance sensor for all other days (not shown here). We observed that the relative moisture content data obtained by the capacitance sensor are not reliable for a quantitative investigation. More importantly, such data cannot be used as a reference to control geophysical responses in our study. These data might be used for a qualitative comparison of moisture content over the long time. Therefore, we stopped measuring moisture content by the capacitance sensor and we did not use these data in section 4.3 to convert resistivity changes to moisture content changes. It is worth mentioning that we only used one capacitance sensor bought from Sentek Company in this experiment. Therefore to measure the moisture content along the access tube, we manually moved the sensor inside the access tube in order to measure moisture content in different depths. It would be one of the sourced of inaccuracy in our study.

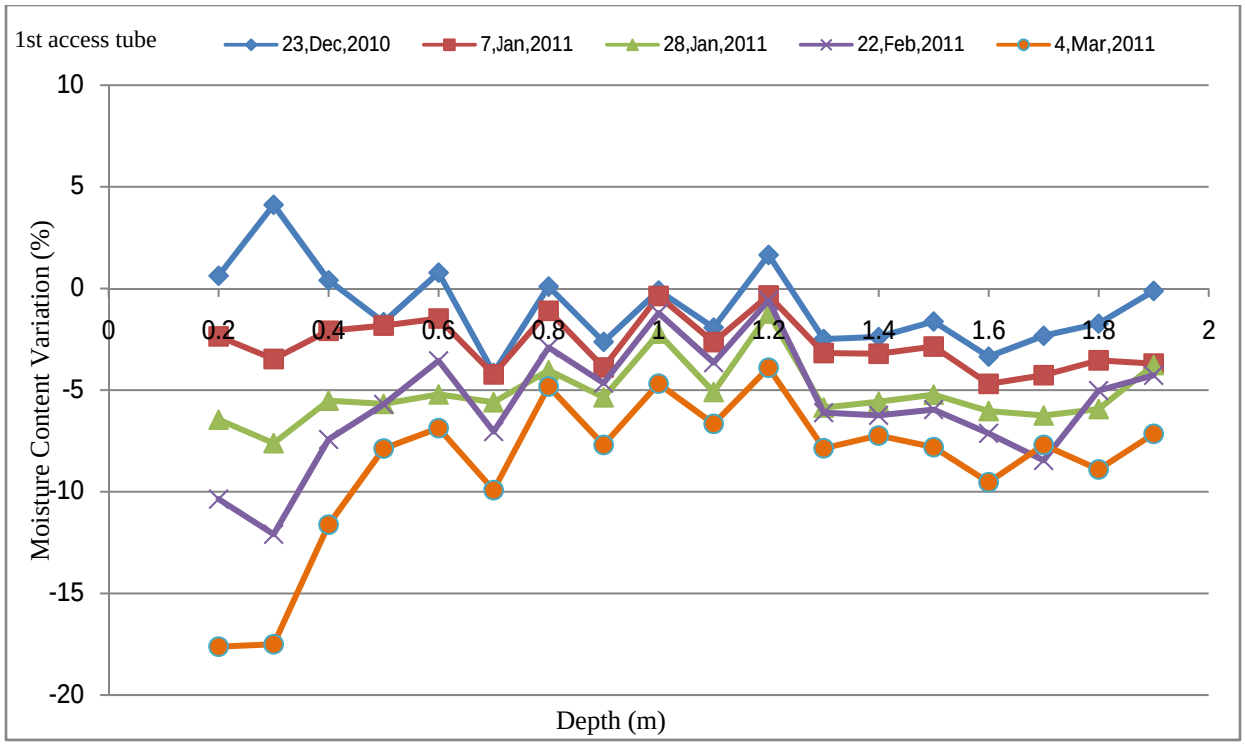

Fig.4.12. Moisture content variations with respect to background as function of the depth obtained from the capacitance sensor in the first access tube in x=6m during three months.

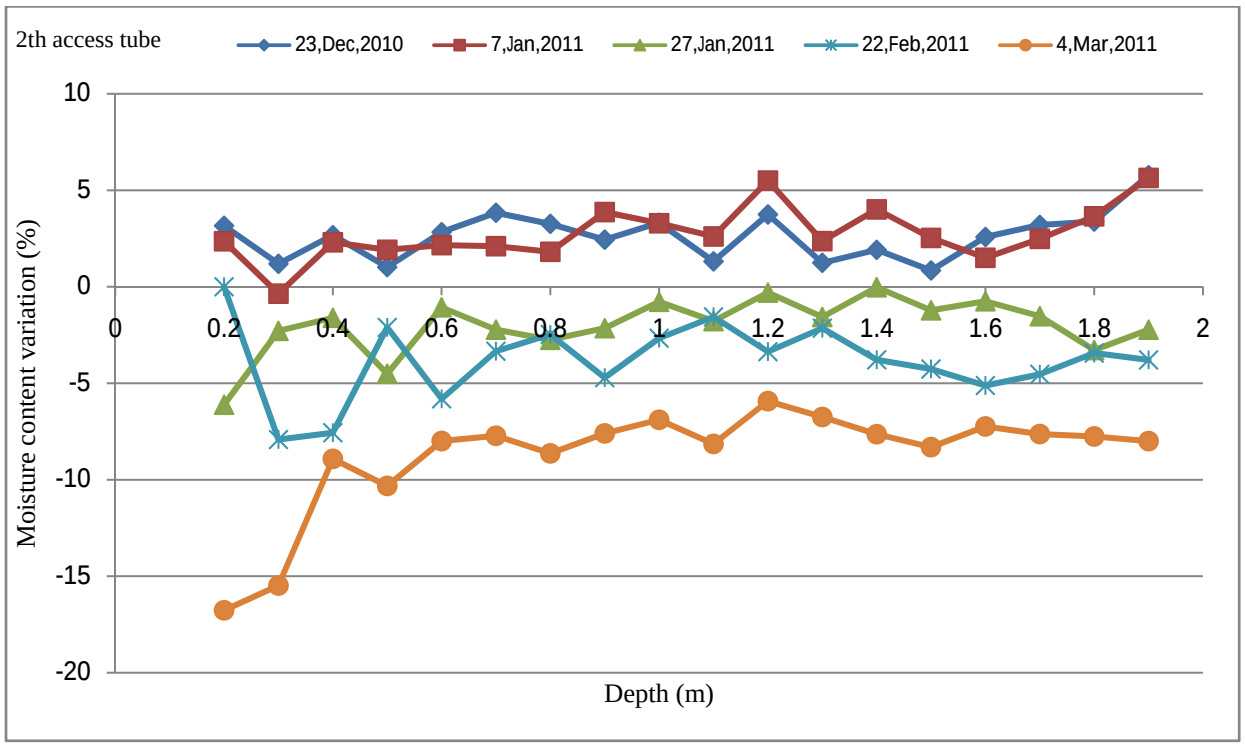

Fig.4.13. Moisture content variations with respect to background as function of the depth obtained from the capacitance sensor in the second access tube in x=9m during three months.

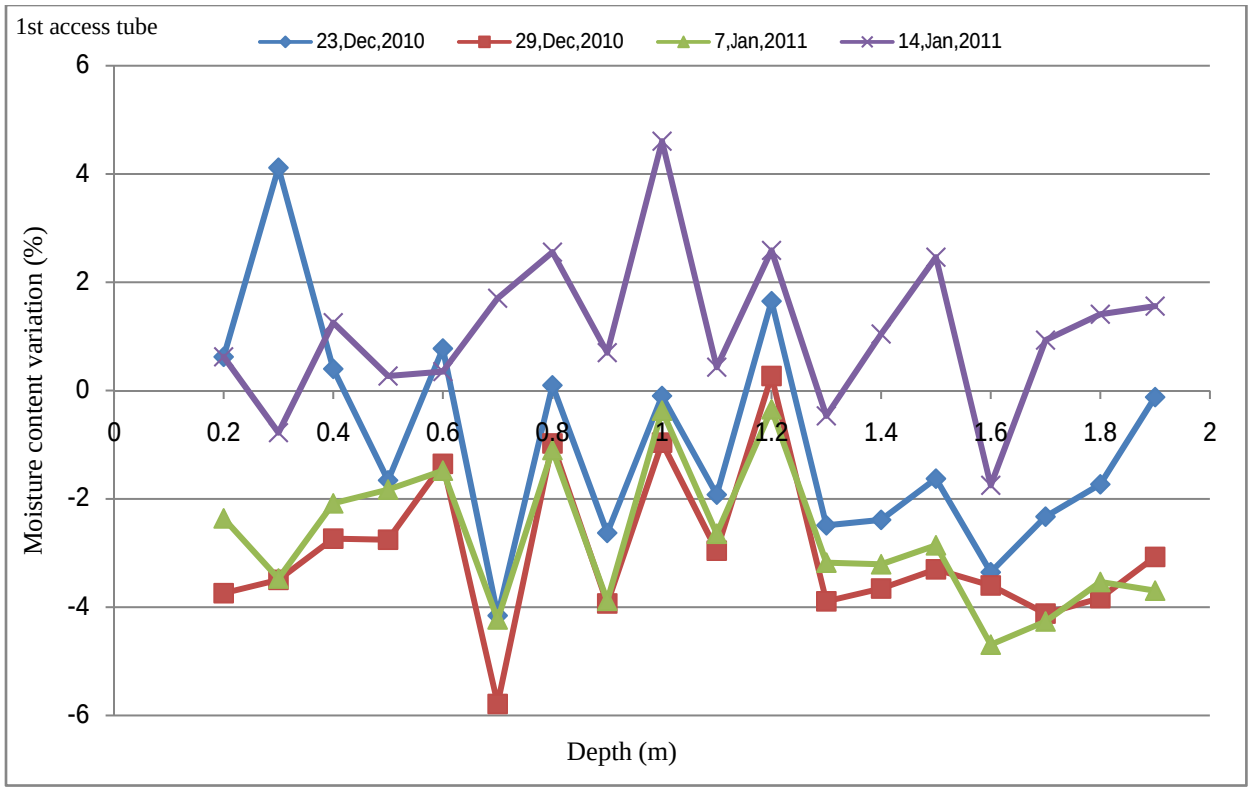

Fig.4.14. Moisture content variations with respect to background as function of the depth obtained from the capacitance sensor in the first access tube in x=6m in one month.

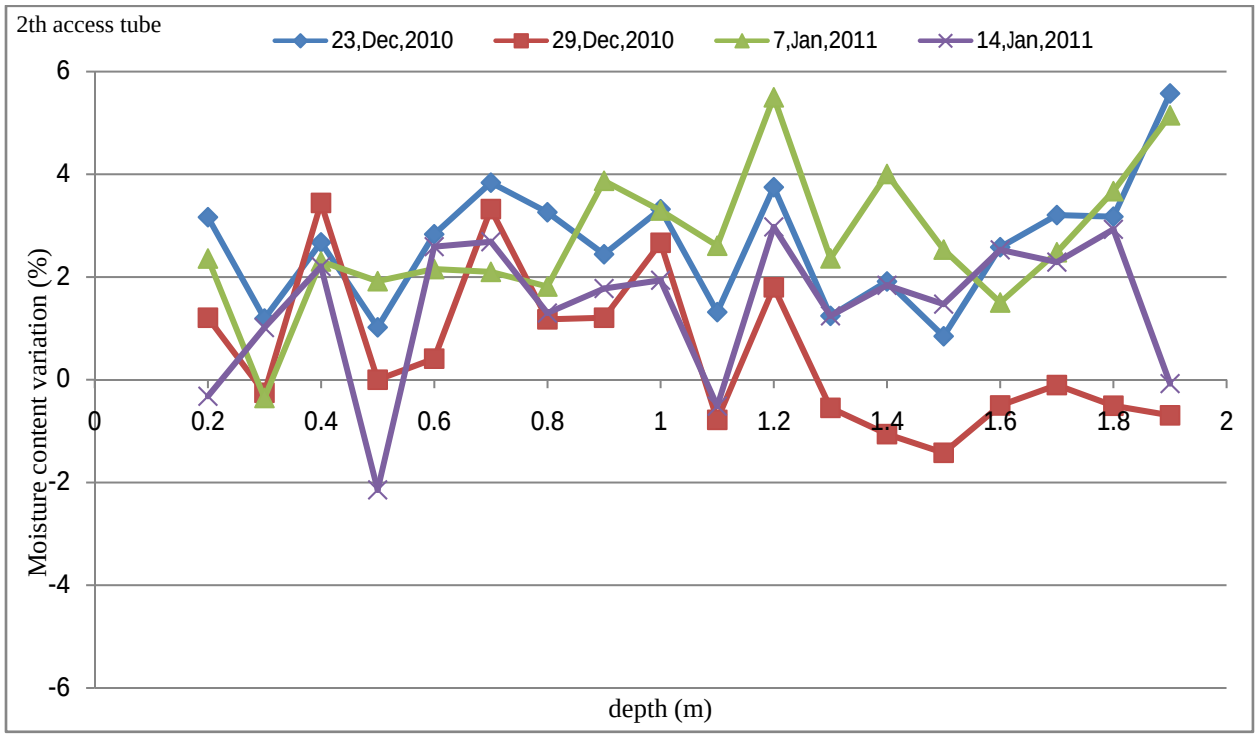

Fig.4.15. Moisture content variations with respect to background as function of the depth obtained from the capacitance sensor in the second access tube in x=9 m in one month.

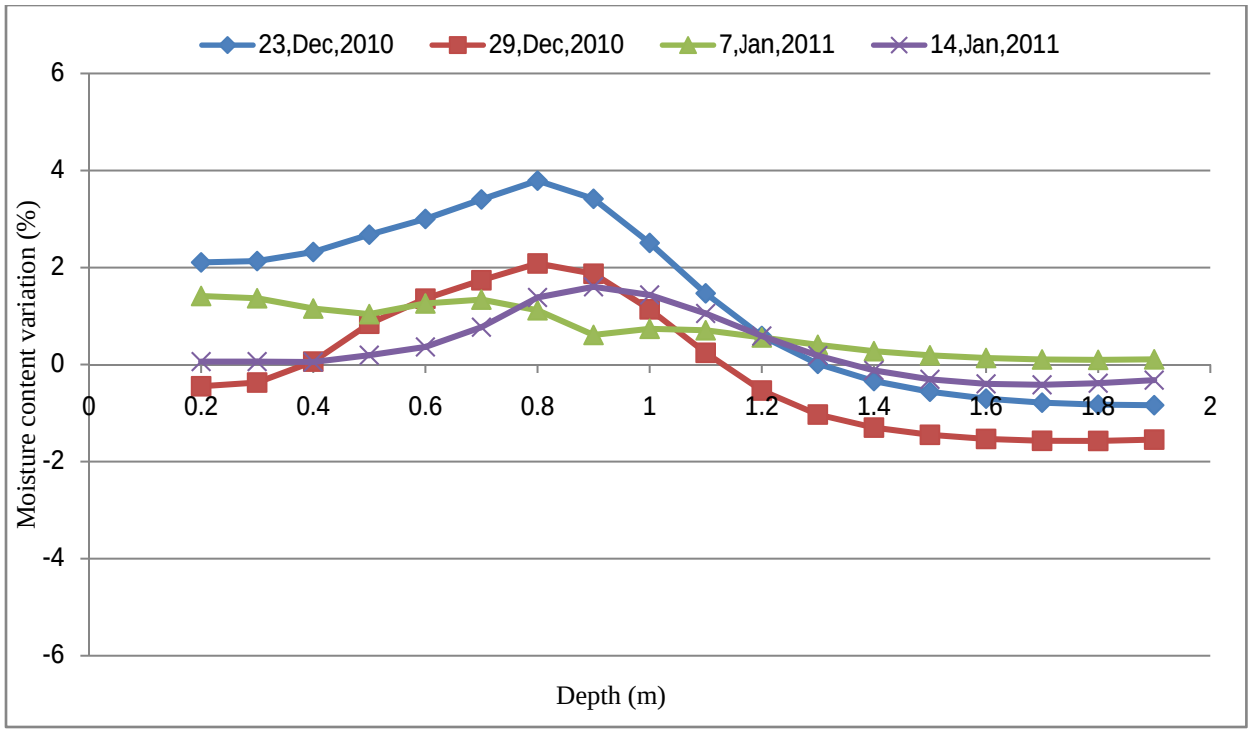

Fig.4.16. Moisture content variations with respect to background as function of the depth, inferred from the resistivity models near the first access tubes in one month.

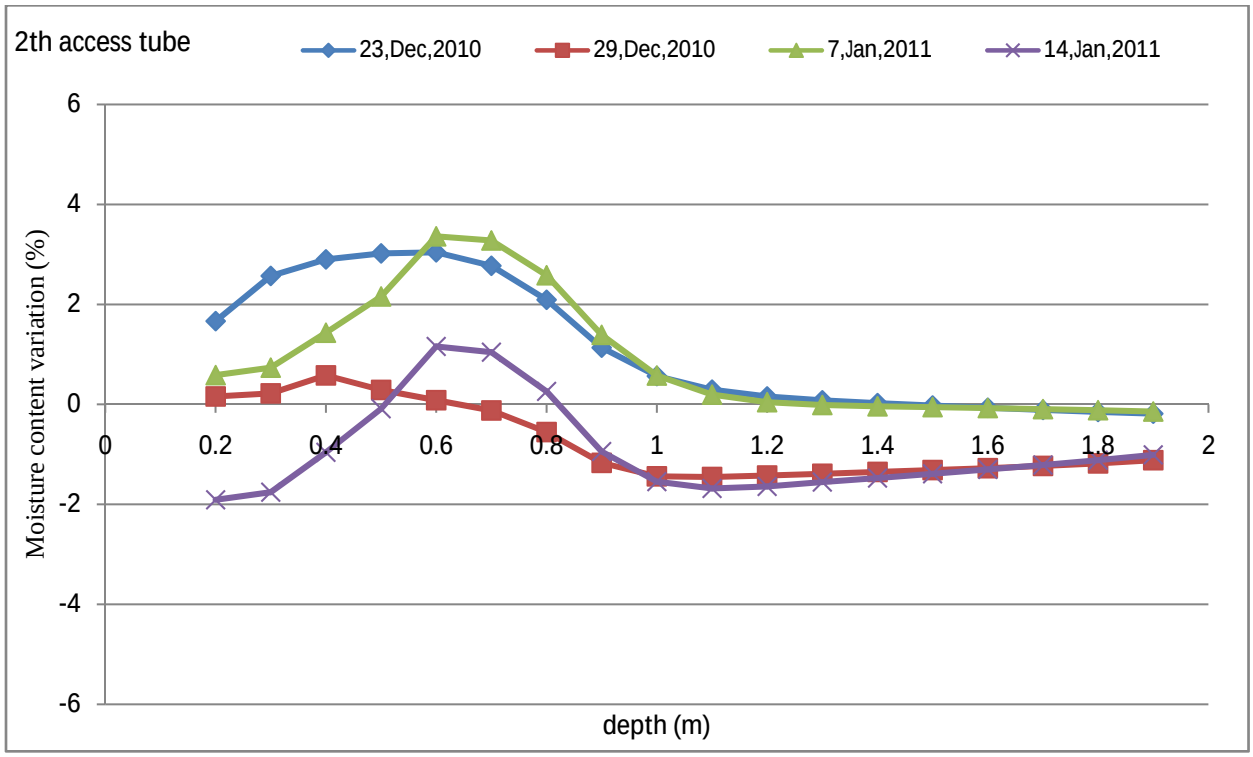

Fig.4.17. Moisture content variations with respect to background as function of the depth, inferred from the resistivity models near the second access tubes in one month.

4.5. Moisture content maps

Fig. 4-18 to 4-22 illustrate moisture content distribution computed by converting ERT images using equation 4.1, respectively for 28-Oct and 4-Nov 2010, 11-Feb, 21-Apr, and 20- Jun 2011. Maps of moisture distribution clearly show how the moisture content of the unsaturated zone changes during the experiment. The moisture content changed from an average of 28-32% in November to 22-27% in June. The right zone of the profile shows lower moisture content and greater variation during the experiment. Moisture distribution maps obtained using Wenner and Schlumberger configurations are consistent as expected, but the estimated moisture content using Dipole-Dipole is slightly lower than Wenner and Schlumberger configurations in the right side of the profile. Fig. 4.23a to Fig.4.23f show moisture distribution maps inferred from EM38 images in 28-Oct, 4-Nov and 25-Nov 2010, 20-Jan, 11-Feb and 20- Jun 2011 respectively. An investigation of calculated maps in Fig. 4.23(a-f) indicates that the highest and lowest moisture content levels are seen in November and June respectively. The maps inferred from EM38 images displays slightly greater moisture content and less lateral changes along the profile in comparison with ERT images, yet the results are acceptably consistent. The spatiotemporal moisture content changes barely exceeded 10% during the experiment which indicates that the soil is semi-pervious and relatively homogeneous. The analysis of four soil cores taken in 2 Dec, 2010, 20-Apr and 20-June 2011 for moisture content are consistent with moisture content distribution maps inferred from EM38 and ERT images.

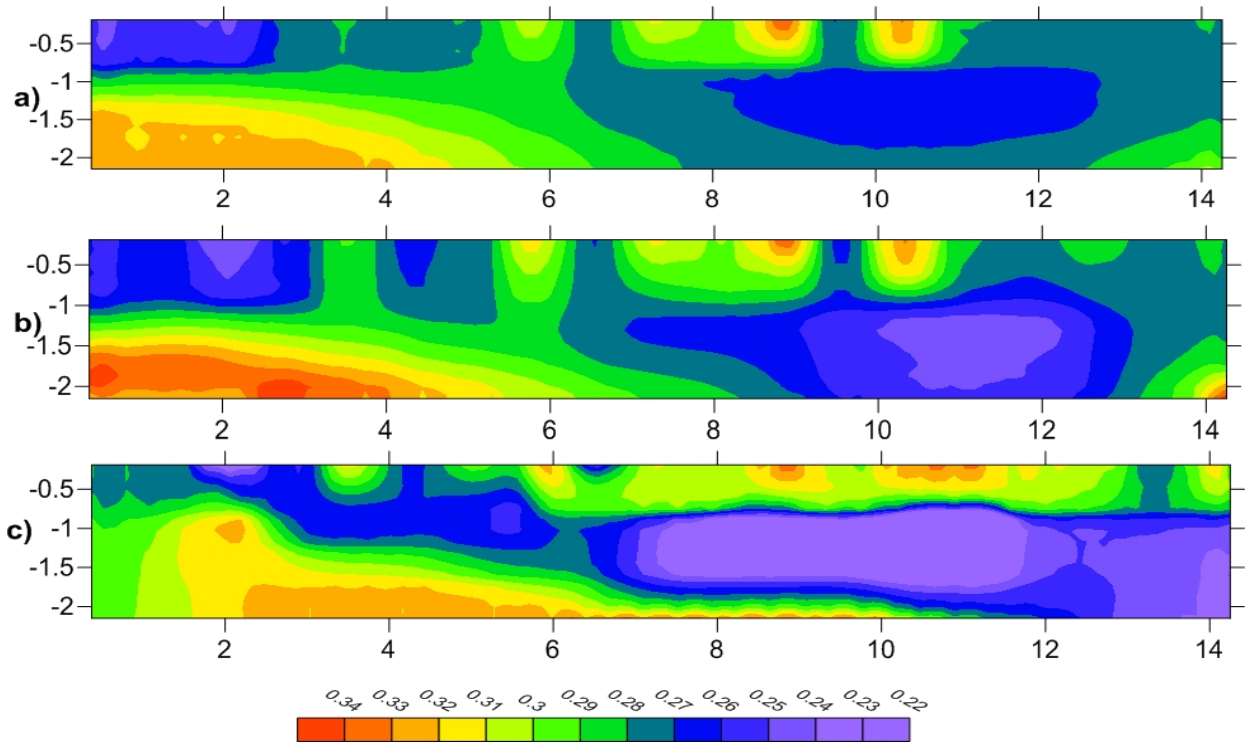

Fig.4.18. 2D moisture content distribution in 28-Oct 2010 inferred from ERT image obtained by a) Wenner, b) Schlumberger and c) Dipole-Dipole electrode configurations using equations 4a-c.

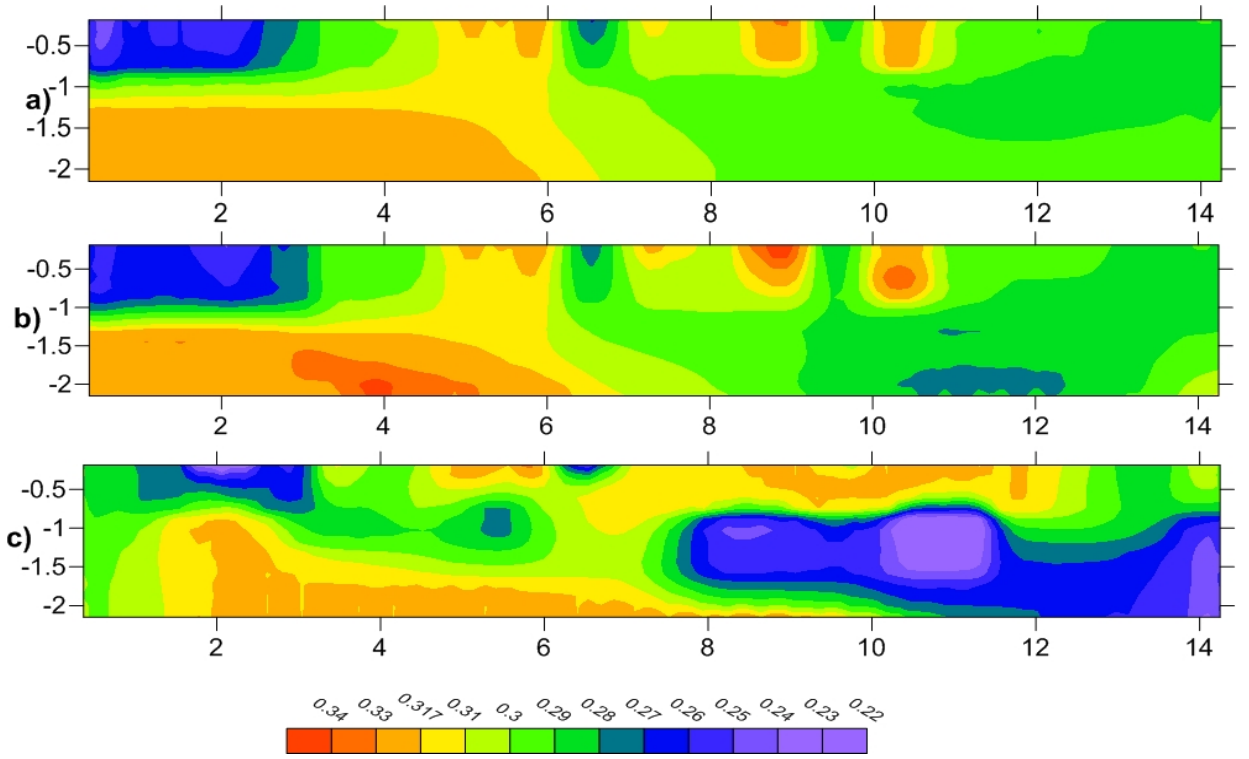

Fig.4.19. 2D moisture content distribution in 4-Nov 2010 inferred from ERT images obtained by a) Wenner b) Schlumberger and c) Dipole-Dipole electrode configurations using equations 4a-c.

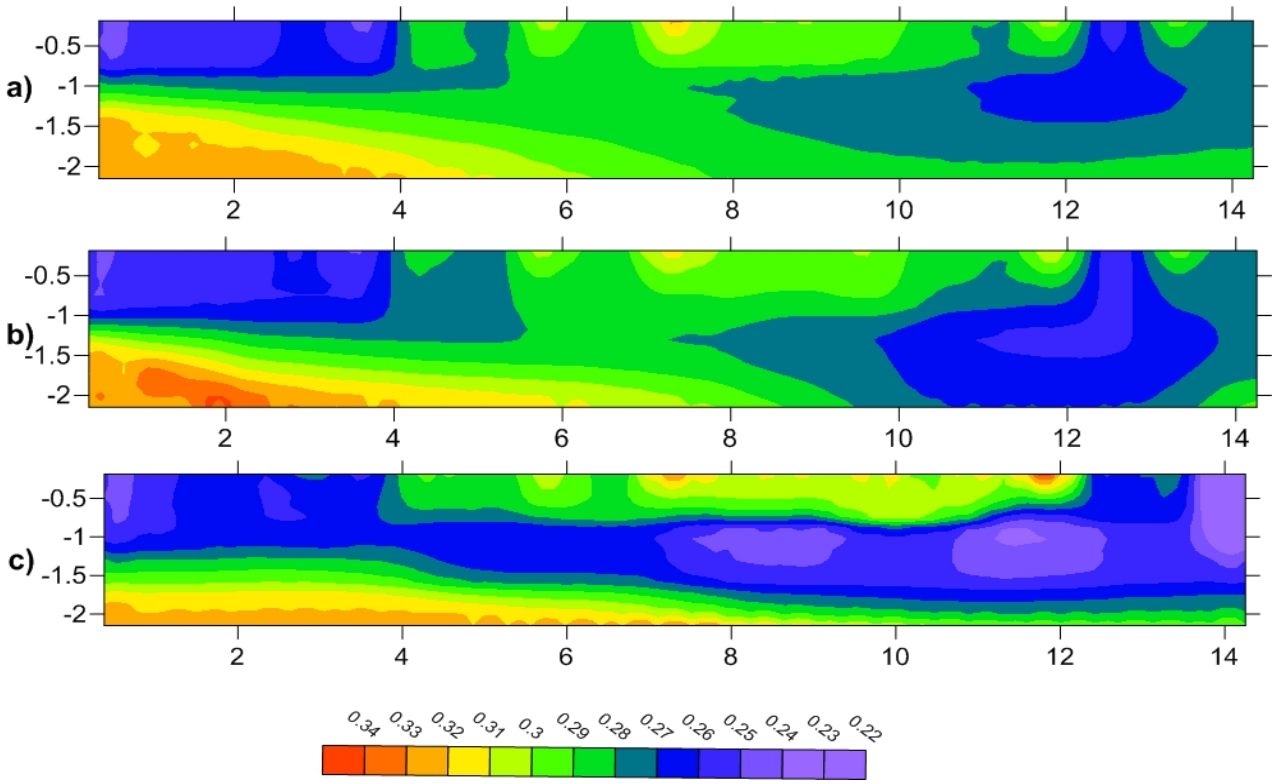

Fig.4.20. 2D moisture content distribution in 11-Feb 2011 inferred from ERT images obtained by a) Wenner, b) Schlumberger and c) Dipole-Dipole electrode configurations using equations 4a-c.

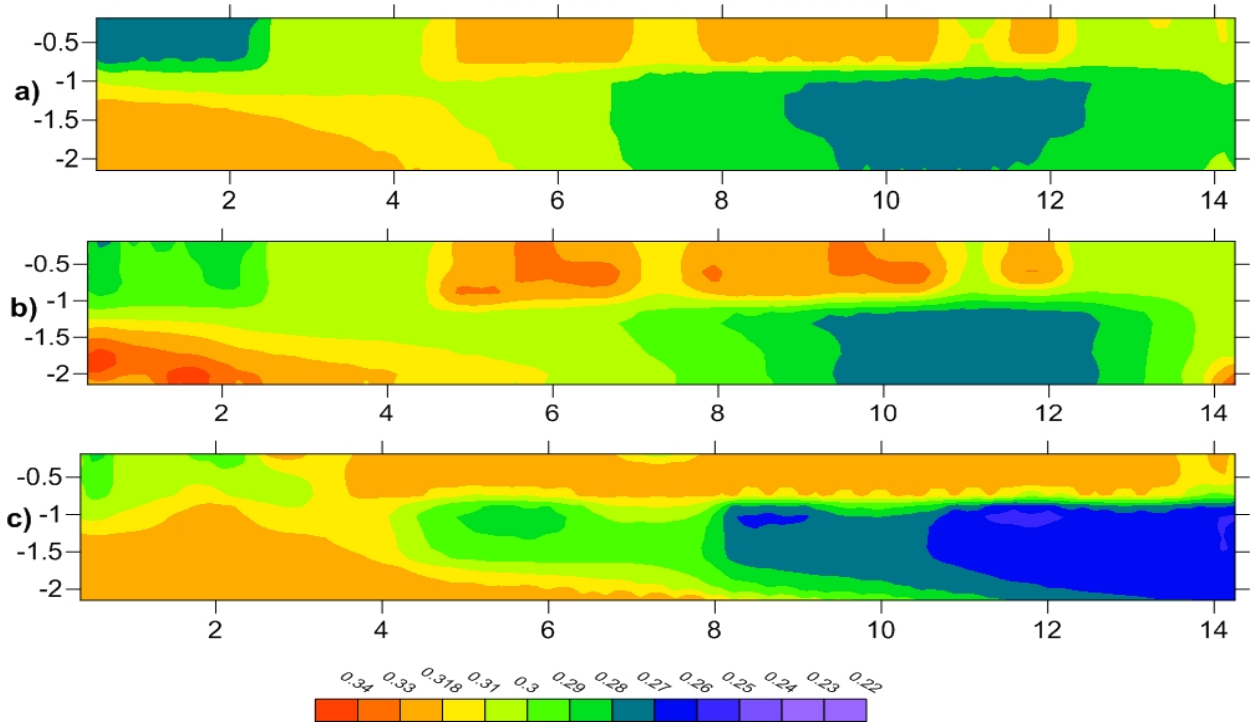

Fig.4.21. 2D moisture content distribution in 21-Apr 2011 inferred from ERT images obtained by a) Wenner b) Schlumberger, and c) Dipole-Dipole electrode configurations using equations 4a-c.

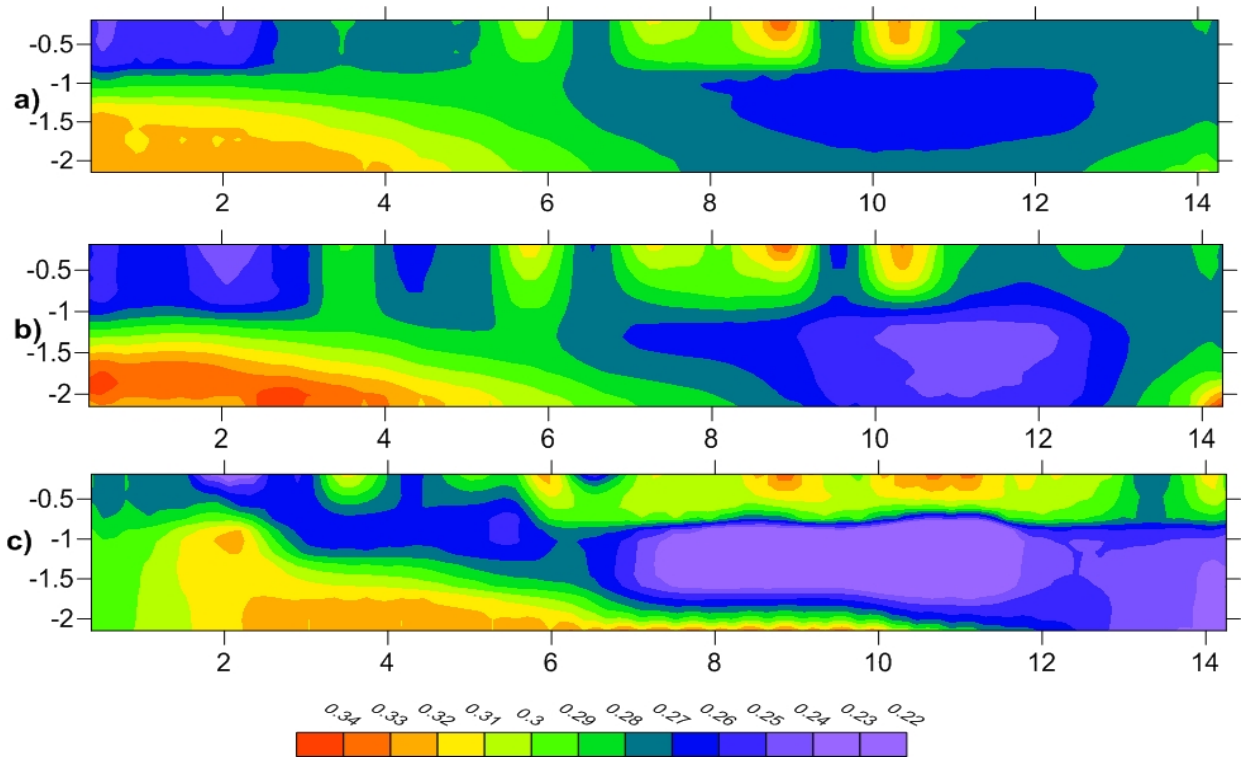

Fig.4.22. 2D moisture content distribution in 20-Jun 2011 inferred from ERT images obtained by a) Wenner, b) Schlumberger and c) Dipole-Dipole electrode configurations using equations 4a-c.

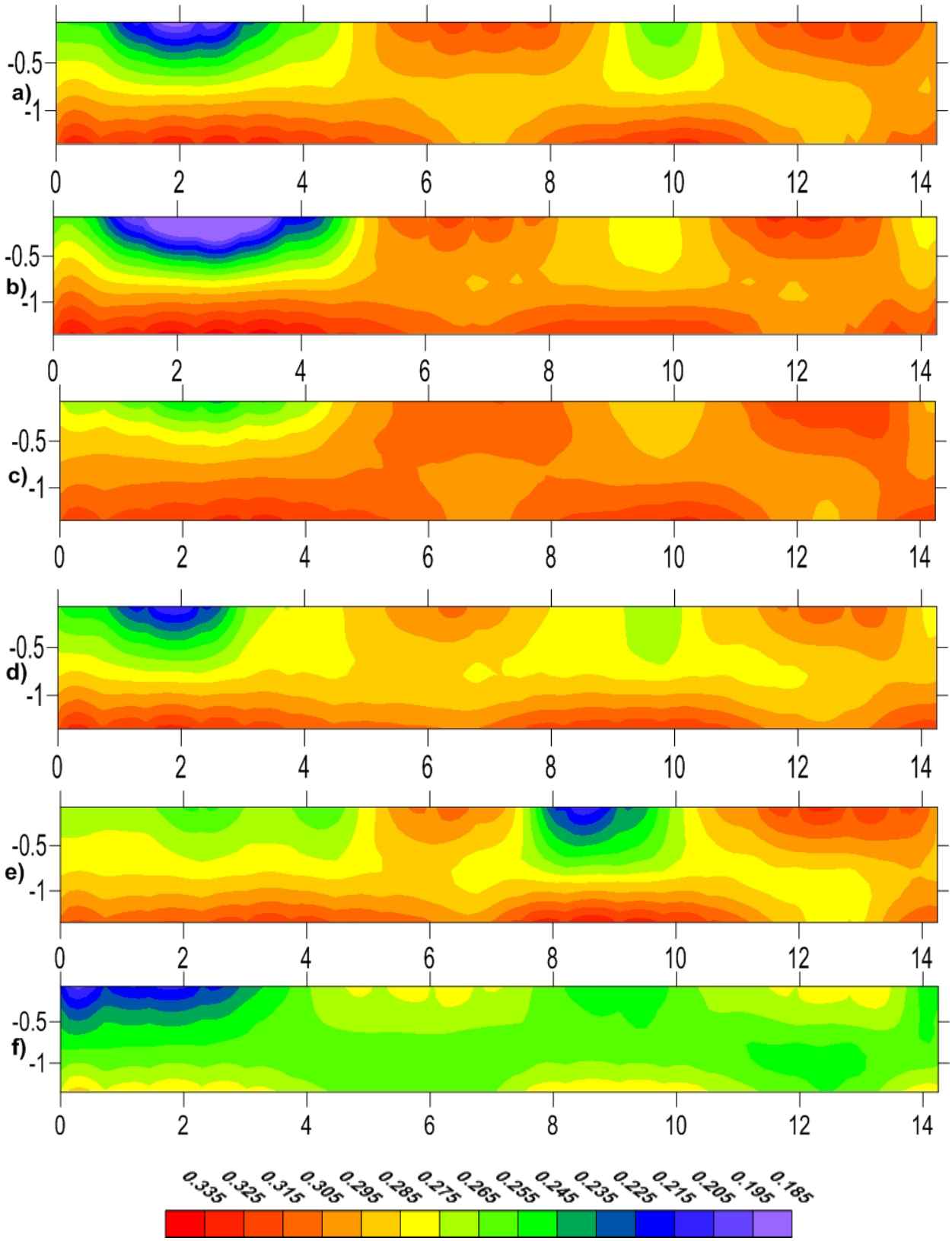

Fig.4.23. 2D moisture content distribution inferred from EM38 images by using equations 4d in a) 28-Oct, b) 4-Nov and c) 25-Nov 2010, d) 20-Jan, e) 11-Feb and f) 20- Jun 2011.

4.6. Geophysical and hydrological parameters

Many researchers that (e.g. Binley et al. 2002a; Looms et al. 2008a, 2008b; Dienna et al. 2007) have shown that how geophysical monitoring could be applied for estimating hydraulic conductivity and constraining the hydrological model. EM38 images and also ERT images obtained using Wenner and Schlumberger electrode configurations were used in this study in order to estimate hydraulic conductivity.

4.6.1. Unsaturated flow modeling

Unsaturated flow model was built by a finite-element formulation using Hydrus 2D. Van Genuchten equations were applied as retention and hydraulic conductivity functions in this model. As mentioned in section 3.5.2, van Genuchten´s parameters (θr, θs, α, n, and Ks) for all samples were estimated by Rosetta software based on the particle size distributions and bulk density. The ranges of van Genuchten´s parameters of soil samples are presented in table.4.1a. We simplified the soil texture of the profile to two scenarios. A homogeneous soil was considered first, assuming uniform hydraulic parameters throughout the investigated area (table 4.1b). Close inspection of grain size analyses from core sampling (discussed in section 4.1) and the obtained geophysical models indicated that the subsurface may be roughly subdivided into two soil zones with slightly different hydraulic characteristics. Therefore we divided the soil to two zones, the left side from 0-7.5 m and right side from 7.5-15 m. Estimated van Genuchten´s parameters for each zone are given in table 4.1(c).Van Genuchten's equations along with estimated values were used as input for unsaturated flow simulation. Each simulation was initiated separately by using the moisture content images inferred from ERT (Wenner and Schlumberger electrode configurations) and EM38 background images. Simulating the moisture content distribution, we used the same grid as the one used in EM38 and ERT inversions so as to make it possible to compare geophysical responses with flow simulations and evaluate the hydraulic conductivity. The upper and bottom boundaries of the soil were simulated by implementing atmospheric and free drainage boundary conditions respectively. The evaporation and precipitation data during the experiment were collected and used in these simulations. The simulations were carried out for 238 days during 28-Oct 2010 to 20-Jun 2011 time period.

Table.4.1. Van Genuchten parameters estimated by Rosetta

Parameters Estimation		θ_r	θ_s	α (cm-1)	n	k_s(cm/day)
a		0.041-0.05	0.33-0.36	0.01-0.02	1.32-1.45	3.5-8.25
b		0.046	0.34	0.015	1.35	4.5
c	0-7.5 m	0.048	0.33	0.015	1.36	4
	7.5-15 m	0.043	0.35	0.014	1.38	5.3

4.6.2. Estimating and constraining the hydrological parameters by geophysical data

To evaluate whether individual hydrologic models represent the field conditions, the geophysical response and simulating flow were compared using a misfit value:

$$Misfit\ error = 100 * \sqrt{\sum_i^N [(\theta_s - \theta_g)^2]/N} \quad (4.3)$$

Where θ_s is the simulated moisture content and θ_g is the moisture content inferred from ERT or EM38 images and N is the number of pixels of models. We compare the geophysical response and simulating flow based on the smallest misfit. The first ten time-lapse data sets collected by ERT and EM38 were used in this evaluation.

Fig. 4.24, 4.26 and 4.28 presents a comparative illustration of the misfit error of simulating flow using estimated van Genuchten's parameters for homogeneous soil (presented in table.4.1b) and ERT and EM38 images. Among van Genuchten's parameters, the saturated hydraulic conductivity plays the most important role in dynamics of the vadose zone and in particular, it controls the speed of water infiltration (looms et al., 2008). Therefore we fixed all others Genuchten's parameters so as to make them the same as those shown in table.4.1b. Afterwards, several new simulations were carried out by changing saturated hydraulic conductivity values to find the smallest misfit on the basis of the moisture content distribution. Percent of mass recovery of ERT and EM38 images in monitoring moisture content were also calculated and plotted in Fig. 4.25, 4.27 and 4.29 in order to provide a better quantitative comparison of geophysical model and simulating flow for hydraulic conductivity estimation. An investigation of ERT results in Fig.4.24 to Fig.4.27 shows good consistency between Wenner and Schlumberger electrode configurations results. The results of the misfit errors and present mass

indicate that hydraulic conductivity value of 4.5 cm/day can reasonably reproduce the moisture content distribution during the experiment. Greater values of hydraulic conductivity yield higher misfit error and underestimate mass recovery, while lower hydraulic conductivity overestimates mass recovery of the moisture content distribution and increases misfit error. The results of EM38 images are shown in Fig 4.28 and 4.29. An investigation of the misfit errors and present mass indicate that the hydraulic conductivity of 8 cm/day can better reproduce the moisture content distribution during the experiment. Lower hydraulic conductivities largely overestimate mass recovery and show greater misfit errors. On the other hand, greater hydraulic conductivities underestimate mass recovery and also yield greater misfit errors. Hydraulic conductivity estimated using EM38 images is two times greater than that estimated by ERT images, yet all results constrained hydraulic conductibility to be in 1-10 cm/day range. We also calculated the misfit error and mass recovery of ERT images in comparison with simulating flow using 2-layers soil and estimated van Genuchten's parameters in table 4.1c. The misfit error and mass recovery of ERT images in comparison with simulating model are shown in Fig 4.30 and 4.31 with α =1. We only presented ERT images inferred from Schlumberger electrode configuration since the results of ERT images inferred from Wenner electrode configuration are very similar. Several new simulations were carried out using multiple values for hydraulic conductivity reported in Table 4.1c. The goal was to find the smallest misfit and best mass recovery. Results indicate that smallest misfit and best mass recovery are achieved by a 2-layer model with hydraulic conductivity of 4 and 5.3 cm/day among our flow simulations. Comparing misfit error obtained using ERT images; we found that 2-layers soil (Fig 4.32b) reproduced moisture content distribution slightly better than homogenous soil (Fig 4.32a) did. We also analyzed different scenarios for 2 layers soil such as greater hydraulic conductivity for the left zone rather than the right zone or greater differences between the hydraulic conductivity of the left and right zone (e.g. see Fig. 4.32c, d). Our investigation indicates that the hydraulic conductivity of soil slightly increases along the profile from the left to the right side. We did the same procedure for EM38 images to see whether yield better fit with 2-layer soil model. Different from ERT images, EM38 images did not better match to 2-layer soil model.

In Fig.4.33 and Fig.4.34, the moisture-content simulations in 4-Nov 2010, 11-Feb, 21-Apr and 20- Jun 2011 were presented so as to better visualize moisture-content distribution. A homogenous and a 2-layer soil with Van Genuchten parameters defined in table.4.1b and 4.1c

were used to produce Fig.4.33 and Fig.4.34 respectively. The goal was to helps compare moisture-content distribution inferred from ERT images with flow simulations that shows the most similarity among simulations.

An investigation of Fig.4.33 and Fig.4.34 in comparison with Fig.4.18 to Fig.4.22 show an acceptable estimation of moisture content values along the profile during the period of the experiment. This finding indicated that the estimated hydraulic conductivity acceptably reproduce the water movement. The moisture content distribution maps inferred from ERT images are to some extent different from flow simulations shown in Fig.4.33 and Fig.4.34. This is not surprising because our simulations limited to only homogenous and 2-layer soil scenarios while a significant degree of heterogeneity had been observed in the soil texture analysis. This disparity is not the only source of disagreement of flow simulations and ERT images, the lateral water movement, the inversion process of ERT data and the noise level in the ERT images (particularly in background ERT image) might explain this level of discrepancy. Yet, the flow simulations using 2-layer soil with higher hydraulic conductivity in right side of the profile better matches with ERT images.

In Fig.4.35, moisture-content simulations in 4-Nov and 25-Nov 2010, 20-Jan, 11-Feb and 20-Jun 2011 were presented. A homogenous soil with Van Genuchten parameters defined in table.4.1b and hydraulic conductivity of 8 cm/min was selected in order to compare the results with EM38 images. A comparison of Fig. 4.35 with Fig.4.23 indicate that the water movement is well reproduced using a saturated hydraulic conductivity equal to 8 cm/min, but the moisture content distribution inferred from EM38 images is relatively different from flow simulations due to the above-mentioned reasons discussed for ERT images. In addition, lower inherent accuracy of EM38 in comparison with ERT surveys and the absences of time-lapse inversion process for EM38 data contributed to creation of the discrepancy mentioned in these comparisons.

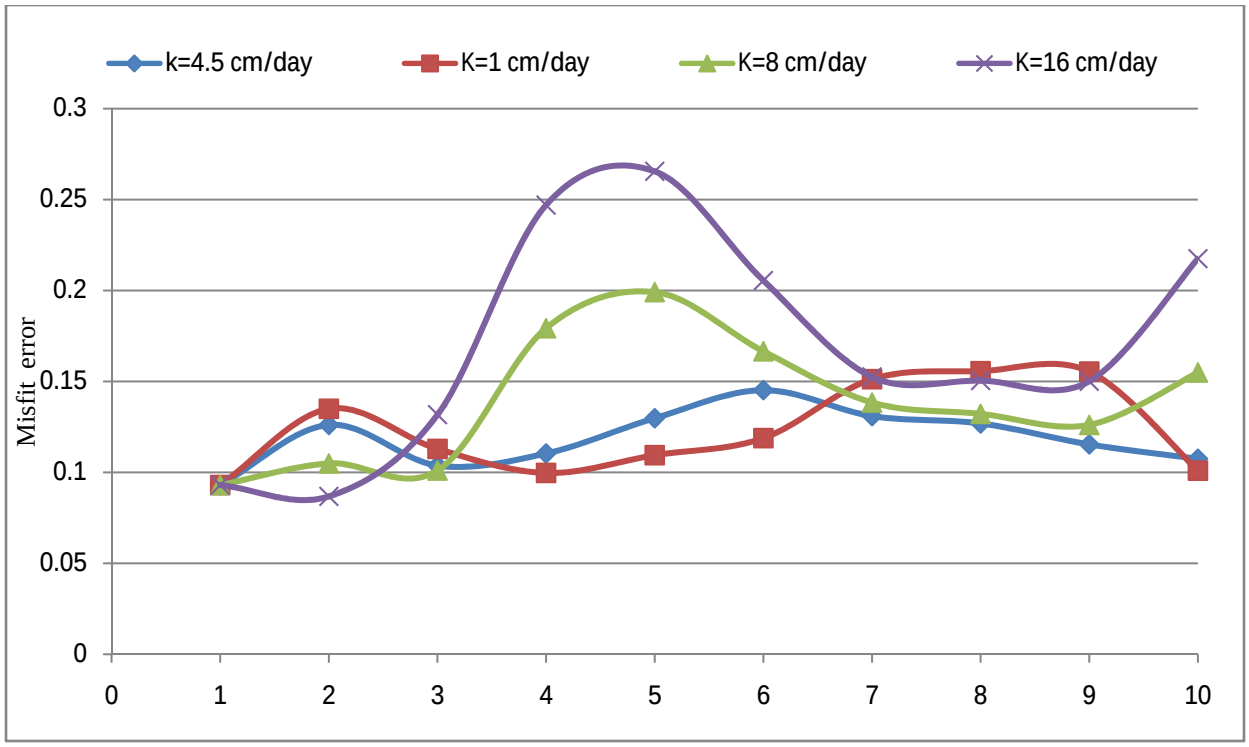

Fig.4.24. Misfit error of moisture content distribution inferred from simulating flow with ERT images using Wenner electrode configuration. Four values of saturated hydraulic conductivity (Ks) and homogenous subsoil were used in these simulations.

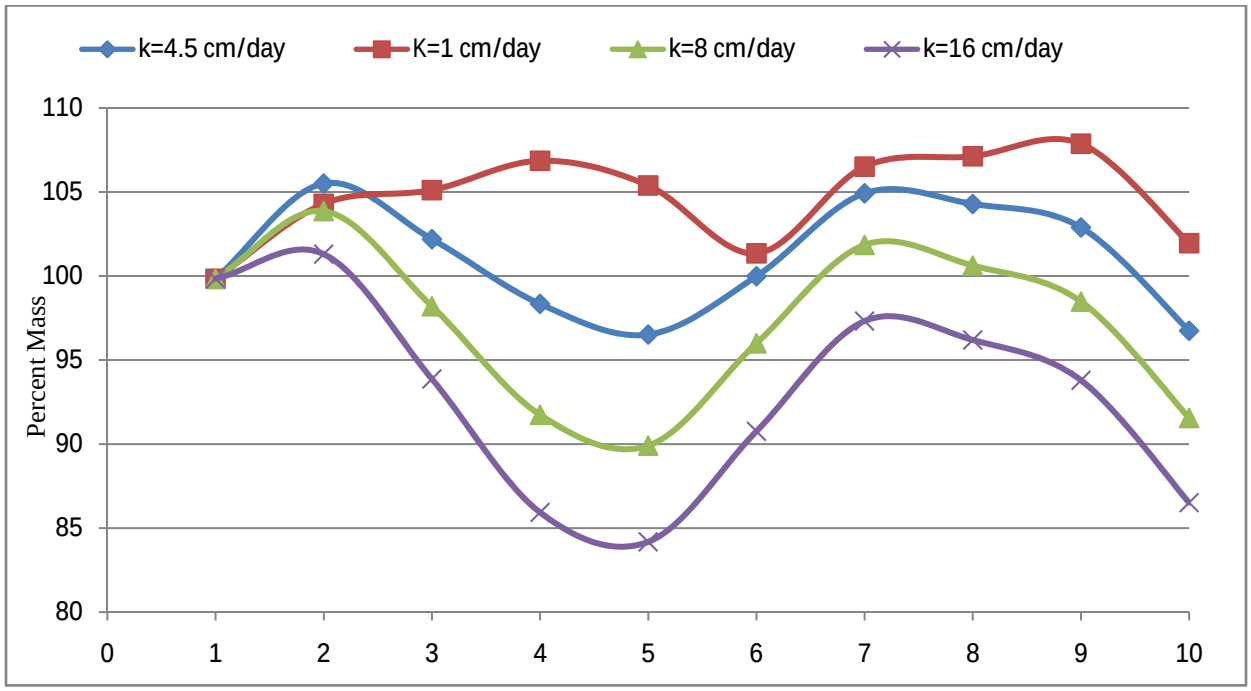

Fig.4.25. Present mass recovery of simulating models in comparison with ERT images using Wenner electrode configurations. Four values of saturated hydraulic conductivity (Ks) and homogenous subsoil were used in these simulations.

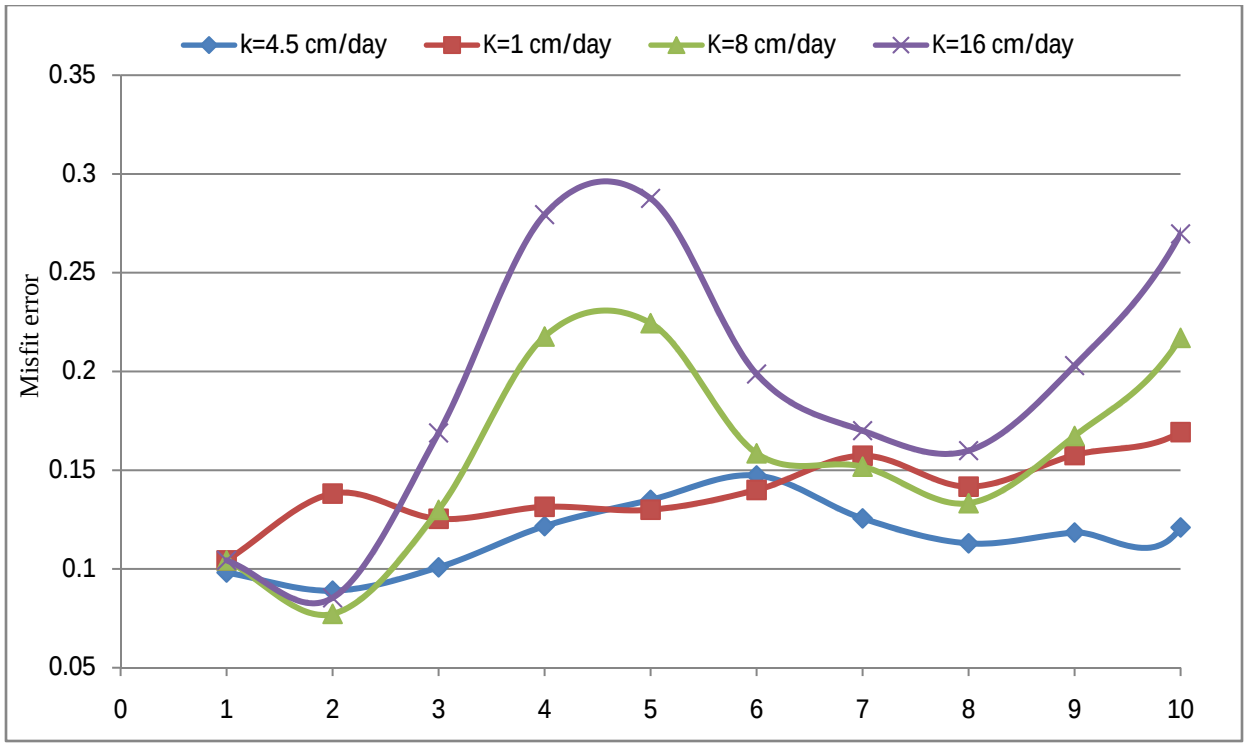

Fig.4.26. Misfit error of moisture content distribution inferred from simulating flow with ERT images using Schlumberger electrode configuration. Four values of saturated hydraulic conductivity (Ks) and homogenous subsoil were used in these simulations.

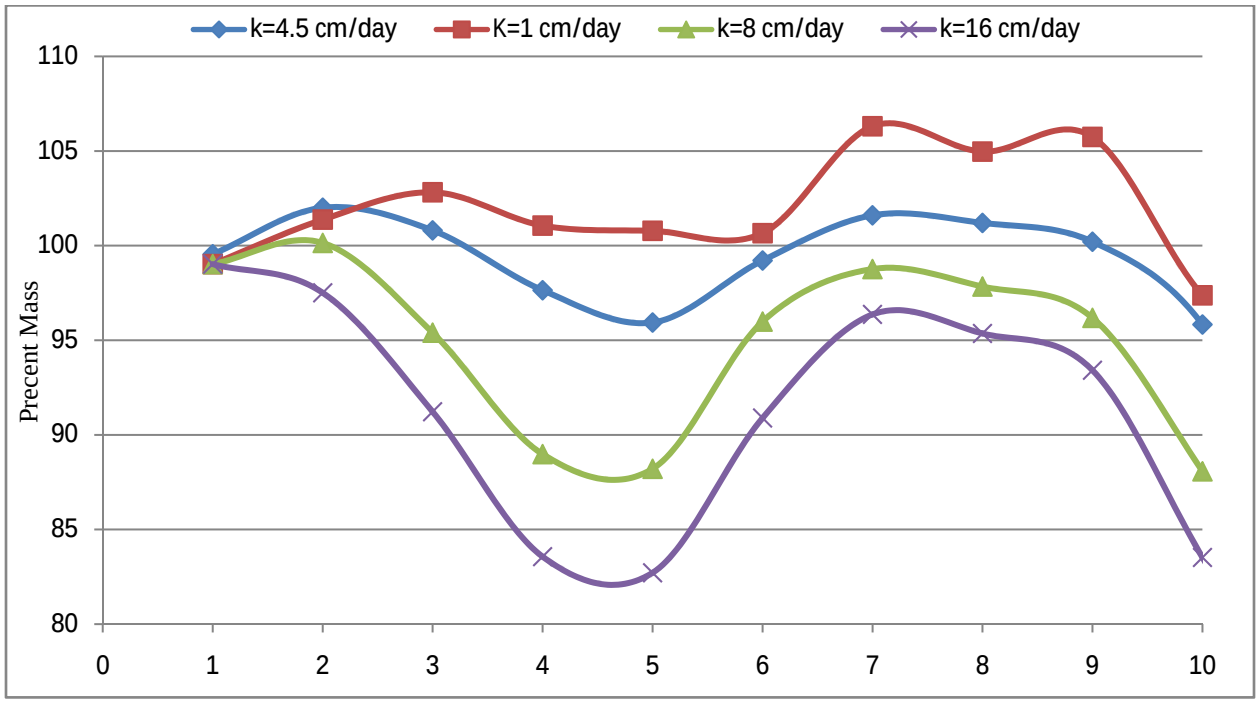

Fig.4.27. Present mass recovery of ERT images using Schlumberger electrode configurations in comparison with simulating models. Four values of saturated hydraulic conductivity (Ks) and homogeneous subsoil were used in these simulations.

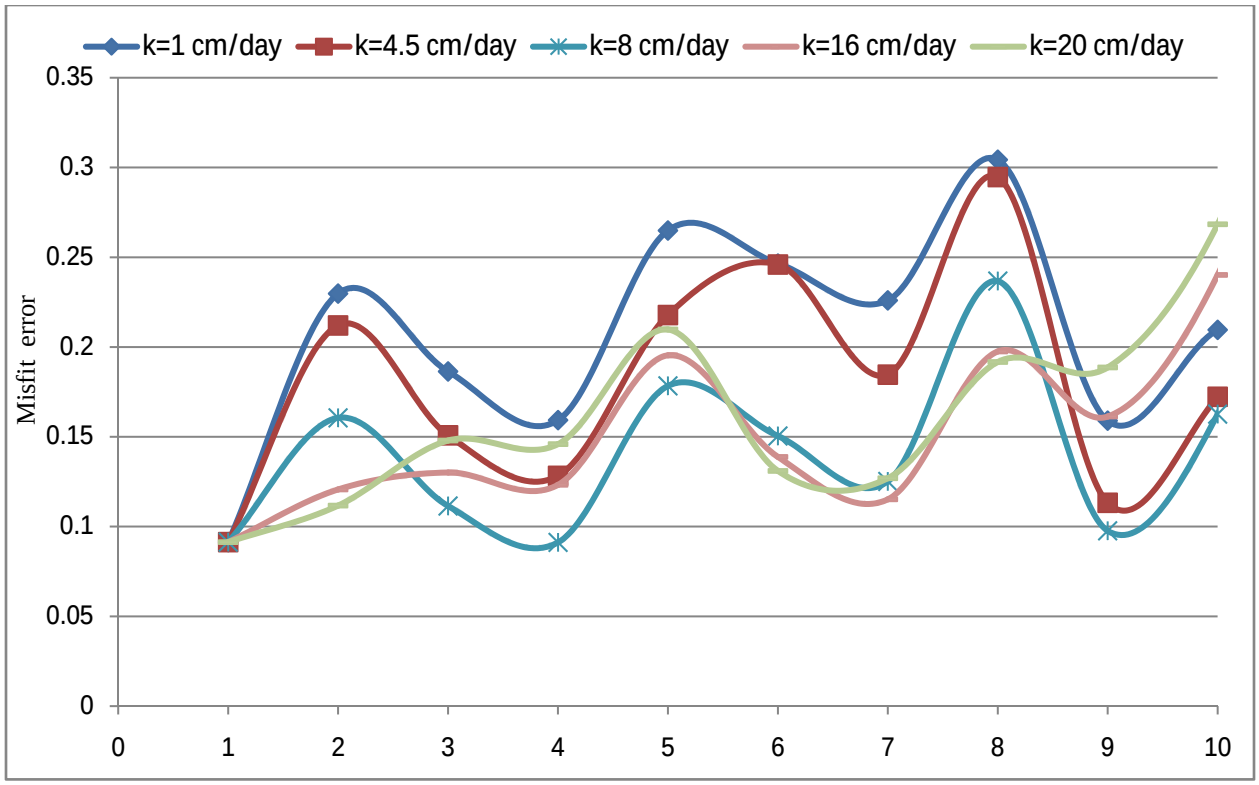

Fig.4.28. Misfit error of moisture content distribution inferred from simulating flow with EM38 images. Five values of saturated hydraulic conductivity (Ks) and homogenous subsoil were used in these simulations.

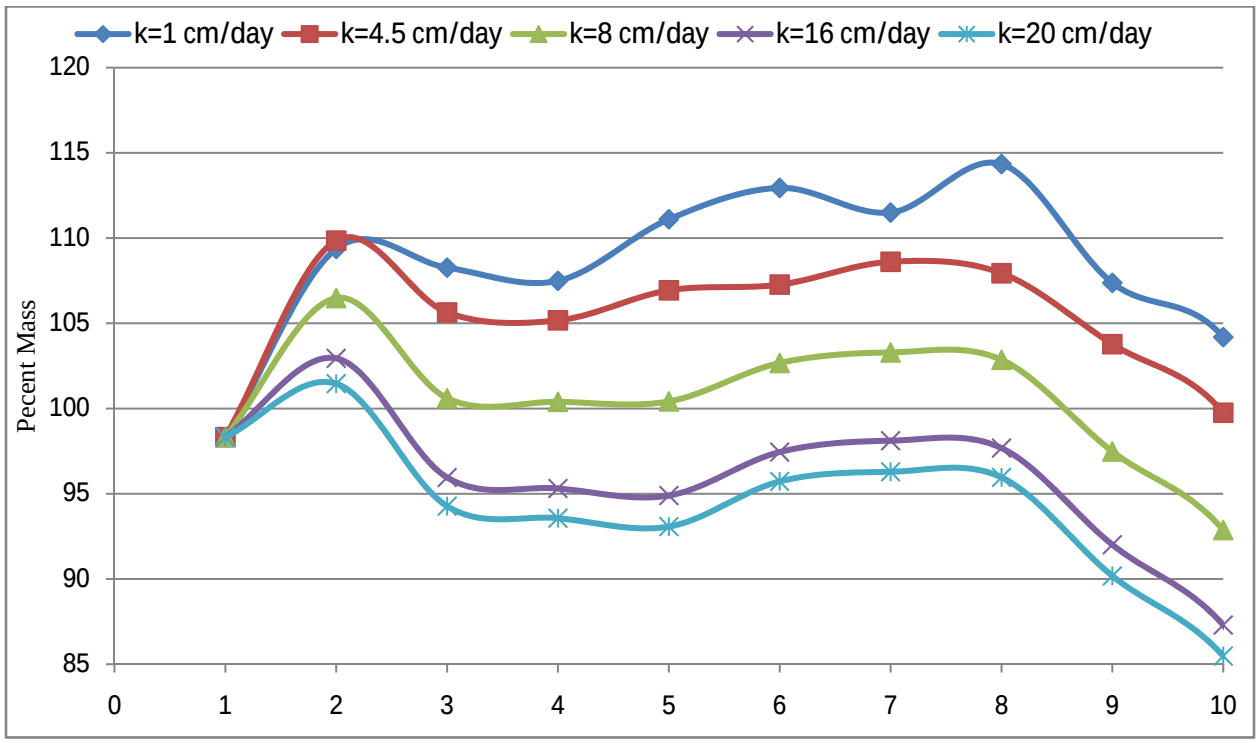

Fig.4.29. Present mass recovery of EM38 images in comparison with simulating models. Five values of saturated hydraulic conductivity (Ks) and homogeneous subsoil were used in these simulations.

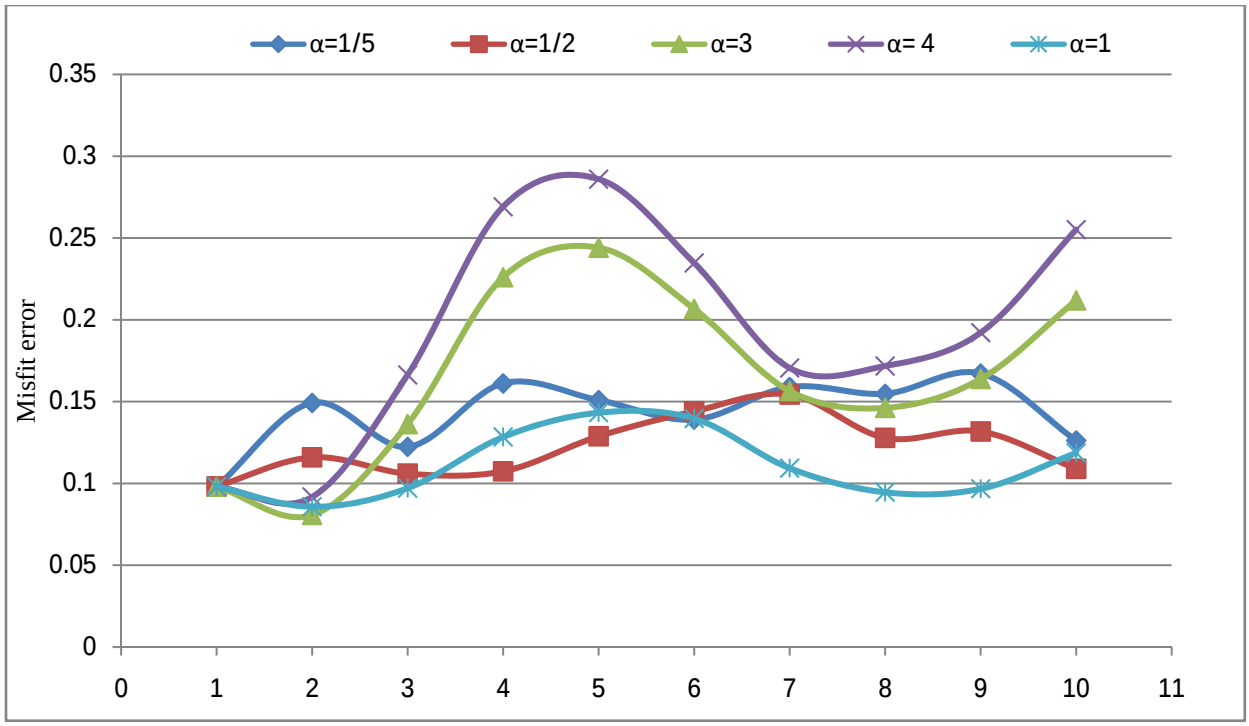

Fig.4.30. Misfit error of moisture content distribution inferred from simulating flow with obtained ERT images using Schlumberger electrode configuration. Five values of saturated hydraulic conductivity (Ks) and two-layer subsoil were used in these simulations.

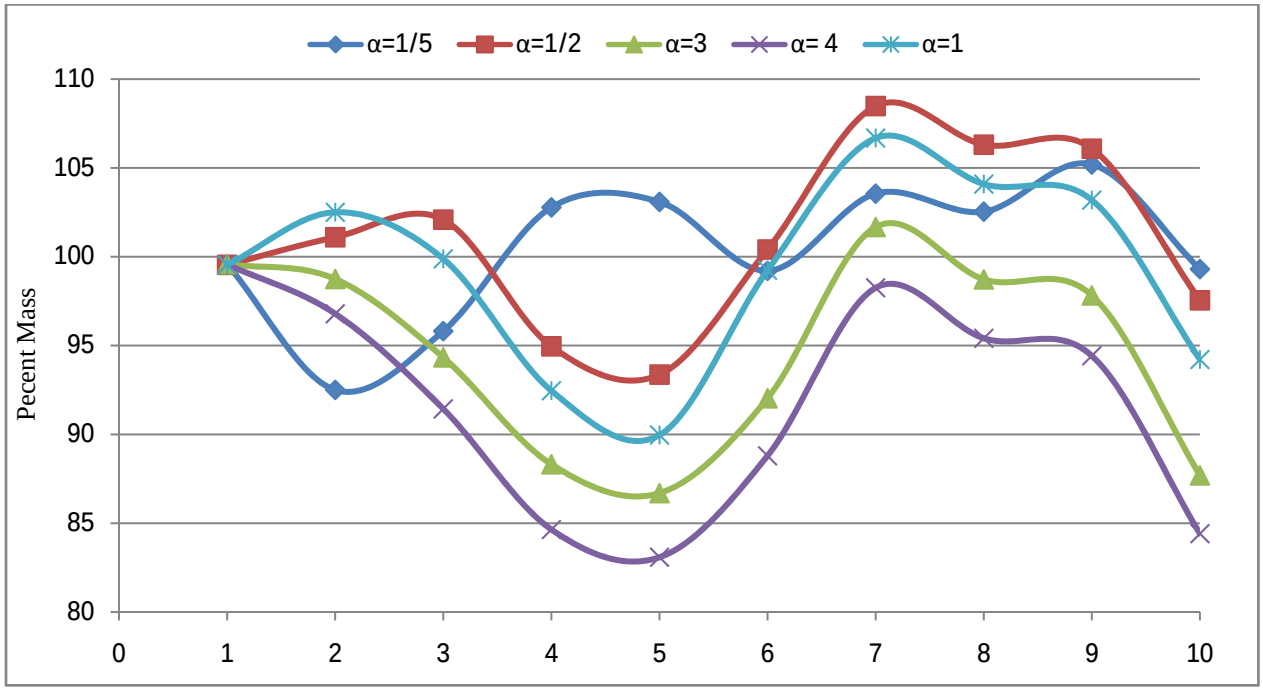

Fig.4.31. Present mass recovery of ERT images using Schlumberger electrode configurations in comparison with simulating models. Five values of saturated hydraulic conductivity (Ks) and two-layer subsoil were used in these simulations.

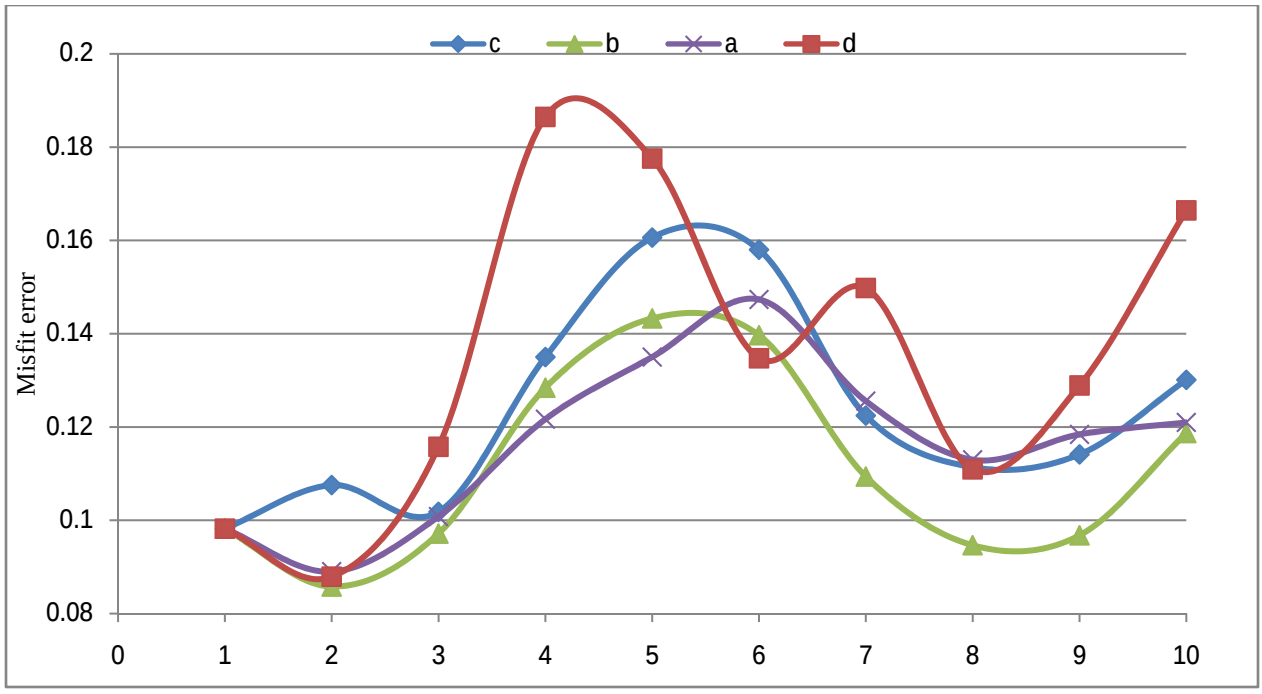

Fig.4.32. Misfit error of moisture content distribution inferred from simulating flow with obtained ERT images using Schlumberger electrode configuration. Four values of saturated hydraulic conductivity (Ks) and subsoil were used in these simulations: 1- a) Homogenous soil with Ks=4.5 cm/day. 2- two-layer subsoil defined in table1c with Ks= b) 4, 5.3; c) 5.3, 4; d) 7, 3.

a)

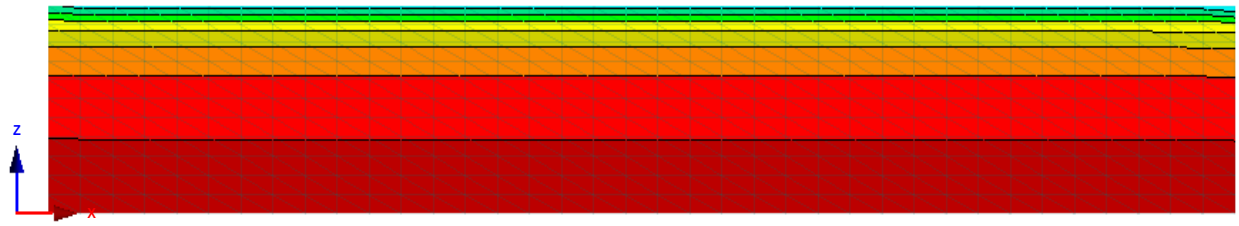

b)

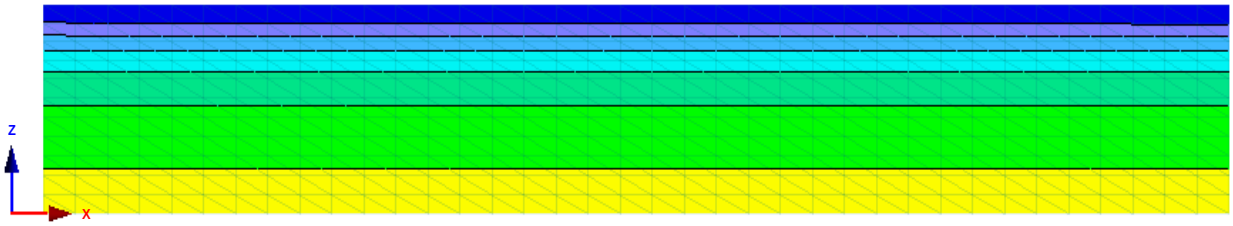

c)

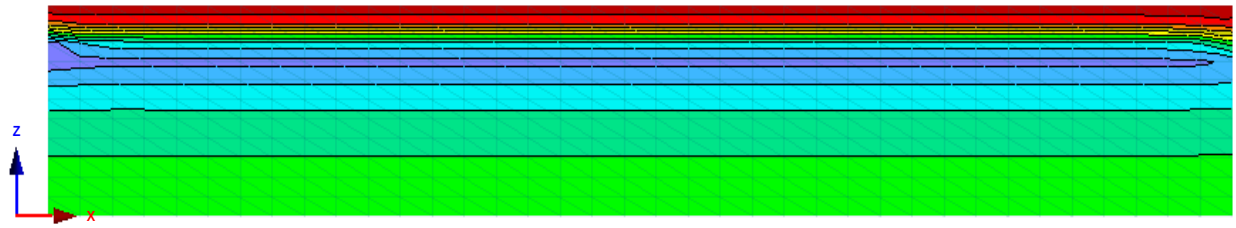

d)

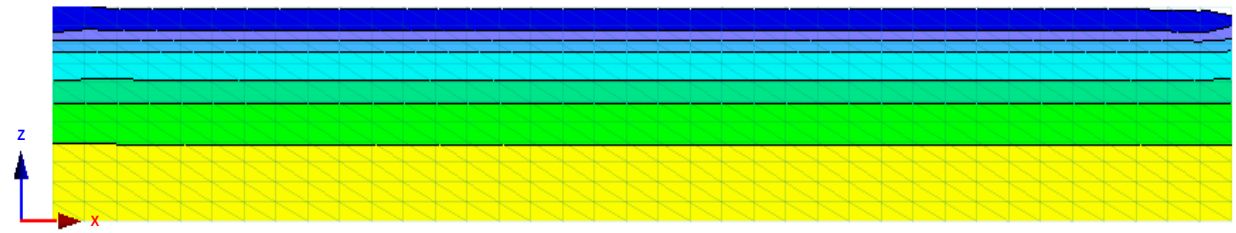

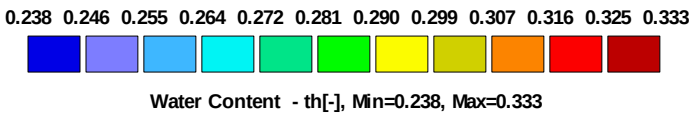

Fig.4.33. Moisture-content distribution simulated using a 2D- unsaturated flow model, using a homogenous soil and isotropic saturated hydraulic conductivity equal to 4.5 cm/min in a) 4-Nov 2010, b) 11-Feb, c) 21-Apr and d) 20-Jun 2011 respectively.

a)

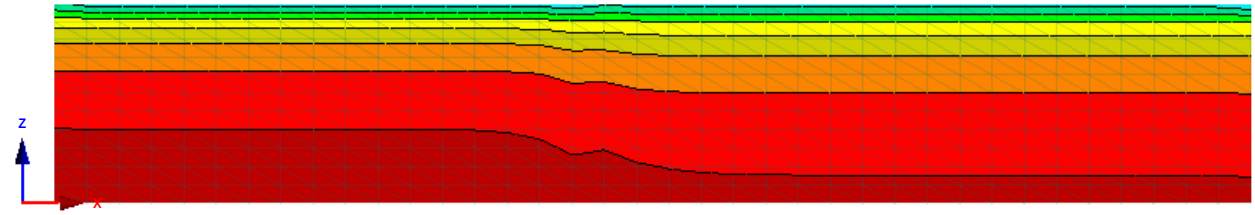

b)

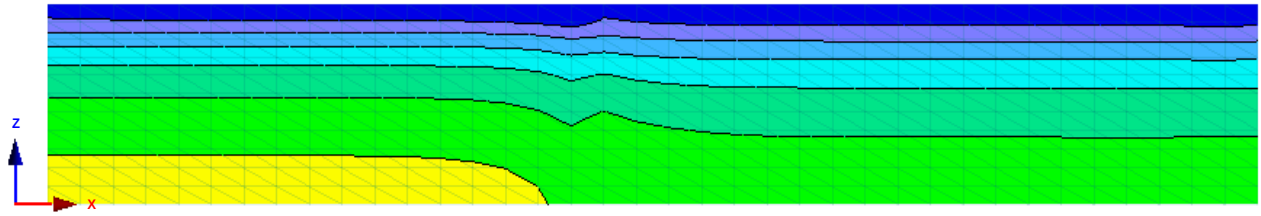

c)

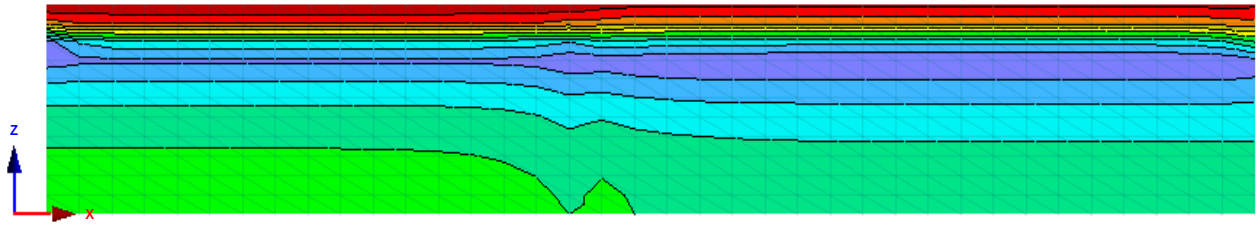

d)

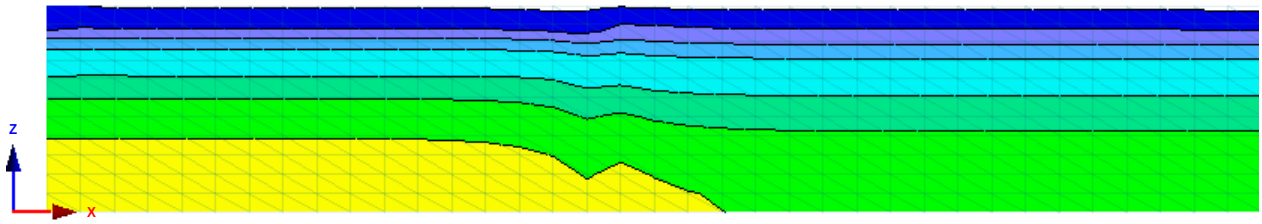

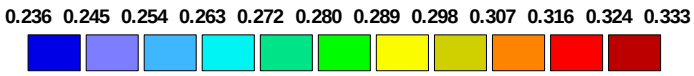

Fig.4.34. Moisture-content distribution simulated using a 2D- unsaturated flow model, using a two-layer subsoil defined in table1c and isotropic saturated hydraulic conductivity equal to Ks= 4, 5.3 cm/min in a) 4-Nov 2010, b) 11-Feb, c) 21-Apr and d) 20- Jun 2011 respectively.

a)

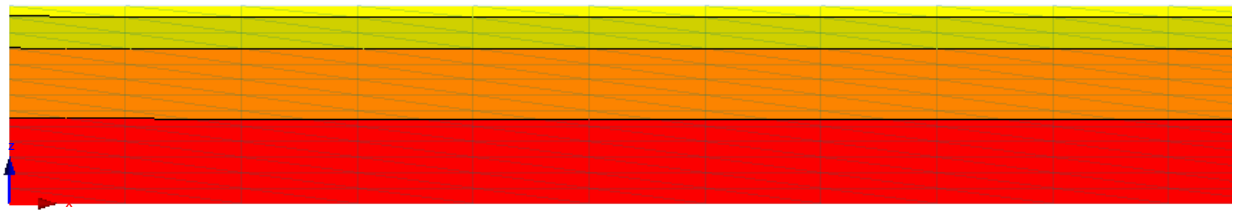

b)

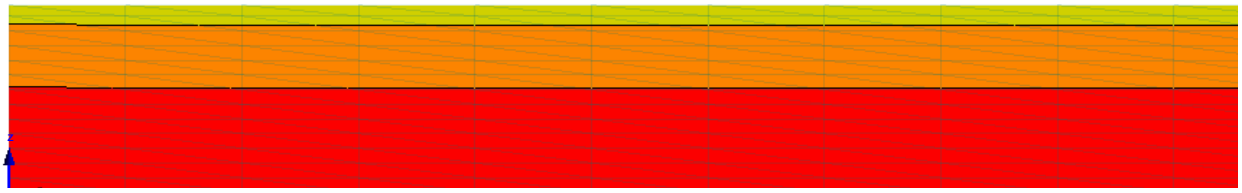

c)

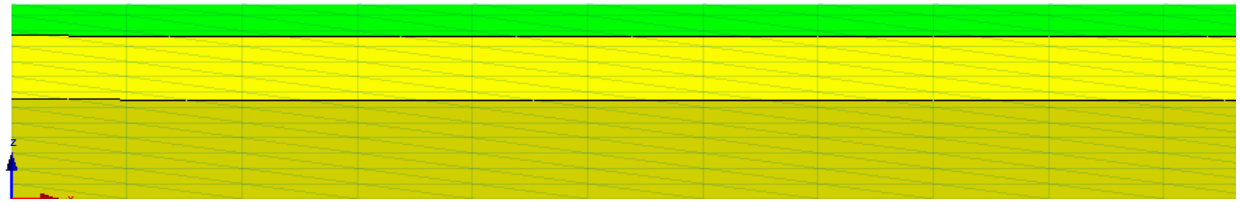

d)

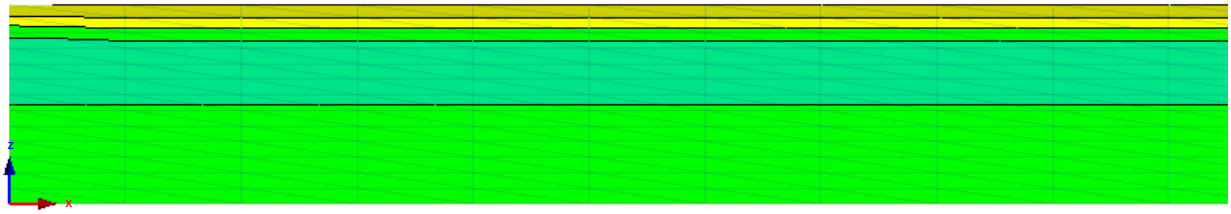

e)

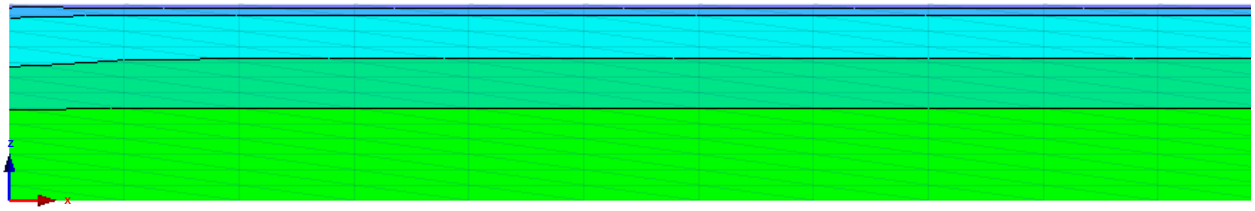

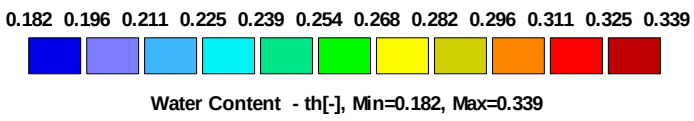

Fig.4.35. Moisture-content distribution simulated using a 2D- unsaturated flow model, using a homogenous soil and isotropic saturated hydraulic conductivity equal to 8 cm/min in in a) 4-Nov, b) 25-Nov 2010, c) 20-Jan d) 11-Feb and e) 20- Jun 2011 respectively.

4.7. Water Injection Test

A small circular hole with total volume of 2512 cm3 was drilled to conduct an artificial water injection test. The hole was filled by tap water with electrical conductivity of 110 ms/m once per day. The evolution of the injected water was monitored by symmetrical ERT surveys using a pole-pole array in four directions in order to monitor lateral water movement. A total of 80 electrodes were installed and connected to 80 active boxes to monitor water movement in four directions. The expansion of each profile was the same and equal to 6.05m. 20 electrodes with the electrode positions of X= 0, 1, 1.5, 2, 2.25, 2.5, 2.6, 2.7, 2.8, 2.9, 3.15, 3.25, 3.35, 3.45, 3.55, 3.80, 4.05, 4.55, 5.05 and 6.05m were used in each profile. The borehole was located in the middle of the all four profiles in X=3-3.05m. Smaller electrode separations were selected near borehole (10 cm) for a higher resolution near the borehole and were subsequently increased to 25, 50 and finally 100 cm at the both sides of the profile. A total of 190 measurements were taken for each image. The total time required for each acquisition was about 15 minutes.

ERT data was collected in each profile twice per day for a week starting in 21-Sep 2011. Data collection was done in early morning immediately after water injection and in the afternoon, when the borehole was almost empty of water. We collected two backgrounds for each profile, one with empty borehole and one immediately after filling the borehole for the first time.

Considering similarities between profiles, we only show and discuss the results of the first profile. The background model (collected with filled borehole) is shown in Fig.4.36. The modeling result shows relatively high resistivity values (higher than 150 Ω.m) in very shallow zone (less than 30 cm) and low resistivity with average value of 20 Ω.m in deeper zone along the profile.

The inversion of the time-lapse ERT data was carried out using RES2DINVx32 ver. 3.71. To better present resistivity changes near the borehole, we only used the data in the range of x=2.5-3.5 meter with the maximum depth of 1.5m for time-lapse inversion process. Fig. 4.37 shows the results of the resistivity inversions for the first profile with data collected immediately after filling the borehole, in terms of percentage resistivity changes with regard to background.

Fig.4.37 shows the resistivity decrease around the borehole over the period of time to some extent. Unfortunately, we were not able to draw out a quantitative model of resistivity changes in order to trace the water movement. A number of factors resulted in this undesired outcome for the experiment:

1- The volume of borehole and consequently the amount of injected water were not enough to trace the water movement.
2- The electrical conductivity of the injected water (110 ms/m) was not significantly greater than the average electrical conductivity of the soil (50 ms/m) to trace the water movement based on the electrical conductivity contrast. Of course, applying a saline tracer could aim at monitoring water movement more effectively, but it might distort the field site for further investigation under the natural condition.
3- The high level of moisture content before the water injection test was the main reason of the low electrical conductivity of soil. Although the experiment was conducted in driest period of the year, the soil was still too wet for such experiment.
4- We should have designed and installed a device to refill the borehole automatically to keep the injected water in the ground level. The present of air gap (as a high resistivity anomaly) distorted ERT images near the borehole considerably.
5- The electrical conductivity of the most important zone of the experiment (x=2.5-3.5m and z=0-20cm) in four directions were dramatically influenced by electrical conductivity of 40 electrodes connected to the ground. The observed data in this zone was noisy and the obtained model was also very unstable in inversion process.
6- Due to lack of security, it was impossible to leave the equipment in the field to collect dense dataset for a better monitoring of resistivity changes.
7- The period of ERT monitoring was not long enough to trace water movement. In fact we had overestimated the hydraulic conductivity when designed the experiment.

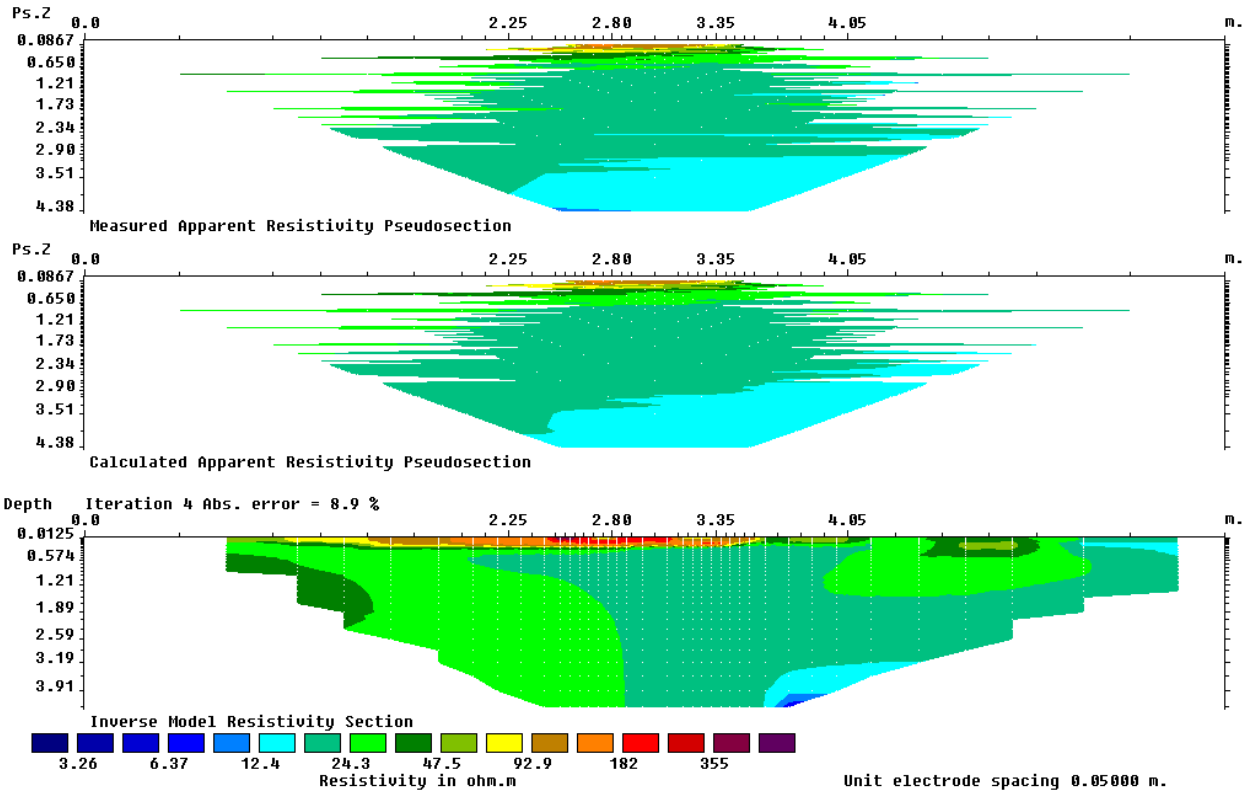

Fig.4.36. 2D vertical resistivity models of ERT background using pole-pole electrode configurations for water injection test.

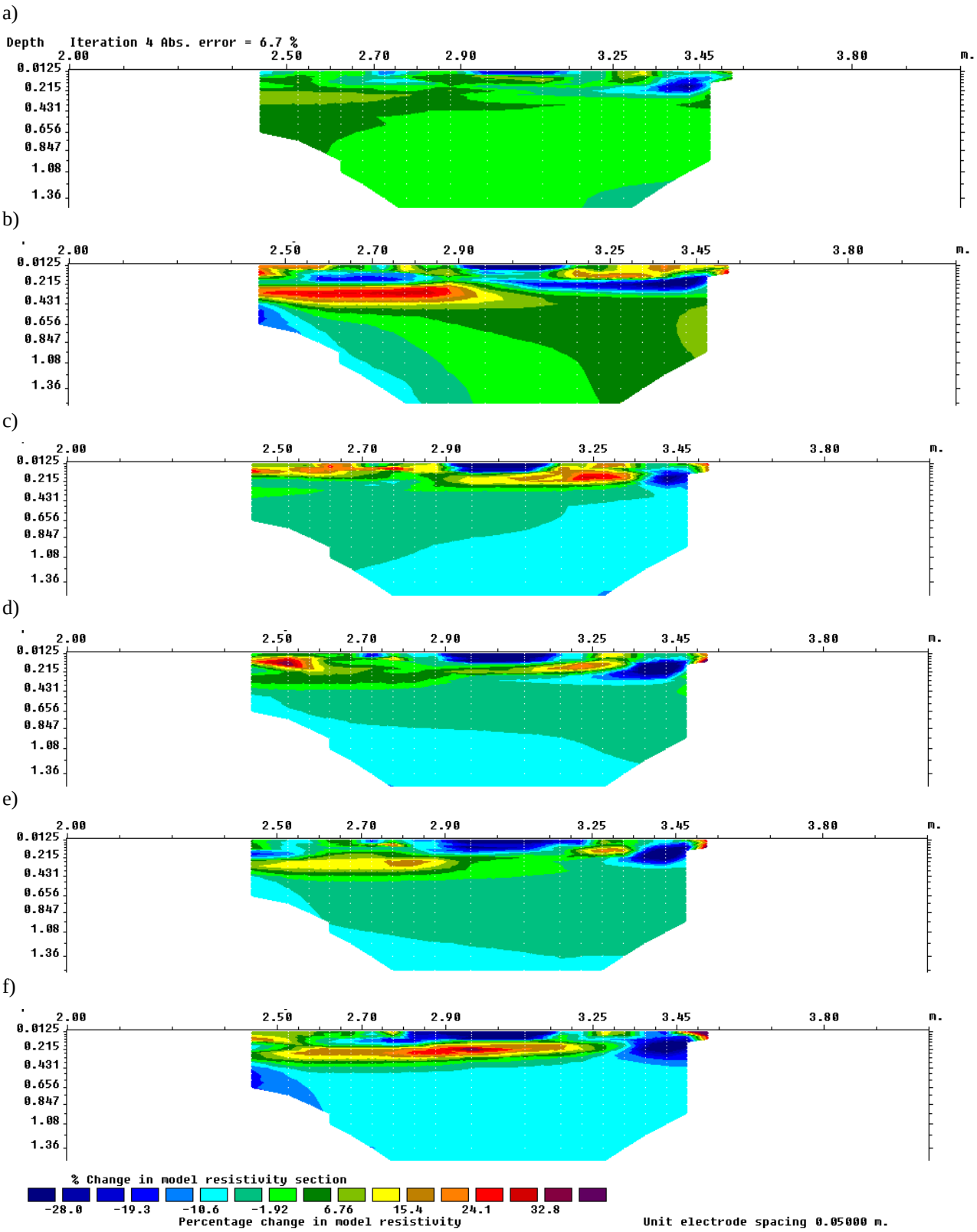

Fig.4.37. Sequence of percentage resistivity changes inferred from inversion results using pole-pole electrode configuration with respect to background in 22, 23, 24, 25, 26 and 27-Sep, 2011.

4.8.Conclusions:

The results of our experiment, where the moisture content distribution was monitored using ERT and EM38, allow for the following conclusions:

1. Both EM38 and ground surface ERT methods were capable of imaging changes in bulk resistivity in order to map seasonal moisture content distribution. The study of soil indicated that the soil moisture content hardly fall below 20% in dry season. We only observed lower values of moisture content in very shallow zone in summer. In contrast, the soil moisture content reached 30% during the rain period.

2. The experiment conducted at the campus of university of Lisbon proves that the soil is semi-pervious sediment. The spatiotemporal moisture content change during the experiment barely exceeds 10%. Our calculations using ERT and EM38 images constrain the range of the saturated hydraulic conductivity to be in 1-10 (cm/day). The low contrast of the electrical conductivity between the excess moisture content and soil and also insufficient temporal variation changes under natural condition in this study added to the complication of using the ground surface ERT and EM38 to present an accurate quantitative model in order to estimate hydraulic conductivity. Constraining and estimating of hydraulic variables in unsaturated soil usually requires very dense monitoring of geophysical data under a designed-infiltration. In addition, a tracer with large electrical conductivity contrast might be needed to better visualize how tracer sinks.

3. Based on comparison of outcomes obtained using EM38 and those from ERT, EM38 proved to be acceptably capable in monitoring moisture content changes and water movement in shallow zone. EM38 has the advantage of being less expensive, much faster, and easier to use in data collection in comparison with the ERT method. Furthermore, EM38can cover a larger area in regional investigation. Paying special attention to both data collection and inversion is greatly important in order to achieve a quantitative model.

4. A careful consideration of inverse problem should be taken into account to avoid the effects of overparameterization and smoothing from regularization that can impact the quantitative estimates of hydrogeologic parameter values using geophysical data. Several time-lapse inversion algorithms were developed in geoelectrical modeling in order to obtain a quantitative model of subsurface. In this study, the method proposed by Kim (2009) was used to invert ERT data. This method introduces the regularizations not only in the space domain but also in time to reduce inversion artifacts and improve stability of the inverse problem even if changes in the subsurface properties during the data acquisition cannot be ignored. Different methods mentioned in section 3.3 were used and compared (not shown here) in this research and we found that the space-time parameterization method yields better results and is more user-friendly among those methods.

5. Applying the established in-situ relationship for conversion of electrical conductivity to moisture content has the advantage of using an approach same as ERT and EM38 images to calibrate field data which aims to reduce heterogeneity in moisture content distribution mapping. In contrast, the degree of saturation of extracted sample was limited and did not cover 0-1 range which made impossible to achieve a more accurate relationship. Moreover, localizing and estimating of the electrical conductivity of the related samples based on the obtained inverted model is another source of uncertainty in an established in-situ relationship. Using Archie's law instead of the established in-situ relationship for conversion of the electrical conductivity to moisture content would considerably overestimate moisture content estimation in this study.

6. In spite of the reported poor resolution of ERT images in mass recovery in many publications, the obtained results in this study shows a very good mass recovery at simulating the moisture excess with respect to background. This is probably because of using in-situ resistivity-saturation relationship which reduces the disagreement. In addition, the low degree of moisture content variations made the mass recovery calculation more realistic.

7. Neglecting temporal fluctuations in temperature when using electrical conductivity images to monitor the moisture content distribution leads to errors when a quantitative estimate of moisture content is required. Many studies have tried to convert ERT images to moisture content maps however, if this is to be meaningful, then temperature variations within the image must be accounted for (Hayley et al. 2007). The temperature data shows 12°c variations during the experiment. Such a variation significantly affects ERT and EM38 images and is required to be modified for a quantitative model.

CHAPTER-FIVE

Using EM38 and ERT methods in soil characterization at the Campanhia das Lezirias – Samorra Correia

5. Study of EM38 and ERT methods at the Campanhia das Lezirias – Samorra Correia

Investigation of the EM38 and ERT methods in monitoring moisture content changes and hydraulic conductivity estimation on a deep Arenosol soil with high permeability and a low water retention capacity was conducted in the Campanhia das Lezirias – Samorra Correia under natural condition and forced-infiltration experiment. This chapter investigates the result of the EM38 and ERT surveys in soil moisture content monitoring and hydraulic conductivity estimation. A synthetic test was also performed in order to identify errors associated with the ERT method and inversion process.

5.1. Field Site Selection

To select a new suitable field site for the study, several 2D ground surface ERT surveys were carried out. The goal was to find a fairly homogeneous soil, based on resistivity changes along the profiles. Among several ERT images obtained in Samora- Correia, the ERT model shown in Fig.5.1 shows the minimum lateral changes. An investigation of this model indicates a very resistive topsoil in the first two meter with smooth lateral resistivity variations along the profile particularly between x=7.5m and x=27.5m (marked by red rectangular). Decrease of resistivity by depth is clearly visible in this model where it falls below 10 Ω.m in the deeper zone. The sharp decrease of resistivity is related to groundwater level in field area. We repeated ERT survey in the same profile between x=7.5m and x=27.5m where shows the minimum lateral changes (Fig.5.2) to more accurately investigate the lateral resistivity changes. Two soil cores were taken to a depth of approximately 2m to analyze particle size distribution. We found supportive evidence that the selected profile shown in Fig.5.2 is suitable to conduct our study in this zone. Therefore further investigation was carried out in this profile.

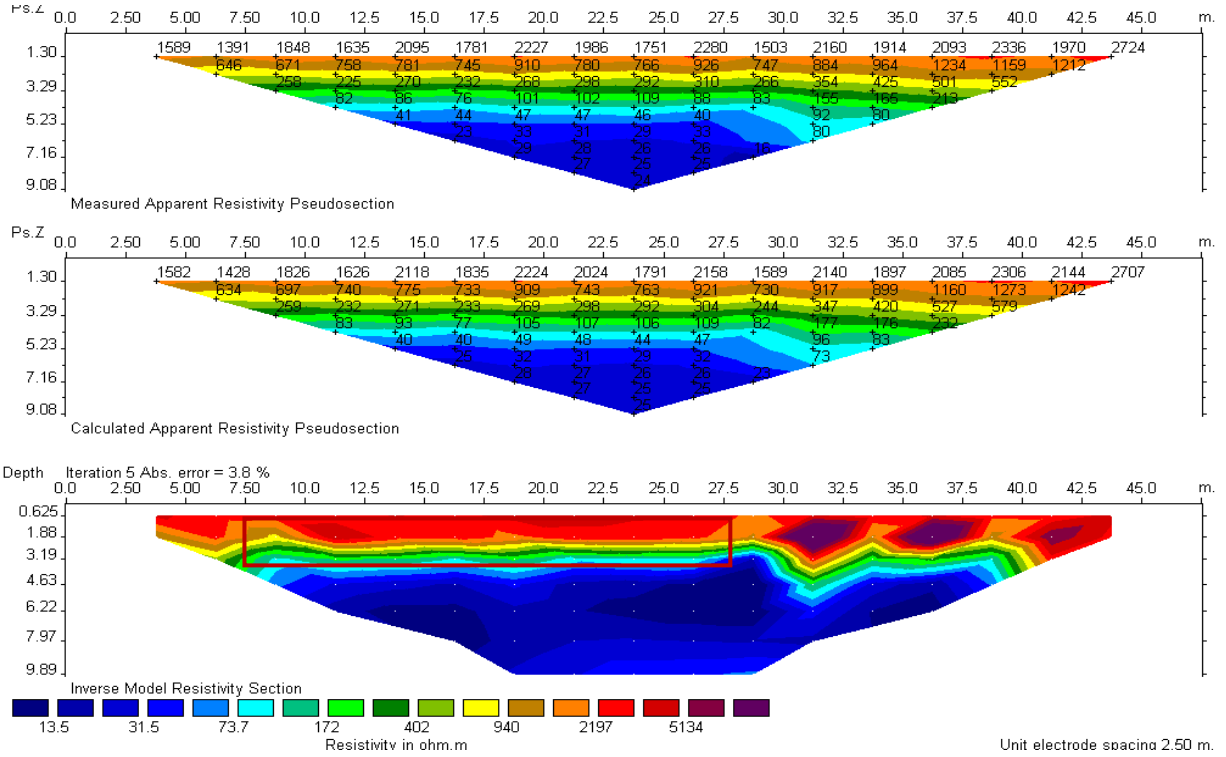

Fig.5.1. 2D vertical resistivity image of selected profile using Schlumberger electrode configuration with maximum current electrode (AB/2) expansion of 25 m and electrode spacing of 2.5 m.

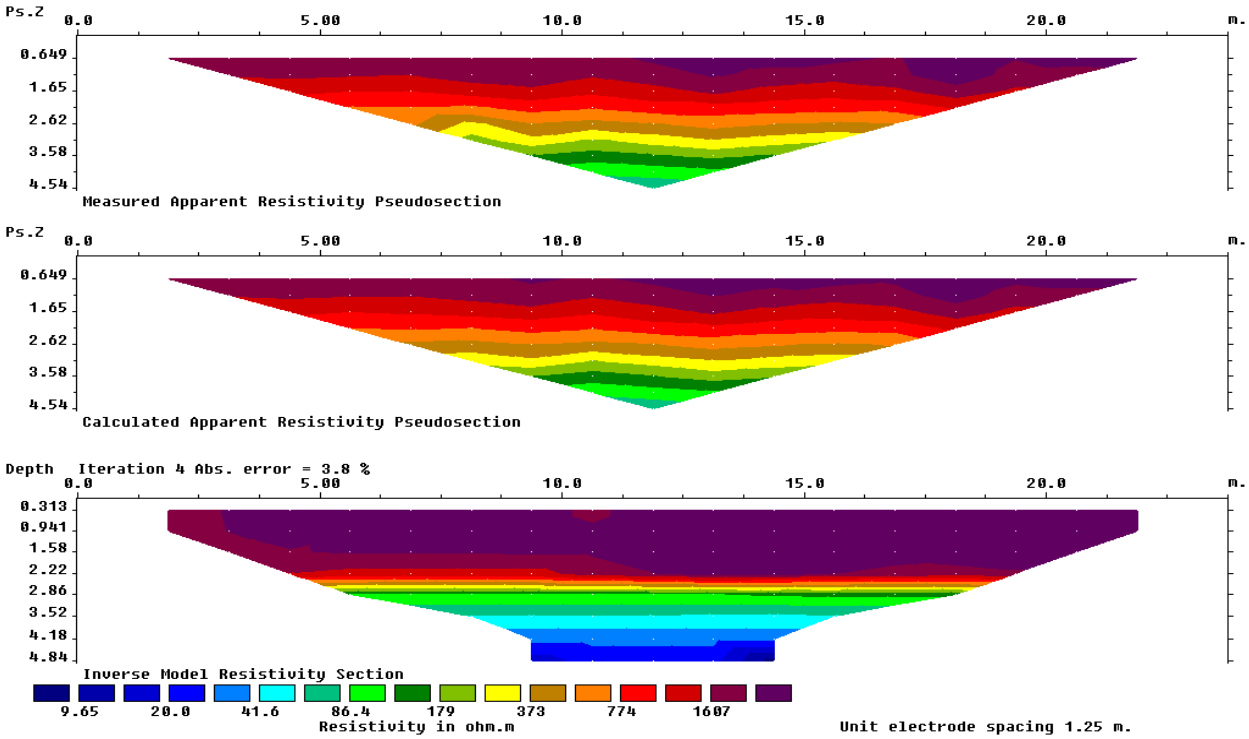

Fig.5.2. 2D vertical resistivity image of the selected zone of the profile shown in Fig. 5.1 using Schlumberger electrode configuration with maximum current electrode (AB/2) expansion of 12.5 m and electrode spacing of 1.25 m.

5.2. Soil Test

A total of eight soil cores down to a depth of approximately 1.8-2.5 m were extracted along the profile since 17th Oct 2011 until 16th Oct 2012 (Fig.5.3). These cores were sectioned into 0.2 m lengths (Fig.5.4) and prepared for laboratory analysis of soil physical properties namely particle density, bulk density, texture and gravimetric water content. The particle size distribution analyses of two cores along the profile were shown in Fig.5.5 and Fig.5.6. The particle size distribution analysis indicated a sand texture class with less than five percent clay and silt, on average. The observed average particle density and bulk density were 2.65 and 1.66 respectively and the porosity value was equal to 37%. As the average particle density and bulk density exhibited a low degree of variation along the field site, the site was considered homogeneous and the porosity was fixed at 37%.

Fig.5.3. A view of soil sapmling by auger. The auger is screwed into the ground then lifted out and retained soil on the blades of the auger is packed for testing.

Fig.5.4. Soil samples taken from argered hole in Samora-Correia

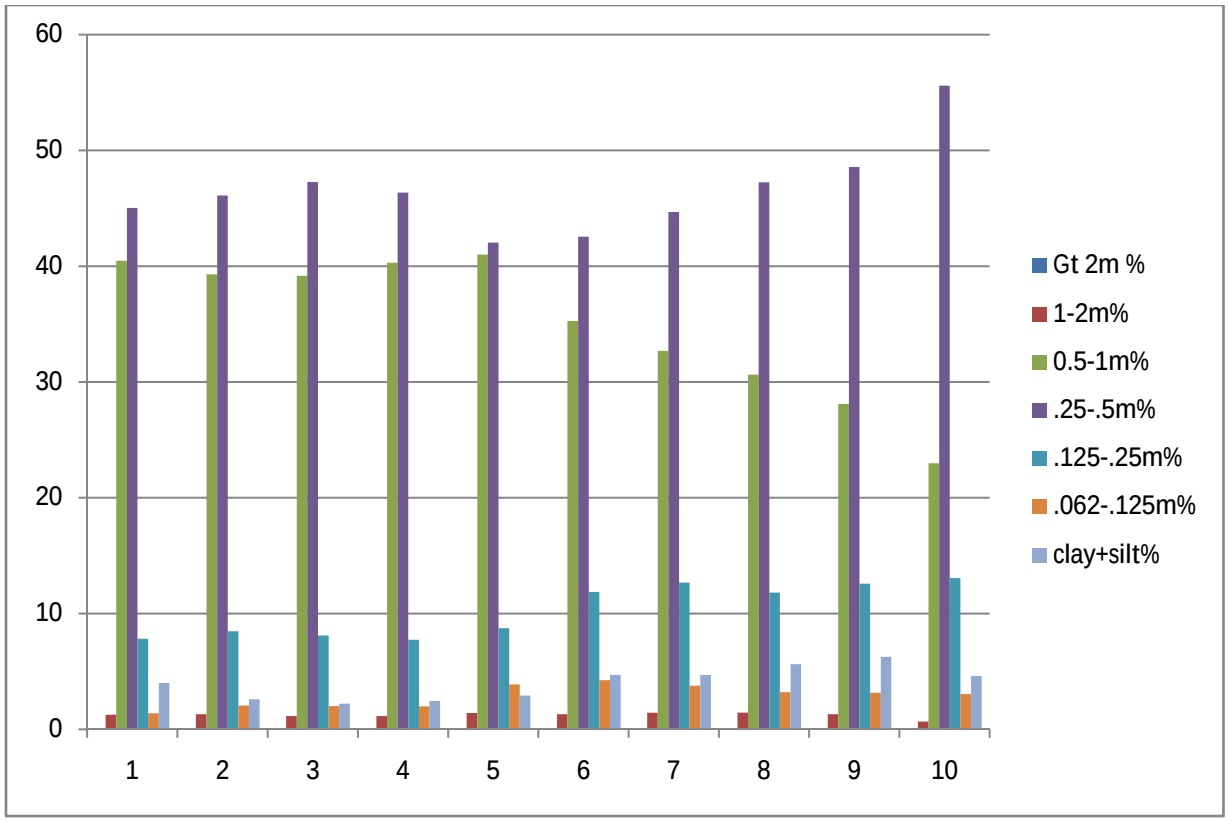

Fig.5.5. Soil texture grade for core samples in X=8 m

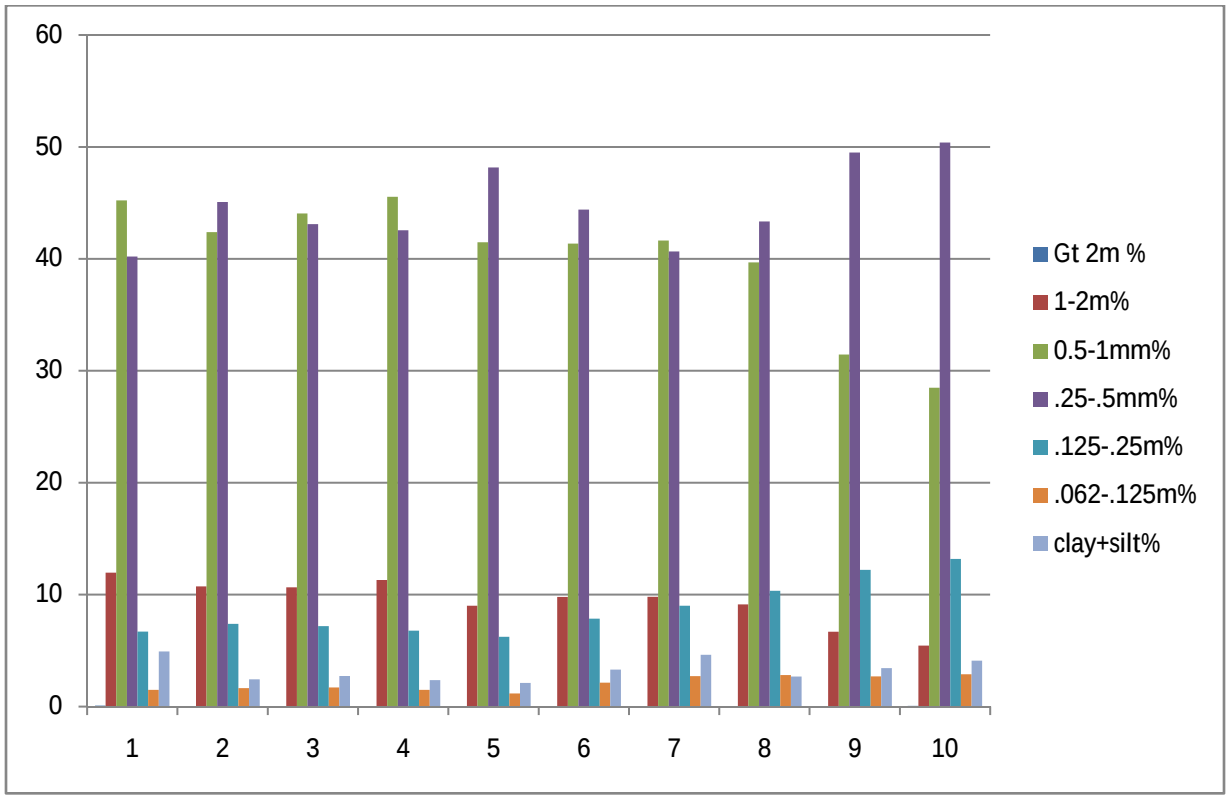

Fig.5.6. Soil texture grade for core samples in X=16.5 m

5.3. Geophysical monitoring

The evolution of the moisture content distribution was monitored by the ground surface ERT surveys since 17th Oct 2011 until 16th Oct 2012 under the natural conditions (Fig.5.7). Geophysical surveys were repeated monthly. The possibility of using EM38 and borehole ERT were also examined in this study.

Fig.5.7. A view of resistivity mapping using 4 point light 10W device and 40 active boxes for multi-electrodes connections. The devise is connected to laptop and all necessary setting and data collection is programmed by Geotest software.

5.3.1. Geoeletrical monitoring

2D ground surface ERT survey was performed using Schlumberger electrode configurations and using 4 point light 10W devise with maximum current electrode (AB/2) expansion of 10 m and electrode spacing of 0.5 m (40 electrodes). A total of 361 measurements were done for each dataset. All data were inverted using RES2DINV with two iterations. Effect of change in

temperature with respect to background dataset was removed from all ERT data by applying a value of 2% change per degree before inversion. The models obtained from inversion of data collected in Dec-2011, Jan, March, May, Jun and Aug-2012 were shown in Fig.5.8a to Fig.8f respectively. The inversion images obtained during the experiment period show very resistive topsoil in the first 2 meters followed by a sharp fall in resistivity in deeper zone. This pattern of change in resistivity is attributed to the groundwater level and sharp moisture content variations in the transition zone. Comparisons of the successive models clearly show a fall in groundwater level during the Dec, 2011-Aug, 2012 time period. The highest level of the groundwater is seen in Dec-2011, while lowest groundwater level is seen in Aug-2012. The unsaturated zone shows a smooth resistivity change during the experiment. The analysis of soil samples collected during the experiment indicates that the groundwater level varies in 2.6-3.6 meter range. The highest groundwater level was 2.6 meter seen in Dec-2011 and the lowest was slightly deeper than 3.6 meters seen in Aug-2012. Relative seasonal groundwater level changes inferred from ERT images are acceptably consistent with sampling results. Nevertheless ERT images overestimated the width of the transition zone and consequently overestimated the groundwater level.

a)

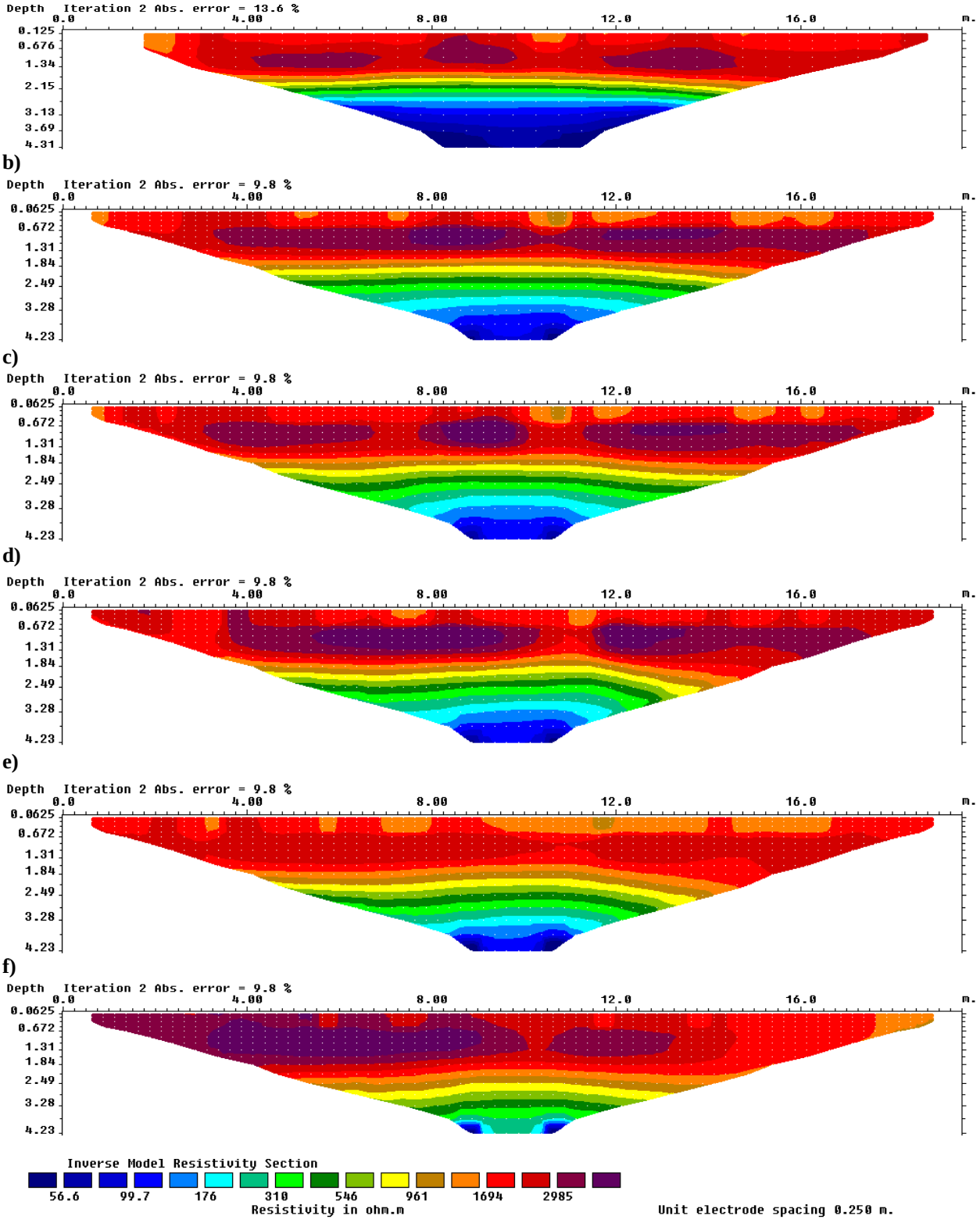

Fig.5.8. 2D vertical resistivity images in a) Dec-2011, b) Jan, c) March, d) May, e) Jun and f) Aug 2012.

5.3.2. In-situ resistivity and saturation relationship

To determine changes in soil moisture from ERT images, we did not again assume the validity of Archie's law in this study. We repeated the same procedure explained in 4.3 and established an in-situ approach based on ρ vs. S changes. The obtained relationship (Fig.5.9) is given by the following equation:

$$\rho = 39.604\, s^{-2.367} \qquad (5.1)$$

Where S is the degree of saturation and ρ is the resistivity of the porous medium in relevant degree of saturation. Equation (5.1) was used to convert resistivity changes to moisture content changes.

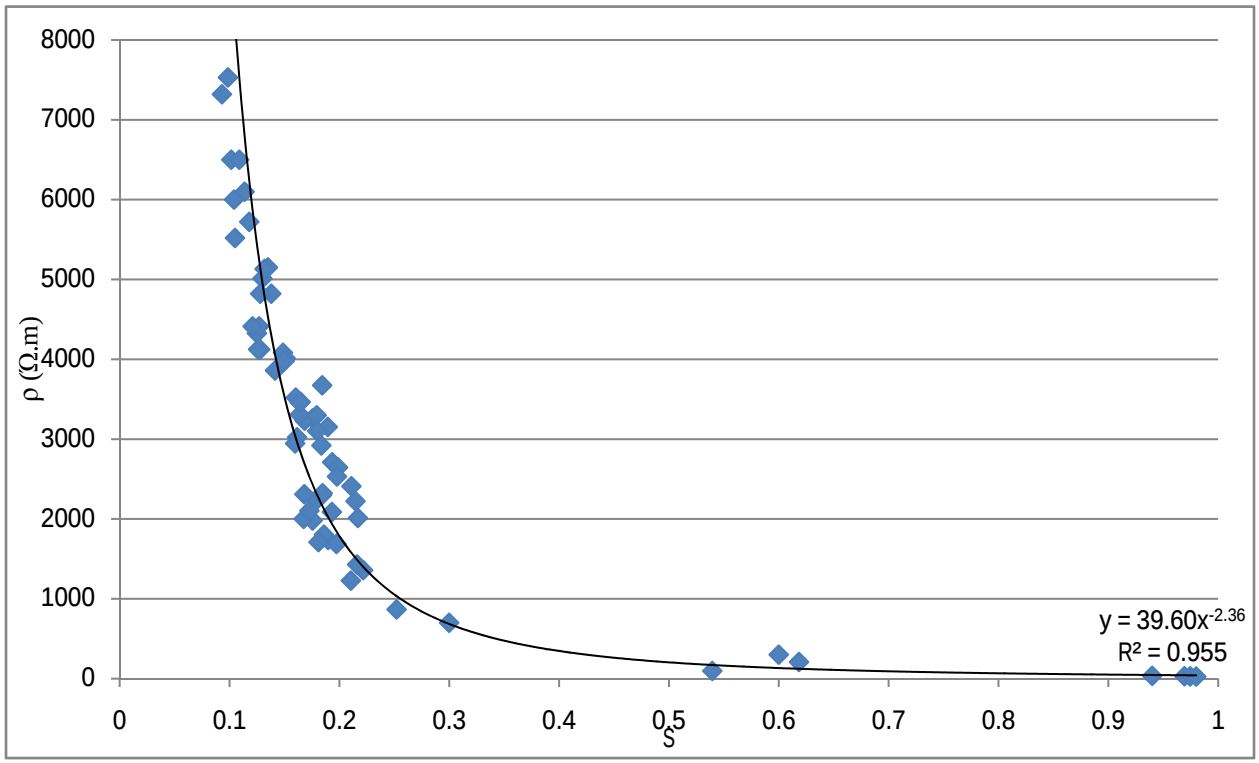

Fig. 5.9. Electrical resistivity of extracted samples as a function of the saturation

5.3.3. Moisture content maps

Fig.5.10 shows the moisture content distribution map in 17-Jan 2012 inferred from ERT images by using equation (5.1). This dataset was collected with 1 day delay after about 10mm rainfall. An investigation of this maps show a dry unsaturated zone in the first 2 meter with less than 8% moisture content. In deeper zone, a very sharp moisture content rise from 8% to more than 25%

is seen. This rise is related to the groundwater influence in this zone. The data collected in 17-Jan 2012, was selected as background for time-lapse inversion since the dataset collected in Dec-2011 was very noisy and unsuitable to be used as background. Fig.5.11 (a-f) show the inversion results, in terms of percentage desaturation which obtained from converting differences of ERT images with regard to background by using equation (5.1). An investigation of Fig.5.11 reveals the influence of the seasonal groundwater level fall in ERT images in deeper zone. ERT image obtained in Aug (Fig.5.11f) shows the maximum level of desaturation with more than 25% with respect to background in depths that are over 2 m. The moisture content changes in this zone are mainly influenced by seasonal rainfall. In contrary, the resistivity changes and consequently the moisture content variations in unsaturated zone (less than 1.5-2m) are mainly influenced by daily rainfall due to the fast infiltration in high-permeability sediments. Unfortunately the monthly ERT images could not aim at monitoring the water movement in unsaturated zone in order to estimate and constrain hydrologic parameters. We also examined whether we could map moisture changes under natural condition with daily ERT monitoring. For instance, ERT images shown in Fig.5.11 (b, c and d) were modeled by inverting data collected in 6, 7 and 8-Apr 2012 after the rainfall. Our investigations indicated that the very fast water movement in the unsaturated zone makes ERT images application complicated under the natural condition. Imaging water movement in high-permeability sediments under natural conditions requires a very dense data set collection during and after a heavy rain. Since the field site was not in Lisbon and arrangements were required to book a car and access to the field site, it was not possible to find access to the field site at the right time. Neither was it possible to leave the monitoring equipment at the site, mainly due to security reasons. Therefore we designed a forced infiltration experiment for soil characterization. The details of the forced infiltration experiment will be shown and discussed in section 5.4.

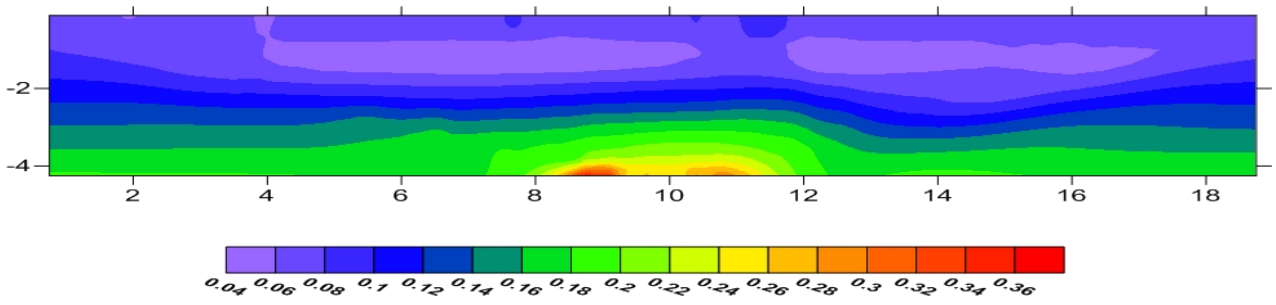

Fig.5.10. 2D moisture content distribution in 17-Jan, 2012 inferred from ERT images.

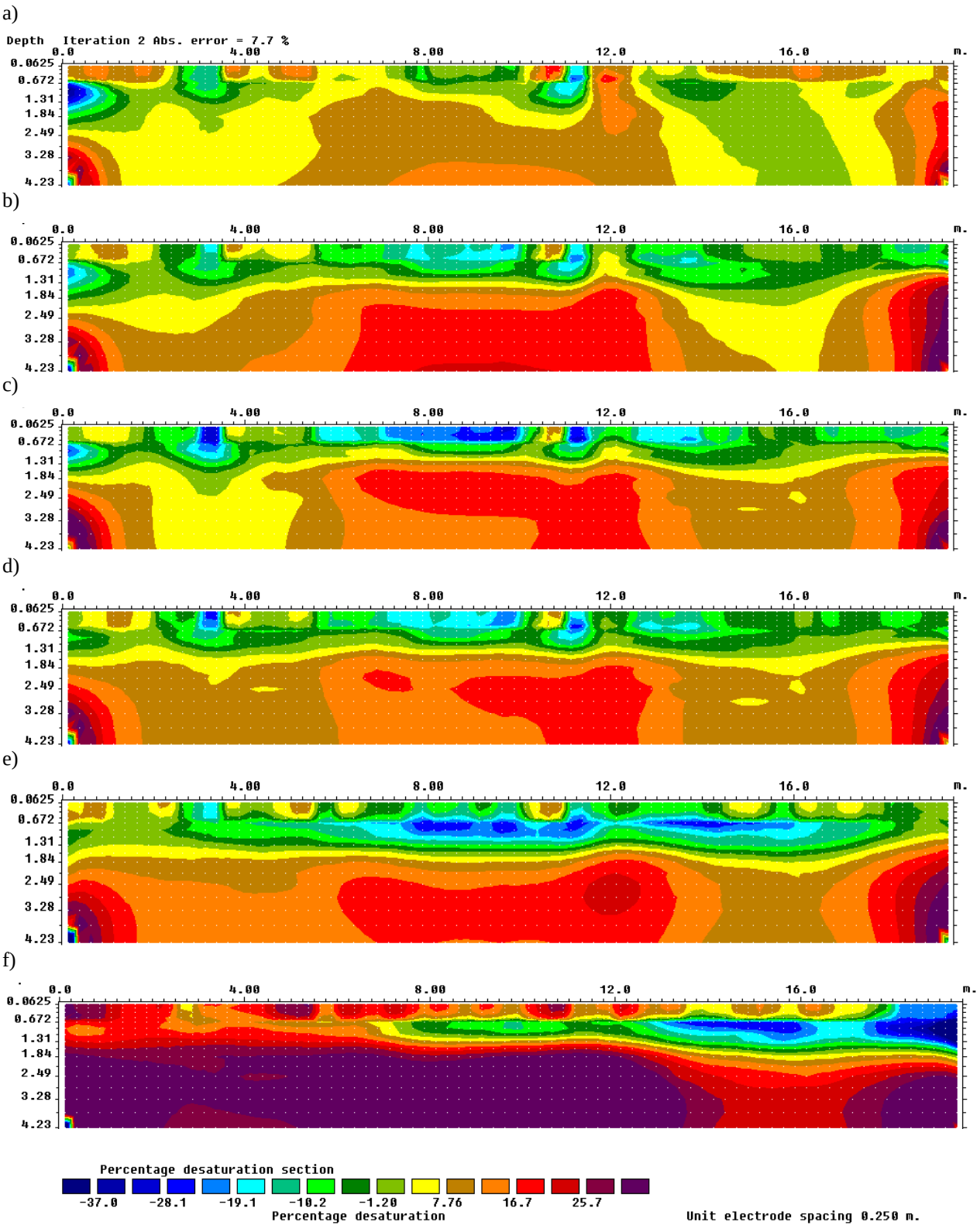

Fig.5.11. Sequence of percentage desaturation inferred from inversion results with respect to background in a) 16-Mar, b) 6, c) 7, d) 8 May e) 5-June and f) 2-Aug 2012.

5.3.4. Borehole ERT

Resolution of ground surface ERT imaging decreases with depth. Cross borehole ERT usually provides a more uniform vertical model resolution particularly when detailed information and quantitative model are required. Electrodes are usually installed in four or more boreholes to monitor 3d spatial resistivity image. Also, it is possible to use mixed surface and borehole electrodes for better resolution as long as all electrodes are in the same plane. In this study we tried to use borehole ERT in order to collect more accurate data to achieve a better quantitative model for hydraulic conductivity estimation.

5.3.4.1. Borehole ERT devise

We built a borehole tool in the lab and used 4 point light 10W devise and active boxes to monitor resistivity images in the field. 18 stainless steel nails were used as electrodes. They were soldered to cables then taped to a PVC pipe every 10 cm (Fig.5.12a). The tube was then installed in an augured hole (Fig.5.12b). To ensure a good contact between the electrode and the surrounding material, we filled the hole using dried sand by using a funnel and a long tube. In that way we could ensure that the dry sand was filled from the bottom and did not create cavities. We also shacked the PVC tube with the electrodes while backfilling to ensure a good packing. To survey mixed surface and borehole ERT, we firstly connected all 18 cables (electrode) to the active boxes (Fig.5.12c) and checked the contact resistance. Unfortunately, despite all efforts made on this device, the contact resistance of the electrodes connection was not good enough for borehole resistivity images. The dryness of the soil as well as the loose packing of sand grains in the field were the most important reasons that resulted in a less than satisfactory outcome.

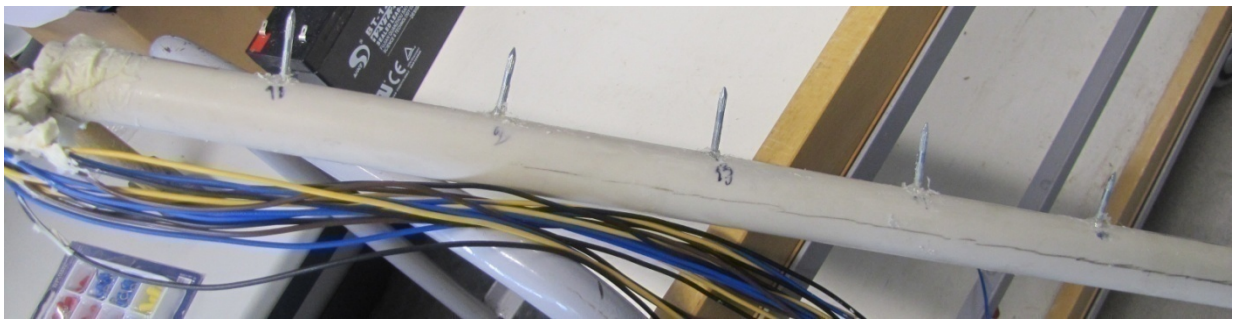

Fig.5.12. a) Borehole ERT tool made in Laboratory. b) Tool installment in the field c) Electrode connection to active boxes.

5.3.5. The EM38

EM38 measurements were made in the vertical (EM38v) and horizontal (EM38h) modes of operation with 0.5m separation along the profile and consequently 40 points were measured in each survey. To facilitate multi-height EM38 measurement, the ladder was again used and EM38 measurements were also collected in both vertical and horizontal in 0, 0.3, 0.6 and 0.9 m heights. The ECa data collected in Dec-2011 is shown in Fig.5.13. The data indicate very low electrical conductivity (less than 10 ms/m) in both vertical and horizontal modes and all four heights. These values indicated a very dry soil along the profile as expected.

Joint inversion of multi-height EM38 measurements was carried out using the algorithm proposed by Santos, (2004). The data of each survey were inverted considering initial five- layer

earth model. The first four layers were initialized with the same depth of 0.3m and electrical conductivity of 2, 3, 4 and 5 mS/m respectively from the ground surface. The electrical conductivity of the last layer was selected to be 7 mS/m. These values were estimated based on the resistivity model obtained in previous section and also data shown in Fig.5.13. The inverted models of the EM38 data are presented in Fig.5.14a. The model was obtained using all 8 dataset shown in Fig.5.13 by applying the 1-D laterally constrained inversion and using damping factor of $\lambda = 3$ and 15 iterations. The inverted model indicates high resistivity topsoil along the profile in the first 0.5 m followed by a sharp vertical resistivity fall with depth increment. The total misfit error of the model is about 21%. We changed the electrical conductivity of layers in initial model and also damping factor frequently to see whether it can improves the misfit error. We could not achieve significant improvement in inversion process and there was a clear disagreement in models in comparison with ERT images and soil samples moisture content.

Again we changed the initial models, but this time by increasing the depth of investigation to 2.8 m (the underground water level). The reasons for increasing of depth of investigation to be more than 1.5 m were that the average of the electrical conductivity collected in vertical mode on the ground and 0.3 m height was about 8ms/s which is considerably greater than the expected electrical conductivity of the first 1.5 m with a very dry soil. Therefore, the influence of transition zone and groundwater on data was obvious to us and of course is not unexpected a deeper penetration of electromagnetic induction where the subsoil is not conductive. The inverted model was obtained using a damping factor of 3, 15 iterations and a 5 layers initial models with depth of 1, 1.5, 2, 2.8 and electrical conductivity of 2, 4, 6 and 15 ms/m respectively. The electrical conductivity of the last layer (deeper than 2.8 m) was selected to be 50 ms/m. The new model contains considerably less total misfit error (about 13%). An investigation of the obtained image (shown in Fig.5.14b) is in a fairly good agreement with ERT image in Fig 5.8a. We repeated EM38 data collection in Jan and Feb, 2012 and we made the same procedure of data modeling (not shown here). Our investigation show that EM38 cannot effectively aims at monitoring resistivity changes in unsaturated sandy soil under natural conditions to present a quantitative model in order to estimate saturated hydraulic conductivity and we stopped collecting EM38 data because:

1- As was mentioned in section 5.3.3, imaging water movement in high-permeability sediments under natural conditions requires a dense data set collection during and after a heavy rain when a significant moisture changes are expected which was not possible to achieve it.
2- A very dry unsaturated soil is not an ideal media for EM38 investigation when a quantitative and temporal study is required. Low values of electrical conductivity (less than 9 ms/m) are very sensitive to noise. The main effective noise source is setting and maintaining EM38 in Zero. It is necessary that this Zero be accurately achieved and obtained. Such an error would be negligible over the usual range of conductive soils, but it was significant in our study.
3- The great contrast of the electrical conductivity of groundwater has strong influence in EM38 images in the unsaturated zone with very dry sandy soil which make it complicated to draw out lateral and vertical moisture variation in unsaturated zone.

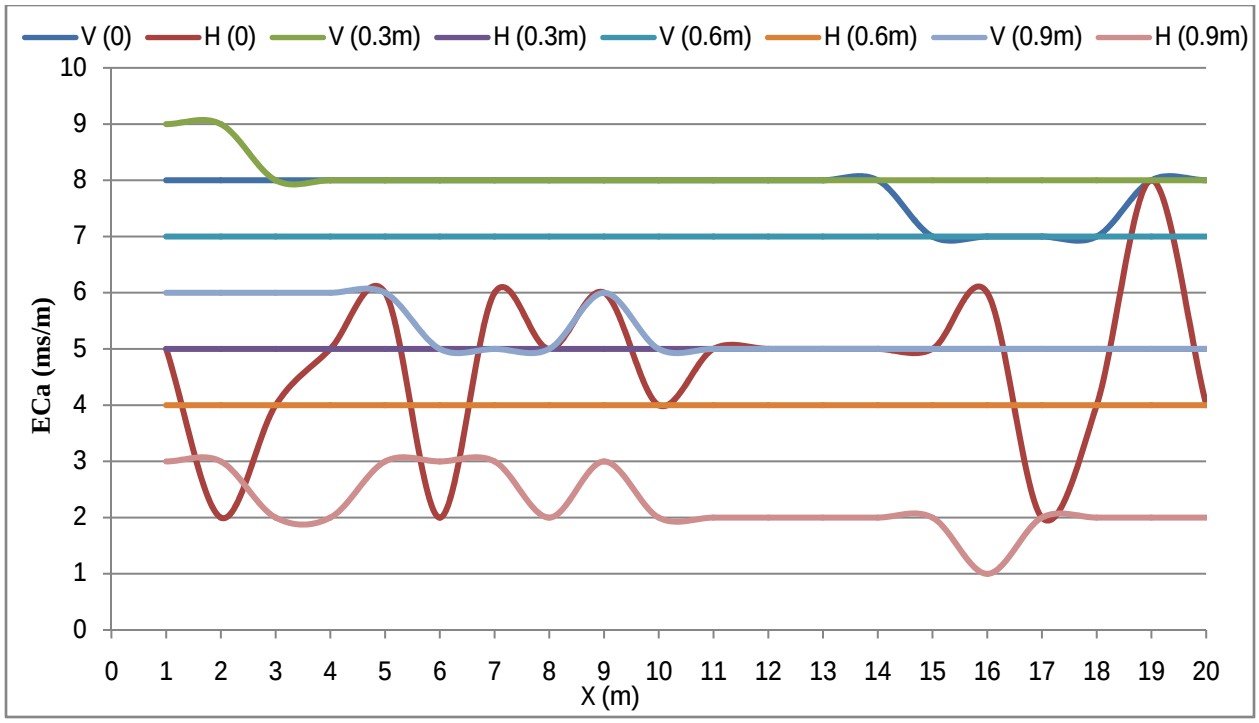

Fig.5.13. Spatial distribution of ECa (mS/m) along the profile in Dec, 2011 using EM38 in vertical and horizontal modes of operation on the ground and heights of 0.3, 0.6, and 0.9 m.

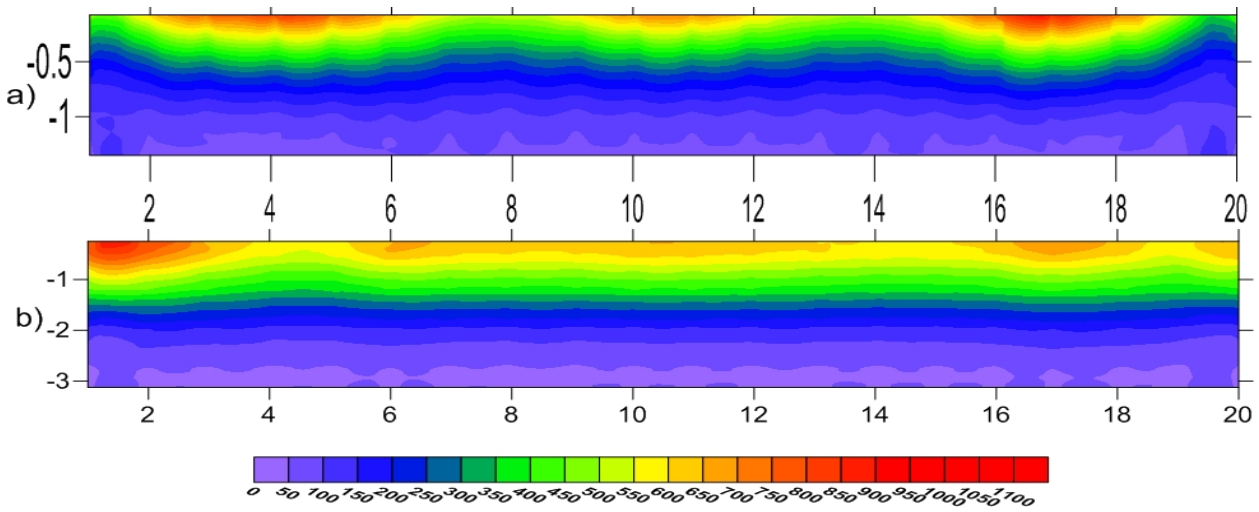

Fig.5.14. Joint inversion of multi-height EM38 collected in Dec, 2011 using vertical and horizontal apparent soil electrical conductivity of collected data at height of 0, 0.3, 0.6 and 0.9 m. The model was obtained using a 1-D inversion algorithm with 2-D smoothness constraints using a damping factor of 3 and 15 iterations. Initial five layers models were selected by a) depth of 0.3, 0.6, 0.9, 1.2 meters from the ground surface with electrical conductivity of 2, 3, 4 and 5 mS/m respectively and electrical conductivity of 7 mS/m was selected for the last layer. b) depth of 1, 1.5, 2, 2.8 and electrical conductivity of 2, 4, 6 and 15 ms/m respectively. The electrical conductivity of the last layer (deeper than 2.8 m) was selected to be 50 ms/m.

5.4. Water injection test

An artificial water-injection experiment was carried out at a rate of 8.96 cm/h over a 12.6 by 2.1 m^2 area of the field site, using drippers spaced every 30 cm over the surface (294 drippers) for about 3 hours (Fig. 5.15a). Therefore, about 0.71 m^3 of water was injected during the experiment. The pressure compensating drippers with drip rate of 8 liters per hour (Fig. 5.15b) were used for all 294 drippers in this experiment to guarantees uniform water distribution along the entire lines. The water supplied from a nearby groundwater access to a water tank (Fig. 5.15c) and was distributed to the drippers by using a pump to ensure constant flow during the experiment. A water flow meter was connected to the system to verify a constant flow rate of water and also measured the final amount of injected water.

a)

b)

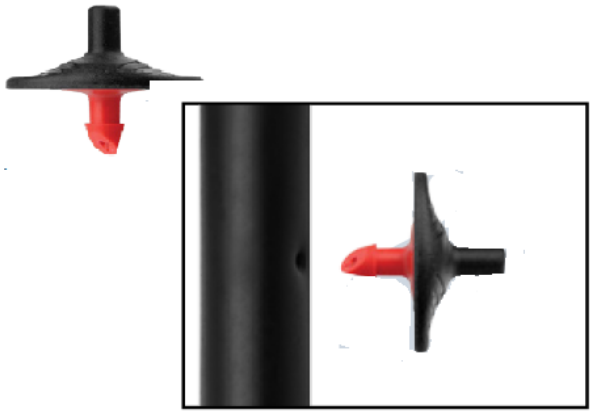

c)

Fig.5.15a) a view of artificial water-injection experiment over a 12.6 by 2.1 m^2 area and ERT monitoring, b) A sample of the pressure compensating drippers with drip rate of 8 liters per hour (294 drippers in this experiment was used to guarantees uniform water distribution along the entire lines), c) A view of water tanker and the electric generator in this experiment.

5.4.1. Temperature Sensor installation

14 soil temperature sensors were installed in 2 boreholes at depths of 0.1 m, 0.3 m, 0.5 m, 0.7 m, 0.9, 1.1 and 1.3 m. The sensors monitored temperature changes minutely during the experiment. Fig.5.16 illustrates changes in temperature of the first borehole during injection of water at the experiment. The temperature graphs for sensors in depths over 30 cm in Fig.5.16b show that the temperature decreased sharply at the beginning of the water injection and followed by a gradual rise as water injection went on. Sensors with less than 30 cm but more than 10 cm show

increasing trends during the water injection. Fig. 5.16a represents variation in temperature during the experiment for five days. The first two sensors in depth of 10 and 30cm are mainly influenced by the daily climate temperature changes, while, the temperature sensors in depths over 30 cm show a gradual decrease after the water injection which is mainly influenced by the water injection experiment. Pattern of changes in temperature of the second borehole (not shown here) show a similar results. The effect of the temperature changes were removed from the all ERT data by applying a value of 2% change per degree.

a)

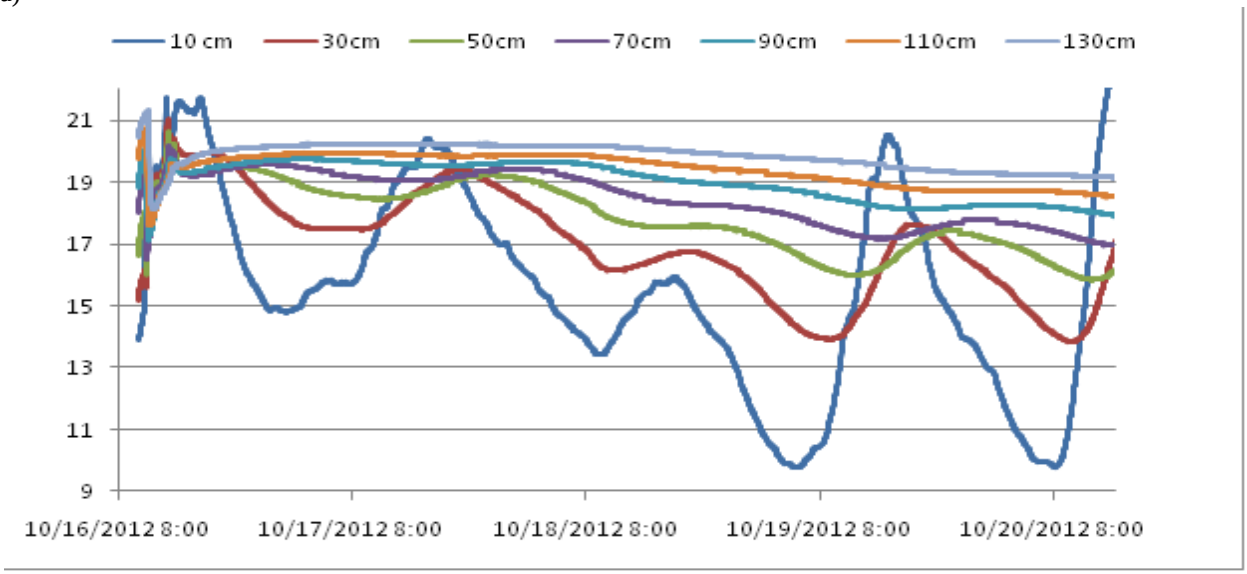

b)

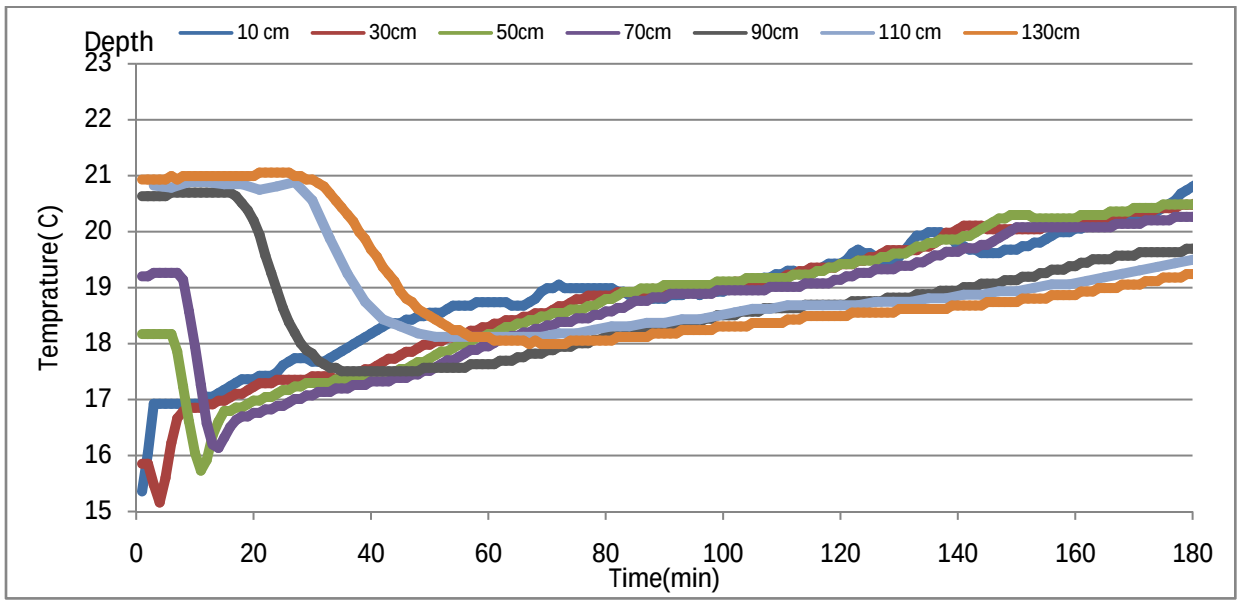

Fig.5.16. In situ temperature variations inferred from the first borehole during a) geophysical surveys b) the water injection for 3 hours.

5.4.2. Geophysical monitoring

The evolution of the injected water was monitored by ERT surveys. A 2D ground surface ERT survey using Schlumberger electrode configuration, with maximum current electrode (AB/2) expansion of 5.85m and electrode spacing of 0.30 m was performed on this experiment. A total of 361 measurements were taken for each image. The total time required for each acquisition was about 22 minutes and 149 data sets were obtained during the water-injection and also three data sets were collected before the experiment to use as a background ERT image. The water injection test was started at 10h30 in 16-Oct, 2012. ERT surveys were started by water injection and continued until 20-Oct, 2012. Smaller electrode separation was used in this experiment in comparison with the previous section to allow a more detailed and dense lateral vertical data collection in first 1.5 meter. It aims to better visualize and monitor resistivity changes in unsaturated zone and also eliminate the groundwater influence in ERT images for a better focus on the unsaturated zone. The simpler bottom boundary conditions for flow simulations is also expected when the simulations are carried out in unsaturated zone far from the groundwater, otherwise the details information from the groundwater level variation is required for an acceptable flow simulation.

All 3 background ERT data sets were inverted and the more stable and less noisy model was selected for further investigation in time-lapse inversion. The background model is shown in Fig.5.17. The modeling result shows a resistive media along the profile which indicate the soil was very dry before the water-injection (as discussed in section 5.3.1.).

Fig.5.18 show the results of the resistivity inversions, in terms of percentage water content changes which obtained from converting differences of ERT images with regard to background by using equation (5.1). We presented all ERT images collected during the water injection (Fig.5.18a to Fig.5.18h) until 2 hours after the water injection (Fig.5.18i to Fig5.18m) and some selected images from 17-Oct (the day after water injection) at 00h30, 4h50 and 18h40 in Fig.5.18 (n, o and p), at 18h00 from 18-Oct in Fig.5.18 (q), at 17h20 from 19-Oct in Fig.5.18(r) and 18h12 from 20-Oct in Fig.5.18 (s). Two iterations were only used to invert all data in this study since the greater number of iterations caused misleading anomalies in some time-lapse images.

Fig.5.18 (a-h) shows clearly the infiltrating water front into the unsaturated zone shortly after the injection. Focusing on the first eight subsequent images, sharp water content changes during 180 minutes indicates that the sediments are highly permeable and the infiltration process is very fast

in a downward movement and vertical spreading. There is no sign of water front movement ceasing or changing which again confirms that the soil is fairly homogenous. Fig. 5.18 (i-m) shows a scatter pattern of water decrease at near surface immediately after stopping water injection. Finally, ERT images since 17-20 Oct shows how the water vertically is infiltrated along the profile with time.

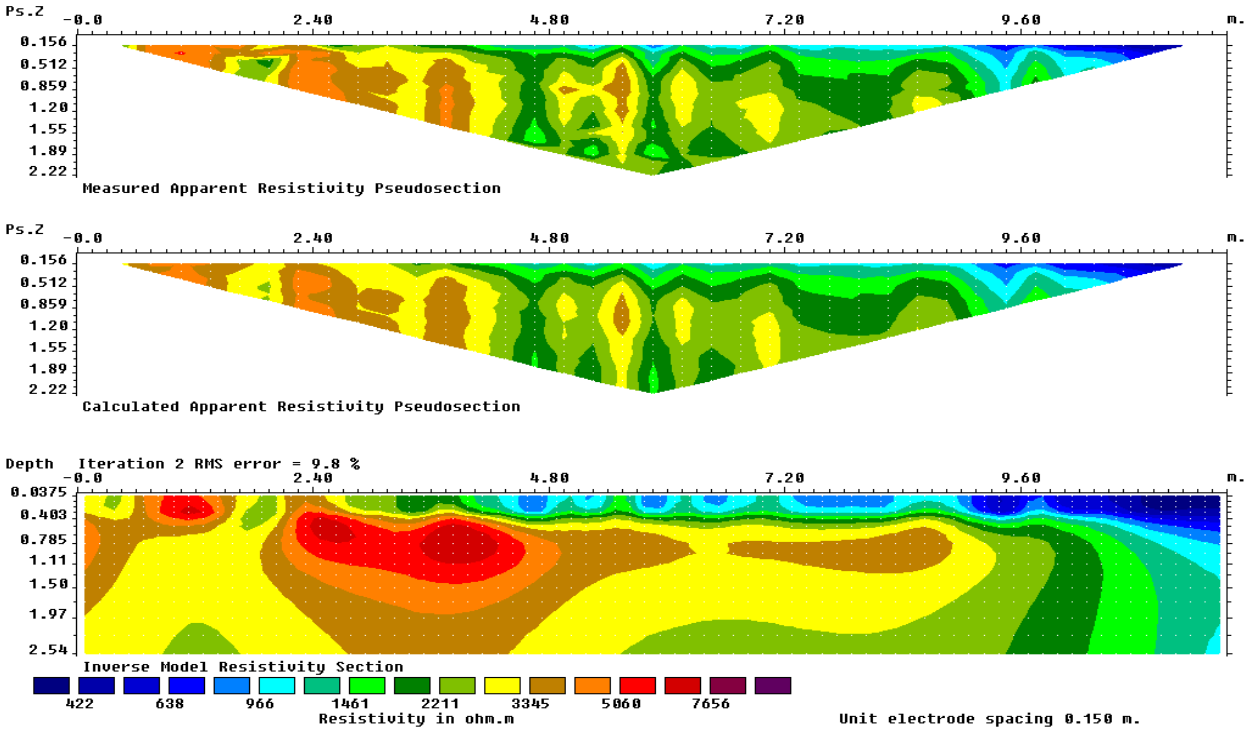

Fig.5.17. 2D vertical resistivity image of background before water-injection test

a)

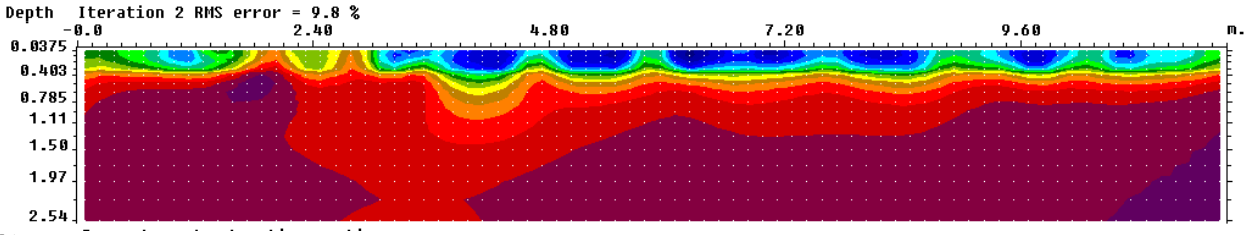

b)

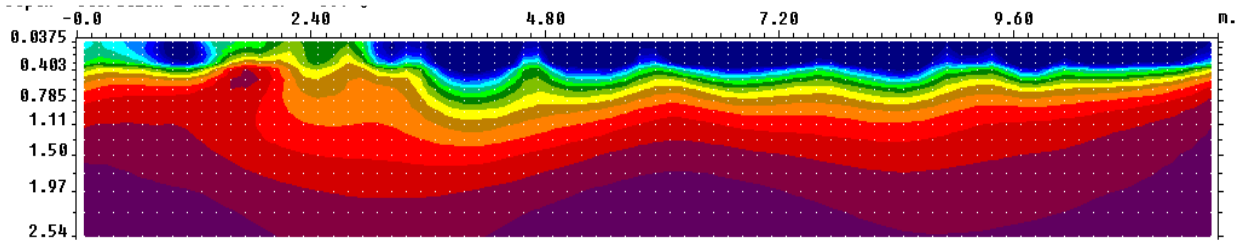

c)

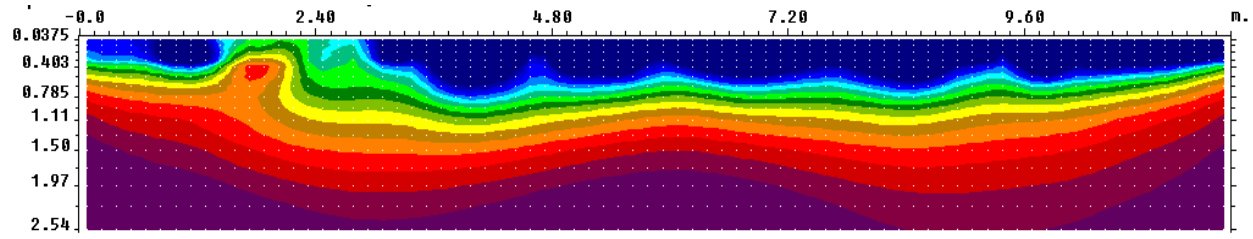
-0.0
2.40
4.80
7.20
9.60
m.
0.0375
0.403
0.785
1.11
1.50
1.97
2.54

d)

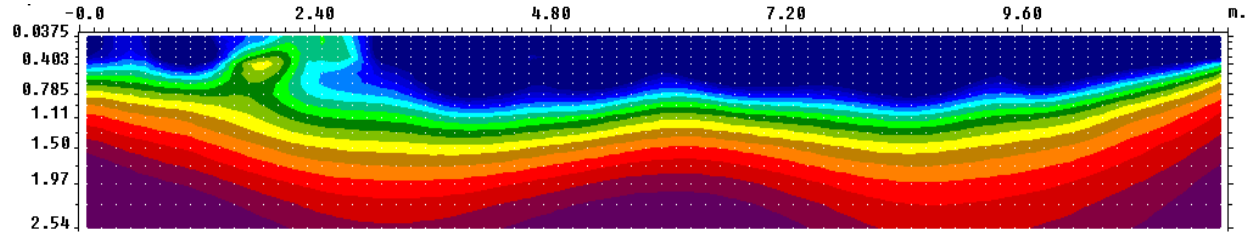
-0.0
2.40
4.80
7.20
9.60
m.
0.0375
0.403
0.785
1.11
1.50
1.97
2.54

e)

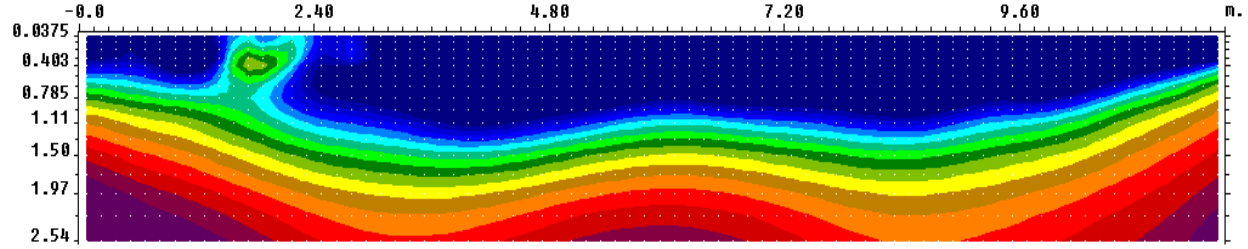
-0.0
2.40
4.80
7.20
9.60
m.
0.0375
0.403
0.785
1.11
1.50
1.97
2.54

f)

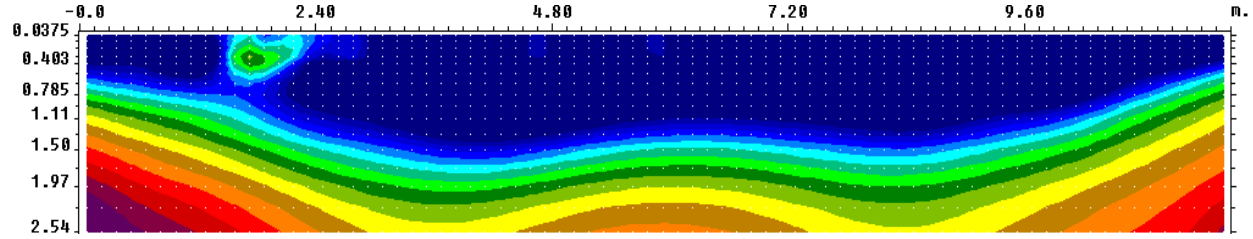
-0.0
2.40
4.80
7.20
9.60
m.
0.0375
0.403
0.785
1.11
1.50
1.97
2.54

g)

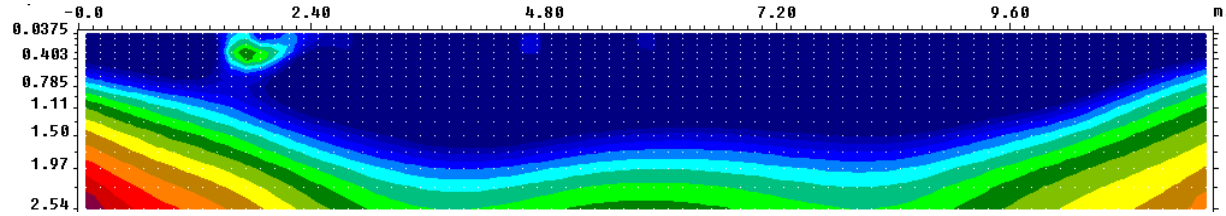
-0.0
2.40
4.80
7.20
9.60
m.
0.0375
0.403
0.785
1.11
1.50
1.97
2.54

h)

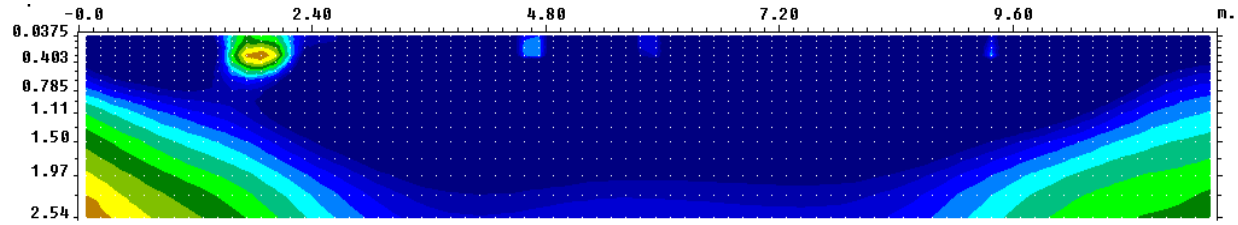
-0.0
2.40
4.80
7.20
9.60
m.
0.0375
0.403
0.785
1.11
1.50
1.97
2.54

i)

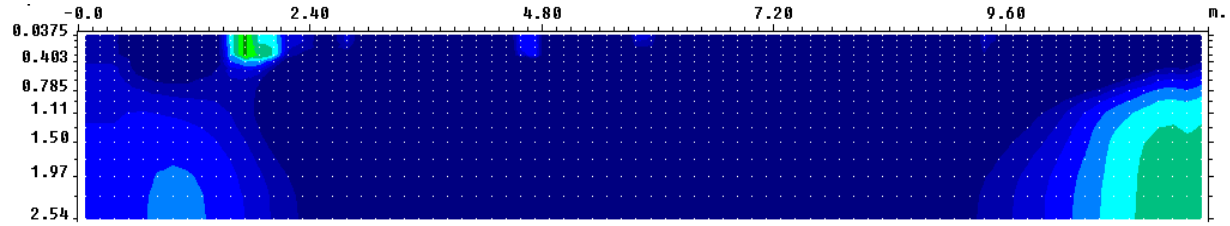
-0.0
2.40
4.80
7.20
9.60
m.
0.0375
0.403
0.785
1.11
1.50
1.97
2.54

j)

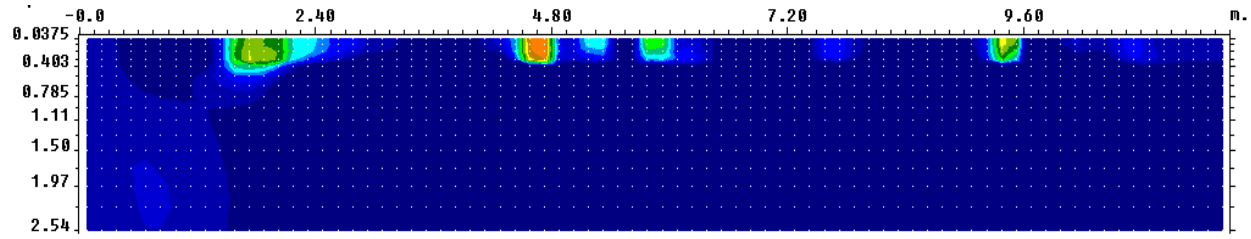
-0.0
2.40
4.80
7.20
9.60
m.
0.0375
0.403
0.785
1.11
1.50
1.97
2.54

k)

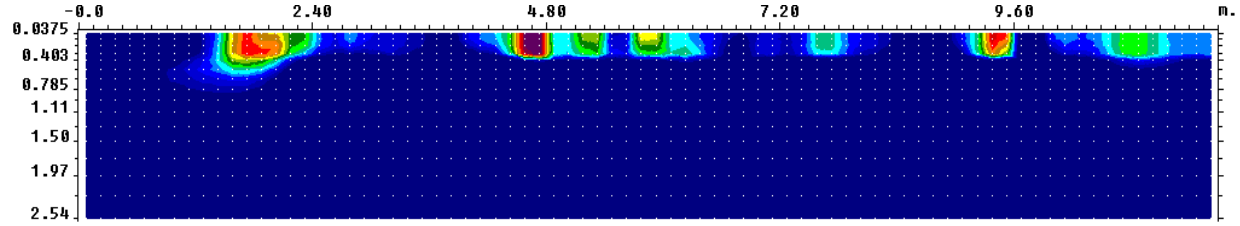
-0.0
2.40
4.80
7.20
9.60
m.
0.0375
0.403
0.785
1.11
1.50
1.97
2.54

l)

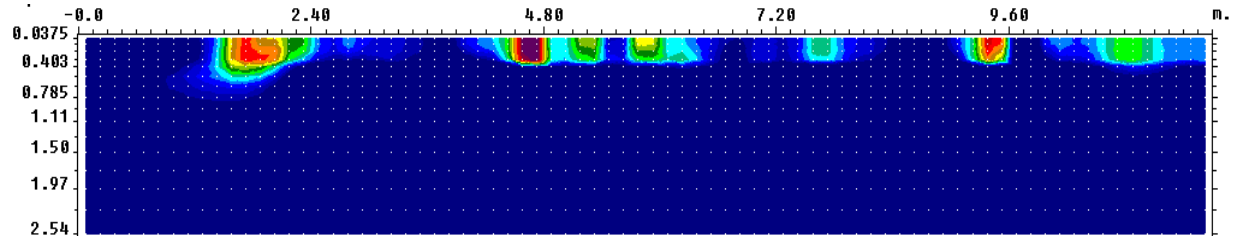
-0.0
2.40
4.80
7.20
9.60
m.
0.0375
0.403
0.785
1.11
1.50
1.97
2.54

m)

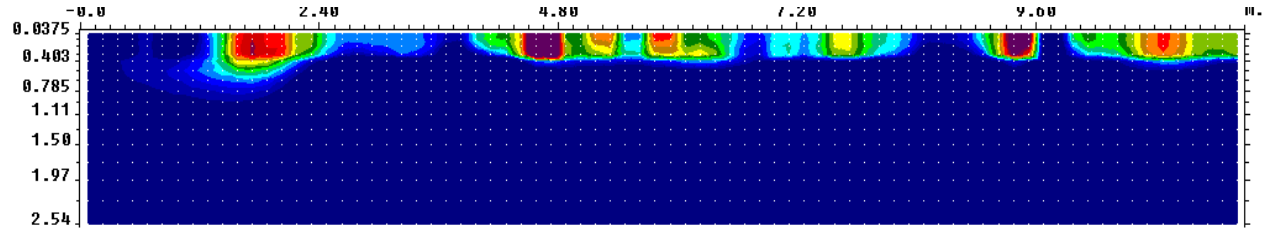
-0.0
2.40
4.80
7.20
9.60
m.
0.0375
0.403
0.785
1.11
1.50
1.97
2.54

n)

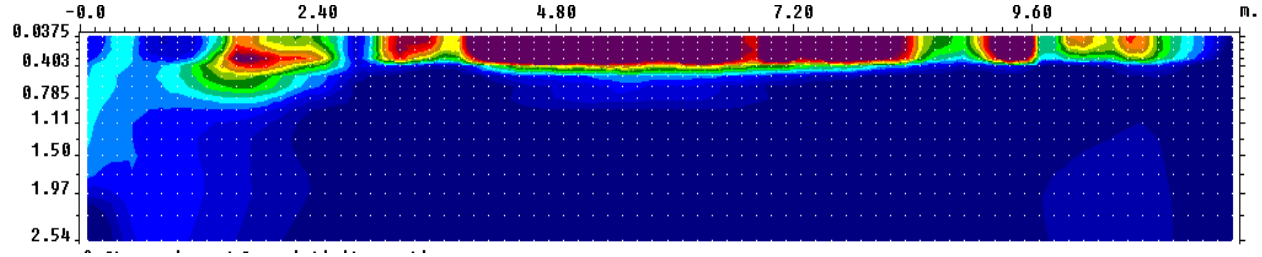
-0.0
2.40
4.80
7.20
9.60
m.
0.0375
0.403
0.785
1.11
1.50
1.97
2.54

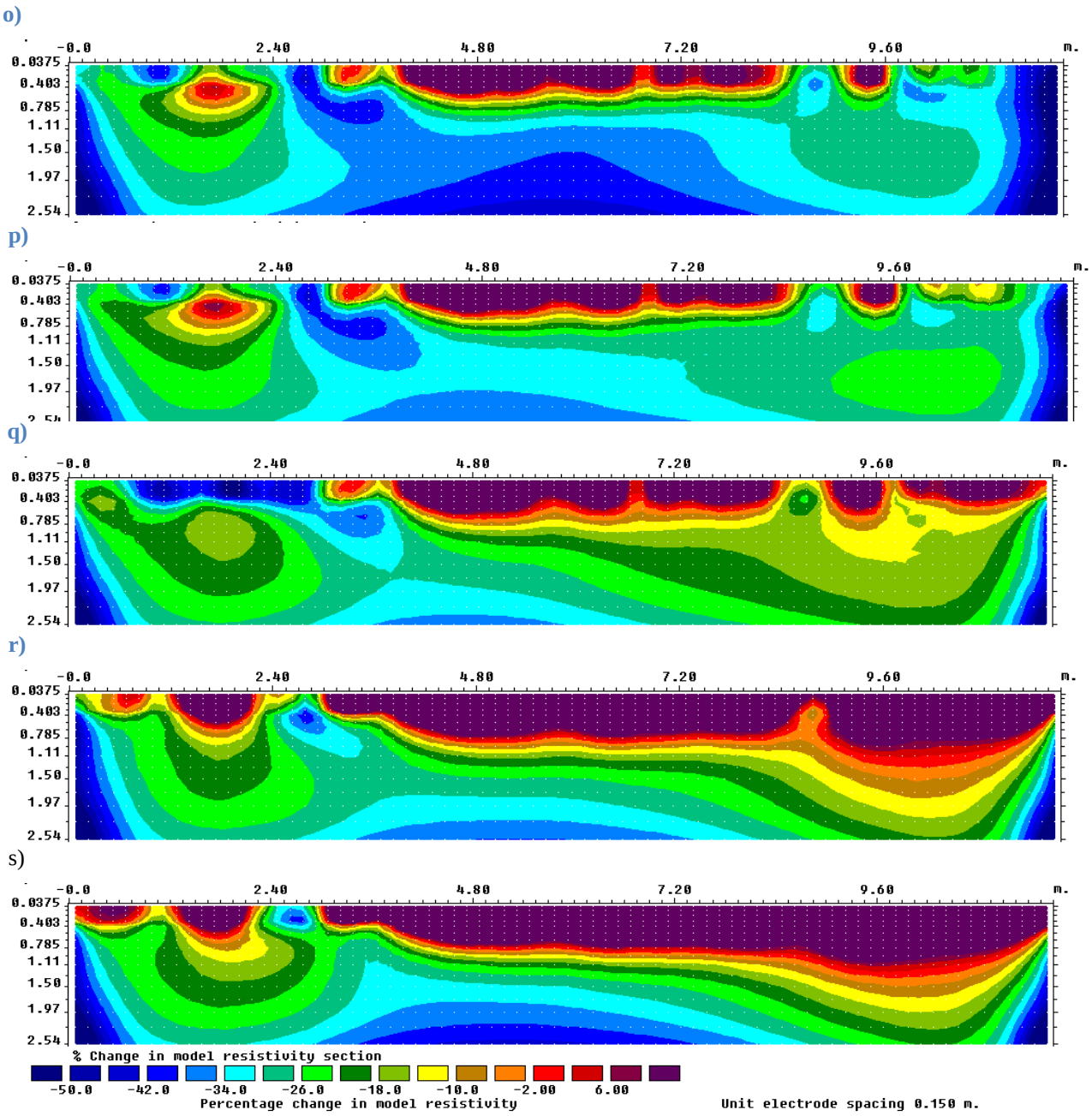

Fig.5.18. Sequence of percentage water content changes inferred from inversion results with respect to background in a-m) 30, 51, 73, 95, 117, 139, 160, 180, 202, 225, 245, 267, 288 minutes after injection respectively n) 00h30, o) 4h50, p) 18h40 in 17-Oct , q) 18h00, 18-Oct, r) 17h20, 19-Oct and s) 18h12, 20-Oct. The vertical water movement is clearly visible shortly after injection.

5.4.3. Moment Analysis

2D spatial moments were calculated from the resistivity images according to the description of moment analysis discussed in 3.6. We only used the first 8 ERT images which were collected during the water injection. We also used the inverted resistivity data in x=2.5-9.5m range in this calculation to avoid the extrapolation effect of the ERT inversion model in moment analysis.

The results of these analyses are plotted in Fig.5.19 (a-c). The percent mass calculated using equation (3.48) after removing the mass from the background (Fig.5.19a) shows a poor resolution at simulating the amount of injected water. The mass error is fairly steady over the experiment with a gradual decrease from 23% to 19.5%. As pointed out by many authors (see e.g. Looms et al., 2008; Binley et al., 2002b; Singha and Gorelick, 2005) the poor sensitivity of ERT method (particularly ground surface ERT) in imaging water content amount might be explained by the lateral water movement out of the measurement area in 2D survey, the inversion process, the noise level in the background resistivity image and the use of inadequate petrophysical relationships. Although, we used in-situ resistivity and saturation relationship to reduce this disagreement; however, the methods still suffers from the mass error balance.

To estimate the centre-of-mass vertical motion, the first moment, M01 was calculated using (3.48) and then normalized by the mass of the system. The centre-of-mass vertical motion is shown in Fig.5.19b. The ERT-estimated of centre-of-mass vertical motion indicates clearly the very fast infiltration and vertical downward migration. The centre of mass moved approximately 55 cm from the injection source over 180 minutes. The centre of mass is in preference to other measures, such as the position of the tracer front, because (a) it has a physical basis, and (b) will be sensitive to the hydraulic conductivity of the sandstone for gravity dominated flow. The vertical spread of water tracer was also calculated by using equation (3.49) and plotted in Fig.5.19c. The graph shows a fairly monotonic trend of increasing in the vertical spread over the experiment as water migrates downward. The vertical spread of the excess water content show a greater scatter comparing the first moment. It is not unexpected due to the high sensitivity of the second moment computation to noisy data sets and smoothness optimization method used in inversion process.

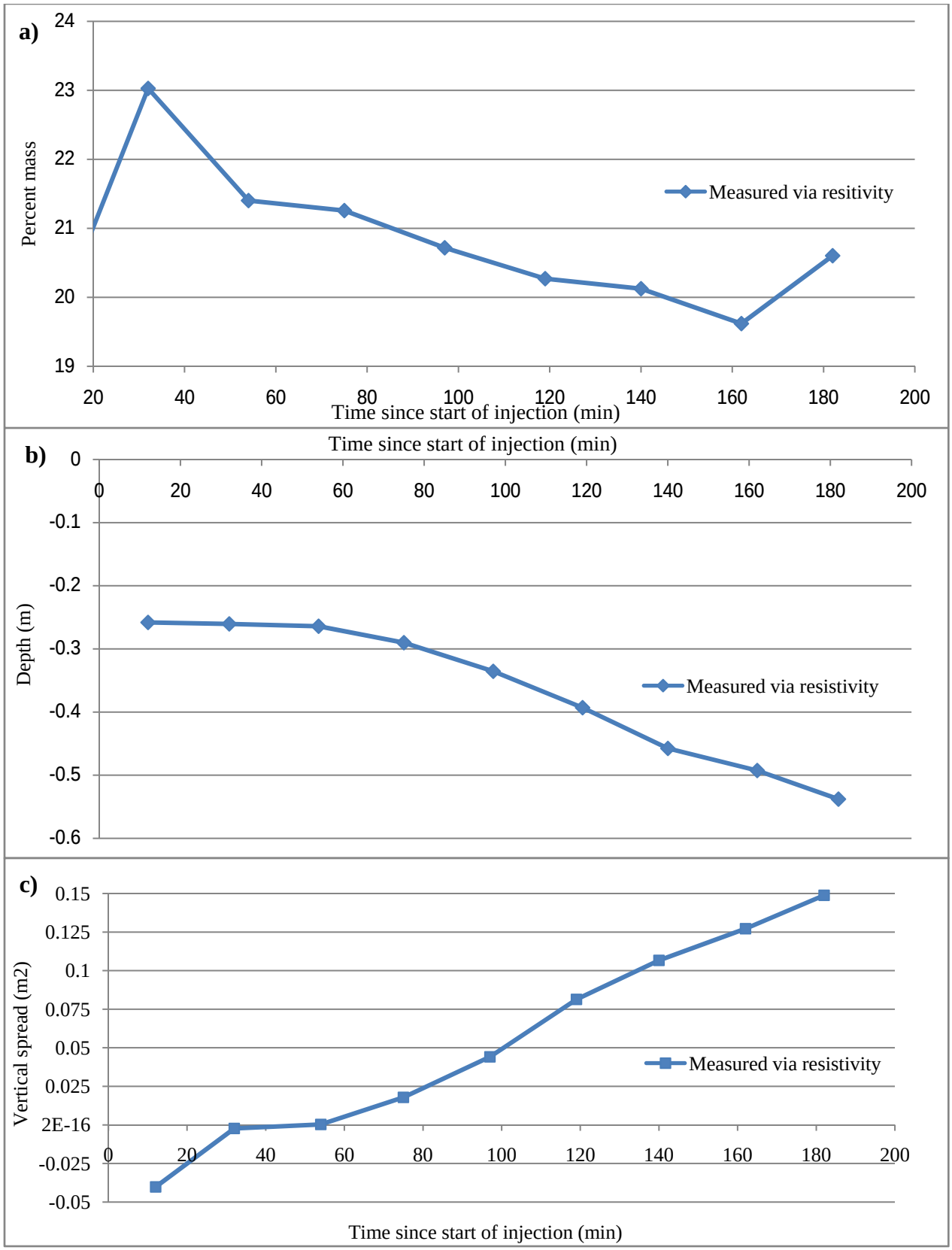

Fig.5.19. Results of the moment analysis: (a–c) results computed using ERT images

5.4.4. Unsaturated flow modeling

Unsaturated flow models were built using finite-element formulation. Hydrus 2D was used to simulate unsaturated flow. Van Genuchten equations were applied as retention and hydraulic conductivity functions in this model. Two different methods were used in this study to estimate all five van Genuchten parameters. At first, these parameters were estimated by Rosetta software based on the particle size distributions and bulk density. The obtained values are given in table 5.1(a).

In addition, to estimate van Genuchten's parameters we used a mini disk infiltrometer in ten points along the profile. At each point, the same consecutive tensions at -6, -4 and -2 were applied to the soil. One sample from each point was also taken before the experiment to measure the initial water content in lab. Due to the very fast infiltration of sandy soil, it was impossible to take a sample to measure final water content. Therefore we fixed the saturated water content to be 0.37 to constrain the retention curve during the optimization. The cumulative infiltrations for two examples of mini disk infiltrometer data sets were plotted in Fig.5.20 as a function of time. These data were used as input for DISK software to estimate van Genuchten's parameters. The obtained values in the inversion process are shown in table 5.1(b and c) for the first and second cumulative infiltrations shown in Fig.5.20. The minimum and maximum estimated hydraulic conductivity using mini disk infltrometer data along the profile were 0.01, 0.12 cm/min respectively. Afterward, van Genuchten's equations with the estimated values in table 5.1 were used as input to the unsaturated flow simulation. Initial conditions were developed based on the water content of samples which were taken just before the water injection. Regarding all above-mentioned evidences, a homogenous soil was selected for simulations. The bottom boundary of the soil column was simulated by implementing a free drainage boundary condition. The simulations were carried out for 180 minutes and the evaporation was neglected in all simulations. Three simulations were obtained using van Genuchten's parameters estimations shown in table 5.1. The first, second and third simulation shown in Fig.5.21 present the calculated centre-of-mass vertical motion of the simulating flow based on van Genuchten's parameters in table 5.1a, b and c respectively. The simulations derived from the cumulative infiltrations, show a much slower infiltration in comparison with ERT images. This is not unexpected in coarse texture, since mini disk underestimates hydraulic conductivity by failing to incorporate to macropores.

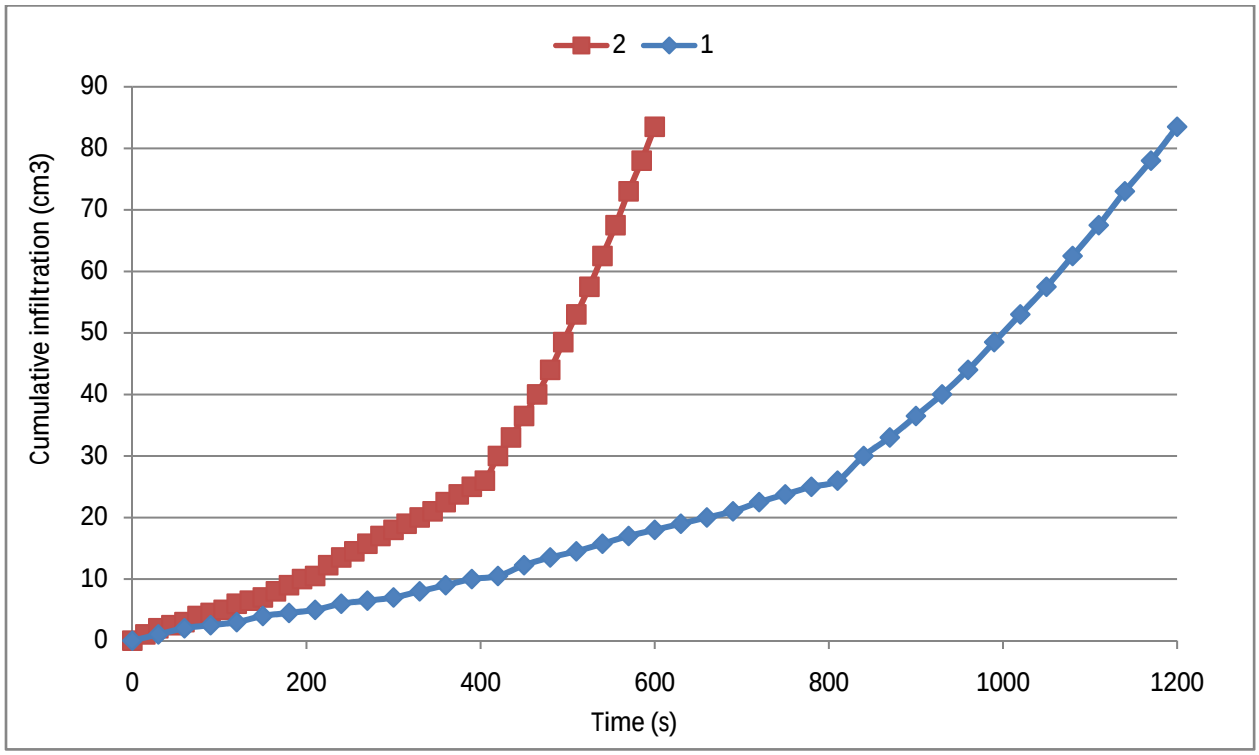

Fig.5.20. Cumulative infiltrations for two examples of obtained data using mini disk infiltrometer as a function of time

Table.5.1. Van Genuchten's parameters estimated by (a) Rosetta, b and c) mini disk infiltrometer based on the first and second cumulative infiltrations data respectively.

Parameters Estimation Method	θ_r	α (cm-1)	n	k_s(cm/min)
(a) Rosetta	0.0489	0.0330	3.56	0.26
(b) DISK (1)	0.035	0.06	4.7	0.018
(c) DISK (2)	0.04	0.05	2.1	0.054

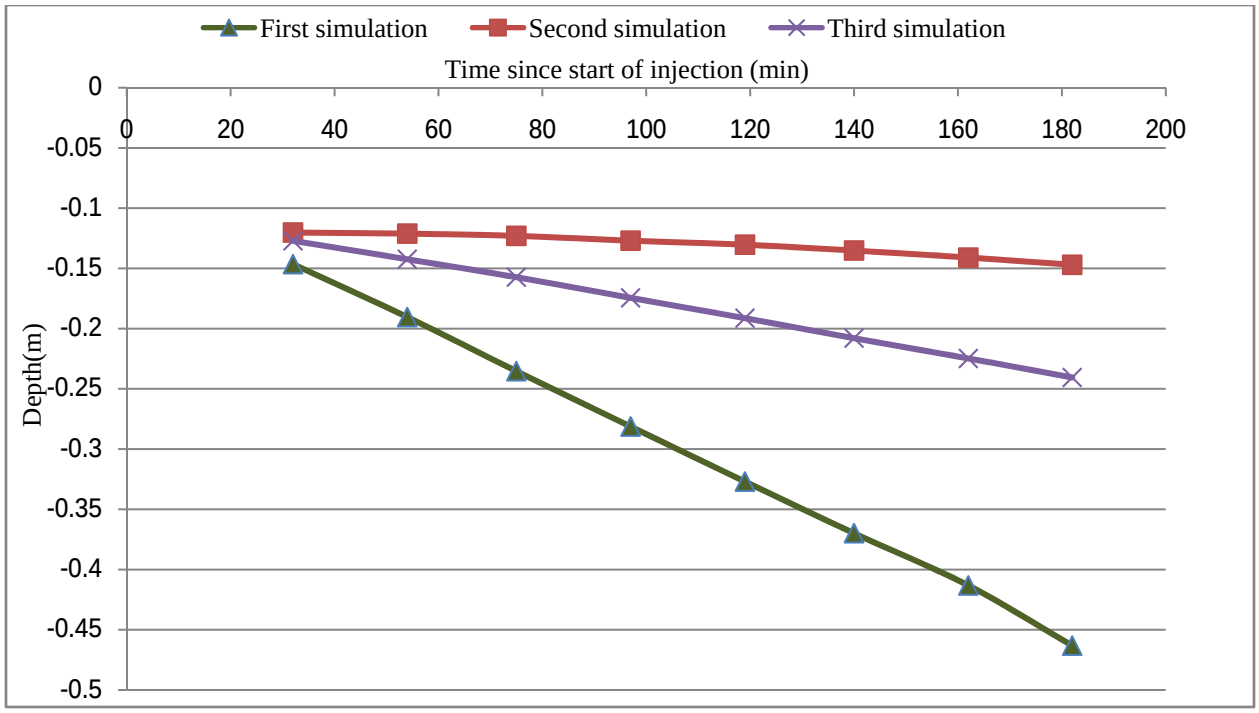

Fig.5.21. Centre-of-mass vertical motion as computed by infiltration flow simulations, based on Van Genuchten parameters shown in table.5.1.

5.4.5. Estimating and constraining the hydrological parameters by geophysical data

The centre-of-mass vertical motions of simulated flow model in section 5.4.4 (Fig.5.21) were compared to the centre-of-mass vertical motions of ERT images calculated in section 5.4.3 and were shown in Fig.5.22. A comparison of the centre-of-mass vertical motion graphs shows that the water trace sinks faster in the graph, derived from ERT images. As discussed in 3.6.2 how the hydraulic conductivity of unsaturated soil plays the most important role among van Genuchten's parameters, we fixed all others van Genuchten's parameters to be the same values of the table 5.1(a) and then several new simulations were carried out by changing saturated hydraulic conductivity value to find the best match on the basis of the sinking process of the water during the water-injection experiment. Several values of saturated hydraulic conductivity from ROSETTA database range for sand (Table.5.2) were used for new simulations.

The results of the centre-of-mass vertical motions shown in Fig. 5.23 indicate that a hydraulic conductivity value of 0.65 cm/min can well reproduce the centre of mass vertical motion of tracer during the period of measurements. The vertical spread of the excess water content (with respect to background) resulting from simulating models was also plotted in Fig 5.24 in order to provide a better comparison of the simulated models and ERT images. The scatter pattern of

vertical spread inferred from ERT images make this comparison complicated; however a hydraulic conductivity value of 1cm/min can better reproduce the vertical spread of tracer during the period of measurements.

In addition, in order to analyze the influence of other Van Genuchten´s parameters in our case study, we fixed hydraulic conductivity value to be 0.65 cm/min and several new simulations were carried out by changing θ_r , α and n and then were compared with the first moment analysis inferred from ERT images. We used the Rosetta range of Van Genuchten´s parameters for sands in Table.5.2. We fixed the saturated water content to be 37% and constrained the residual water content not to exceed from 4% based on the observed water contents of the extracted samples. We found that although changing theses parameters in mentioned range influenced the simulated model significantly, it is still insignificant comparing to the importance of the hydraulic conductivity role in dynamics of the unsaturated sandstone. To better visualize the influence of these changes in our simulations, the maximum deviation of centre-of-mass vertical motions by θ_r , α and n changes were shown in Fig.5.25.

The vertical water movement simulations were shown in Fig.5.26 to provide a mean to better visualize the water movement in unsaturated zone in order to compare the flow simulations with results inferred from ERT images. A homogenous soil using Van Genuchten's parameters listed in table5.1a and saturated hydraulic conductivity equal to 0.65 cm/min were used in this simulation. The water distribution inferred from ERT images (Fig.5.18 a-h) is to some extent different with flow simulations shown in Fig.5.26 (particularly near the borders); however the vertical water movement is consistent. The results indicates that the estimated hydraulic conductivity well reproduce the water movement. The observed discrepancy between ERT and simulated model is not surprising due to simplification of our simulations to homogenous soil, while based on findings summarized in section 5.2 we knew that the soil texture is not fully uniform along the profile. In addition, the water injection test always contains some unexpected errors (e.g. damaged pressure compensating dripper) which make water injection during the experiment not to be ideally uniform. Also, the inversion process and the presence of the noise in ERT data are other factor that may contribute to observed disparities between the ERT and simulated model.

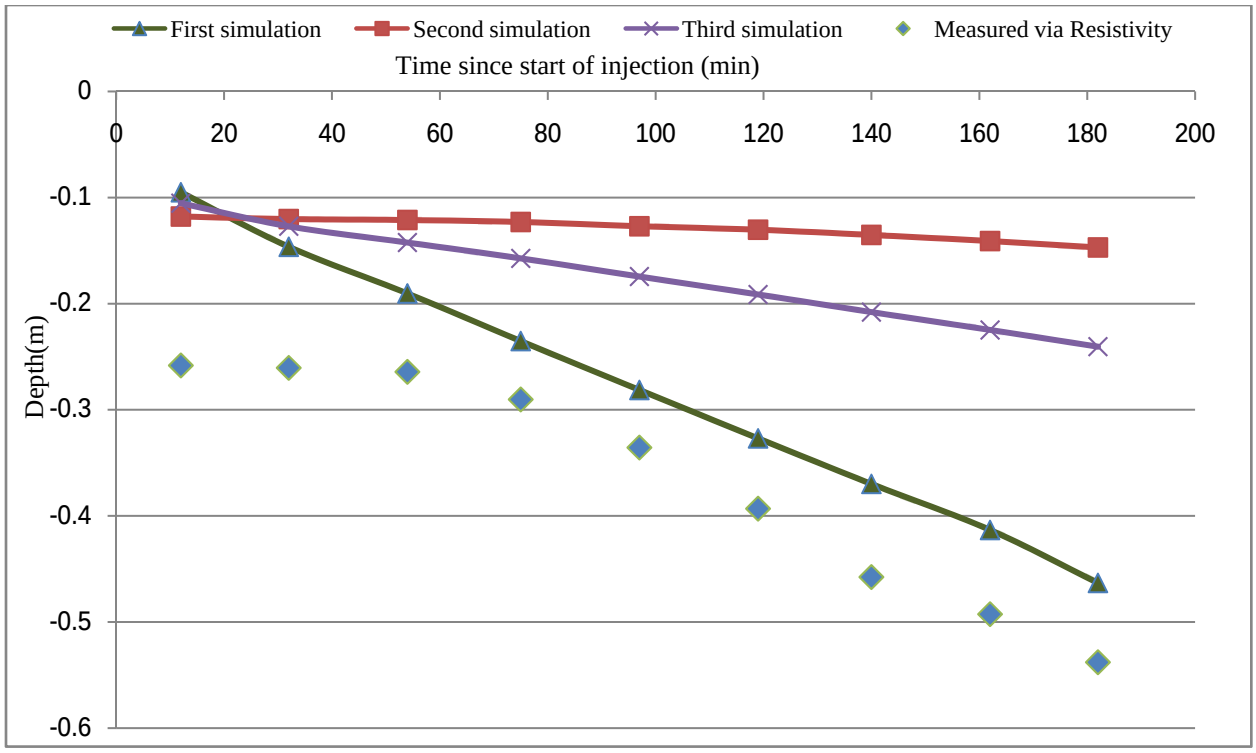

Fig.5.22. Comparison of the centre of mass vertical motion of the water tracer measured via ERT with simulating models in section 5.4.4.

Table.5.2. Range of van Genuchten's parameters for sand found in the ROSETTA database, computed from the average and one standard deviation of 308 sands samples.

Parameter	θ_r	θ_s	α (cm-1)	n	k_s(cm/min)
Rosseta range	0.024-0.082	0.32-0.43	0.02-0.06	2.10-4.81	0.115-1.735
Selected range	0.024-0.04	0.38	0.02-0.06	2.10-4.81	0.115-1.735

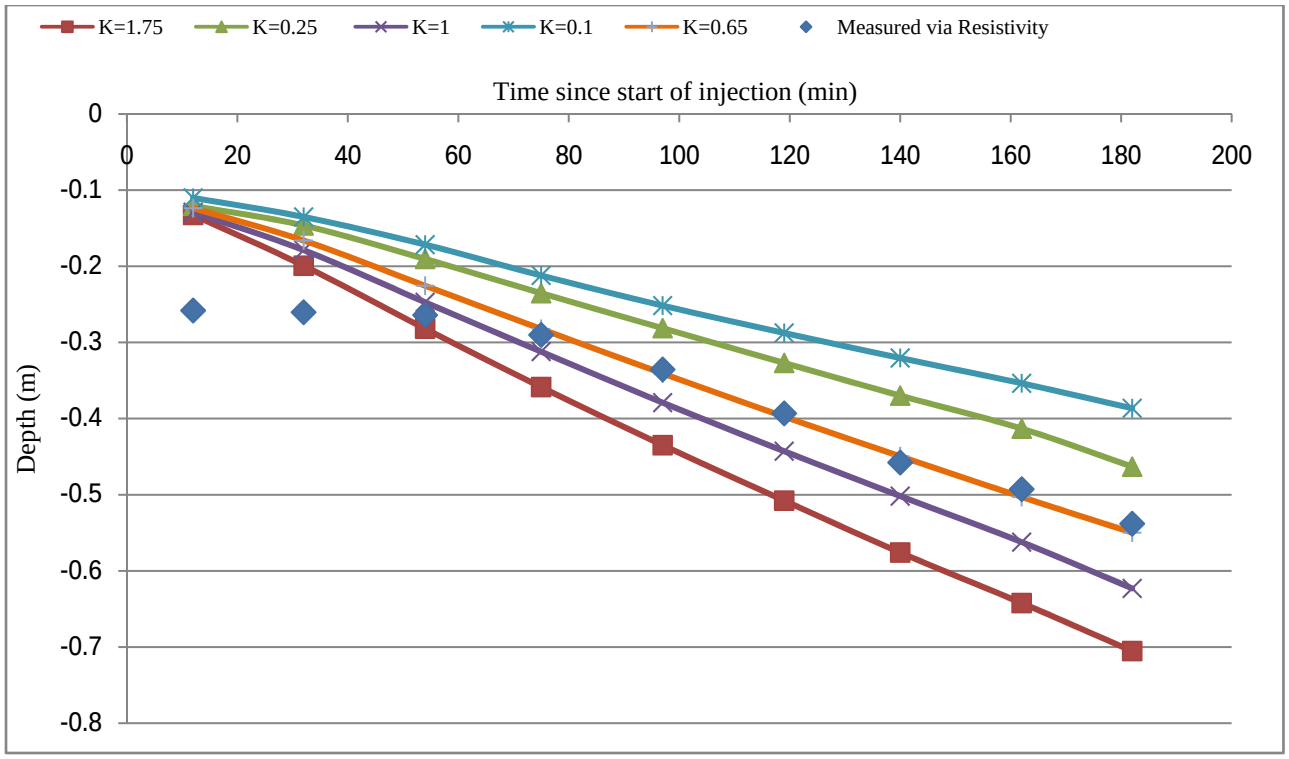

Fig.5.23. Comparison of the centre of mass vertical motion of the tracer measured via ERT with simulating models. Five values of saturated hydraulic conductivity (Ks) of the subsoil were used in these simulations.

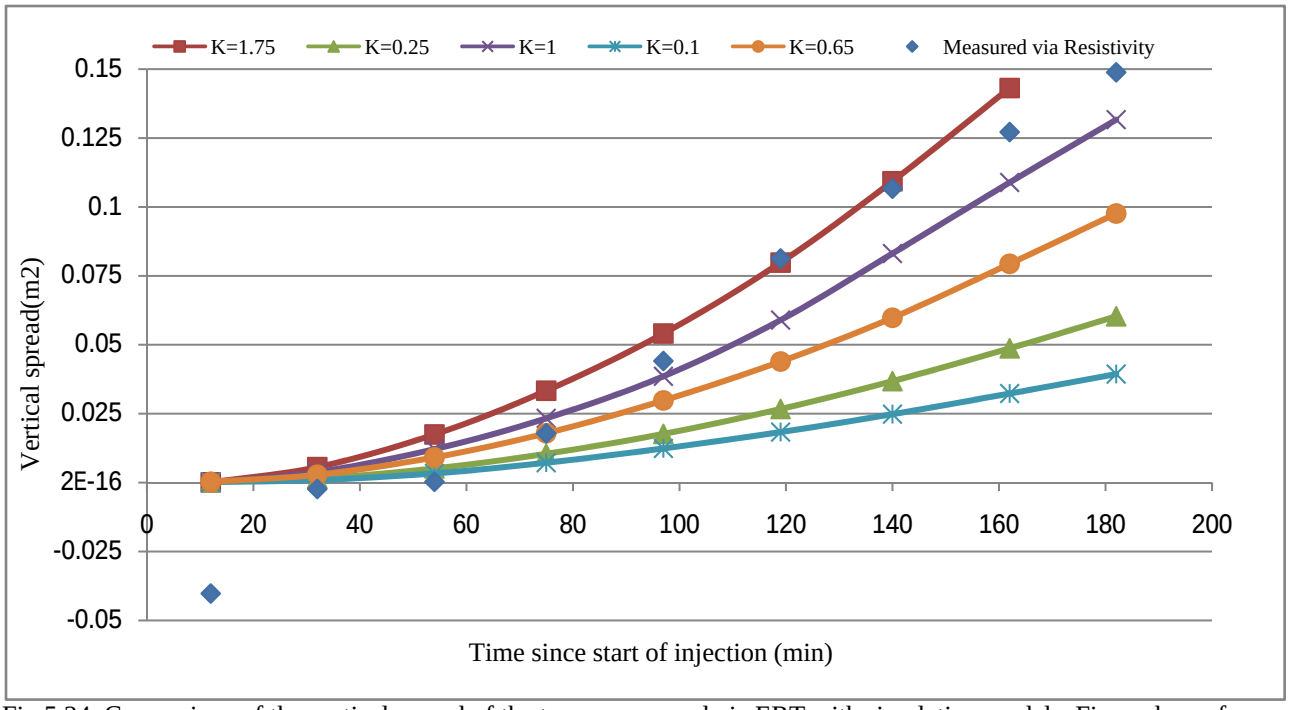

Fig.5.24. Comparison of the vertical spread of the tracer measured via ERT with simulating models. Five values of saturated hydraulic conductivity (Ks) of the subsoil were used in these simulations.

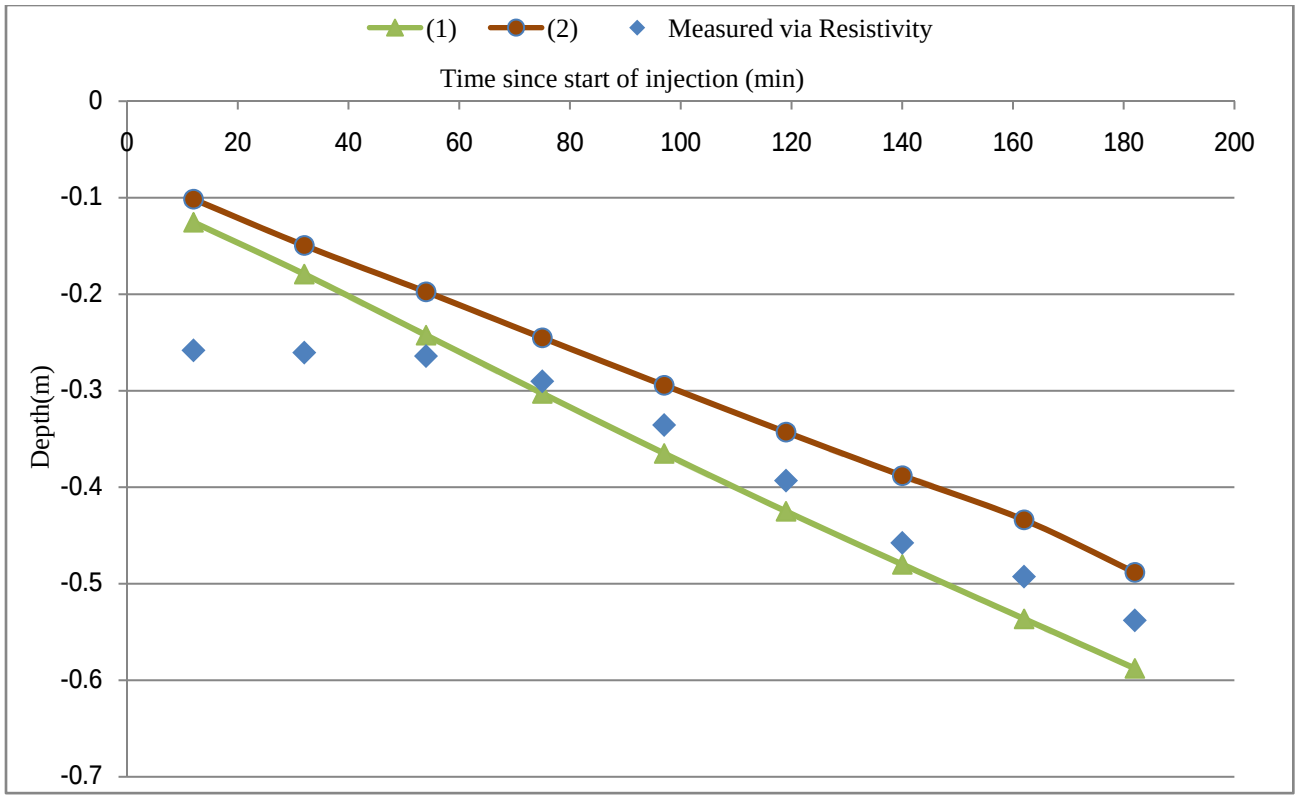

Fig.5.25. Comparison of the centre of mass vertical motion of the tracer measured via ERT with maximum and minimum deviation of simulating models based on $\boldsymbol{\theta_r}$, $\boldsymbol{\alpha}$ and n changes.

a)

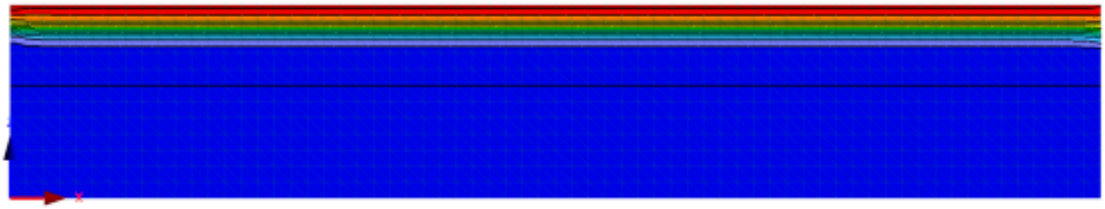

b)

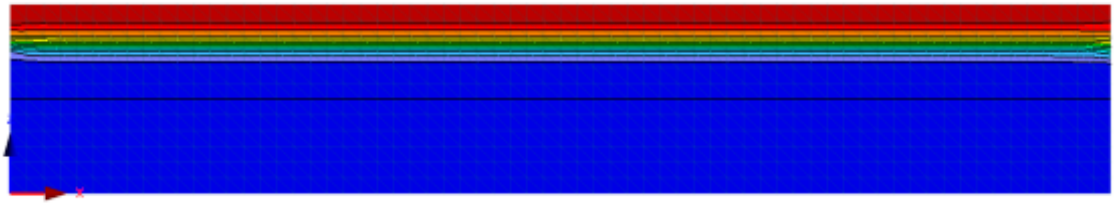

c)

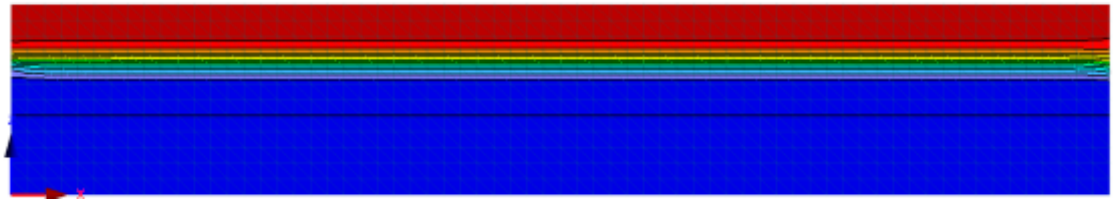

d)

e)

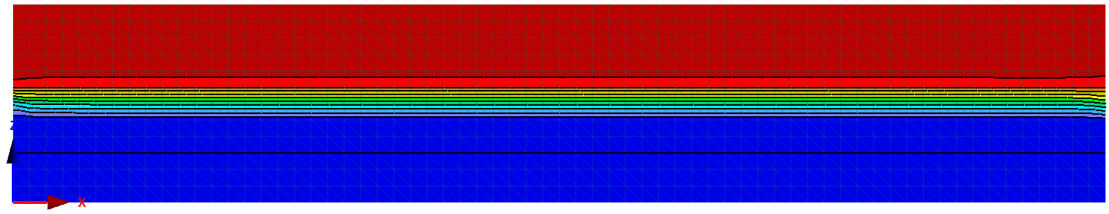

f)

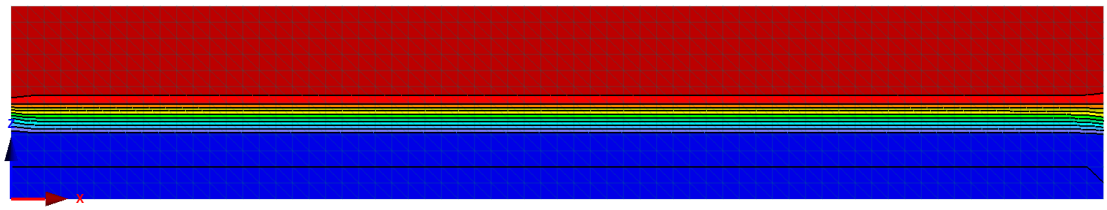

g)

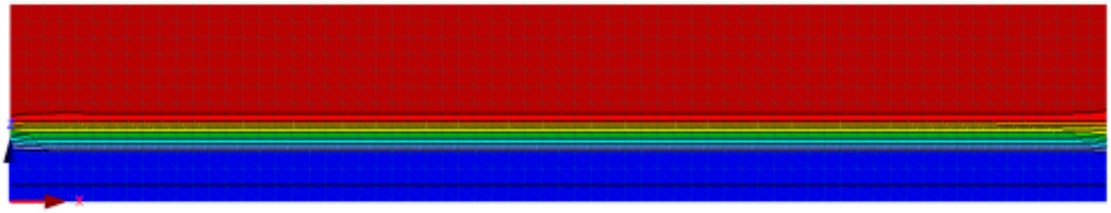

h)

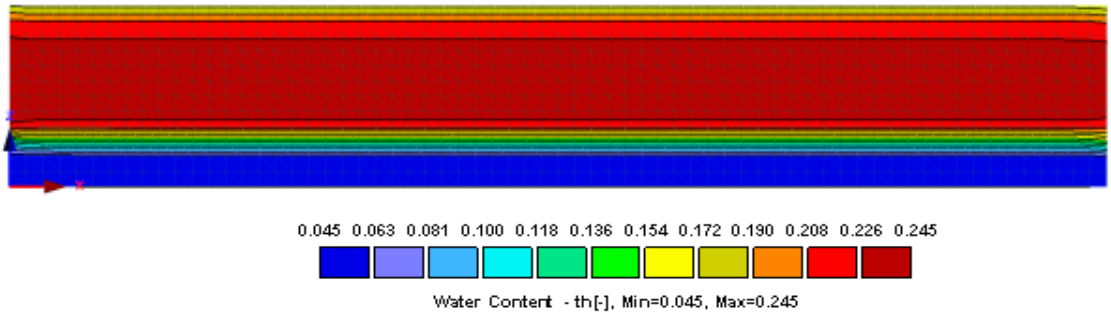

Fig.5.26. Water movement simulation using a 2D- unsaturated flow model, using a homogenous soil and isotropic saturated hydraulic conductivity equal to 0.65 cm/min in a-h) 30, 51, 73, 95, 117, 139, 160 and 180 minutes after the injection respectively.

5.4.6. Synthetic Test

Synthetic numerical experiment was performed to examine how the ERT method could inherently alter the spatial moment analysis results and thereby influence the resulting of hydrologic parameters characterization. Forward hydrologic simulation of water movement during the water injection was performed. The van Genukhten parameters listed in Table 5.1a with Ks equal to 0.65 were used in this synthetic test. Afterward, the development of water infiltration was inverted to electrical resistivity maps using equation 5.1. The electrical resistivity maps were then used as input for a forward model calculation using the RES2DMOD program. We used the same measurement configuration as used in the field. The forward models obtained with RES2DMOD program were subsequently used as input for inversion. 5% random errors were added to the synthetic data and the forward models were then inverted using RES2DINV. Finally, the inverted models were used to calculate spatial moment analysis. The inversion of the synthetic data were carried out using independent inversion, the crossmodel regularization and 4D space–time methods (discussed in 3-3) in order to provide an insight into different inversion method resulting in spatial moment analyzes. The same discretization was used for all inversion process as well as simulated model. The synthetic test was designed only to be used as a means to identify errors associated with the ERT method and inversion process and therefore cannot be compared with the moment analysis results conducted on the real data.

The estimated values of mass, centre of mass vertical motion and vertical spread based on the simulation of water movement and the synthetic data are shown in Fig. 5.27, 5.28 and 5.29 respectively. (I) in Fig.5.27 to 5-29 show the spatial moment analyzes inferred from the simulated model and (II), (III) and (IV) were inferred from the synthetic data inverted by independent inversion, the crossmodel regularization and 4-D space–time methods respectively. Fig.5.27, illustrates that the water tracer mass is overpredicted by the ERT method. All inversion methods used in the synthetic test overestimated the mass in system; however, the 4-D space–time model yielded a better resolution in mass recovery particularly at the beginning of the experiment.

The centre of mass vertical motion was shown in Fig.5.28. The centre of mass vertical motion inferred from the synthetic test is ahead of the simulated model. There is a significant difference between the 4-D space–time model and two other inverted models at the beginning in Fig.5.28. Although the centre of mass vertical motion inferred from the 4-D space–time model was also

overpredicted, the estimated values are nonetheless quite close to the true value (difference ≤20%). On the other hand, the vertical spread is more difficult to determine correctly. Fig. 5.29 shows a drastic difference between the values inferred from the synthetic test and simulated model. This result is not surprising, since the ERT data were inverted using a smoothness optimization method which spreads the water tracer location more widely over the area of interest.

The results of synthetic test indicates a great difference between the spatial moment analyzes inferred from 4-D space–time model and two others inversion models at the beginning of the experiment. Although, in all inversion methods a coarser vertical discretization was used near the electrodes to increase the sensitivity, the water tracer is a small target at the beginning to capture properly in inversion process. The large contrast between the electrical conductivity of injected water and background also make the inversion process more difficult to recover the sharp anomaly accurately. The 4-D space–time model did a better job and the result of this method is very close to simulated model. As the water tracer penetrated deeper and became more dispersed, the results of other inversion methods become more similar and stable and ERT method is more successful in capturing the water movement and therefore the centre of mass vertical motion and the vertical spread were estimated more accurately.

The synthetic test results and moment analyze calculations indicate that the determination of the centre of mass vertical motion is fairly robust when the water tracer penetrated to deeper zone (with the less than 20% difference between synthetic test and simulated model). In contrary, predicting the vertical spread of the water tracer is more troublesome. The high sensitivity of the second moment analysis computation due to inversion process and noisy dataset in borehole ERT survey were also reported by e.g. Binley et al. (2002b), Singha and Gorelick, (2005) and Looms et al. (2008).

The first and second moment computations of field ERT data show also a drastic distortion at the beginning in comparison with the synthetic test. Apart from the inversion effect, the influence of electrodes at near surface and also water injection might have intensified this contrast between field data and synthetic test.

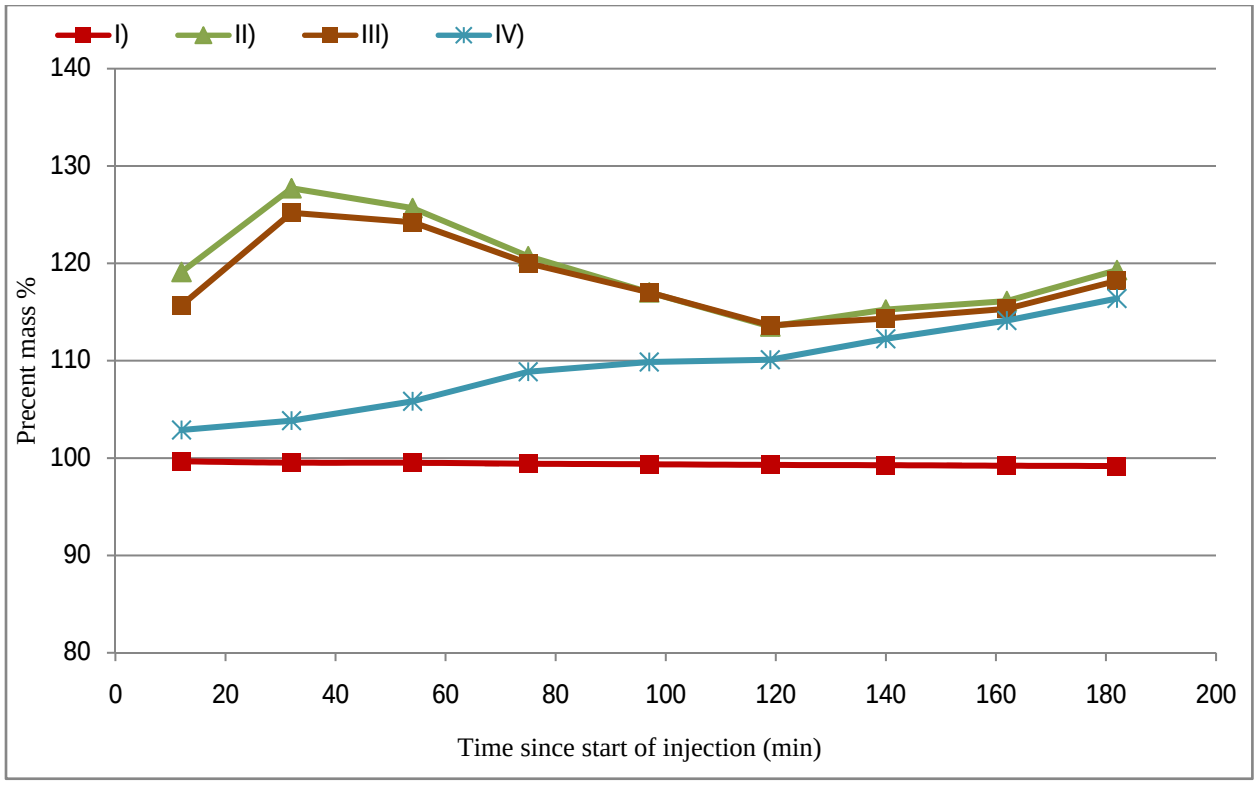

Fig.5.27. Results of the mass balance: I) inferred from simulated model. II, III and IV) inferred from synthetic test using: independent inversion model, cross model regularization and 4-D space–time model respectively.

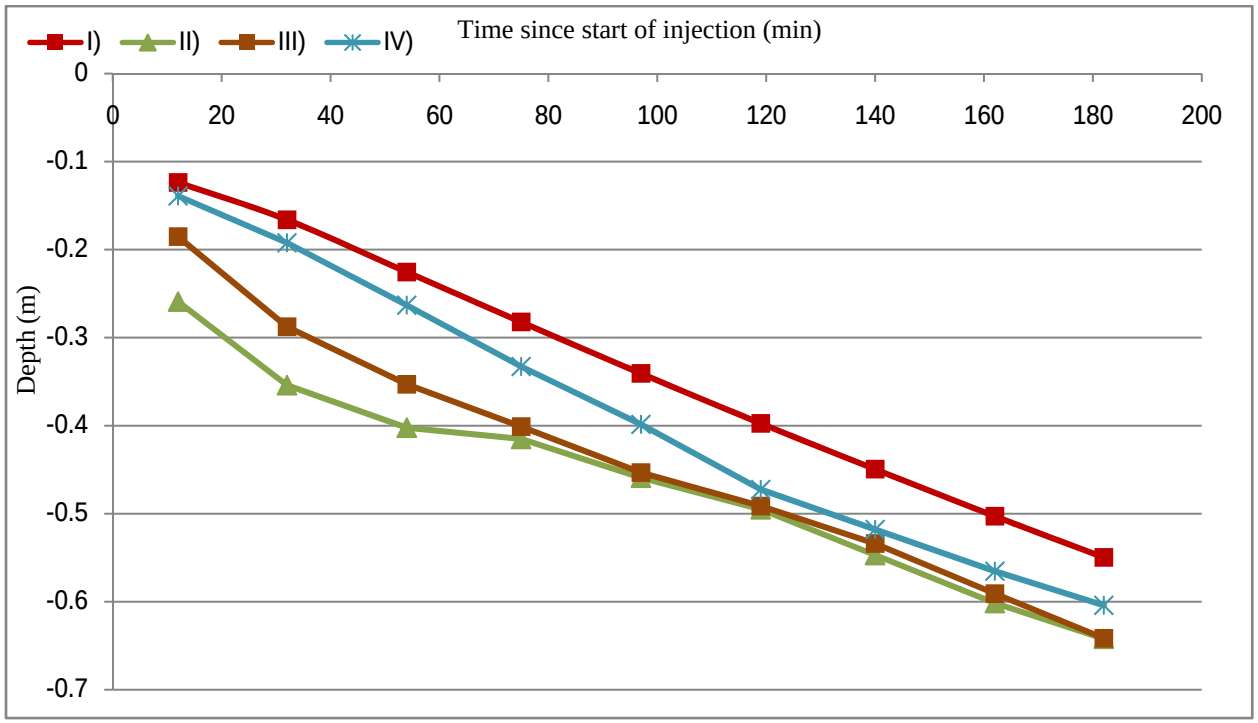

Fig.5.28. Results of the centre of mass vertical motion: I) inferred from simulated model. II, III and IV) inferred from synthetic test using: independent inversion model, cross model regularization and 4-D space–time model

respectively.

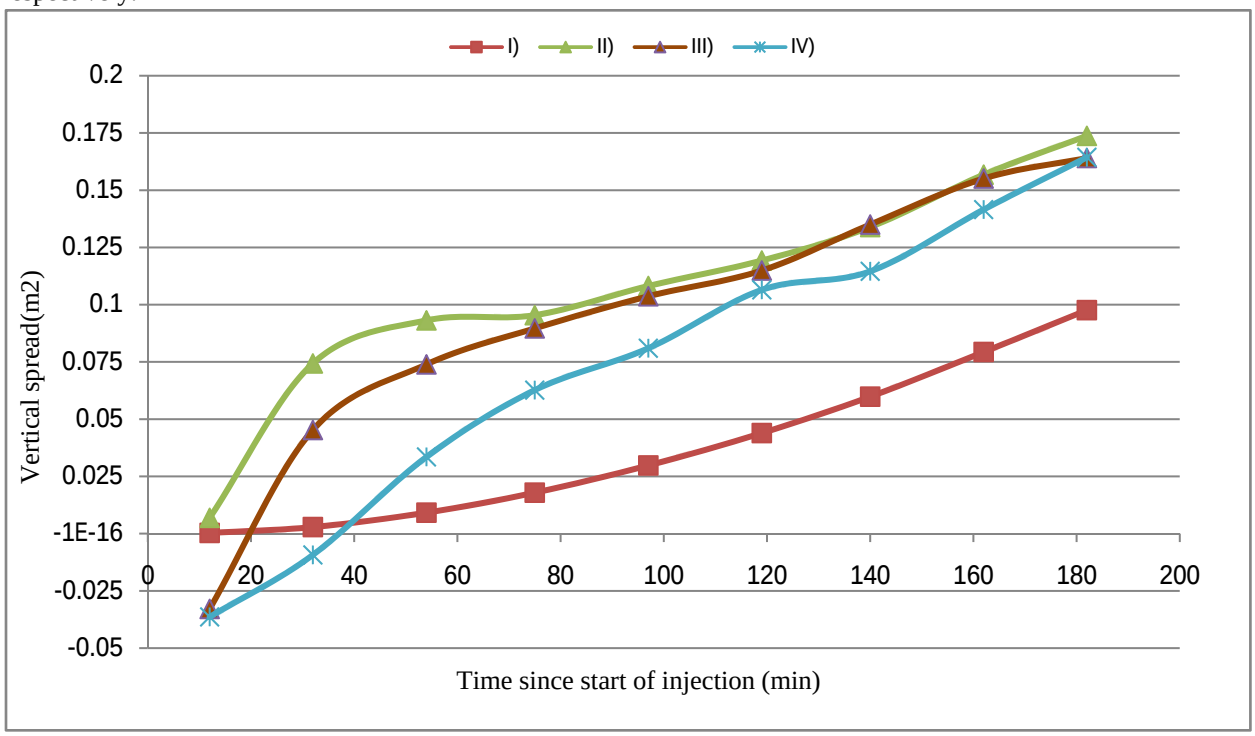

Fig.5.29. Results of the vertical spread: I) inferred from simulated model. II, III and IV) inferred from synthetic test using: independent inversion model, cross model regularization and 4-D space–time model respectively.

5.5. Conclusions:

The results of our experiment in Samora-Correia, where the infiltration process was monitored under natural condition and also forced infiltration experiment using ERT and EM38 allow to the following conclusions:

1. The moisture content variations in unsaturated sandstone and consequently the resistivity changes are mainly influenced by daily rainfall due to the fast infiltration in high-permeability sediments. The both ERT and EM38 are capable to present qualitative maps of moisture content distribution; however the fast infiltration in unsaturated sandstone, make it impractical to monitor water movement under natural condition to estimate and constrain hydrologic parameters. In addition, we found it very difficult to work with EM38 over a dry sandy soil due to the reasons discussed in 5.3.5.

2. The water injection test conducted at the Samorra Correia proves that fast infiltration in permeable sediments can be monitored by ground surface ERT successfully. The large contrast between the electrical conductivity of injected water and soil in this study simplified using the ground surface ERT to monitor unsaturated sandstone and was not essential to apply a saline tracer which might cause gravitational sinking of the tracer during the experiment and requires more complicated interpretation.

3. In spite of poor resolution of ERT images to reproduce the precise water tracer mass, moment analysis aimed at constraining the hydrological model. The first and second moment analysis in this study constrains the range of the saturated hydraulic conductivity to be in 0.5-1.2 (cm/min). Moreover, the investigation of the influence of van Genuchten's parameters in unsaturated flowing simulation confirms again the importance of the saturated hydraulic conductivity estimation among van Genuchten's parameters. Since the synthetic test indicates that ERT method and inversion effects could dramatically overestimate and distorts the vertical spread in this experiment, the first moment is a more reliable tool to constrain the hydraulic conductivity. On the other hand, the first moment also was slightly overestimated by ERT method, therefore the

range of 0.5-0.7 cm/min could be a more accurate estimation for hydraulic conductivity in this study.

4. The synthetic test shows that the 4-D space-time inversion model is significantly more successful in mapping resistivity changes in this experiment. We also found that the 4-D space-time method is more user-friendly among methods discussed in section 3-3. It was very difficult to apply the crossmodel regularization on our data due to the presence of noise in initial data sets. In addition, the synthetic test in this study shows how ERT method and inversion process inherently changes the shape and magnitude of the water tracer. The correct estimation of the hydrologic parameters depends highly on how well the vertical changes in electrical resistivity are captured by the ERT method. Therefore, the survey design, i.e., electrode spacing, measurement configuration, the inversion algorithm and the electrodes contacts should be optimized in order to improve the vertical resolution. This is one of many factors that could have an impact on the results.

5. The temperature data shows more than 5°c variations during the water injection that affects significantly (about 10%) in ERT images and is highly required to be modified for a quantitative model.

6. Using Archie's law instead of the established in-situ relationship for conversion of the electrical conductivity to moisture content will considerably underestimates moisture content estimation in this study (despite previous filed site).

CHAPTER-SIX

1D Coupled Geoelectric-Infiltration Model

6.1. Introduction

ERT images are increasingly being converted to hydrological models to estimates of water content or solute mass using petrophysical relationships. The converted images can then be used for the estimation of soil hydraulic and transport properties. This method is referred to as uncoupled hydrogeophysical inversion (Ferre et al., 2009). In fact in uncoupled hydro-geophysical inversion, ERT data first are inverted and then converted to soil hydraulic and transport properties. This method was used in previous chapters to estimate hydraulic parameters. As discussed in chapter four and five and was also demonstrated in the synthetic test in chapter 5, the inversion procedures may propagate measurement errors and uncertainties related to parameter resolution that arise during the independent inversion of the geophysical data to the hydrologic analysis. Geophysical inverse procedures commonly require the use of prior information (e.g. a smoothness constraint) to stabilize inversion problems (e.g. Menke, 1984). It has been recognized that this regularization may not reflect the hydrologic conditions and can limit the value of hydraulic property estimates derived from geophysical observations. Temporal inversion techniques as we used can effectively reducing the inversion uncertainty by interpreting multiple images simultaneously. However, time-lapse inversion still relies on an independent ERT inversion step to infer hydrologic states. We also showed in the synthetic test in 5.4.6 that even time-lapse inversion can lead to uncertain estimates of soil hydraulic properties.

In contrary, in the coupled approach, geophysical measurements are directly used in the hydrological model by coupling a forward model of the geophysical measurements with a hydrological model. The parameters of the hydrological model (e.g. hydraulic conductivity) are changed until the closest match is obtained between simulated model and observed data. The link between these simulated hydrological properties (e.g. soil water content) and the geophysical properties required for the modeling of the geophysical measurements (e.g. bulk electrical conductivity) is provided by appropriate local-scale petrophysical relationships (Hinnel et al., 2010). The distinguishing factor in the coupled inversion strategy is that, for any observed geophysical data set, we couple a hydrologic and geophysical model to represent the forward model in the optimization. In practice, this is achieved through a straightforward process where an initial set of hydraulic parameters is proposed and a forward hydrologic is run using these parameter values. The model predicted hydrologic states (e.g. water content) are converted to

geophysical properties using petrophysical relations. The hydraulic properties are optimized to minimize the difference between predicted and measured geophysical observations. Coupled model does not require a geophysical inversion step, thereby avoiding geophysical resolution problems due to inversion artifact. Rather, all of the data are considered in a single process technique by coupling the hydrologic model and the geophysical models. In summary, because coupled inversion interprets the geophysical data in the context of the proposed hydrologic model, it provides a better test of the consistency of the proposed hydrologic model with the geophysical observations. Flowcharts of uncoupled (a) and coupled (b) integration of geophysical and hydrological analysis are outlined in Fig.6.1.

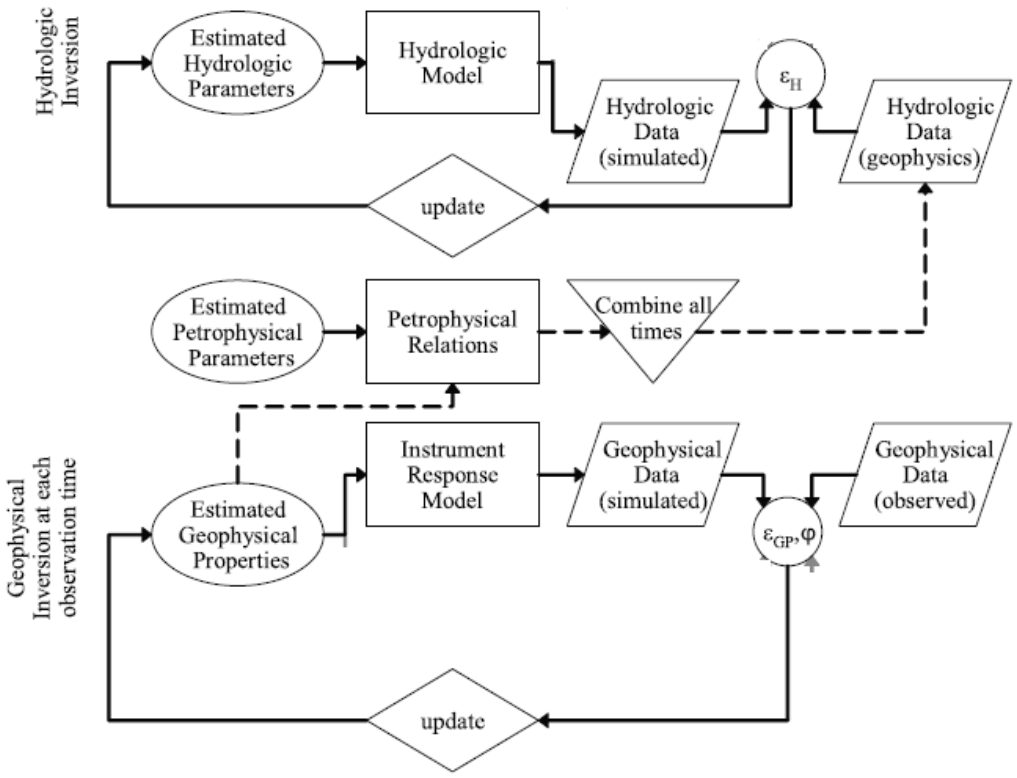

a) Uncoupled

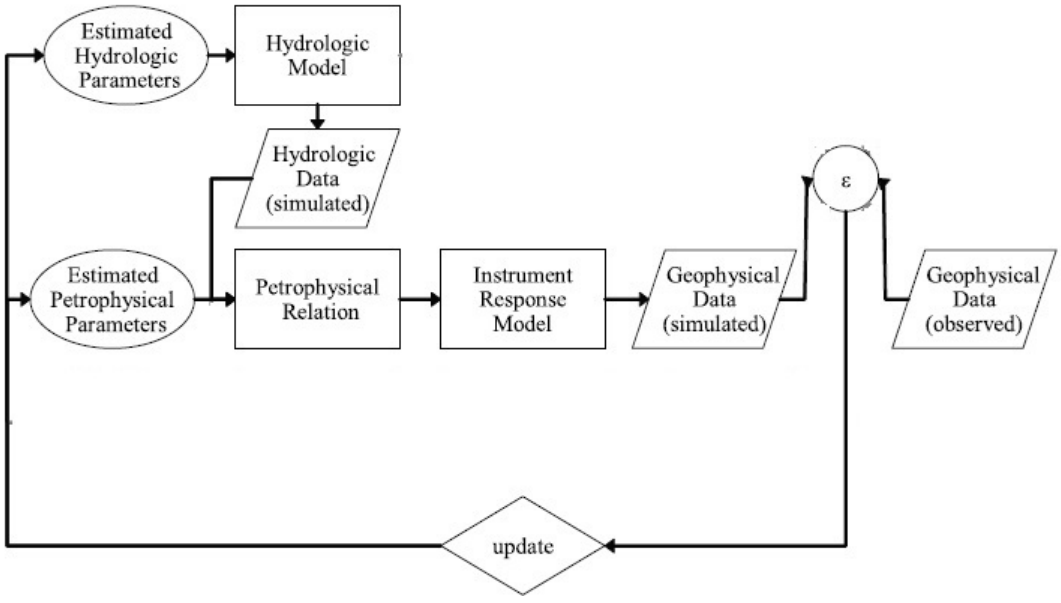

b) Coupled

Fig.6.1. Analysis flowcharts for (a) uncoupled and (b) coupled integration of geophysical data in hydrologic analysis (Hinnel et al., 2010).

6.2. 1D coupled hydrogeoelectrical model

In this study, we used the 2D surface ERT data collected under forced-infiltration with a constant flux rate (discussed in section 5.4.2) to apply the coupled hydrogeoelectrical approach to ERT and inflow data for the estimation of topsoil hydraulic properties. We will present and discuss here the results of five Vertical Electric Sounding (VES) data from 2D ERT datasets with the largest depth of investigation. In Fig.2, we highlighted selected VES by a black rectangle. The deepest VES is in the middle of electrodes spread (Marked with "M") includes 19 measurements with minimum and maximum current electrode (AB/2) expansion of 0.45 m and 5.85m respectively. The first left and right side of M (Marked with "L1" and "R1" respectively) include 18 measurements with maximum AB/2 of 5.55m. Finally the second left and right side of M (Marked with "L2" and "R2" respectively) include 17 measurements with maximum AB/2 of 5.25m.

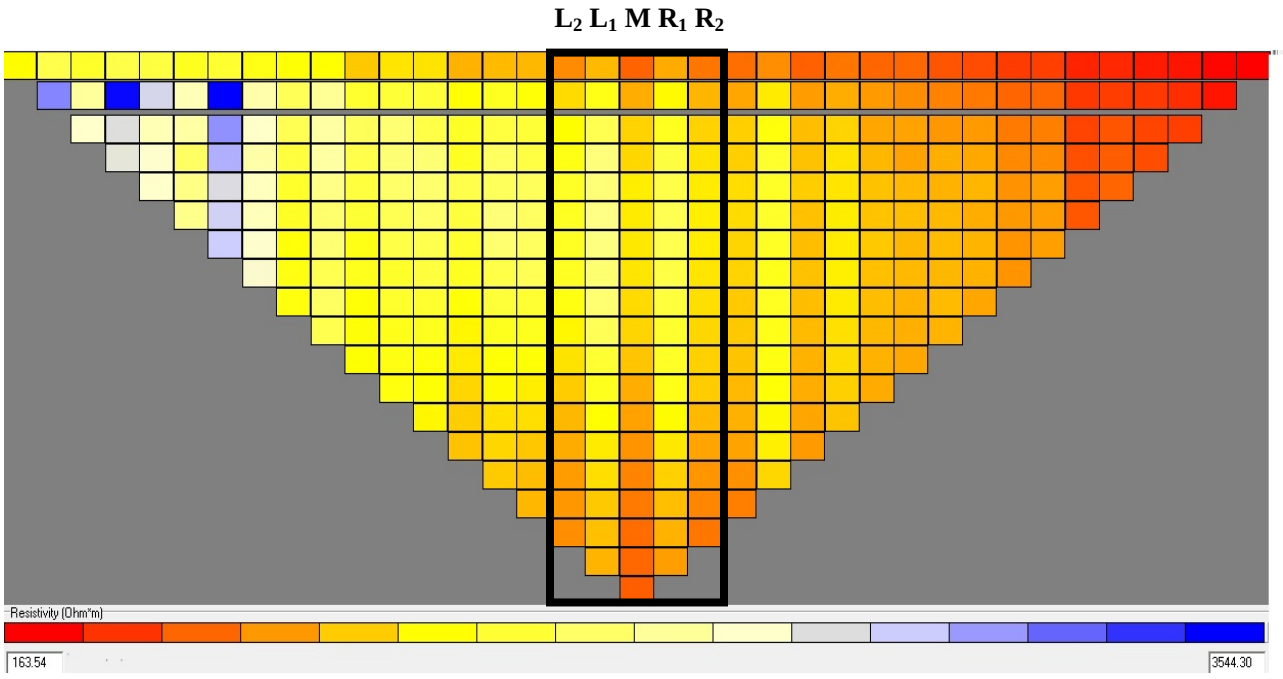

Fig.6.2. The graphical display of the measured resistiviteis (Pseudo Section) by using multi-electrode connections in Geotest software. The displayed Pseudo Section shows an example of resistivity monitoring using Schlumberger electrode configuration during the water injection. The black rectangle distinguished the selected VES for coupled hydrogeoelectrical model.

The specific problem we consider is the use of VES data to monitor the water movement over a homogenous soil during 1D infiltration medium with uniform initial pressure head. As discussed in 5.4.2, the ERT data consisted of a time series of measurements during and after the water injection test. We used the first eight time-lapse ERT data which were measured during the water injection for our investigations.

The coupled hydrogeoelectrical model requires two forward models: a hydrologic model and a geoelectrical model and also a petrophysical relation.

6.2.1. 1D hydrologic model

The hydrologic model enables the simulation of water movement with depth and time based on a numerical solution of Richards'equation. To develop a simplified 1D model of unsaturated flow, h-based formulation of equation 3.39 was used as discussed in 3.5.3. We used van Genuchten equations (3.37 and 3.38) to obtain a predictive equation for the unsaturated hydraulic conductivity function in terms of soil water retention parameters. The time step (Δt) and space step (Δz) in all simulations were selected to be 1 second and 1 cm respectively. The infiltrations models were tested against HYDRUS 1d software to evaluate the results. The results were consistent with HYDRUS 1d (not shown here). The mass errors in our simulations were less than 2%.

6.2.2. 1D resistivity forward modeling

In the forward modeling problem, the subsurface resistivity distribution is specified and the purpose is to calculate the apparent resistivity that would be measured by a survey over such a structure (Loke, 2004). For the 1-D case, where the subsurface is restricted to a number of horizontal layers, the linear filter method discussed in 3.2.3 is commonly used. The subroutine developed by Santos et al. (1997) based on the filter method was used to calculate the apparent resistivity.

6.2.3. Petrophysical Relation

The hydrologic and electrical conductivity models are linked by the dependence of the soil electrical conductivity on the soil water content. Equation 5.1 was used in order to convert soil water content to bulk resistivity.

6.3. Solution of the Analytical Model

First, a hydrological model was developed. To achieve an infiltration model, all five van Genuchten´s parameters (θr, θs, α, n, and Ks) must be estimated. We fixed θr and θs to be 0.37 and 0.03 based on the results discussed in 5.2. α, n and Ks parameters range were extracted from ROSETTA database range for sandstone listed in Table.6.1. The parameter ranges were then sampled using a Latin hypercube method (LHS). This method works like a constrained Monte Carlo sampling approach (McKay et al., 1979). Each parameter range is subdivided into M equally probable intervals. For each interval, one value is selected at random and subsequently paired at random with similarly determined values of the remaining parameters, resulting in M independent realizations. All parameters were assumed to be uniformly distributed within the specified intervals. A public domain software Latin hypercube sampling tool was used (http://www.mathepi.com/epitools/lhs/nrpage.html). In this study, the hydraulic parameters were assumed to be uncorrelated.

Afterward, a forward resistivity model was coupled to each hydrological model using Equation.5.1. This allows the simulation of soil water content can be converted into simulated resistivity distributions. The simulated resistivity images were then used as input for resistivity forward modeling to calculate ERT data. The simulated data were finally compared with the field ERT data using following equation:

$$Misfit = \sqrt{\frac{1}{N}\sum_{i=1}^{N}\frac{1}{\varepsilon_r^2}\left[log_{10}\left[\frac{Measured}{Simulated}\right]\right]^2} \quad (6.1)$$

where ε_r is the average relative data error of the transfer resistances and is equal to 0.08 (Looms et al., 2008)

6.4. Results

1000 parameter sets were sampled using LHS. Flow and transport simulations were then run for each parameter set using the same initial and boundary conditions. A homogenous soil was selected for all simulations. The bottom boundary of the soil column was simulated by implementing a free drainage boundary condition. The upper boundary condition was a specified flux of 1.792 cm h−1 corresponding to 20% of the applied irrigation. This value was estimated from the mass error calculated using moment analysis in 5.4.3. The simulations were carried out for 180 minutes and the evaporation was neglected in all simulations.

To evaluate whether the unsaturated hydraulic parameters are constrained by the data, we plotted the misfit value (calculated from Equation.6.1) as a function of parameter values Ks, n and α in Fig.6.3, 6.4 and 6.5 respectively. Each figure has five sections which are related to the misfit values of different VES datasets. a, b, c, d and e in each figure presents the results of misfit values obtained using L2, L1, M, R1 and R2 datasets respectively. Only the 100 realizations with the lowest misfit are included in the figures for illustration purpose. The parameter ranges of the realizations with the lower misfit values are highlighted with red arrows in all figures and were also listed in table.6.1. By comparing the extent of the range of each parameter with the a priori range of the selected parameter and by evaluating whether the dots with low misfit values are clustered at certain parameter ranges, it becomes clear whether the data can reduce the uncertainty of the hydraulic parameters investigated.

Fig.6.3 and 6.4 indicate that the parameter ranges of Ks and n are constrained compared with the a priori range. Values of Ks in Fig 6.3 (expect 6.3b) centered around 0.80 cm min^{-1}, appear to result in slightly lower misfits between the simulated and ERT model and the misfit plots exhibit a clustering at this intermediate Ks value. The results of L2, M, R1 and R2 are acceptably consistent while L1 exhibits a wider range. The estimated range of Ks shows a very good consistency with the results in chapter 5. Values of n in Fig.6.4 (expect 6.3d) are also constrained in range of 2-3.6. The results of L2, L1, M and R2 are to some extent consistent, but R1 shows a wider range.

In contrary, Fig.6.5 show that the parameter α is not constrained by the ERT data, since the range of the lower misfit realizations is almost identical to the a priori range in most of ERT datasets and the dots do not exhibit any structure.

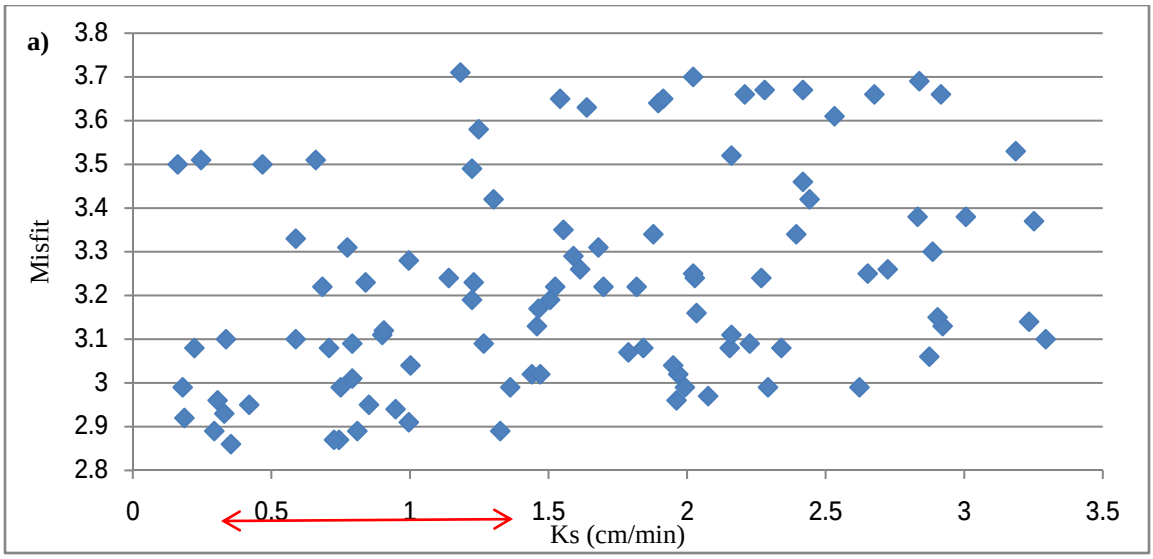
a)
Misfit
3.8
3.7
3.6
3.5
3.4
3.3
3.2
3.1
3
2.9
2.8
0
0.5
1
1.5
2
2.5
3
3.5
Ks (cm/min)

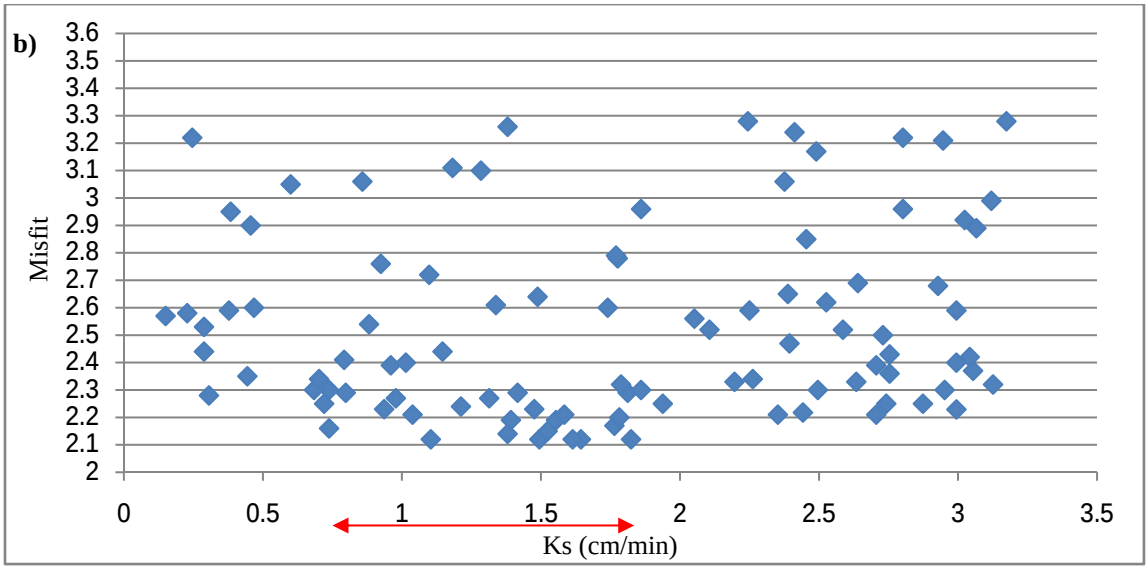
b)
Misfit
3.6
3.5
3.4
3.3
3.2
3.1
3
2.9
2.8
2.7
2.6
2.5
2.4
2.3
2.2
2.1
2
0
0.5
1
1.5
2
2.5
3
3.5
Ks (cm/min)

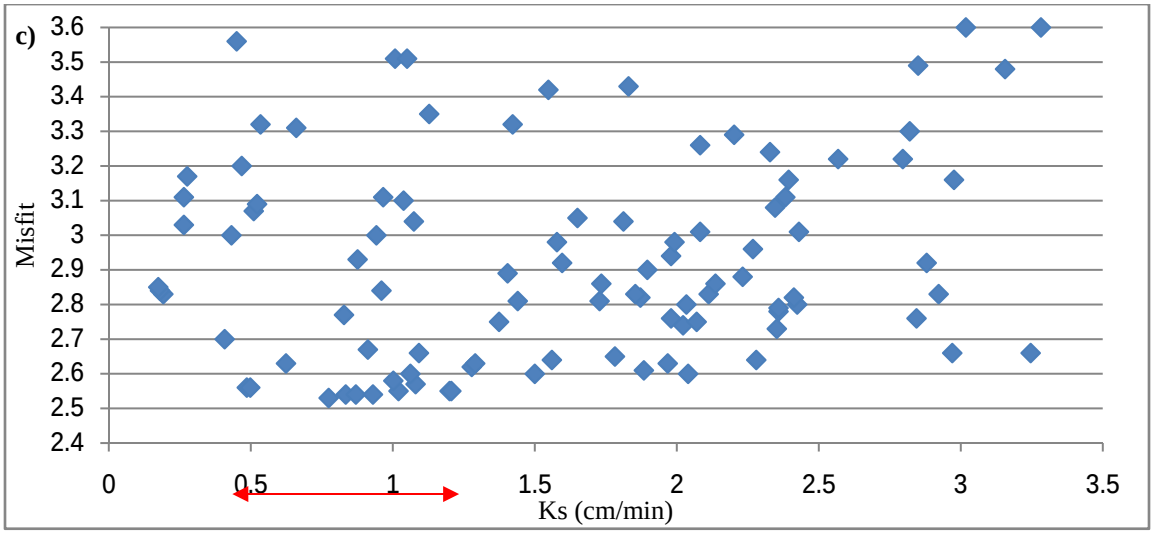
c)
Misfit
3.6
3.5
3.4
3.3
3.2
3.1
3
2.9
2.8
2.7
2.6
2.5
2.4
0
0.5
1
1.5
2
2.5
3
3.5
Ks (cm/min)

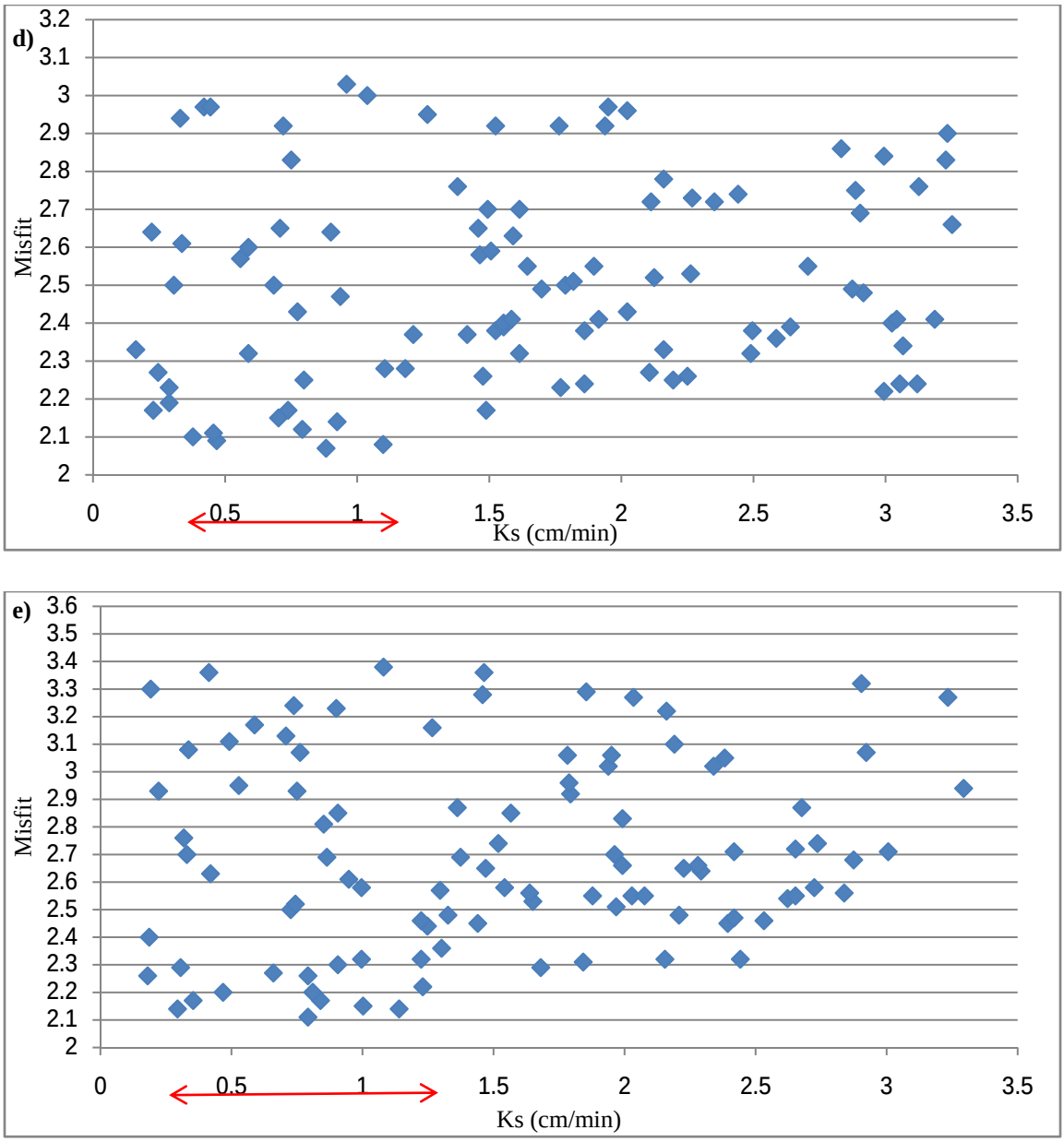

Fig.6.3. the misfit values of the simulated models with VES data as a function of Ks. For illustration purposes, only the 100 realizations with the lowest misfit values are included in the figures. The parameter ranges of the realizations with the lowest misfit values are indicated with red arrows. a, b, c, d and e was obtained using L2, L1, M, R1 and R2 datasets respectively.

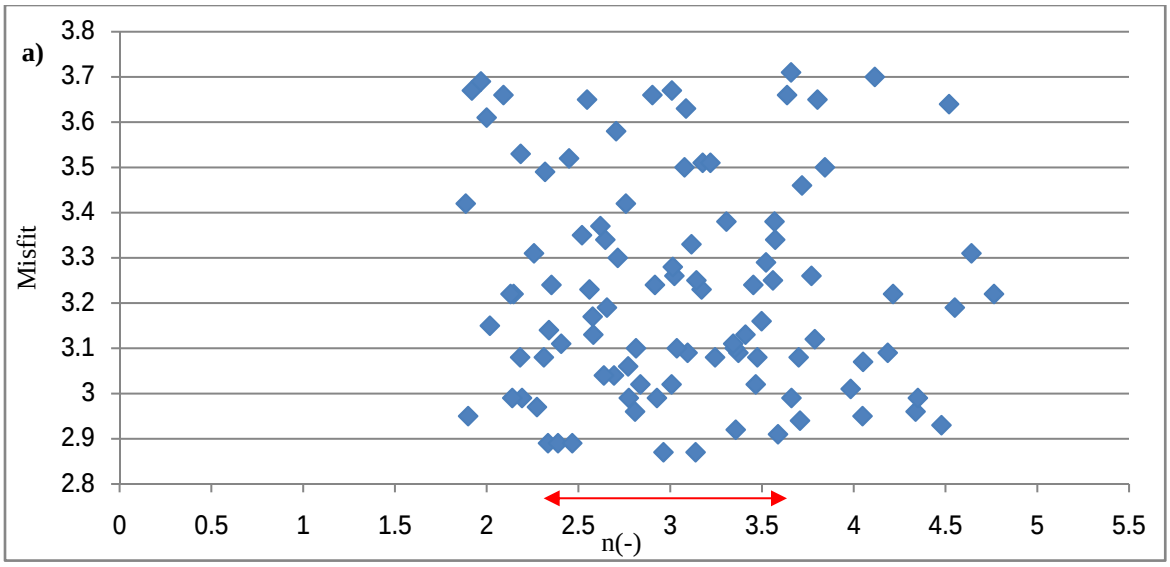
a)
Misfit
3.8
3.7
3.6
3.5
3.4
3.3
3.2
3.1
3
2.9
2.8
0
0.5
1
1.5
2
2.5
3
3.5
4
4.5
5
5.5
n(-)

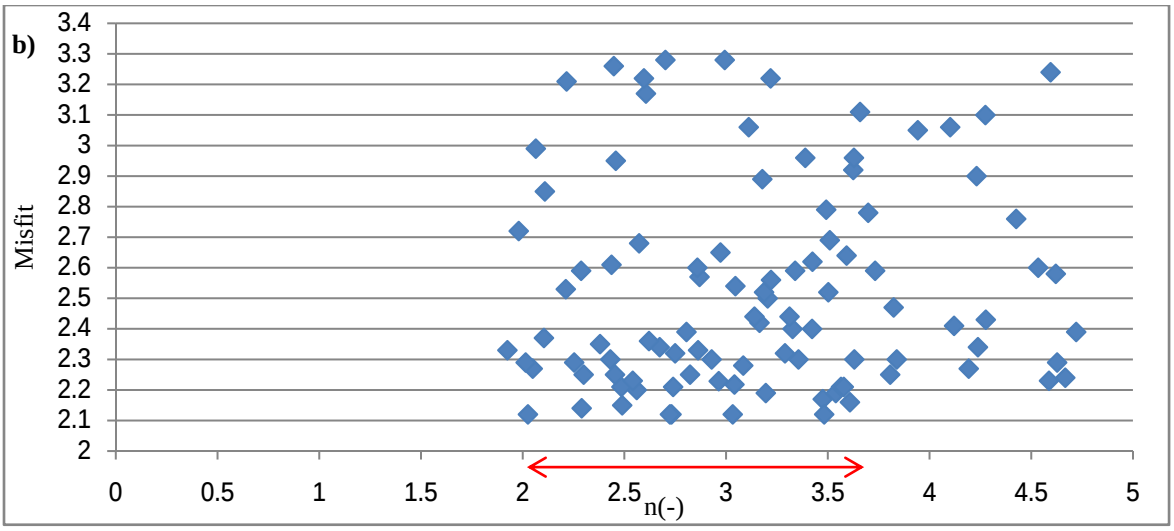
b)
Misfit
3.4
3.3
3.2
3.1
3
2.9
2.8
2.7
2.6
2.5
2.4
2.3
2.2
2.1
2
0
0.5
1
1.5
2
2.5
3
3.5
4
4.5
5
n(-)

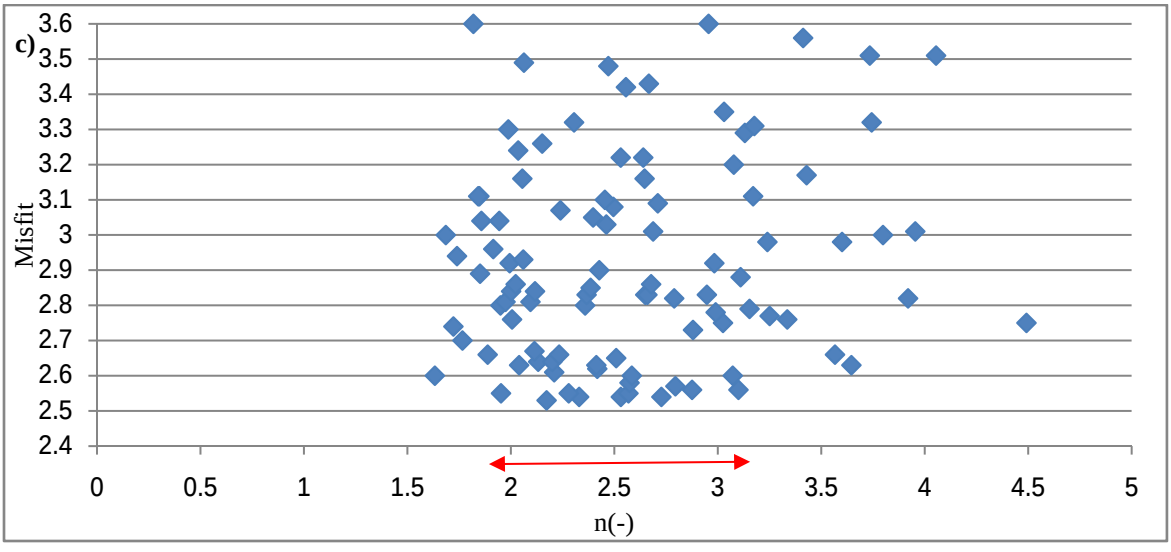
c)
Misfit
3.6
3.5
3.4
3.3
3.2
3.1
3
2.9
2.8
2.7
2.6
2.5
2.4
0
0.5
1
1.5
2
2.5
3
3.5
4
4.5
5
n(-)

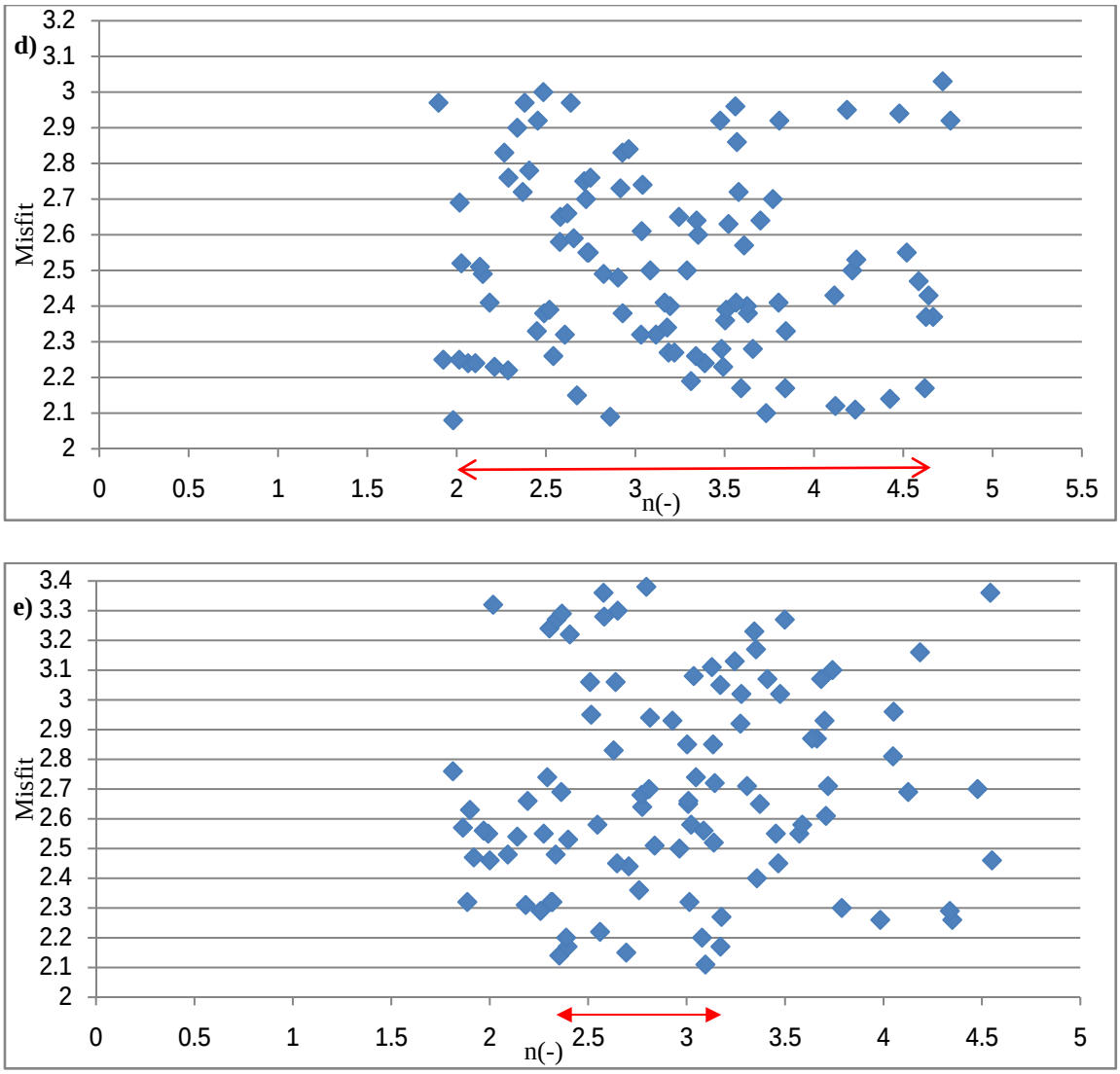

Fig.6.4. the misfit values of the simulated models with VES data as a function of n. For illustration purposes, only the 100 realizations with the lowest misfit values are included in the figures. The parameter ranges of the realizations with the lowest misfit values are indicated with red arrows. a, b, c, d and e was obtained using L2, L1, M, R1 and R2 datasets respectively.

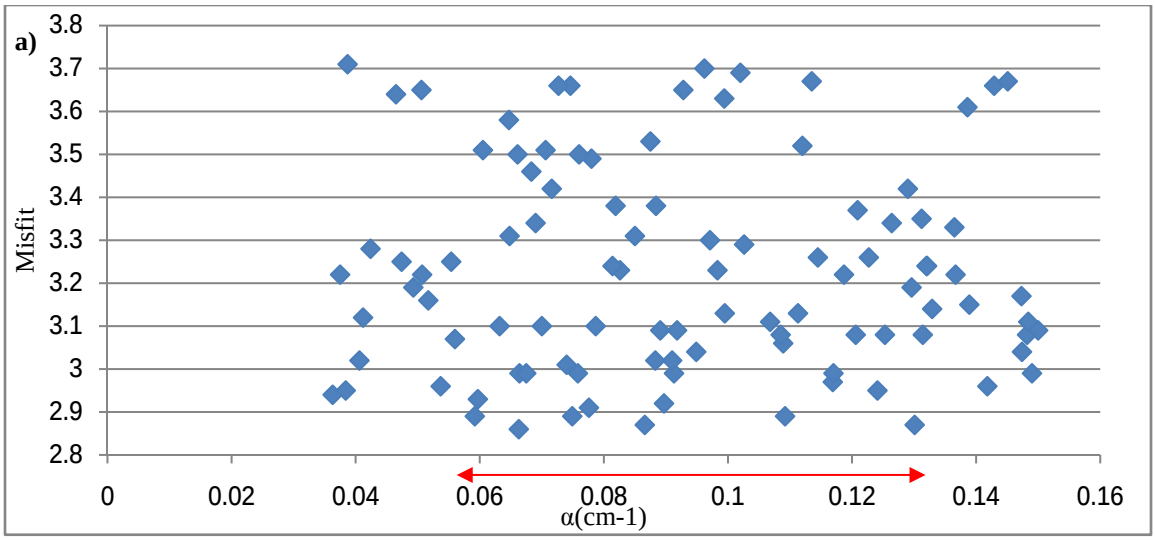
a)
Misfit
3.8
3.7
3.6
3.5
3.4
3.3
3.2
3.1
3
2.9
2.8
0
0.02
0.04
0.06
0.08
0.1
0.12
0.14
0.16
α(cm-1)

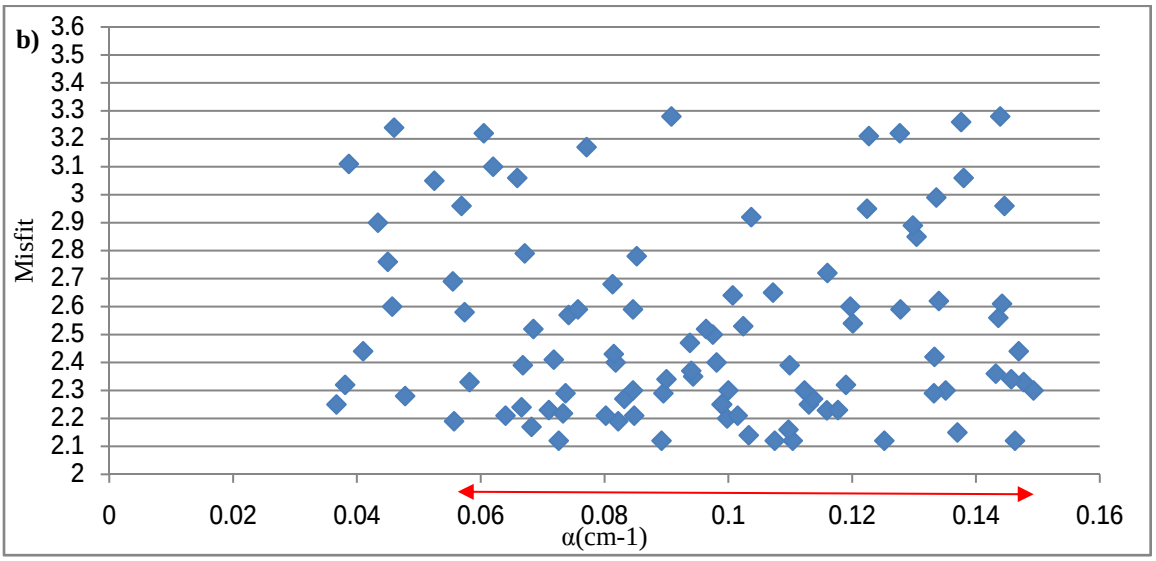
b)
Misfit
3.6
3.5
3.4
3.3
3.2
3.1
3
2.9
2.8
2.7
2.6
2.5
2.4
2.3
2.2
2.1
2
0
0.02
0.04
0.06
0.08
0.1
0.12
0.14
0.16
α(cm-1)

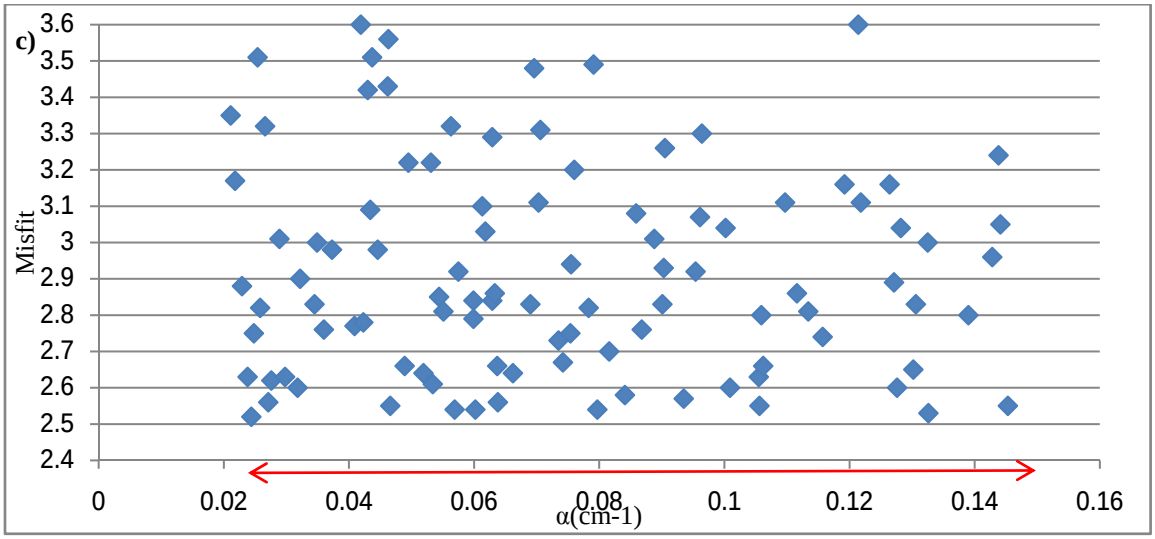
c)
Misfit
3.6
3.5
3.4
3.3
3.2
3.1
3
2.9
2.8
2.7
2.6
2.5
2.4
0
0.02
0.04
0.06
0.08
0.1
0.12
0.14
0.16
α(cm-1)

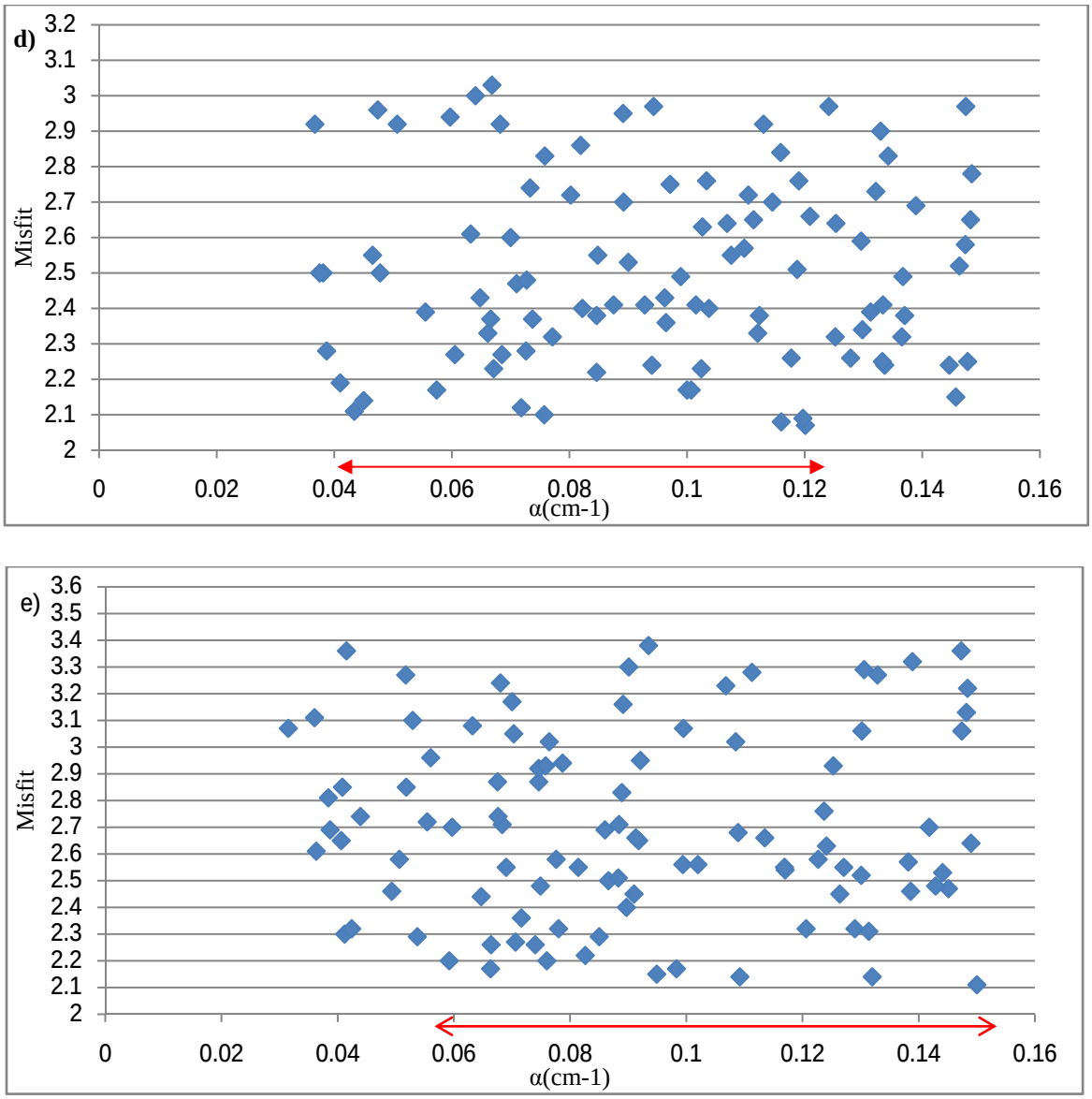

Fig.6.5. the misfit values of the simulated models with VES data as a function of α. For illustration purposes, only the 100 realizations with the lowest misfit values are included in the figures. The parameter ranges of the realizations with the lowest misfit values are indicated with red arrows. a, b, c, d and e was obtained using L2, L1, M, R1 and R2 datasets respectively.

Table.6.1. Range of van Genuchten's parameters (α , n and Ks) for sand

a) Found in the ROSETTA database, computed from the average and one standard deviation of 308 sands samples,

b) Selected range for hydrogeoelectrical model.

c, d, e, f and g) Constrained range obtained using L2, L1, M, R1 and R2 datasets respectively

Parameter	α (cm-1)	n	k_s(cm/min)
a) ROSETTA range	0.02-0.06	2.10-4.81	0.115-1.735
b) Selected range	0.02-0.15	1.6-4.81	0.115-3.3
c) L2	0.059-0.13	2.33-3.6	0.35-1.32
d) L1	0.056-0.146	2.02-3.6	0.73-1.82
e) M	0.024-0.146	1.95-3.1	0.49-1.2
f) R1	0.043-0.12	1.98-4.42	0.38-1.1
g) R2	0.059-0.15	2.35-3.2	0.3-1.23

6.5. Conclusions

We have developed a coupled hydrogeoelectrical inversion framework in order to estimate three van Genuchten parameters (α, n and Ks) from electrical resistances and inflow measurements obtained during constant head infiltration. The collected data were used in a forward manner to evaluate a series of plausible hydrologic models. By avoiding the use of geophysical inversion tools, uncertainties connected with inversion, such as artifacts and subjective constraints (e.g. regularization choice) were eliminated. The results showed that the joint interpretation of inflow and resistance measurements provide reasonably good constraints on the estimation of Ks and n.

Mass balance considerations in simulated model revealed that water was being diverted away from the measurement area; however, the consistency of the water loss during the infiltration led us to adopt an effective average infiltration rate of 20% the applied irrigation. We feel confident that this assumption is valid, but one could consider estimating the effective infiltration in future analyses to minimize this uncertainty. It is not the only source of uncertainty in our study. The proposed methodology still required assumptions regarding choice of petrophysical relationships, soil structure, investigated parameter ranges, misfit functions and data error levels. All these variables are connected with uncertainty and represent subjective considerations that may influence the obtained results markedly.

CHAPTER-SEVEN

Conclusion and Recommendations

7.1. Conclusions

The key finding of this research was that the apparent electrical conductivity data produced by ERT and EM38 can be used to measure soil moisture and estimate hydrological properties of unsaturated zone. These methods can efficiently develop the dense datasets for describing spatial soil properties variability.

The results of this study show that the EM38 is a useful tool for soil moisture measurement and hence potentially useful in agricultural industry. EM38 proved to be capable in mapping moisture content variation in shallow zone where the soil is not very dry. A very dry soil is not an ideal target when a quantitative and temporal study is required due to the strong influence of noise in low values of electrical conductivity. EM38 has the advantage of being less expensive, much faster, and easier to use in data collection in comparison with the ERT method. Furthermore, EM38 can cover a larger area in regional investigation. Paying special attention to both data collection and inversion is greatly important in order to achieve a quantitative model.

The ground surface ERT study in Samorra Correia proves that fast infiltration in permeable sediments can be monitored successfully by ERT surveys. ERT method also yielded an acceptable quantitative model at the campus of University of Lisbon in a location where had a loam soil with low permeability and high water retention capacity. The results of ERT surveys show a better resolution in mapping the spatiotemporal resistivity changes in comparison with EM38 where a quantitative model is required.

1D coupled hydrogeoelectrical model developed in this study showed that the data collected provided information enough to constrain the saturated hydraulic conductivity, Ks, and the van Genuchten parameter n, while it was not possible to constrain the parameter α. Using additional geophysical data such as GPR and EM38 might aim at better constraining the van Genuchten parameters. Additional information, such as pressure measurements and correlation of the van Genuchten parameters could be also incorporated to constrain the hydrologic model.

Our study on inversion effects in soil characterization reveals the importance of a careful consideration of inverse problem to avoid the effects of overparameterization and smoothing from regularization. Our investigation in both study areas demonstrates that the 4-D space-time method proposed by Kim et al. (2009) could results in a more accurate model with lower artefacts; however the synthetic test indicates that even the 4-D space-time method still changes the shape of the model. Extending the use of coupled hydrological and geophysical models in hydrology investigation can be significantly reducing the uncertainty by avoiding the uncertainties connected with inversion.

Assumptions in both study areas regarding the conceptual geologic model, including the 1D or 2D flow assumption, the homogonous soil setup and the assumed constant petrophysical parameters. Most of these assumptions were made to simplify the conceptual model and minimize the number of free parameters.

7.2. Recommendations

This study was confined to two small study areas with nearly uniform soil, to minimize the influence of factors other than soil moisture on EM38 and ERT data. While the results of the study are positive, extension of the study to different areas with a range of soil types is required to evaluate and generalize the results.

Further recommendations include:

To our knowledge no attempt has been made to develop time-lapse inversions in EMI field. The absence of time-lapse inversion of EM38 data made the results unstable and noisy in this study where independent inversion of dataset was carried out and resistivity variation maps were achieved by subtraction of pixel-by-pixel values from a background image. Developing a time-lapse inversion algorithm for EM38 data will be a concrete step for expansion of EM38 use in soil characterization where a dense multiple dataset is required.

In this study, the hydraulic parameters were assumed to be uncorrelated. In future work, it would be of benefit to include correlation between parameters to constrain the parameter ranges. Considering the parameters correlation allows a more efficient sampling of the parameter space by constraining less free parameters. In addition, all analysis was based on the key assumption that the hydrologic model could be expressed using the van Genuchten parameterization. These models may not be the best in the study areas where we were working. Attempts should therefore be made to test additional parameterization approaches to evaluate our research.

The 1D coupled hydrogeoelectrical model developed in this study was used to constrain three parameters (Ks, n and α) of Van Genukhten parameters. The coupled approach can be used to evaluate whether or not the approach can aim at constraining $\boldsymbol{\theta}_r$ and $\boldsymbol{\theta}_s$ where information of these parameters is not available. Since the result of the coupled model is positive, extension of the coupled approach to integrating EM38 and hydrologic model is recommended. In addition, this coupled model was limited to 1d approach. In order better to describe the hydraulic properties of the subsurface, 2D extension of this program for both EM38 and ERT methods can be achieved using 2D forward geophysical and hydrological models.

References

Archie, G.E., 1942. The electrical resistivity log as an aid in determining some reservoir characteristics. J. Trans. Am. Inst. Miner. Engng. 146, 54–61.

Barker, D.L., Scott, H.D., 1998. A Limited Tutorial on Using Finite Differences in Soil Physics Problems. **www.aquarien.com**

Binley, A.M., Henry-Poulter, S., Shaw, B., 1996. Examination of solute transport in an undisturbed soil column using electrical resistance tomography. J.Water Resour. Res. 32 (4), 763–770

Binley, A.M., Winship, P., Middleton, R., Pokar, M., West, J., 2001. High resolution characterization of vadose zone dynamics using cross-borehole radar. J.Water Resour. Res. 37(11), 2639–2652.

Binley, A.M., Winship, P., West, L.J., Pokar, M., Middleton, R., 2002a. Seasonal variation of moisture content in unsaturated sandstone inferred from borehole radar and resistivity profiles. J. Hydrol. 267(3–4), 160–172.

Binley, A.M., Cassiani, G., Middleton, R., Winship, P., 2002b. Vadose zone flow model parameterisation using cross-borehole radar and resistivity imaging. J. Hydrol. 267(3–4), 147–159.

Binley, A.M., Kemna, A., 2005. DC Resistivity and Induced Polarization Methods. Springer Hydrogeophysics Series: Water Science and Technology Library. 50, (eds Y. Rubin and S.S. Hubbard).

Brevik, E. C., Fenton, T. E., Lazari, A., 2006. Soil electrical conductivity as a function of soil water content and implications for soil mapping. J. Precision Agric. 7: 393 - 404.

Brooks, R. H., Corey, A. T., 1964. Hydraulic properties of porous media. J. Hydrol. 3, Colorado State Univ., Fort Collins, CO.

Cassiani, G., Strobbia, C., Gallotti, L., 2004. Vertical radar profiles for the characterization of deep vadose zones. J. Vadose Zone. 3, 1093–1115.

Cassiani, G., Strobbia, C., Giustiniani, M., Fusi, N., Crosta G.B., Frattini, P., 2006. Monitoring of hydrological hillslope processes via time-lapse ground-penetrating radar. Bollettino di Geofisica Teorica ed Applicata. 47 (1–2), 125–144.

Celia, M.A., Ahuja, L.R., Pinder, G.F., 1987. Orthogonal collocation and alternating-direction procedures for unsaturated flow problems. J.Water Resour. Res. 10, 178-187.

Celia, M. A., Bououtas, E. T., Zarba, R. L., 1990. A general mass-conservative numerical solution for the unsaturated flow equation. J.Water Resour. Res. 26, 1483-1496.

Corwin, D.L., Lesch., S.M. 2005. Apparent soil electrical conductivity measurements in agriculture. J. Comput. Electron. Agric. 46,11–43.

Daily, W.D., Ramirez, A.L., LaBrecque, D.J., Nitao, J., 1992. Electrical resistivity tomography of vadose water movement. J.Water Resour. Res. 28(5), 1429–1442.

Davis, L.A., Neuman, S.P., 1983. Documentation and user's guide: UNSAT2- variable saturated flow model. NUREG/CR-3390, US Nuclear Regulatory Comm., Washington, DC.

Daily, W., Ramirez, A., 1995. Electrical resistance tomography during in-situ trichloroethylene remediation at the Savannah River Site. J. Appl Geophys. 33, 239–249.

Dean, T. J., Bell, J. P., Baty, A. J. B., 1987. Soil moisture measurement by an improved capacitance technique, Part I. Sensor design and performance. J. Hydrol. 93, 67 - 78.

Deiana, R., Cassiani, G., Kemna, A., Villa, A., Bruno, V., Bagliani, A., 2007. An experiment of non invasive characterization of the vadose zone via water injection and cross-hole timelapse geophysical monitoring. J. NSGS. 5(3), 183-194.

deGroot-Hedlin, C., Constable, S., 1990. Occam's inversion to generate smooth, two dimensional models form magnetotelluric data. J. Geophysics. 55, 1613-1624.

Durner, W., 1994.Hydraulic conductivity estimation for soils with heterogeneous pore structure. J.Water Resour. Res. 32(9), 211-223.

Edwards L.S., 1977. A modified pseudosection for resistivity and induced-polarization. J. Geophysics. 42, 1020-1036.

Evett, S. R., Steiner, J. L., 1995. Precision of neutron scattering and capacitance type soil water content gauges from field calibration. J. Soil Sci. Soc. Am. 59, 961 - 868.

Ferre, T.P.A., Bentley, L., Binley, A.M., Linde, N., Kemna, A., Singha, K., 2009. Critical steps for the continuing advancement of hydrogeophysics. Eos Transactions of American Geophysical Union 90, 200.

Griffiths D.H., Barker R.D., 1993. Two-dimensional resistivity imaging and modeling in areas of complex geology. J. Appl Geophys. 29, 211-226.

Hanson, B. R., Kaita, K., 1997. Response of electromagnetic conductivity meter to soil salinity and soil water content. J. Irrig Drain E-Asce. 123, 141-143.

Halvorson, A. D., Rhoades, J. D., 1974. Assessing soil salinity and identifying potential saline seep areas with field soil resistance measurements. J. Soil Sci. Soc. Am. 38, 576-581.

Hauck, C., 2002. Frozen ground monitoring using DC resistivity tomography J.Geophys. Res. Lett. 29(21), 2016.

Hayley, K., Bentley, L. R., Gharibi, M., Nightingale, M., 2007. Low temperature dependence of electrical resistivity: Implications for near surface geophysical monitoring. J. Geophys. Res. Lett. 34, L18402.

Hayley, K., Bentley, L.R., Gharibi, M., 2009. Time-lapse electrical resistivity monitoring of salt-affected soil and groundwater. J.Water Resour. Res. 45, W07425.

Hayley, K., Pidlisecky, A., Bentley, L.R., 2011. Simultaneous time-lapse electrical resistivity inversion. J. Appl. Geophys.75, 401–411.

Hendrickx, J. M. H., Borchers, B., Corwin, D. L., Lesch, S. M., Hilgendorf, A. C., Schlue, J., 2002. Inversion of soil conductivity profiles from electromagnetic induction measurements: Theory and experimental verification. J. Soil Sci. Soc. Am. 66, 673 - 685.

Hezarjaribi, A., Sourell, H., 2007. Feasibility study of monitoring the total available water content using non-invasive electromagnetic induction-based and electrode based soil electrical conductivity measurements. J. Irrig Drain E-Asce. 56, 53 - 65.

Hills, R.G., Porro, I., Hudson, D.B., Wierenga, P.J., 1989. Modeling one-dimensional infiltration into very dry soils. Model development and evaluation. J. Water Resour. Res. 25, 1259-1269.

Hinnell, A.C., Ferre, T.P.A., Vrugt, J.A., Huisman, J.A., Moysey, S., Rings, J., Kowalsky, M.B., 2010. Improved extraction of hydrologic information from geophysical data through coupled hydrogeophysical inversion. J. Water Resour. Res. 46, W00D40.

Huang, K., Mohanty, B.P., van Genuchten, M.Th., 1996. A new convergence criterion for the modified Picard iteration method to solve the variably saturated flow equation. J. Hydrol. 178, 69-91.

Huisman, J.A., Snepvangers, J.J.J.C., Bouten, W., Heuvelink, G.B.M. 2002, Mapping spatial variation of surface soil water content: comparison of ground-penetrating radar and time domain reflectometry. J. Hydrol. 269, 194–207.

Huisman, J.A., Sperl C., Bouten W., Verstraten, J.M., 2001. Soil water content measurements at different scales: Accuracy of time domain reflectometry and ground-penetrating radar. J. Hydrol. 245(1–4), 48–58.

Huyakorn, P.S., Thomas, S.D., Mercer, J.W., Lester, B.H., 1983. SATURN: A finite element model for simulating saturated-unsaturated flow and radionuclide transport. Electric Power Research Institute, Palo Alto, CA.

Huyakorn, P.S., Kool, J.B., Robertson, J.B., 1989. VAM2D-variably saturated analysis model in two dimensions (Version 5.0 with hysteresis and chain decay transport): documentation and user guide. NUREG/CR-5352, HGL89-01, Nuclear Regulatory Comm., Washington, DC.

Kachanoski, R. G., Gregorich, E. G., Van Wesenbeck, I. J., 1988. Estimating spatial variations of soil water content using non contacting electromagnetic inductive methods. Can. J. Soil Sci. 68, 715-722.

Kemna, A., Vanderborght, J., Kulessa, B., Vereecken, H., 2002. Imaging and characterization of subsurface solute transport using electrical resistivity tomography (ERT) and equivalent transport models. J. Hydrol. 267(3–4), 125–146.

Kim, J.H., Yi, M.J., Park, S.G., Kim, J.G., 2009. 4-D inversion of DC resistivity monitoring data acquired over a dynamically changing earth model. J. Appl. Geophys. 68, 522–532.

Kirkland, M.R., Hills, R.G., Wierenga, P.J., 1992. Algorithms for solving Richards's equation for variably saturated soils. J. Water Resour. Res. 28, 2049-2058.

Kool, J.B., van Genuchten, M.Th., 1991. HYDRUS: one-dimensional variably saturated flow and transport model, including hysteresis and root water uptake. Res. Rep. 124, US Salinity Laboratory, USDA, ARS, Riverside, CA.

Kosugi K., 1996. Lognormal distribution model for unsaturated soil hydraulic properties. J. Water Resour. Res. 32(9), 2697-2703.

Koefoed, O., 1968. The Application of the Kernel Function in Interpreting Geoelectrical Measurements, Geoexploration Monographs, Series I, NO.2, Gebriider Borntraeger, Berlin-Stuttgart.

LaBrecque, D. J., Ramirez, A. L., Daily, W. D., Binley, A. M., Schima, S. A., 1996a, ERT monitoring on environmental remediation processes. J. Meas Sci. 7, 375–383.

LaBrecque D.J., Miletto, M., Daily ,W.D., Ramirez, A.L., Owen, E., 1996b. The effects of noise on Occam's inversion of resistivity tomography data. J. Geophysics. 61, 538–548.

LaBrecque, D.J., Yang, X., 2001. Difference inversion of ERT data, a fast inversion method for 3-D in-situ monitoring. J Environ Eng Geoph. 6, 83–89.

Loke, M.H., Barker, R.D., 1996. Rapid least-squares inversion of apparent resistivity pseudosections using a quasi-Newton method. J.Geophys. Prospect. 44, 131–152.

Loke, M.H., 1999. Time-lapse resistivity imaging inversion. Proceedings of the 5th Meeting of the Environmental and Engineering European Section, Em1.

Loke, M. H., 2001. Tutorial: 2-D and 3-D electrical imaging surveys. Course Notes for USGS Workshop ‘‘2-D and 3-D Inversion and Modeling of Surface and Borehole Resistivity Data’’, Storrs, CT.

Looms, M.C., Jensen, K.H., Binley, A.M., Nielsen, L., 2008a. Monitoring unsaturated flow and transport using cross-borehole geophysical methods. J.Vadose Zone. 8, 227–237.

Looms, M.C., Binley, A.M, Jensen K.H., Nielsen, L. and Hansen, T.M., 2008b. Identifying unsaturated hydraulic parameters using an integrated data fusion approach on cross-borehole geophysical data. J. Vadose Zone. 7, 238–248.

McNeill, J. D., 1980. Electromagnetic terrain conductivity measurement at low induction numbers. Technical Note TN-6. Geonics Limited, Mississauga, Ontario, Canada.

McNeill, J. D., 1986. Rapid, Accurate Mapping of Soil Salinity Using Electromagnetic Ground Conductivity Meters. Tech. Note TN-18. Geonics Limited. Mississauga, ON, Canada.

Menke, W., 1984. Geophysical Data Analysis: Discrete Inverse Theory. Academic press, San Diego.

Michot, D., Benderitter, Y., Dorigny, A., Nicollaud, B., 2003. Spatial and temporal monitoring of soil water content with an irrigated corn crop cover using surface electrical resistivity tomography. J. Water Resour. Res. 39 (5),1138.

Monteiro Santos, FA., 2004. 1-D laterally constrained inversion of EM34 profiling data. J. Appl Geophys. 56, 123-134.

Monteiro Santos, F. A., Dupis, A., Andrade Afonso, A.R., Mendes-Victor, L. A., 1997. 1D joint inversion of AMT and resistivity data acquired over a graben. J. Appl Geophys. 38, 115-129.

Mualem, Y., 1976. A new model for predicting the hydraulic conductivity of unsaturated porous media. J. Water Resour. Res. 12(3), 513-522.

Munoz-Carpena, R., 2004. Field devices for monitoring soil water content. Bulletin No. 343. Florida Cooperative Extension Service, Institute of Food and Agricultural Sciences, University of Florida.

Musgrave, H., Binley, A.M, 2011. Revealing the temporal dynamics of subsurface temperature in a wetland using time-lapse geophysics. J. Hydrol. 396, 258-266.

Neuman, S. P., 1975. Galerkin approach to saturated-unsaturated flow in porous media, Chapter 10 in Finite Elements in Fluids, Vol. I, Viscous Flow and Hydrodynamics, edited by Gallagher, R. H., Oden, J. T., Taylor, C., Zienkiewicz, O.C. John Wiley & Sons, London, 201-217

Oldenborger, G.A., Knoll, M.D., Routh, P.S., LaBrecque, D.J., 2007. Time-lapse ERT monitoring of an injection/withdrawal experiment in a shallow unconfined aquifer. J. Geophysics. 72, 177–188.

Pinder, G. F., Gray, W. G., 1977. Finite Element Simulation in Surface and Subsurface Hydrology, Academic Press, New York, N.Y.

Ramirez, A., Daily, W., LaBrecque, D., Owen, E., Chesnut, D., 1993, Monitoring an underground steam injection process using electrical-resistance tomography: J.Water Resour. Res. 29, 1, 73-87

Reedy, R. C., Scanlon, B. R., 2003. Soil water content monitoring using electromagnetic induction. J. Geotech Geoenviron. 129, 1028 - 1039.

Revil, A., Cathles , L. M., Losh, S., Nunn, J. A., 1998. Electrical conductivity in shaly sands with geophysical applications, J. Geophys. Res. 103, 23,925–936.

Rhoades, J. D., Corwin, D. L., 1981. Determining soil electrical conductivity depth relations using an inductive electromagnetic soil conductivity meter. J. Soil Sci. Soc. Am. 45, 255-260.

Robinson, E. A., 1967, Statistical Communication and Detection, Chanes Griffin and Co. Ltd., London.

Sasaki, Y., 1989. Two-dimensional joint inversion of magnetotelluric and dipole– dipole resistivity data. J. Geophysics. 54, 254– 262.

Schaap, M.G., Leij, F.J., van Genuchten, M.Th., 2001. ROSETTA: A computer program for estimating soil hydraulic parameters with hierarchical pedotransfer functions. J. Hydrol. 251. 163–176.

Schön, J.H., 2004. Physical properties of rocks: fundamentals and principles of petrophysics. Seismic Exploration. vol. 18. Elsevier.

Sen, P. N., Goode, P. A., 1992. Influence of temperature on electrical conductivity on shaly sands. J. Geophysics. 57(1), 89– 96.

Sheets, K. R., Hendrickx, J. M. H., 1995. Non-invasive soil water content measurement using electromagnetic induction. J.Water Resour. Res. 31, 2401–2409.

Sherlock, M. D., McDonnell, J. J., 2003. A new tool for hydrologists: spatially distributed groundwater level and soil water content measured using electromagnetic induction. J. Hydrol. Process. 17, 1965 - 1977.

Shima, H., Sakashita, S., Kobayashi, T., 1996. Developments of non-contact data acquisition techniques in electrical and electromagnetic explorations. J. Appl Geophys. 35, 167-173.

Šimůnek, J., van Genuchten, M. Th., 1996. Estimating unsaturated soil hydraulic properties from tension disc infiltrometer data by numerical inversion. J. Water Resour. Res. 32(9), 2683-2696.

Šimůnek, J., van Genuchten, M. Th., 1997. Estimating unsaturated soil hydraulic properties from multiple tension disc infiltrometer data. J. Soil Science. 162(6), 383-398.

Šimůnek, J., van Genuchten, M. Th., 2000. The DISC computer software for analyzing tension disc infiltrometer data by parameter estimation. Versions 1.0, Research Report No. 145, U.S. Salinity Laboratory, USDA, ARS, Riverside, California, 34 pp.

Šimůnek, J., Šejna, M., van Genuchten, M. Th., 2006. The HYDRUS Software Package for Simulating Two- and Three-Dimensional Movement of Water, Heat, and Multiple Solutes in Variably- Saturated Media, User Manual, Version 1.0, PC Progress, Prague, Czech Republic.

Singha, K., Gorelick, S.M., 2005. Saline tracer visualized with three-dimensional electrical resistivity tomography: Field-scale spatial moment analysis. J. Water Resour. Res. 41, W05023.

Singha, K., Gorelick, S.M., 2006. Hydrogeophysical tracking of three-dimensional tracer migration: The concept and application of apparent petrophysical relations. J. Water Resour. Res. 42, W06422.

Slater, L., Sandberg, S., 2000. Resistivity and induced polarization monitoring of salt transport under natural hydraulic gradients. J. Geophysics. 65, 408–420.

Slater, L., Binley, A.M., Daily, W.D., Johnson, R., 2000. Cross-hole electrical imaging of a controlled saline tracer injection. J. Appl. Geophys. 44, 85–102.

Triantafilis, J., Monteiro Santos, FA., 2010. Resolving the spatial distribution of the true electrical conductivity with depth using EM38 and EM31 signal data and a laterally constrained inversion model. J. Aust Soil Res. 48, 434-446

Triantafilis, J., Monteiro Santos, FA., 2009. 2-Dimensional soil and vadose-zone representation using an EM38 and EM34 and a laterally constrained inversion model. J. Aust Soil Res. 47, 809-820.

Triantafilis, J., Lesch, S.M., Lau, K.L., Buchanan, S.M., 2009. Field level digital soil mapping of cation exchange capacity using electromagnetic induction and a hierarchical spatial regression model. Aust. J. Soil Res. 47:651–663.

Vanderborght, J., Kemna, A., Hardelauf, H., Vereecken, H., 2005. Potential of electrical resistivity tomography to infer aquifer transport characteristics from tracer studies: A synthetic case study. J. Water Resour. Res. 41, W06013.

Van Genuchten, M. Th., 1980. A closed-form equation for predicting the hydraulic conductivity of unsaturated soils, J. Soil Sci. Soc. Am. 44, 892-898.

Van Overmeeren, R.A., Gehrels, J.C., Sariowa, S.V., 1997. Ground penetrating radar for determining volumetric soil water content: results of comparative measurements at two test sites. J. Hydrol. 197, 316–338.

Vatson, G. N., 1966. A treatise on the theory of Bessel functions, Cambridge University press, 2nd. edition reprinted.

Vogel, T., Císlerová, M., 1988.On the reliability of unsaturated hydraulic conductivity calculated from the moisture retention curve. J. Transport Porous Med. 3, 1-15,

Wait, J. R., 1982. Geo-electromagnetism. Academic Press, New York.

Waxman, M. H., Thomas, E. C., 1974. Electrical conductivities in shaly sands: I. The relation between hydrocarbon saturation and resistivity index; II. The temperature coefficient of electrical conductivity, J. Pet.Technol. 26(2), 213– 225.

Whalley, W. R., Dean, T. J., Izzard, P., 1992. Evaluation of the capacitance technique as a method for dynamically measuring soil water content. J. Agr Eng Res . 52, 147-155.

Williams, B. G., Hoey, D., 1987. The use of electromagnetic induction to detect the spatial variability of the salt and clay content of soils. Aust. J. Soil Res. 25, 21 - 27.

Wollenhaupt , N. C., Richardson, J. L., Foss, J. E., Doll, E. C., 1986. A rapid method for estimating weighted soil salinity from apparent soil electrical conductivity measured with an above ground electromagnetic induction meter. Can. J. Soil Sci. 66, 315 - 321.

Ye, M., Khaleel, R., Yeh, T. C. J., 2005. Stochastic analysis of moisture plume dynamics of a field injection experiment. J. Water Resour. Res. 41, W03013.

Zhu, Q., Lin, H.S., Doolittle, J.A., 2010. Repeated Electromagnetic Induction Surveys for improved Soil Mapping in an Agricultural Landscape. J. SWC. 74(5), 1763-1774.

Zienkiewicz, O.C., 1977.The Finite Element Method, 3rd ed., McGraw-Hill, London, United Kingdom.

Resumo Alargado

A caracterização hidrológica dos primeiros 1-2 metros do solo, é amplamente reconhecida como sendo crucial em agricultura. A condutividade hidráulica é uma propriedade do solo que determina a capacidade de movimentação da água neste meio e, embora se reconheça a sua grande importância continua a ser um dos parâmetros mais difíceis de estimar.As técnicas laboratoriais têm limitações devido ao tamanho da amostra e ao facto das condições laboratoriais não serem as mesmas que no terreno, havendo preferência pelas técnicas de medição in-situ. Assim, o desenvolvimento de métodos de monitorização espaço-temporal do conteúdo em água no solo é muito importante para o controlo daquele parâmetro. Investigações recentes mostraram que os métodos de geofísica aplicada são uma alternativa económica, e com a vantagem de serem métodos não evasivos, para a caracterização hidrológica do solo. Os métodos directos, baseado em furos, provocam alterações nas condições naturais do terreno. Acresce que as medições usando métodos directos não podem ser repetidas no tempo e no mesmo local, embora a caracterização hidrológica do solo exija essa repetição. A monitorização geofísica, usando métodos 4D (espaço-tempo) é uma ferramenta poderosa que pode ser usada para adquirir dados que permitam a estimativa das variáveis hidrológicas que dependem do tempo, como a condutividade hidráulica.

Neste estudo, utilizaram-se medidas da condutividade eléctrica obtidas através de tomografia eléctrica e da aplicação do equipamento EM38 para a construção de uma base de dados, com o objectivo de estudar as variações espaço-temporais do conteúdo em água e, também, estimar as propriedades hidráulicas de um solo não saturado. Este estudo foi realizado em dois locais distintos: um em condições naturais e um outro em situação de injecção de água. O primeiro estudo foi realizado no Campus da Universidade de Lisboa, num local em que o terreno é predominantemente argiloso, com permeabilidade baixa e grande capacidade de retenção de água. O segundo estudo foi realizado em Samora Correia (a Leste de Lisboa) num local de solo arenoso com permeabilidade elevada e com fraca capacidade de retenção de água. As variações de temperatura do solo foram medidas durante as experiências e o efeito da variação da condutividade com a temperatura foi avaliado em ambos os conjuntos de dados adquiridos (EM38 e resistividade), assumindo uma variação da resistividade de 2% por cada grau Celsius de variação da temperatura.

A estimativa das propriedades hidráulicas do solo não saturado foi feita com base em simulações de fluxo de água. Os modelos hidrológicos utilizados permitem a simulação do

movimento da água em profundidade e em função do tempo com base na solução numérica da equação de Richard. Assumiu-se que a capacidade de retenção da água e a condutividade são bem representadas pelos parâmetros de van Genuchten (1980). A equação de Richard foi utilizada para o desenvolvimento de um modelo 1D, utilizando um passo temporal de 1 s e espacial de 1 cm. Os resultados do modelo foram comparados com os do programa HYDRUS 1D com o objectivo de validar o modelo, tendo-se observado que os resultados são consistentes com os calculados pelo HYDRUS. Os erros associados às estimativas da massa de água são, aproximadamente de 2%. Para as simulações do movimento de água em meio 2D utilizou-se o programa HYDRUS.

O cálculo dos parâmetros de Genuchten foi feito utilizando-se duas aproximações.Na primeira, sem os constrangimentos dos dados geofísicos e,na segunda usando esses constrangimentos. No primeiro caso os dados geofísicos foram invertidos e os modelos obtidos usados na estimativa dos parâmetros hidrológicos utilizando-se as relações empíricas (determinadas in-situ) entre a resitividade e o conteúdo em água (ρ vs. S). Esta aproximação foi usada considerando um modelo 2D. A inversão, utilizando todos os dados recolhidos na experiência de monitorização, foi realizada usando-se técnicas de inversão conhecidas por "time-lapse", com o objectivo de reduzir as incertezas. Mais especificamente, foram usados os seguintes métodos: o método da razão (ratio method), das diferenças (difference inversion method), model cruzado (cross model) e a inversão 4D. Os modelos de resistividade (ERT) e EM38 foram então usados para o cálculo do conteúdo em água usando-se as relações entre a resistividade (condutividade) e o conteúdo em água, previamente estabelecidas para cada local.Utilizou-se o método da análise dos momentos, aplicado aos modelos geofísicos, para se calcularem as condutividades hidráulicas. Neste método procura-se quantificar a massa do sistema, a localização do centro demassa e o modo como a massa se desloca no tempo. Comparando os resultados do método dos momentos com os obtidos das simulações de infiltração, foi possívelobter uma estimativa da condutividade hidráulica.

O estudo relizado no campus da Universidade de Lisboa, usando o primeiro método mostrou que ambos os conjuntos de dados geofísicos (EM38 e ERT) conseguiram detectar variações da resistividade do solo representativas da variação sazonal do conteúdo de água. Os resultados indicaram que o conteúdo em água, mesmo no verão, dificilmente diminui abaixo de 20%. Apenas se observaram valor baixos de conteúdo em água em zonas muito superficiais do terreno e durante o verão.Durante o período chuvoso, o conteúdo em água atinge valores de 30%. Os resultados mostram que o solo no campus é semi-permeável. A

variação espaço-temporal do conteúdo de água é da ordem de 10%. Os cálculos realizados usando os dados de EM38 e ERT sugerem que a condutividade hidráulica deverá ser da ordem de 1-10 cm/dia. Neste local, os resultados obtidos com o EM38 são compatíveis com os obtidos pelaresistividade (ERT).

Na segunda zona de estudo (em Samora Correia), os resultados mostraram que as variações do conteúdo em água e, consequentemente, da resistividade.São fundamentalmente condicionadas pela precipitação diária devido à rápida infiltração e elevada permeabilidade hidráulica dos sedimentos arenosos. Os dados de ERT e de EM38 são capazes de mostrar de modo qualitativo a distribuição do conteúdo em água. Ambos os métodos são capazes de detectar variações na distribuição do conteúdo em água, no entanto, a rápida infiltração na zona não saturada, torna impraticável a monitorização para a estimativa e constrangimento dos parâmetros hidrológicos do movimento da água em condições naturais. Adicionalmente, verificou-se ser muito difícil trabalhar com o EM38 em solo arenoso e seco. Assim, desenhou-se e levou-se a efeito uma experiência de injecção controlada de água. Nestas condições foi possível monitorizar a rápida infiltração usando o méodo da resistividade. O método do momento constrangiu o intervalo dos valores da condutividade hidráulica saturada entre 0.5 e 1.2 cm/min.

Foi realizado um estudo numérico com o objectivo de verificar até que ponto a inversão (não contrangida) de dados de resistividade pode alterar a análise do método dos momentos e influenciar a estimativa dos parâmetros hidrológicos. Os resultados deste teste mostram que há uma influência significativa da inversão. Contudo, foi possível verificar que a inversão 4D apresenta resultados satisfatórios.

No segundo método utilizado neste estudo, os dados geofísicos foram usados directamente no modelo hidrológico. Nesta aproximação os parâmetros hidrológicos foram alterados até se obter concordância entre os dados experimentais e as respostas do modelo. Desenvolveu-se um modelo 1D com o objectivo de determinar os três parâmetros de van Genuchten (α, n and Ks)a partir da resistividade eléctricae da água infiltrada. Os dados adquiridos em Samora Correia, no teste de injecção deágua foram então utilizados na avaliação de um conjunto de modelos hidrológicos prováveis. Dado que não se utilizou nenhuma inversão de dados geofísicos, as incertezas devido ao processo de inversão, tais como artefactos matemáticos e constrangimento subjectivos foram eliminados. Os resultados obtidos da aplicação deste método, revelaram-se constrangimentos razoáveis na estimativa de Ks e n. Os valores obtidos

mostram uma boa coerência com os obtidos com a aplicação do primeirométodo assumindo modelos 2D.